Measurement and modelling of soil-structure interaction for open caisson shafts

Jack O. Templeman
St Catherine's College
University of Oxford

A thesis submitted for the degree of
Doctor of Philosophy

Michaelmas 2022

Abstract

Measurement and modelling of soil-structure interaction for open caisson shafts

Jack O. Templeman
St Catherine's College, University of Oxford
A thesis submitted for the degree of *Doctor of Philosophy*
Michaelmas 2022

Monolithic open caissons are a common method of constructing underground shafts, for applications including storage tanks, pumping stations, deep foundations and tunnelling. The caisson construction process uses concurrent casting of massive reinforced concrete walls and excavation of soil within the structure, causing the caisson to 'sink' into the ground under its self-weight. Achieving controlled sinking relies on accurate estimation of the resistance generated by the interaction between the caisson and the surrounding soil. The lack of dedicated research and design methods means there is significant uncertainty in determining the frictional and bearing resistances during design, particularly in cohesionless soils.

This thesis aims to explore the soil-structure interaction during caisson sinking in sands, through numerical modelling and experimental testing. The outputs of recent caisson field monitoring were limited by critical failures of electrical sensors. To facilitate measurement of the caisson-soil contact stresses, the development of more robust sensor technology is necessarily pursued. A new framework for multi-axis force sensing is demonstrated, to enable optical strain measurement in the form of FBGs to be utilised. This is applied to create a sensor for detailed measurements of combined normal and frictional interface stresses in underground construction applications. Numerical simulation and physical testing build confidence in the new design, as well as exploring a novel approach for measuring effective normal stress.

Friction at the caisson external surface is explored through laboratory-scale testing in dense sand, using a bespoke large-displacement interface shear apparatus. The new optical sensors are employed to obtain localised contact stress measurements and particle image velocimetry provides observations of the soil displacements. The results give insight into the mechanisms associated with different interface conditions, including over-cut creation and lubrication.

The bearing capacity at the base of the caisson wall is explored through numerical modelling. An extensive parametric study using finite element limit analysis considers the influence of salient caisson parameters, including the taper angle and cutting shoe. A complimentary targeted study with finite element analysis is used to assess the influence of soil non-associativity and the development of horizontal reaction. Detailed observations of the soil failure mechanisms provide new insight into the bearing behaviour in sands. The numerical results are compared against recent laboratory-scale experimental tests and used to develop simplified closed-form expressions for bearing capacity estimation in routine design.

Acknowledgements

First and foremost, I would like to thank my supervisor Dr Brian Sheil for his invaluable support and guidance throughout my DPhil. I am very grateful for his advice and continuous encouragement, as well as the detailed reviews of my writing. His friendly manner, passion for engineering and unwavering work ethic have greatly enriched my time at Oxford.

I am very grateful to the Department of Engineering Science for supporting the studentship for this research. I would like to thank Professor Guy Houlsby and Dr Róisín Buckley for their assessment and review of my work throughout my time at Oxford. I also thank Professor Byron Byrne for his useful advice and guidance in pursuing commercialisation. Thanks also go to Ward & Burke Construction, in particular to Michael Ward and Ronan Royston, for helping to guide the research focus and facilitating the experimental work.

This research would not have been completed without the significant support of many individuals. In particular, thanks go to Bryn Phillips for all the help in the lab and maintaining my sanity during the challenges and delays of COVID-19. The unhealthy amount of chicken tikka baguettes and frequent reminders of ‘aren’t soils cool’ got us through! Special thanks go to Clive Baker for all the support and advice over the past three years. Clive’s technical expertise and experience were invaluable to the experimental work and I will sorely miss his good humour and stories. Thanks also go to Alison May for assistance with procurement and general problem solving! I am also very grateful for help of everyone in the Department’s workshop, maintenance and stores teams, in particular Duncan Constable, Chris Hatcher and Lewis Burke.

I would like to thank everyone in the FOCUS research group for their interesting discussions, presentations and helpful suggestions over the past few years. I wish you all the best for the rest of your research and your future endeavours. Particular thanks go to Dr. Geyang Song for his assistance on all aspects of sensor development, and to Dr. Zhandos Orazalin for advice on numerical modelling. Thanks also go to Alex Swallow for assistance in the experimental work and the hours spent shovelling sand.

It has been a pleasure to be part of the Civil Engineering Group at Oxford and I thank everyone that has frequented the Jenkin building for making the past few years so enjoyable. Special thanks go to the pre-COVID climbing and Wallis room lunch groups, for the welcome distraction and questionable discussions respectively.

I would like to thank my family for their endless support and encouragement over the years. Thanks also go to Gwen for all of the overly enthusiastic affection over the past two years. Finally, I would like to thank Robyn for her love, support and patience though this challenging period. I thoroughly look forward to our next chapter in life.

Table of Contents

Notation

2D	Two-dimensional
3D	Three-dimensional
CPT	Cone penetration test
DOF	Degree of freedom
DTG	Draw tower grating
EC7	Eurocode 7
EMI	Electromagnetic interference
ERSG	Electrical resistance strain gauge
FBG	Fibre Bragg grating
FEA	Finite element analysis
FELA	Finite element limit analysis
FS	Factor of safety
HLM	Hierarchical linear model
ID	Internal diameter
LB	Leighton Buzzard
LB	Lower bound
LR	Linear regression
LVDT	Linear variable differential transformer
NI	National Instruments
PIV	Particle image velocimetry
PSD	Particle size distribution
PSLG	Planar straight line graph
PT	Pressure transducer
PTFE	Polytetrafluoroethylene

RC	Reinforced concrete
SLSI	Soil-lubricant-structure interface
SSCS	Soil-structure contact stress
SSI	Soil-structure interaction
TP	Test piece
UB	Upper bound

a	Meridional yield function rounding parameter
a_{0-4}	Repeating pattern layout FBG orientation angles
A	Footing embedded area
A, B, C	Yield function coefficients
A_f	Sensor face area
A_u	Sensor face underside area
B	Caisson wall thickness
B_w	Footing embedded width
c	Soil cohesion
C	Bayesian optimisation cost function
C_U	Soil coefficient of uniformity
C_Z	Soil coefficient of curvature
d	FBG array centre spacing distance
d_{10}, d_{30}, d_{50}, d_{60}	Soil effective particle sizes
D	Caisson internal diameter
D_R	Relative density
e_min, e_max	Soil minimum / maximum void ratio
E	Young's modulus
f	Yield function
$\boldsymbol{f}$	Vector of actions applied to multi-axis sensor
$\hat{\boldsymbol{f}}$	Vector of outputs from multi-output linear regression model

F_x, F_y, F_z	Force component in x, y, z direction
G_s	Soil particle specific gravity
h	Caisson external embedment depth
h_crit	Critical caisson embedment depth
h_int	Caisson internal overburden soil depth
H	Horizontal bearing force
H'	Dimensionless horizontal bearing capacity factor
K	Coefficient of lateral earth pressure
K	Function controlling yield function shape in octahedral space
l	FBG length
l	Caisson cutting shoe length (ahead of cutting face apex)
l_b	Caisson cutting shoe length (behind cutting face apex)
L	Sensor wall axial length
m	Number of multi-axis sensor outputs
m	Curve fitting parameter
M_x, M_y, M_z	Moment component about x, y, z axis
n	Number of strain measurements/FBGs on multi-axis sensor
N'	Dimensionless vertical bearing capacity factor
$N'_{h=0}$	Dimensionless vertical bearing capacity factor - zero embedment case
$N'_{R=\infty}$	Dimensionless vertical bearing capacity factor - plane strain case
$N'_{t=0}$	Dimensionless vertical bearing capacity factor - no cutting shoe case
$N'_{\beta=90^\circ}$	Dimensionless vertical bearing capacity factor - flat footing case
$N'_{\psi'=\phi'}$	Dimensionless vertical bearing capacity factor - associated flow case
q_c	CPT cone resistance
r_o	Box sensor corner outer radius
R	Caisson internal radius
R^2	Coefficient of determination
R_a	Average surface roughness

R_i	Cylinder inner radius
R_o	Cylinder outer radius
s	Box sensor wall side width
s_xx, s_yy, s_zz	Deviatoric normal stress components in 3D Cartesian coordinate system
t	Caisson cutting shoe/over-cut thickness
t	Sensor wall thickness
T	Temperature
u	Pore pressure
$\boldsymbol{u}$	Vector of strain/FBG measurements from multi-axis sensor
V	Vertical bearing force
$\boldsymbol{W}$	Coefficients matrix for multi-output linear regression model
x	Cartesian coordinate direction
y	Cartesian coordinate direction
z	Cartesian coordinate direction
$\boldsymbol{z}$	Vector of FBG axial positions on multi-axis sensor
z_i	Axial position of ith FBG on multi-axis sensor

α	Interface roughness factor
α_f	Cutting face interface roughness factor
α_s	Coefficient of thermal expansion of sensor structure
α_s	Cutting shoe interface roughness factor
β	Cutting face taper angle
γ'	Soil effective unit weight
γ'_min, γ'_max	Soil minimum / maximum dry unit weight
γ_{12}	Sensor wall shear strain
δ	Interface friction angle
δ_f	Cutting face interface friction angle
$\delta_\mathrm{v,ext}$	Caisson vertical external surface interface friction angle

$\Delta\lambda_{\mathrm{i}}$	Peak wavelength shift of *i*th FBG on multi-axis sensor
$\Delta\lambda_{\mathrm{p}}$	FBG peak wavelength shift
ΔT	Temperature change
ε	Strain
ε_{11}	Sensor wall lateral strain component
ε_{22}	Sensor wall axial strain component
$\varepsilon_{2'2'}$	Sensor wall strain aligned with FBG axis
θ	FBG orientation angle
θ	Stress invariant (Lode angle)
$\boldsymbol{\theta}$	Vector of FBG orientation angles for multi-axis sensor
θ_{i}	Orientation angle of *i*th FBG on multi-axis sensor
θ_{T}	Transition angle for yield function rounding in octahedral plane
$\lambda_{0,\mathrm{i}}$	Zero peak wavelength reading of *i*th FBG on multi-axis sensor
λ_{i}	Peak wavelength of *i*th FBG on multi-axis sensor
λ_{p}	FBG peak wavelength
ν	Poisson's ratio
ρ_1, ρ_2	CPT density fitting coefficients
$\bar{\sigma}$	Stress invariant (deviatoric stress measure)
σ_{m}	Stress invariant (mean normal stress)
σ_{11}	Sensor wall lateral stress component
σ_{22}	Sensor wall axial stress component
σ_{n}	Total normal stress
σ'_{n}	Effective normal stress
σ'_{v}	Vertical effective stress
σ_{xx}, σ_{yy}, σ_{zz}	Normal stress components in 3D Cartesian coordinate system
σ_{xy}, σ_{yz}, σ_{zx}	Shear stress components in 3D Cartesian coordinate system
τ	Shear stress
τ_{12}	Sensor wall shear stress component

τ_{x}, τ_{y}	Shear stress in x, y direction
ϕ	Column sensor circumferential angular position
$\boldsymbol{\phi}$	Vector of FBG circumferential angular positions on column sensor
ϕ'	Soil friction angle
ϕ'_{cs}	Soil critical state angle of friction
ϕ_{i}	Circumferential positions of ith FBG on column sensor
χ_{c}	Normalised CPT cone resistance
ψ'	Soil dilation angle

Chapter 1

Introduction

1.1 Background

Infrastructure development has been coherently identified as being of national importance, underpinning the functioning of society and the economy (HM Treasury, 2020). Underground construction is a vital means of delivering many infrastructure solutions. Tunnels, shafts and deep excavations are important components for sectors including transportation, clean and waste water, and energy. The global underground construction sector was estimated to be worth €125 billion annually in 2019, with an annual growth of around 9% (International Tunnelling and Underground Space Association, 2019). In the UK alone, examples such as High Speed 2 (£72–98 billion; 2019 prices), Crossrail (£18.8 billion) and Thames Tideway (£4.3 billion) indicate the scale and profile of current major underground construction projects.

The demand for underground construction is largely driven by the need to upgrade or create new infrastructure systems, either because existing systems are reaching the end of their design life or are insufficient to meet modern requirements (National Infrastructure Commision, 2017). There is often a predilection for underground construction in urban environments, to minimize above-ground disruptions where available land space is very limited. Urban populations are increasing at a rapid rate, with a predicted increase of 2.5 billion people living in urban areas between 2018 and 2050, reaching 68% of the global population (United Nations, 2018). This growth, combined with the impact of climate change and higher environmental standards, are placing significant pressure on existing services and utilities. Continued development in urban centres is likely to face considerable challenges in future, such as the density of infrastructure

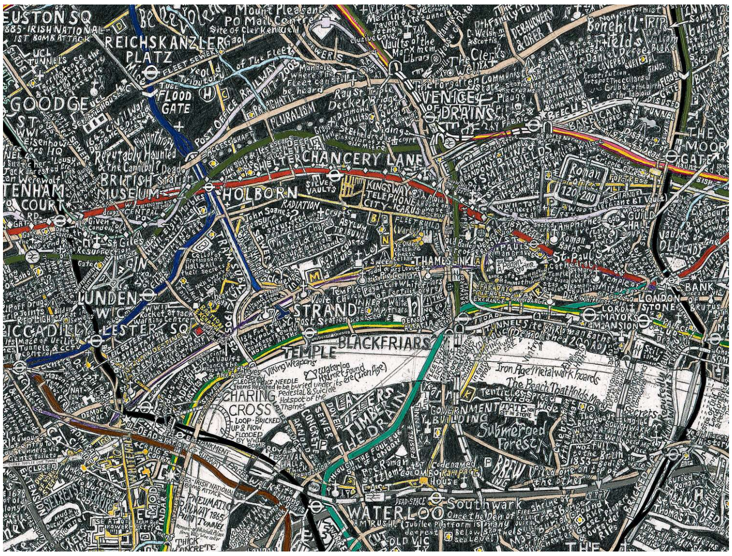

Figure 1.1 Detail of *London Subterranea* (2012) by Stephen Walter. Artwork commissioned by The London Transport Museum

in the underground space, as illustrated in London in Figure 1.1.

There is a significant drive for improvement and advancement in construction. The joint Government and Industry strategy ‘Construction 2025’ sets clear long-term targets, including a 33% reduction in construction costs and 50% reductions in both overall construction time and greenhouse gas emissions (Department for Business, Innovation & Skills, 2013). These targets are being addressed by major Government led initiatives such as the ‘Transforming Construction’ Industrial Strategy Challenge Fund, which aims to promote innovation and the creation of new construction techniques (UK Research and Innovation, 2018).

To meet modern infrastructure demands whilst adhering to the strict targets, there is a need for enhanced understanding of underground construction processes. Significant benefit could be gained from improving our knowledge of fundamental mechanisms, developing more comprehensive design methods and expanding measurement capabilities to gather robust data during construction. Potential outcomes could include reductions in design conservatism, lowering of construction risk and enabling more advanced solutions to be considered. Given the current and planned high-profile projects, even 1% efficiency gains can lead to major economical and environmental savings.

1.2 Open caisson shaft construction

1.2.1 Overview

Shafts are commonplace in the construction industry for the provision of vertical underground structures or passageways. The most commonly employed method of shaft construction in the UK is segmental lining, in which pre-cast concrete segments are bolted together to form rings. Shafts can be formed by underpinning, where the ground is excavated under the current structure to allow subsequent rings to be installed below (e.g. Allenby and Kilburn, 2015; Faustin *et al.*, 2018; Figure 1.2a), or by caisson sinking, in which the structure is jacked into the ground by hydraulic rams and rings are placed above (e.g. Newman and Wong, 2011; Figure 1.2b). There are a multitude of other shaft construction methods, including secant piles (e.g. Lindquist and

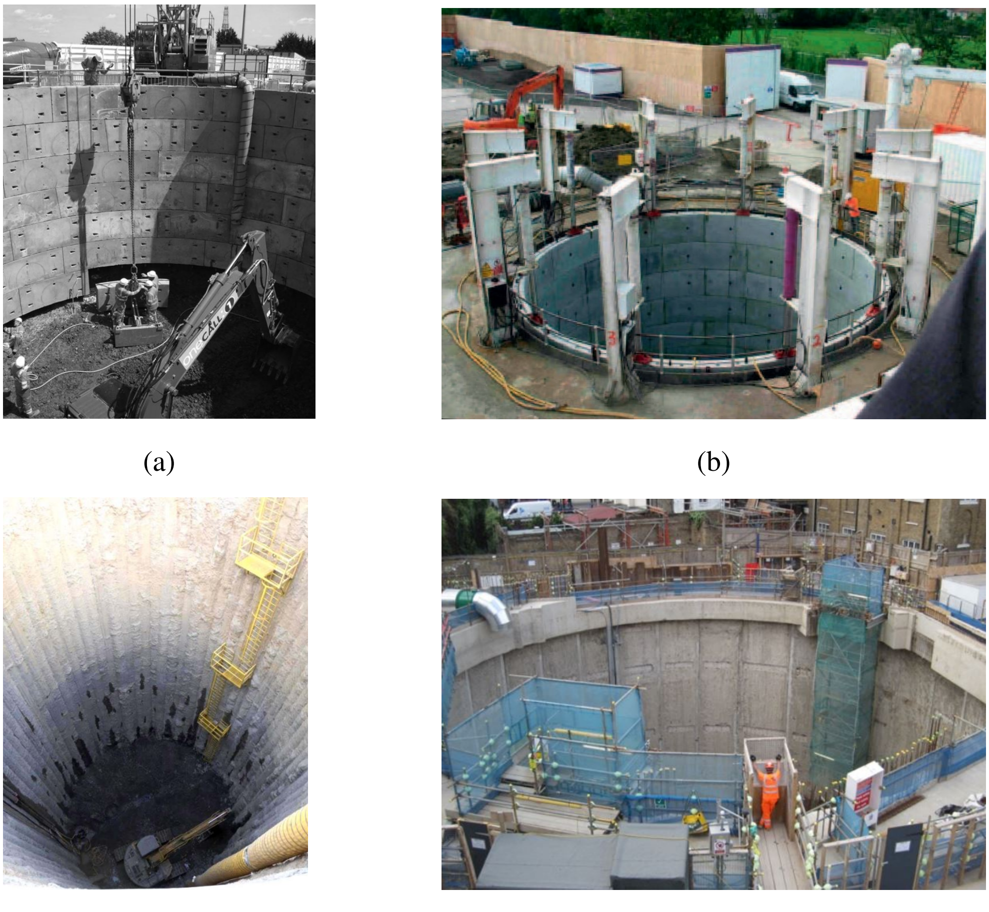

(a) (b)

(c) (d)

Figure 1.2 Examples of shaft construction methods: (a) segmental underpinning (Faustin *et al.*, 2018), (b) segmental open caisson sinking (Newman and Wong, 2011), (c) secant piles (Lindquist and Jameson, 2011), (d) diaphragm walls (D'Alessio and Taylor, 2016)

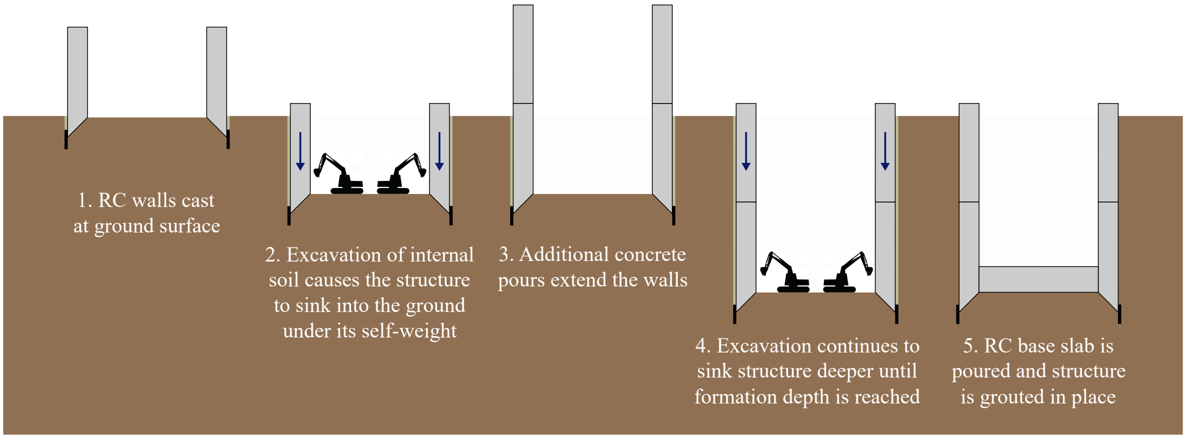

Figure 1.3 Simplified schematic overview of the salient steps of monolithic open caisson shaft construction (not to scale)

Jameson, 2011; Figure 1.2c), diaphragm walls (e.g. D'Alessio and Taylor, 2016; Schwamb, 2014; Figure 1.2d) and sheet piled cofferdams. The most suitable method for a specific application depends on factors such as shaft diameter and depth, soil and groundwater conditions, proximity to other structures and their sensitivity to settlement (Puller, 1996).

Monolithic open caisson sinking is another popular method of constructing vertical shafts for applications including storage tanks and pumping stations for the water and wastewater industry (e.g. Abdrabbo and Gaaver, 2012; Fischer *et al.*, 2004; Nonveiller, 1987; Royston *et al.*, 2022a), launch and reception pits for tunnel construction (e.g. O'Dwyer *et al.*, 2018; Phillips *et al.*, 2019), and deep foundations (e.g. Chandler *et al.*, 1984). The construction procedure involves concurrent casting of massive reinforced concrete (RC) walls and excavation of soil from within structure, as illustrated in Figure 1.3. This process causes the shaft to 'sink' into the ground, driven by the self-weight of the walls. To achieve deeper shaft depths, the height and weight of the walls are increased by performing additional concrete pours, with continued internal excavation. This process (steps 3 and 4 in Figure 1.3) can be repeated until the caisson reaches the desired formation depth. An example of an open caisson shaft at two different stages of construction is shown in Figure 1.4.

Monolithic open caisson shafts (hereinafter referred to simply as 'caissons' for brevity) are typically circular in plan shape. This is efficient as it minimises the friction during sinking for a given base area (Tomlinson, 2001) and loading from the surrounding soil is supported

(a) (b)

Figure 1.4 Construction of a 32 m internal diameter open caisson shaft by Ward & Burke Construction Ltd for an underground pumping station in Blackpool, UK: a) wall casting pre-excavation, b) structure sunk into the ground post-excavation

predominantly in hoop compression. Recent examples of caisson shafts have been constructed with diameters, D, varying between 3 m and 40 m, and over depths, h, between 5 m and 100 m (Royston, 2018). Different caisson shapes, such as rectangular or ellipse, can also be adopted and these are typically selected to suit the specific operational function of the structure.

Excavation of soil from the caisson interior is used to initiate and control the sinking process. Caissons can be sunk in dry conditions using excavators situated within the caisson (as in Figure 1.4) or in wet conditions with soil excavated using a clamshell bucket from the ground level. In suitable ground conditions, caisson sinking can be a safe and efficient method of shaft construction, as the permanent structure is formed as a one-pass system and is used to retain both soil and ground water during excavation. Compared to other methods, it can minimise man-entry requirements and is generally considered to be more economical in terms of both time and cost (Allenby and Kilburn, 2015).

1.2.2 Caisson soil-structure interaction

The sinking stage of the caisson construction process involves carefully controlling the balance between the self-weight of the structure and upwards resistance generated from soil-structure interaction (SSI; Royston *et al.*, 2022a; Sheil *et al.*, 2018b). The latter comprises bearing stresses, v, acting at the base of the caisson and frictional stresses, τ, that are exerted on the exterior surface of the caisson walls by the surrounding soil (see Figure 1.5).

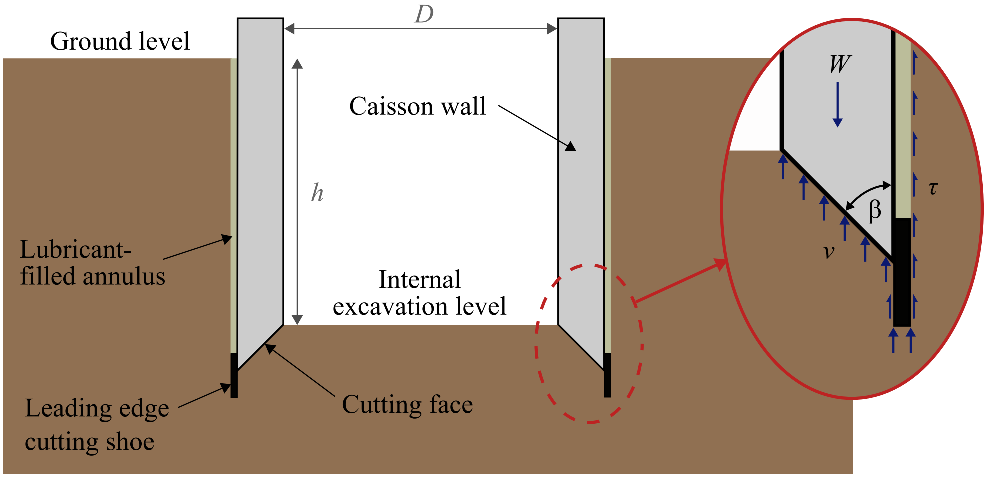

Figure 1.5 Illustration of a section through an open caisson shaft, showing typical construction features and the contact stresses acting on the walls during sinking

Accurate estimation of these contact stresses is essential to reduce design inefficiencies and construction risks. Over-prediction can lead to sudden or excessive caisson movements (Royston *et al.*, 2022a). Furthermore non-uniform resistance, arising through heterogeneity of ground conditions or poor excavation, can cause loss of verticality or tilting (Abdrabbo and Gaaver, 2012). However, the primary risk during caisson sinking is under-estimation of the contact stresses, which can lead to the caisson becoming 'wedged' and unable to reach the desired formation level. Potential remedial measures in this case can be very costly, have significant associated risks and remain largely unverified. Current practice typically relies on using increased caisson wall thickness to ensure sufficient self-weight, W, to comfortably overcome the resistances to sinking. This has obvious inefficiencies in terms of both cost and environmental impact, through excessive material use beyond the structural requirements.

Specific features are incorporated in the design of the caisson to minimise and control the contact stresses between the structure and the surrounding soil during construction. The cross-section of the RC caisson wall is tapered at the base to form a so-called 'cutting face', as shown in Figure 1.5. This is typically created using an angled bearing pad cast from concrete beneath the wall (see Figure 1.6a), which is broken out to commence shaft sinking (Royston, 2018). A footing taper angle, β, of 45° is most commonly used in industry, derived from accumulated site experience (Royston *et al.*, 2016). ISI (1982) and Tomlinson (2001) recommend varying β depending on ground conditions: 30° for stiff clays and 45° for sands and soft clays. The use of

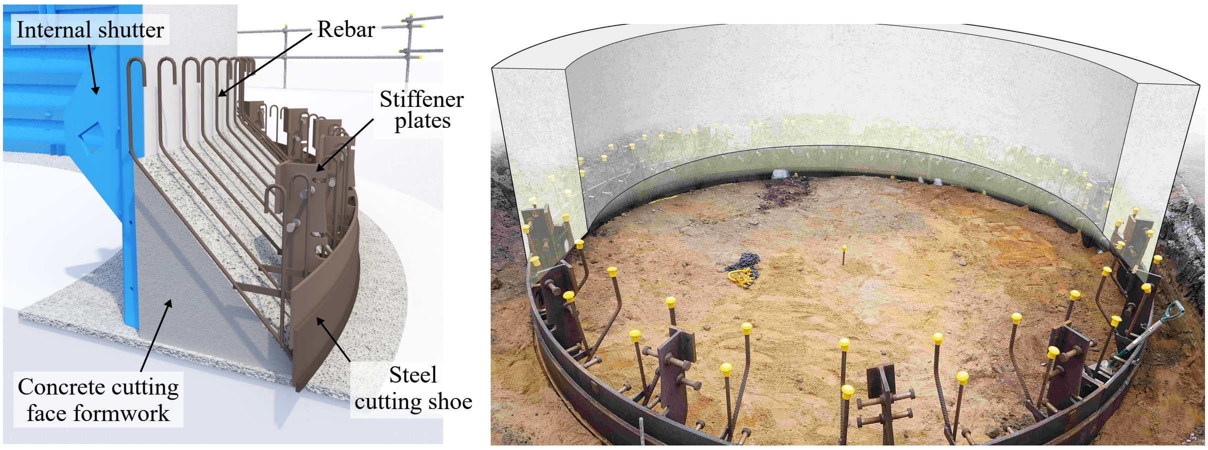

(a) (b)

Figure 1.6 Prefabricated steel cutting shoe used by Ward & Burke Construction Ltd: (a) RC cutting face casting details, (b) assembled shoe with a visualisation of the caisson wall

a tapered cutting face is claimed to aid the sinking process, by cutting into the soil, lowering the vertical bearing capacity, and mobilising the soil failure mechanism to the inside of the caisson for excavation (Chavda *et al.*, 2020; Fischer *et al.*, 2004; Royston *et al.*, 2016).

Another important construction feature is the use of an external over-cut, which was developed and patented by Ozerov in 1945 (Ter-Galustov *et al.*, 1966). The excavation is typically formed with a 30–100 mm larger radius than the shaft itself (Abdrabbo and Gaaver, 2012). This is generally achieved by casting a thicker section of RC wall (e.g. Abdrabbo and Gaaver, 2012; Nonveiller, 1987), or more commonly, by installing a steel 'cutting shoe' at the leading edge of the caisson wall (e.g. Allenby *et al.*, 2009; Newman and Wong, 2011; Royston *et al.*, 2022a), as shown in Figure 1.6b. Similar to pipejacked tunnelling, this forms a void between the caisson and the surrounding soil as the structure sinks, which is typically referred to as the 'annulus'. This is pumped with a support fluid, most commonly a bentonite slurry, which acts to stabilize the excavation and lubricate the interface (Royston, 2018; Sheil *et al.*, 2018b). The behaviour of the resulting soil-lubricant-structure interface (SLSI) at the caisson extrados has a significant influence on the development of frictional stresses during sinking. After the caisson reaches formation depth, the annulus is typically pumped with grout to displace the lubricant, stabilise the excavation and provide frictional resistance in the permanent state (Allenby *et al.*, 2009; step 5 in Figure 1.3).

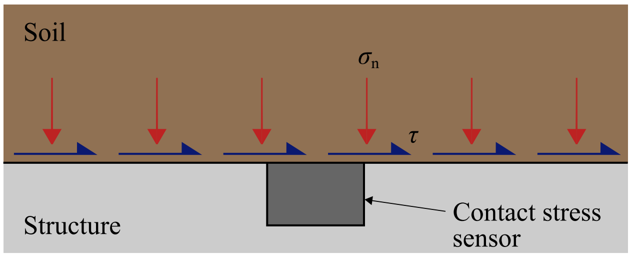

Figure 1.7 Illustration of the contact stresses exerted on an underground structure by the surrounding soil, with an indicative sensor installed at the interface

1.3 SSI measurement

The importance of the contact stresses at a soil-structure interface is not limited to caisson sinking. The normal and frictional stresses exerted on a structure by the surrounding soil, σ_{n} and τ respectively, are a critical aspect in almost all forms of underground construction. Although predictive capabilities have improved significantly in recent years, approaches for calculating soil-structure contact stresses are still remarkably poor for many applications and this remains a key uncertainty in design. Deeper insight into the SSI can be gained by directly measuring the soil-structure contact stresses. The installation of discrete sensors, as illustrated in Figure 1.7, enables detailed measurements of the localised interface stress state to be obtained. These sensors can provide valuable data to inform design method development and validation, as well as providing real-time feedback to site engineers to influence the construction process.

Whilst there are a large number of case studies of instrumentation installed on full-scale construction projects, few include direct measurements of contact stresses. In particular there is a paucity of cases in which frictional contact stresses are measured, despite their critical importance in a range of geotechnical problems. This is likely attributed to the current lack of suitable, robust sensors and installation difficulties. Recent case studies employing multi-axis electrical sensors at SLSIs in both caisson sinking (Royston, 2018; Royston *et al.*, 2022a) and pipejacked tunnelling (Phillips, 2023) showed numerous damaged sensors, high levels of noise and unreliability in the obtained measurements. There is clear motivation for new contact stress sensor technology, to improve the outputs of future monitoring projects and to extract new insights for design method development.

1.4 Research objectives

This research aims to further current understanding of SSI for open caisson shafts in sands. This includes: (a) the bearing capacity beneath the base of the caisson walls, (b) frictional stress development on the external surface of the caisson walls, and (c) the influence of construction features such as the tapered face, cutting shoe and interface lubrication. These aspects are explored through a combination of numerical modelling and reduced-scale laboratory testing. To achieve new insights and knowledge of SSI for open caissons in sand, the laboratory testing involves detailed measurement of the soil-structure contact stresses. To this end, the development of a novel soil-structure contact stress (SSCS) sensor for underground construction applications is necessarily pursued as an auxiliary aim. The developed sensor overcomes critical limitations of current electrical-based sensors, which lack sufficient robustness for construction applications.

This research aims to improve the safety and efficiency of the open caisson construction process. For example, it will develop improved understanding of friction development in sand and the use of interface lubrication. This will reduce uncertainty and therefore allow a reduction in conservatism, giving potential cost and environmental savings. Improved understanding of the bearing capacity and failure mechanisms will allow better prediction of the caisson response at different stages of construction, reducing the risks of unexpected behaviour and the associated costs and time losses. The newly developed sensors also have the potential to facilitate more robust and reliable measurements to be obtained in future laboratory testing and construction monitoring projects.

1.5 Thesis outline

Figure 1.8 provides an overview of this thesis and each chapter is briefly summarised below:

Chapter 2 provides a critical review of the literature to outline the context and motivation to the research in this thesis. The first half of the chapter focusses on open caisson shafts, with particular consideration of the SSI during construction. As a key focus of this research concerns measurement of SSI, a detailed review of SSCS sensors is also presented. Finally, to

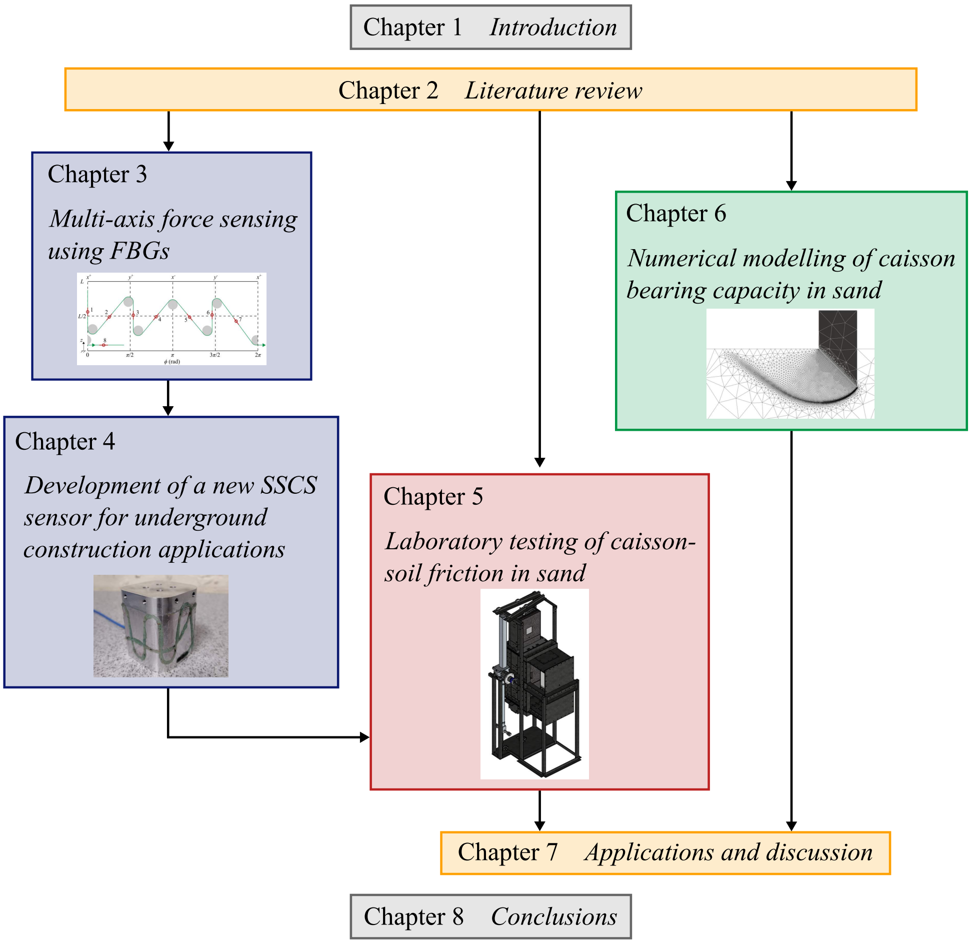

Figure 1.8 Thesis overview

inform the work in Chapter 3, a state-of-the-art review of multi-axis force sensing technology was undertaken. A shortened summary is presented as part of Chapter 2 in this thesis; the full review has been published in the following journal article:

- Templeman, J. O., Sheil, B. B., and Sun, T. (2020). Multi-axis force sensors: a state-of-the-art review. *Sensors and Actuators A: Physical*, 304. https://doi.org/10.1016/j.sna.2019.111772.

Chapter 3 describes the development of a new approach for the design and build of multi-axis force sensors. This work was undertaken to facilitate optical strain measurement in the form of fibre Bragg gratings (FBGs) to be adopted in place of conventional electrical strain gauging. The new framework fuses simplified sensor structures with an innovative instrumentation technique and a machine learning model to handle the measurand mapping. The performance and feasibility of various instrumentation strategies is first investigated using a numerical study of a columnar sensor as an exemplar. These are then verified using a prototype sensor, which was instrumented with FBGs and calibrated in the laboratory.

The potential wider impact of this work has led to significant commercialisation activity, including the filing of a recent UK patent application in June 2022 (Application No. 2209626.7). This work has also been submitted for publication in the following journal article:

- Templeman, J. O., Song, G., Suryasentana, S. K., Zhang, P., and Sheil, B. B. (2023). Multi-axis force sensing using fibre Bragg gratings. *Submitted.*

Chapter 4 presents a new sensor for measuring the contact stresses at a soil-structure interface. FBGs are utilised as the measurement technique by applying and extending the framework introduced in Chapter 3. This seeks to overcome critical limitations associated with using current electrical-based sensors in underground construction monitoring applications. The chapter describes the sensor concept and details of the design, manufacture, instrumentation and calibration of example sensors for laboratory testing. Sensor performance is assessed though a series of validation tests in two operating modes of increasing complexity: a) total stress measurement, b) effective stress measurement. The novel sensor design has been the subject of recent UK and international (PCT) applications (Application No. PCT/GB2020/052163), and has also been submitted for publication in the following journal article:

- Templeman, J. O. and Sheil, B. B. (2023). Development of a new soil-structure contact stress sensor for underground construction applications. *Submitted.*

Chapter 5 documents laboratory-scale testing of open caisson shaft friction in dense sand. The development of a novel large-deformation interface shear apparatus is described, which faithfully recreates the conditions at the SLSI surrounding large diameter caissons during sinking. The sensors developed in Chapter 4 are used to provide detailed information of the normal and frictional contact stresses at the concrete-sand interface. The testing considers the influence of over-cut creation and lubrication on the development of frictional resistance. Visual tracking of the soil displacement is used to provide insight into the underlying interface mechanics.

Chapter 6 presents the results from a suite of finite element limit analyses (FELA) exploring the bearing capacity beneath caisson walls in sand. The influence of a range of salient caisson parameters on the resulting vertical bearing resistance and soil failure mechanisms is considered. The study is extended using finite element analyses (FEA), to consider the influence of soil non-associativity and the development of horizontal reaction force. A user-defined material model and an adaptive remeshing strategy have been implemented to obtain accurate FEA bearing capacity predictions. Further FELA calculations are performed to also consider the effect of including an external cutting shoe on the vertical bearing capacity and soil failure mechanisms.

This chapter extends recent research at the University of Oxford considering caisson bearing capacity in clay (Royston *et al.*, 2022b). The work in this chapter has already been published in two journal articles:

- Sheil, B. B., and Templeman, J. O. (2023). Bearing capacity of large-diameter open caissons embedded in sand. *Géotechnique*, 73(6), 495–505. https://doi.org/10.1680/jgeot.21.00089.
- Templeman, J. O., Phillips, B. M., and Sheil, B. B. (2023). Cutting shoe design for open caissons in sand: influence on vertical bearing capacity. *Proceedings of the Institution of Civil Engineers - Geotechnical Engineering*, 176(1), 58–73. https://doi.org/10.1680/jgeen.20.00218.

Chapter 7 provides a critical discussion on the applications of the numerical modelling and experimental testing in this thesis. The numerical methodologies in Chapter 6 are compared against laboratory testing results in the literature and current design methods. The FELA results are used to inform the development of new closed-form analytical expressions amenable for use in routine design. The implications of the findings on design decisions and the selection of construction features are also explored.

Finally, **Chapter 8** summarises the key contributions of this thesis and provides suggestions for future work which have arisen from the research presented herein.

Chapter 2

Literature review

2.1 Introduction

This chapter presents a literature review covering three primary topics, to provide context to the research in this thesis. Firstly the SSI relating to the sinking of open caisson shafts is considered. The influence of salient components are discussed, including the bearing and frictional resistances and annulus lubrication. Published research and case studies explicitly concerning open caisson shafts are reviewed in detail, whilst also discussing the SSI in the context of comparable geotechnical problems. Secondly a review of SSCS measurement techniques is presented. Previously documented sensor designs and their applications are described, with particular attention given to frictional stress measurement. Finally a broad overview of multi-axis force sensing is provided. A comprehensive review of sensing technologies and sensor designs across a range of disciplines has been published in a separate journal article (see Section 1.5). A shortened summary of the paper is included in this chapter, which informs the development of new sensor technology in Chapters 3 and 4.

2.2 Soil-caisson interaction

2.2.1 Overview of sinking process

Much of the risk in caisson design relates to the relative magnitude of the self-weight of the walls and the resistances generated through SSI. A rudimentary sinking coefficient, K, was used by Yao *et al.* (2014), as an attempt to quantify likely behaviour. The coefficient is calculated as the ratio of the net downward driving force and the total upwards resistance force:

$$K = \frac{W - U}{V + F} \tag{2.1}$$

where W is the downwards force from the self-weight of the caisson walls, which is reduced by a buoyant uplift force, U, if the caisson is below the water table; V and F are upwards forces due to bearing resistance and friction respectively (i.e. v and τ integrated over the applied surface area of the caisson). The magnitudes of the forces in Equation 2.1 vary throughout the sinking process. Nonveiller (1987) suggested ensuring a value of $K \geq 2$ to avoid difficulties during sinking. In practice, a caisson will generally remain close to static equilibrium ($K = 1$); any out of balance force (e.g. due to wall pouring) will be balanced by increases in resistance from the caisson sinking to deeper depths. The sinking process is then initiated and controlled by reducing the resisting forces, primarily through excavation of the internal soil (Sheil *et al.*, 2018b), as well as manipulation of the annulus condition (e.g. injection of support fluid).

Accurately predicting the bearing and frictional resistances at each construction stage is difficult, because there is little applicable guidance in the literature. Research and design methods pertaining to displacement piles can provide some insight, due to the notable similarities with caisson shaft installation. However, fundamentally different SSI can develop due to factors such as the structure size, excavation technique, tapered cutting face, over-cut formation and the use of a lubricated annulus. The influence of these parameters, specific to the caisson sinking problem, are presently not well understood.

In addition to the primary risks from under- and over-prediction of the global resisting forces, other important considerations during caisson sinking include the groundwater conditions and spatial variability of ground conditions. Open caisson sinking ‘in the wet’, followed by pouring a mass concrete plug via a tremie to seal the base, is a well-proven technique for shaft construction below the water table (Royston, 2018). Compared to other methods (Section 1.2.1), this reduces impacts associated with dewatering and the risk of settlement around the caisson, as the internal water level acts to balance the hydrostatic ground pressures. Spatial variability of ground conditions can cause non-uniform resistance to develop around the caisson circumference, which can lead to loss of verticality during sinking. This can be mitigated during design via careful ground investigation, and during construction through the use of a guide collar and targeting excavation in specific locations.

2.2.2 Annulus support and lubrication

The introduction of a support fluid within the annulus has an important influence on the SSI, in particular the external skin friction. The lubrication adopted during caisson sinking has notable similarities to that used in pipejacked tunnelling. The fluid is typically delivered to the annular gap by pumping from lubrication ports behind the cutting shoe (e.g. Chandler *et al.*, 1984; Khasawneh *et al.*, 2017; Royston, 2018) or filling from the ground surface (e.g. Allenby *et al.*, 2009). A spreader pipe can be used to distribute the fluid more effectively around the caisson circumference (Tomlinson, 2001) and additional injection ports can also be located up the caisson wall to allow fluid delivery at different depths and provide redundancy against blockages (Royston, 2018). Although the use of polymer fluids is increasing in popularity, bentonite slurries are still the predominant support fluid used in open caisson shaft sinking applications (see Table 2.1). Bentonite slurry consists of a suspension of bentonite clay particles within water. Polymer additives may also be included to tailor the slurry properties to specific scenarios, including viscosity regulation, filtrate loss reduction and clay inhibition (Jefferis *et al.*, 2011; Praetorius and Schößer, 2017).

The role of the fluid is to support the over-cut excavation and to lubricate the soil-structure interface (Allenby *et al.*, 2009). The support mechanism of bentonite in the annulus around a caisson relies on the formation of a region of low permeability adjacent to the excavated surface, commonly referred to as a ‘filter cake’. The filtration process that drives cake formation is generally determined by the size of the dispersed bentonite particles relative to the pores in the surrounding soil. Two cases are defined: a) external, where bentonite particles are retained in the annulus at the excavated soil boundary (Figure 2.1a), and b) internal, where bentonite particles block pore channels in the soil adjacent to the excavation (Figure 2.1b). According to Praetorius and Schößer (2017), an external filter cake tends to form in cohesive and non-cohesive

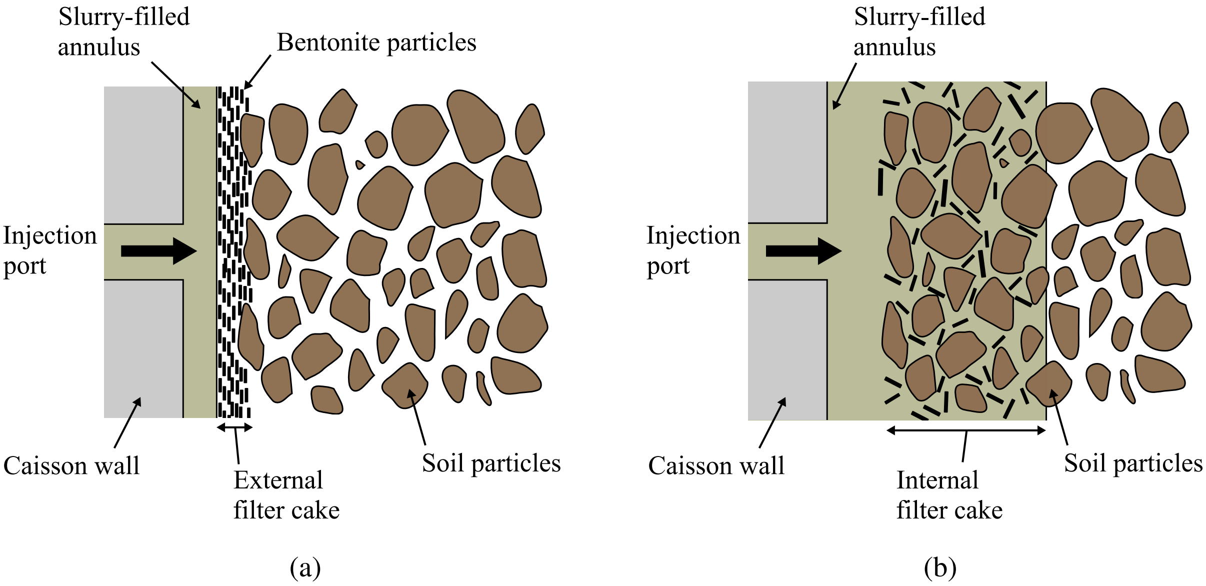

Figure 2.1 Illustration of filter cake formation by bentonite slurry within a caisson annulus, adapted from Praetorius and Schößer (2017): (a) External filter cake, (b) Internal filter cake

soils with effective particle diameters less than 0.06 mm and 1 mm respectively, with an internal filter cake forming in coarser soils. Praetorius and Schößer (2017) also define a mechanism of ‘pure penetration’ for non-cohesive soils with an effective particle diameter greater than 6 mm. The excavation support in this case is derived from the fluid rheological properties, through the transfer of shear stresses as the slurry penetrates the surrounding soil. A similar support mechanism is believed to be associated with polymer support fluids (Lam *et al.*, 2010) and this is an area of significant ongoing research.

The filter cake enables the fluid pressure in the annulus to be transferred onto the grain structure of the surrounding soil, due to the steep pressure drop across the cake. Hydrostatic conditions are typically assumed for the slurry pressure, such that a linearly distributed load is applied to the surface of the excavation (Sheil, 2021), as shown in Figure 2.2. The maximum support pressure is therefore dictated by the unit weight of the support fluid, γ_{f}, and the height of fluid in the annulus, h_{f}.

2.2.3 Friction

Frictional shear stress on the exterior surface of an open caisson shaft is often the dominant penetration resistance during sinking. This is particularly the case for deep and/or large-diameter

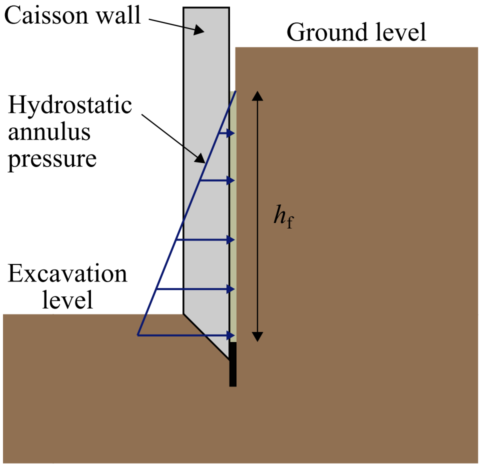

Figure 2.2 Illustration of a section through an open caisson wall showing the assumed distribution of support pressure in the annulus

shafts due to the large wall surface area, and for construction in dense sands, where there is potential for high friction and ineffective lubrication (Abdrabbo and Gaaver, 2012; Royston, 2018). Several examples in the literature have cited skin friction as the primary cause of difficulties encountered during construction (e.g. Abdrabbo and Gaaver, 2012; Khasawneh *et al.*, 2017; Nonveiller, 1987). A summary of documented case studies of open caisson shaft sinking is given in Table 2.1, including salient geometric and construction features.

2.2.3.1 Cohesive soil

In cohesive soils, the frictional shear stress acting on the caisson wall is typically calculated as a multiple of the soil in-situ undrained shear strength, s_u, as:

$$\tau = \alpha s_\mathrm{u} \tag{2.2}$$

where α is the interface roughness factor, defined in the range $0 \leq \alpha \leq 1$. For a smooth interface ($\alpha = 0$) zero shear stress can be sustained, whereas for a fully rough interface ($\alpha = 1$) shearing will tend to occur in the soil immediately adjacent to the structure. Equation 2.2 is applied in design procedures for axially loaded piles (e.g. API, 2002) and for installation of suction caisson foundations (e.g. Houlsby and Byrne, 2005a). The value of α at a particular point is often expressed as a function of the ratio of soil undrained shear strength to the vertical effective stress, $s_\mathrm{u}/\sigma'_\mathrm{v0}$. API (2002) recommends the following relationships for piles:

$$\alpha = 0.5\left(\frac{s_\mathrm{u}}{\sigma'_\mathrm{v0}}\right)^{-0.5} \qquad \frac{s_\mathrm{u}}{\sigma'_\mathrm{v0}} \leq 1.0 \tag{2.3}$$

$$\alpha = 0.25\left(\frac{s_\mathrm{u}}{\sigma'_\mathrm{v0}}\right)^{-0.25} \qquad \frac{s_\mathrm{u}}{\sigma'_\mathrm{v0}} > 1.0 \tag{2.4}$$

Equation 2.2 likely represents an upper bound on the frictional resistance during caisson sinking, corresponding to no over-cut formation. Whilst this may develop on the cutting shoe in practice, extensive remoulding is likely to occur as the caisson penetrates the soil, resulting in reduced skin friction on the shaft wall (Tomlinson, 2001). Furthermore, a fully stabilized annulus will dramatically reduce the skin friction by preventing the shaft from contacting the surrounding soil (Nonveiller, 1987). In this case, the resistance is governed by the shear strength of the lubricating slurry.

Several case studies have described successful use of annulus lubrication on during caisson construction in cohesive soil. Royston (2018) observed very low shear stresses during monitoring of the sinking of an 11 m internal diameter (ID), 20 m deep caisson in soft clay. The magnitude of the measured normal stress on the wall corresponded to the support fluid pressure in the 70 mm thick over-cut, indicating the potential for the annulus to remain open in clay and dramatically reduce skin friction. Fischer *et al.* (2004) described the sinking a 60 ft ID, 75 ft deep caisson in stiff silty clay overlaying soft clay. A bentonite slurry lubrication system was installed in the caisson, but this was not required during sinking. The system was only used to pump grout into the annulus to increase external friction on the shaft after reaching the desired formation depth. However, the use of a water-based lubricant in stiff plastic clays may be counterproductive, as it can cause swelling of the soil (Milligan, 2000). Nonveiller (1987) described the sinking of a 27 m ID, 60 m deep open caisson through stiff clay. A 200 mm over-cut was used to account for the predicted rebound of clay against the shaft with the bentonite slurry lubricant used.

2.2.3.2 Cohesionless soil

The frictional stress on a shaft in a cohesionless soil can be determined using Coulomb friction:

$$\tau = K\sigma'_\mathrm{v}\tan\delta \tag{2.5}$$

Table 2.1 Open caisson shaft case studies documented in the literature

Reference	D (m)	h (m)	B (m)	β (°)	t (m)	Lubrication	Ground conditions
Ter-Galustov *et al.* (1966)	15.4	14.1	0.3	Not given	0.1	Clay-based mud	Dense loams
Chandler *et al.* (1984)	9.8-10.4	91-103	1.8-2.4	Not given	Not given	Bentonite slurry	Silty sands and gravels
Nonveiller (1987)	27	60	1.5	34.1	0.2	Bentonite slurry	Stiff over consolidated clay
Fischer *et al.* (2004)	18.3	22.9	0.9	45	0.15	Bentonite slurry (not used)	Stiff silty clay overlying soft clay
Abdrabbo and Gaaver (2012)	20	33.1	1.6	40.4	0.1	Not given	Weak limestone overlying dense sand overlying sandy silt/silty clay
Khasawneh *et al.* (2017)	41.5	38.1	2.3	22.8	0.05	Bentonite	Clay overlying silt overlying sand
Royston (2018)	11	20	1.0	60	0.07	Polymer (TK60)	Soft clay overlying mudstone
Sheil *et al.* (2018b); Royston *et al.* (2022a)	32	20	1.25	45	0.08	Bentonite and polymer (MX) mix	Dense sand overlying stiff clay

D = ID, h = internal depth (or if not given, overall depth), B = wall thickness, β = cutting face taper angle, t = over-cut thickness. Parameters either stated in references or inferred from figures.

where K is the coefficient of lateral earth pressure, σ'_v is the vertical effective stress and δ is the interface angle of friction between the soil and structure. Equation 2.5 has been adopted in design procedures for axially loaded piles (e.g. API, 2002) and suction caisson foundations (e.g. Houlsby and Byrne, 2005b).

The interface angle of friction is dependent on the soil properties and surface roughness of the structure (Uesugi and Kishida, 1986). It is typically expressed as a proportion of the soil internal friction angle, ϕ', with $\delta = 0$ corresponding to a perfectly smooth interface and $\delta = \phi'$ for a fully rough interface, where failure moves to a soil-soil interface. Due to the large displacements occurring during caisson sinking, the operative frictional parameter is the critical state interface friction angle, δ_cs. This has been observed for shaft friction on displacement piles in sand (Lehane *et al.*, 1993).

For a concrete-soil interface, the surface roughness, and therefore the interface friction angle,

Table 2.2 Documented values of interface angle of friction, δ, obtained from elemental interface shear tests for a dry sand-concrete interface

Reference	δ/ϕ'	**Test method**
Potyondy (1961)	0.89 (smooth), 0.99 (rough)	Interface direct shear
Reilly and Orr (2017)	0.91–1.0 (rough)	Interface direct shear
Uesugi *et al.* (1990)	0.85–0.99 (rough)	Interface simple shear

both depend on the roughness of the concrete casting formwork. For example, metal moulds tend to produce a smoother surface compared to plywood (Uesugi *et al.*, 1990). BSI (2004) recommends adopting a design value of $\delta = \phi'$ for cast-in-situ concrete and $\delta = 2/3\ \phi'$ for smooth precast foundations. Whilst $\delta = 2/3\ \phi'$ may be conservative for foundation capacity design, it is unconservative for estimating sinking resistance. An upper bound of $\delta = \phi'$ is generally considered for the caisson problem (Royston, 2018). More accurate estimates of δ can be obtained from elemental interface shear tests, such as direct shear (e.g. Potyondy, 1961; Reilly and Orr, 2017), simple shear (e.g. Uesugi *et al.*, 1990), or modified triaxial-type tests (e.g. Reilly and Orr, 2017). A summary of δ/ϕ' values documented in the literature for dry sand-concrete interfaces is given in Table 2.2. These values likely represent upper bounds on δ for the caisson sinking problem, due to the use of a lubricated interface.

The frictional resistance during caisson sinking in cohesionless soil also depends on the horizontal or radial stresses that develop on the external wall surface. In Equation 2.5, these stresses are expressed as a multiple of the vertical effective stress via the coefficient of lateral earth pressure, K. For a given geotechnical problem, the value of K and the resulting friction depend strongly on the ground conditions, the installation method and the corresponding induced soil movement. Applying Equation 2.5 with a constant K implies a linear increase in τ_s indefinitely with overburden pressure. API (2002) recommends $K = 0.8$ or 1.0 for driven open-ended unplugged and plugged piles respectively.

The development of friction during open caisson shaft sinking is often compared to the installation of displacement piles. However, there are a number of salient differences that may strongly affect the development of horizontal stress and therefore friction. The global friction on displacement piles is typically observed to be limited with continued penetration. A reduction in local shear stress at a given plane in the soil is observed, as the distance of the plane above the pile tip increases during installation (Heerema, 1978; Lehane *et al.*, 1993). This has been largely attributed to the closed-ended nature of the piles, which causes soil compression and outwards displacement, with associated high stresses and friction at the tip (Lehane *et al.*, 1993; White and Bolton, 2002). Similar behaviour may not be expected for caisson shafts due to the different geometry at the base of the walls. The angled cutting face mobilises soil failure to the interior of the structure, where soil excavation reduces the level of overburden pressure. This would be expected to cause much less outwards displacement of soil and therefore less increase in stress at the exterior of the caisson leading edge. Similar observations have been made for open-ended piles (Igoe *et al.*, 2011).

The formation of an over-cut via the cutting shoe may act to further reduce the horizontal stress on the caisson wall exterior (Royston, 2018; Tomlinson, 2001). Even if the annulus is not stabilized (and the caisson is sunk dry), soil translation into the annular void may result in lower horizontal earth pressures via a reduced K value. The cutting shoe itself may experience high loading however, as it is expected that at-rest horizontal earth pressures will develop (Nonveiller, 1987). The reduction of local friction on displacement piles has also been largely attributed to the cyclic loading caused by dynamic driving. White and Lehane (2004) observed significant degradation of shaft friction with cyclic installation methods in drum centrifuge tests on instrumented model piles, which was not observed when using monotonic installation. As caisson sinking is a quasi-static process with no cyclic loading, this may lessen any friction reduction with depth. Furthermore, caisson geometries usually have a much lower aspect ratio, h/D, compared to piles. Measurement locations in the pile tests of Lehane *et al.* (1993) are between $h/D = 4$ and 25, the minimum of which is significantly above what is applicable to typical caisson geometries (see Table 2.1). Comparable measurements during caisson monitoring by Royston *et al.* (2022a) are spaced between $h/D = 0$ and 0.23.

Effective annulus lubrication is likely to have the most significant influence on caisson friction. If the annulus is stabilised and the interface can be maintained as fully lubricated, the caisson may experience almost negligible frictional resistance during sinking. This is similar to

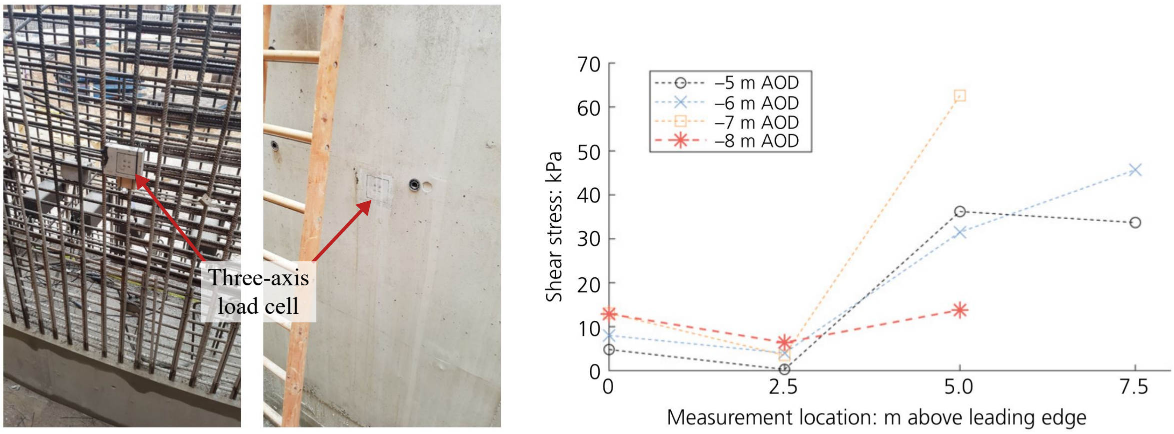

(a) (b)

Figure 2.3 Open caisson shaft monitoring by Royston *et al.* (2022a): (a) Three-axis load cell installed in the RC wall, (b) Measured data showing increases in frictional shear stress as sensors spaced up the wall pass through discrete depths in the soil during sinking

pipejacking with neutral buoyancy conditions, where friction develops only due to the shearing resistance of the lubricating slurry itself (Milligan, 2000). If the soil and caisson come into contact (e.g. due to collapse of the annulus), Milligan (2000) and Praetorius and Schößer (2017) suggest that the layer of mixed soil and lubricant may still result in a reduced coefficient of friction. Howver, direct interface shear tests conducted by Reilly and Orr (2017) demonstrated that an unpressurised layer of bentonite lubrication led to only minor reductions in sand-concrete interface friction angle of 1.9–3.9°. Reilly and Orr (2017) used novel interface triaxial testing to demonstrate that pressurization of the lubricant is required to achieve a significant reduction in interface friction. This was attributed to the formation of a filter cake, enabling a reduction in effective stress at the interface through transfer of the slurry pressure to the soil skeleton.

Several case studies have documented difficulties during open caisson shaft construction in cohesionless soils. Abdrabbo and Gaaver (2012) described the construction of 20 m and 10 m ID caissons through sand, both of which became 'wedged' due to excessive friction on the walls. Extensive remedial works were required to be employed in both cases to complete the sinking. Khasawneh *et al.* (2017) described the construction of a 136 ft ID, 125 ft deep caisson for a combined sewage storage tank. Controlled sinking was achieved through an upper clay layer with limited injection of bentonite lubrication, but the sinking rate significantly slowed in underlaying sand. 'Aggressive' techniques were employed, such as high-pressure water injection and under-cutting, which caused significant ground settlements, loss of verticality and cracking of the caisson structure.

Royston *et al.* (2022a) described monitoring undertaken during the sinking of a 32 m ID, 20 m deep instrumented caisson in predominantly dense sand. Three-axis load cells were installed in the caisson wall external surface (see Figure 2.3a), which showed a consistent increase in both normal and frictional stresses at specific depths in the soil with continued sinking, as shown in Figure 2.3b. This contradicts the well-documented 'friction fatigue' behaviour for displacement piles. Pressure transducers installed alongside the load cells indicated lubricant infiltration into the soil, insufficient support pressure and subsequently annulus collapse. A value of $K = 2$ was observed to provide a reasonable upper bound for the coefficient of lateral earth pressure. Conversely, a stable annulus was observed as the caisson penetrated an underlying clay layer, indicating that effective lubrication may be more problematic in cohesionless soils.

2.2.4 Bearing

In addition to the primary resistance caused by exterior skin friction, significant bearing stresses can also develop beneath the caisson wall during construction. The base of a circular caisson shaft is analogous to an inclined ring footing, with the cutting face at an angle β to vertical (see Figure 1.5). The bearing capacity problem can be assessed as axisymmetric, however for large diameter caissons it is typically approximated as plane strain.

The widely used bearing capacity theory of Terzaghi (1943) uses superposition to express the ultimate vertical bearing capacity, q_u, of a shallow strip footing as:

$$q_\mathrm{u} = \frac{V}{A} = cN_\mathrm{c} + qN_\mathrm{q} + \frac{1}{2}\gamma B_\mathrm{w} N_\gamma \tag{2.6}$$

where V is the vertical bearing force, and A and B_w are the foundation area and width respectively. The dimensionless factors N_c, N_q and N_γ define the bearing capacity contributions from the soil cohesion, c, the surrounding surcharge, q, and soil unit weight, γ, respectively. Exact analytical solutions for N_c and N_q have been determined using the method of characteristics by Prandtl (1920) and Reissner (1924) respectively:

$$N_{\mathrm{c}} = (N_{\mathrm{q}} - 1)\cot\phi' \tag{2.7}$$

$$N_{\mathrm{q}} = \frac{1+\sin\phi'}{1-\sin\phi'}e^{\pi\tan\phi'} = \tan^2(45^\circ + \phi'/2)\, e^{\pi\tan\phi'} \tag{2.8}$$

where ϕ' is the soil friction angle. An exact solution for the factor N_γ has not yet been obtained. Accurate values have been determined numerically (e.g. Martin, 2004) and a wide range of approximate solutions have been proposed (e.g. Brinch Hansen, 1970; Vesić, 1973). A widely used example adopted in BSI (2004) is that defined by Chen (1975):

$$N_\gamma = 2(N_{\mathrm{q}} - 1)\tan\phi' \tag{2.9}$$

Equation 2.6 is commonly adapted to extend its application to a wider range of foundation types, using a series of empirical modification factors:

$$q_{\mathrm{u}} = cN_{\mathrm{c}} \cdot s_{\mathrm{c}}d_{\mathrm{c}}i_{\mathrm{c}} + qN_{\mathrm{q}} \cdot s_{\mathrm{q}}d_{\mathrm{q}}i_{\mathrm{q}} + \frac{1}{2}\gamma BN_\gamma \cdot s_\gamma d_\gamma i_\gamma \tag{2.10}$$

In Equation 2.10, s_{c}, s_{q}, s_γ are ‘shape’ factors for computing the bearing capacity of alternative foundation geometries. Similarly, d_{c}, d_{q}, d_γ are ‘depth factors’ that account for footings founded below the ground surface, and i_{c}, i_{q}, i_γ are ‘inclination factors’ that account for non-vertical loading. Several different expressions for the modification factors have been proposed in the literature, including those by Meyerhof (1951, 1963), Brinch Hansen (1970) and Vesić (1973).

Classical bearing capacity theory has been adopted into design codes (e.g. BSI, 2004) and is commonly used in open caisson shaft design in industry, such as in Royston *et al.* (2022b). For large diameter caissons, the pertinent contributors are depth factors, as well as additional factors, b_{c}, b_{q}, b_γ, which account for inclination of the foundation base. Brinch Hansen (1970) documented one of the earliest sets of such factors, though footing inclination has received less attention in the literature compared to other factors. Equations 2.11 and 2.12 define the base inclination factors according to Eurocode 7 (EC7; BSI, 2004) for undrained and drained conditions respectively:

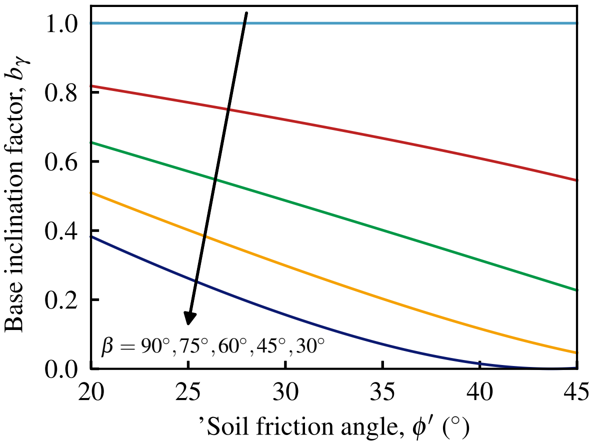

Figure 2.4 Variation of base inclination factor, b_γ, with footing inclination angle, β, and soil friction angle, ϕ', according to EC7 (BSI, 2004)

$$b_c = 1 - \frac{2\alpha}{\pi + 2} \tag{2.11}$$

$$b_\gamma = (1 - \alpha \tan \phi')^2 \tag{2.12}$$

where α is the angle of the footing base to horizontal in radians, $\alpha = \pi/2\,(1 - \beta/90)$. For undrained conditions, Equation 2.11 shows a linear decrease in bearing capacity for steeper inclination angles. For drained conditions, Equation 2.12 show a dependence of b_γ on both α and ϕ', as shown in Figure 2.4. However, the applicability of these expressions at the extrema is questionable; for example, with $\beta = 30°$ and $\phi' = 45°$, Equation 2.12 results in $b_\gamma = 0$.

Many investigators have developed more accurate bearing capacity solutions for foundations with similar characteristics to the caisson problem. For example, shallow conical footings have been considered in both drained (Cassidy and Houlsby, 2002) and undrained conditions (Houlsby and Martin, 2003), for application in offshore spudcan foundations. The bearing capacity was observed to depend strongly on both the cone apex angle and face roughness; similar would be expected for the inclined caisson cutting face. The vertical bearing capacity of ring footings has been studied using various experimental and numerical techniques, in both cohesionless (e.g. Benmebarek *et al.*, 2012; Kumar and Ghosh, 2005; Saha, 1978; Zhao and Wang, 2008) and cohesive soils (e.g. Benmebarek *et al.*, 2017; Lee *et al.*, 2016; Tapper, 2013). Embedded ring footings resemble open caisson shafts with $\beta = 90°$, however the embedment range generally considered is much less than the typical caisson shaft depths.

Although similar foundations have been well researched, there are specific features of the open caisson construction process that complicate accurate bearing capacity estimation. Firstly, the depth of overburden soil generally differs on either side of the caisson wall. The external embedment depth of the footing is typically greater than on the internal side and increases monotonically during sinking. The internal embedment depth can vary throughout the duration of construction, depending on the soil conditions and the sequence of wall casting and soil excavation. Ancillary structures, such as a guide collar or sheet pile wall, may also impact the caisson bearing capacity, particularly if an external soil failure mechanism forms. Furthermore, the influence of the external cutting shoe and annulus lubrication on the caisson bearing capacity are not well understood. The cutting shoe alters the footing geometry near the apex of the cutting face, whereas there is potential for high hydraulic pressures in the annulus to cause support fluid seepage into the internal excavation, or even a complete ’blow-out’ of the annulus.

Published studies explicitly exploring the open caisson bearing problem are limited. Various numerical techniques have been applied in recent research. Chavda and Dodagoudar (2018, 2022b) used FEA to consider the bearing of a caisson cutting face in frictional-cohesive (c-ϕ') soil. The 2D axisymmetric analyses were used to identify the extent of the soil failure mechanisms during vertical displacement into elastic-perfectly plastic Mohr-Coulomb material. Bearing capacity factors were presented for a very limited subset of the parameter space, with important factors omitted including the cutting face roughness and external overburden soil. Royston *et al.* (2022b) explored the vertical bearing capacity of caisson footings in undrained soil using 2D FELA. A large parametric study assessed the influence of the cutting face taper angle and roughness, internal overburden depth, and caisson radius. The numerical outputs informed a closed-form design approach, in which the undrained bearing capacity for a generalised axisymmetric caisson, N_{axi}, can be defined in three stages:

$$N_{\mathrm{ps,h=0}} = \left[2\left(\frac{\beta}{180}\pi\right) + 2\right] + \left(\frac{\alpha_{\mathrm{f}}}{\tan\beta}\right) + \left(\alpha_{\mathrm{f}} + \frac{\pi-4}{2}\alpha_{\mathrm{f}}^2\right) \tag{2.13}$$

$$N_{\mathrm{ps}} = N_{\mathrm{ps,h=0}} + \left[\frac{(h/B_{\mathrm{w}})^{0.452}}{\cos\beta + 0.133\alpha_{\mathrm{f}}}\right] \leq N_{\mathrm{ps,h=0}} + \left[\frac{(h/B_{\mathrm{w}})^{0.452}}{\cos(50) + 0.133\alpha_{\mathrm{f}}}\right] \tag{2.14}$$

$$N_{\text{axi}} = N_{\text{ps}} + m\left(\frac{B_{\text{w}}}{R}\right) \leq A_{\text{b}} \ln\left(\frac{B_{\text{w}}}{R}\right) + B_{\text{b}}\left(\frac{B_{\text{w}}}{R}\right) + C_{\text{b}}\left[\left(\frac{\beta}{180}\pi\right) - \frac{\pi}{6}\right] + \frac{\alpha_{\text{f}}}{\tan\beta} + \alpha_{\text{f}}\left(\frac{B_{\text{w}}}{R}\right) \tag{2.15}$$

where N_{ps} and $N_{\text{ps,h=0}}$ are the plane strain bearing factors corresponding to $B_{\text{w}}/R = 0$, for the generalised and no internal overburden conditions respectively. In Equations 2.13–2.15, β is the cutting face taper angle, α_{f} is the cutting face roughness factor, B_{w} is the embedded footing width, h is the internal overburden depth and R is the caisson internal radius. The coefficients A_{b}, B_{b} and C_{b} are defined as -2·162, 4·277 and 2·52 respectively and $m = 8/9 - 2/3(h/B_{\text{w}})$.

Physical modelling techniques have also been used recently to consider caisson bearing. Royston *et al.* (2016) described a series of laboratory-scale tests exploring the vertical penetration behaviour of plane-strain caisson footings in Leighton Buzzard DA30 sand. The tests primarily considered the influence of taper angle, β, and were all in a shallow embedded state (soil surface below the top edge of the cutting face). Chavda *et al.* (2020) and Chavda and Dodagoudar (2022a) reported a series of 1g vertical penetration tests of full- and semi-circular model caissons in Indian standard (Grade II) sand. These tests considered the influence of β and also the cutting face roughness, α_{f}, by comparing a smooth polytetrafluoroethylene (PTFE) model caisson to

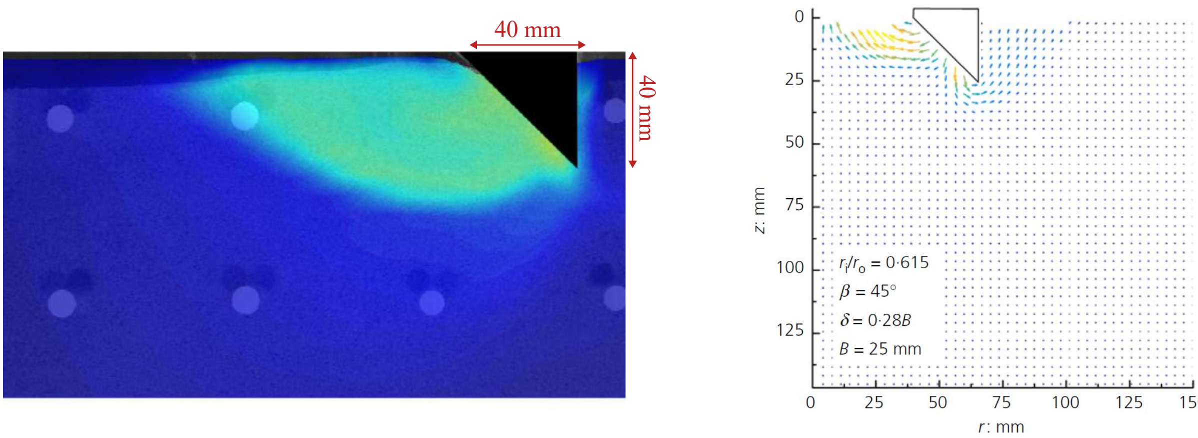

(a) (b)

Figure 2.5 Soil failure mechanisms observed using PIV during laboratory scale vertical penetration testing of a caisson footing with $\beta = 45°$ in sands: (a) Royston *et al.* (2016) (plane-strain), (b) Chavda *et al.* (2020) (half-caisson). In both cases the colours denote the magnitude of the resultant displacements.

one covered with epoxy and sand.

Chavda *et al.* (2020) documented an increase of 5–15% in N_γ between the ‘smooth’ and ‘rough’ cutting faces. Both Royston *et al.* (2016) and Chavda and Dodagoudar (2022a) observed that steeper footings (lower β) experience reduced vertical resistance at the same penetration depth, due to the reduced embedded area. However Royston *et al.* (2016) noted that the influence of β is minor when compared at the same embedded area, with steeper footings resulting in slightly increased vertical resistance. Steeper footings were also observed to experience significantly higher horizontal forces on the cutting face, up to as much as 90% of the vertical reaction for $\beta = 30°$. Particle image velocimetry (PIV) was used in both studies to visualise the soil failure mechanisms (see examples in Figure 2.5). Soil displacements were observed to occur towards the internal side of the footing for steep taper angles, and on both the internal and external sides for flatter footings. For steeper footings, the increased vertical and horizontal forces were attributed to the deeper and wider failure mechanism that forms.

2.3 SSCS measurement

2.3.1 Soil-structure interface stresses

At a structural interface, the surrounding soil exerts a total normal stress, σ_n (Figure 1.7). The total normal stress comprises two components, which can be expressed as:

$$\sigma_\mathrm{n} = \sigma'_\mathrm{n} + u \tag{2.16}$$

where σ'_n is the effective normal stress transmitted by the solid soil particles, and u is the pore water pressure. Soil contact pressure acting on a sensor face at the interface provides a measurement of the total normal stress. To determine the effective normal stress from a measured total stress, a measurement of the pore water pressure in close proximity is also required.

The effective normal stress is important from a soil mechanics perspective, as it governs the development of frictional shear stresses that act parallel to the interface plane (see Figure 1.7). In the general case, these can be expressed as two perpendicular components in the plane of the interface, τ_x and τ_y. In applications such as caisson shaft sinking and pipe jacking, a significantly larger shear stress component typically develops in the direction parallel to the structure movement (Royston *et al.*, 2022a). By contrast, other structures are exposed to complex combined shear stresses. Examples include the circumferential and axial shear stresses that develop on buried pipelines during cyclic loading (Sheil *et al.*, 2018a) and piled foundations, which are subject to vertical shear stress to support the superstructure dead load and horizontal shear stress during lateral loading (Anagnostopoulos and Georgiadis, 1993; Phillips, 2002).

2.3.2 SSI measurement

Measurement of soil stresses has been considered extensively in the literature for both laboratory testing and field monitoring applications. This can occur in two contexts: measuring the contact stresses exerted at a soil-structure interface and measuring the internal stresses within a bulk soil mass. Although the two cases have distinct challenges and requirements, there is significant overlap in the instrumentation. The most common measurement approach is the installation of discrete sensors, which are capable of measuring one or more components of stress at specific locations (Figure 1.7).

The vast majority of soil stress transducers documented in the literature only provide a measurement of total normal stress and are commonly referred to as 'earth pressure cells'. These sensors can be categorized by the nature of their structure and measurement principle. A large proportion of sensor designs behave as flexible diaphragms, using thin membranes which are fixed at the edges. In other designs the sensor face displaces as a rigid piston on elastic supports. The deformation induced in both of these sensor types is measured using strain transducers such as electrical resistance strain gauges (ERSGs) (e.g. Redshaw, 1954), vibrating-wire gauges (e.g. Thomas and Ward, 1969) and more recently FBGs (e.g. Correia *et al.*, 2009). An alternative strategy is to transform the soil stress into hydraulic fluid pressure which is then measured separately (e.g. Waterways Experiment Station, 1944).

A critical limitation of the majority of SSI measurements is that sensor compliance can lead to local redistribution of stresses in the soil. This means that the presence of the sensor can alter

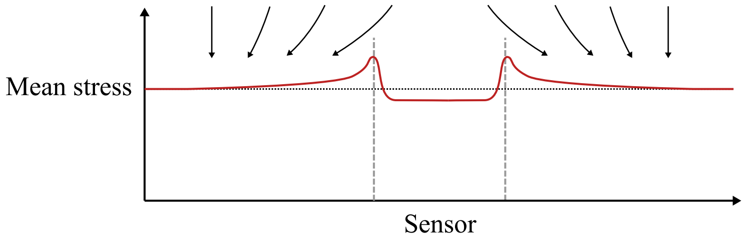

Figure 2.6 Schematic illustration of soil arching over a contact stress cell, showing a reduction in normal stress

the quantity that it is attempting to measure. A contact stress sensor must closely simulate the structure's response to applied stresses, which requires matching both the rigidity of the structure and the surface texture at the boundary (Thomas and Ward, 1969). One of the most common issues encountered is soil arching, on account of the sensor having a lower stiffness than the host structure, resulting in a reduced normal stress acting on the sensor (Figure 2.6). Researchers have previously suggested limiting the deflection:diameter ratio to minimise arching effects. One of the most widely referenced criteria is 1:2000 recommended by Waterways Experiment Station (1944), however others have suggested more stringent limits (e.g. 1:5000; Weiler Jr. and Kulhawy, 1982).

Several authors have attempted to overcome the issue of sensor compliance using a so-called 'null' or 'balanced' pressure approach (Jennings and Burland, 1960; Talesnick *et al.*, 2014). The principle is to pressurise a fluid- or air-filled reservoir behind the sensing diaphragm, in order to actively maintain an undeflected state. A schematic of the design of Talesnick *et al.* (2014) is shown in Figure 2.7a, which uses a high precision linear variable differential transformer (LVDT) to measure any face deflection caused by soil normal stress and determine the required 'null pressure'. Talesnick *et al.* (2014) demonstrated that compliant diaphragm sensors show significant under-reading in coarse soils (see Figure 2.7b), and hysteresis after unloading, both of which were attributed to soil arching. Results from a comparable 'null' pressure sensor show much closer agreement with the applied stress for all soils tested (Figure 2.7c). The deviation with coarse crushed aggregate was attributed to grain size effects on the 23 mm diameter diaphragm

Despite its physical significance, few sensors documented in the literature are capable of measuring effective normal stress at a soil-structure interface. From Equation 2.16, to determine

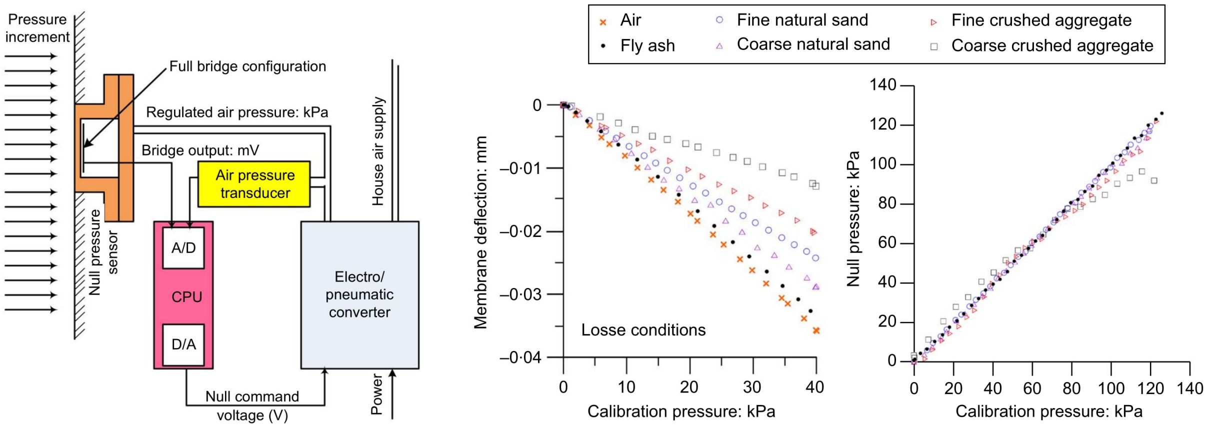

(a) (b) (c)

Figure 2.7 Normal contact stress sensor of Talesnick *et al.* (2014): (a) schematic of 'null' pressure system, (b) response of a 23 mm diameter compliant diaphragm sensor under normal stresses in a range of soils, (c) 23 mm diameter 'null' sensor response in comparable tests

σ'_n a sensor must also measure u or employ a mechanism to counteract the water pressure on the face plate. A common workaround is to install a separate pressure transducer (PT) in close proximity to measure u (e.g. Royston *et al.*, 2022b). This is cumbersome as it requires additional instrumentation and relies on the assumption of there being no variation of pore pressure between the two sensors. Waterways Experiment Station (1944) reported a sensor design in which pore water is allowed into the sensor through a porous stone, counterbalancing water pressure on the measurement diaphragm. Correia *et al.* (2009) presented a sensor containing two diaphragms instrumented with FBGs. One diaphragm responds to total stress and the other to pore pressure, from which σ'_n can be calculated. Temperature compensation was not considered and poor total stress measurement was noted, which the authors attributed to soil arching.

There is a paucity of examples in the literature of transducers capable of measuring shear stress at an interface. This is surprising, given the importance of the development of frictional stresses in foundations and underground structures. Agarwal and Venkatesan (1965) developed a sensor to measure both normal stress and skin friction in a single direction on a driven pile. A diaphragm to measure normal stress is supported on the end of a cantilever. Shear stress on the cell face causes deflection of the cantilever, which is measured by ERSGs near the root. Talesnick and Ringel (2022) proposed a small-scale soil-structure friction sensor, comprising a face plate supported on four columns. The sensor was machined from a single block of stainless

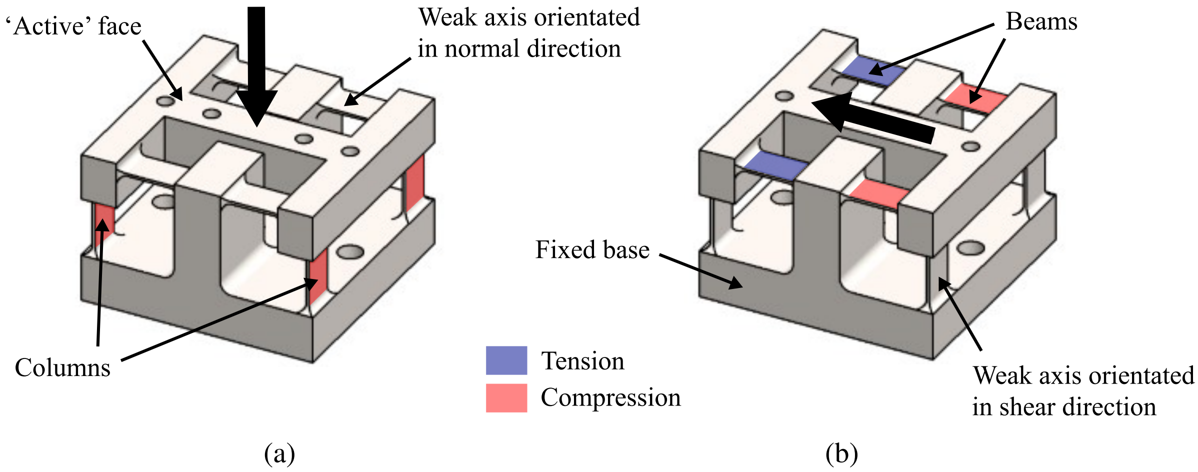

Figure 2.8 SSCS transducer proposed by Stroud (1971), showing primary tension and compression induced in the webs under: (a) normal stress and (b) shear stress

steel and the columns are instrumented with ERSGs to measure the induced bending. However, this design does not provide a measurement of normal stress; the proposed solution is to install the sensor in close proximity to a separate 'null pressure' sensor (Talesnick *et al.*, 2014).

The most widely adopted multi-axis contact stress transducer in the literature is the Stroud cell or 'Cambridge-type' design (e.g. Martin, 1994; Royston, 2018; Sheil *et al.*, 2018a). Stroud cells are capable of measuring normal stress acting on the sensor face, as well as the shear stress and eccentricity of the normal load in a single axis. Stroud (1971) developed one of the more popular designs, comprising four vertical and four horizontal webs which connect an upper and lower block. The webs are instrumented to measure their axial deformation and are designed to be flexible in bending to reduce cross-coupling between sensor outputs. Normal stress induces axial compression in the vertical webs, whereas shear stress induces tension and compression in the opposite pairs of horizontal webs (Bransby, 1972), as shown in Figure 2.8. ERSGs are mounted on both faces of all eight webs to form three Wheatstone bridge circuit outputs.

2.4 Multi-axis force sensors

All of the sensors documented in the literature for measuring multiple interface contact stress components are essentially specialised multi-axis force sensors. Simple uniaxial load cells provide a measurement of force in a single direction, whereas multi-axis force sensors are capable of measuring force and/or moment components in more than one spatial direction. In the most general case, this loading can be six degree of freedom (DOF), comprising three mutually orthogonal force components and three mutually orthogonal moment components.

Multi-axis force sensors have been considered extensively in the literature for a wide range of industrial and research disciplines, including robotics, manufacturing, aerospace, medical applications and civil engineering. The vast majority of documented examples comprise a number of strain-sensitive transducers mounted on a compliant structure, designed to deform elastically under the applied loading. Both the sensor structure and strain transducers require careful consideration to achieve appropriate measurement range, sensitivity, isotropy, stiffness and to minimize undesirable coupling between the outputs.

2.4.1 Strain sensing technologies

Electrical strain measurement techniques are ubiquitous in both simple load cells and more complex multi-axis sensors. The most common type are metallic foil ERSGs, which operate using the change in electrical resistance of a conductor induced by geometry change. To obtain measurable output signals from the small resistance changes associated with ERSGs, multiple gauges are commonly connected into Wheatstone bridge circuits. This also facilitates temperature compensation, as the thermal-induced resistance changes apply to each arm of the bridge, thereby mitigating any influence on the aggregated circuit output.

Other electrical techniques employed in force sensing applications include semiconductor strain gauges (SSGs) and capacitive sensing. SSGs operate using the piezoresistive effect, which typically results in greater strain sensitivity than metallic ERSGs due to the strain-induced change in material resistivity (Mason and Thurston, 1957). Both SSGs and capacitance-based sensors can be manufactured by micro-machining techniques, allowing very small-scale strain sensing to be achieved (e.g. Bekhti *et al.*, 2014; Dao *et al.*, 2002). Key limitations of electrical sensing include its vulnerability to electromagnetic interference (EMI) and susceptibility to damage with exposure to water. These are particularly critical in harsh or industrial environments, as well as applications requiring long transmission distances. The relatively low sensitivity of ERSGs can also be problematic in applications requiring high sensor stiffness.

Optical strain measurement methods have the potential to overcome many of the issues faced by electrical systems. Although a plethora of optical strain measurement methods exist (e.g. Fabry-Perot interferometers, Rayleigh and Brillouin scattering), FBGs have become the most popular for discrete sensor applications. An FBG is a short length of optical fibre that reflects a narrow band of the light spectrum, which is shifted when the FBG is subjected to mechanical strain. FBGs can be bonded to a sensor surface in a similar manner to ERSGs. They offer the advantages of high sensitivity, immunity to EMI and water damage, wavelength-encoded measurement, and the ability to multiplex large numbers of FBGs along a single fibre. Despite their potential benefits, FBGs have only been applied in a limited number of force sensors. There are several major obstacles that have previously slowed the adoption of FBGs in industry, including temperature compensation and the high cost compared with ERSGs. A more detailed discussion on FBG technology is provided later in Section 3.3.

2.4.2 Sensor structures

A considerable number of sensor structures have been proposed in the literature. The main designs can be broadly categorised as: (a) cross-beam, (b) column, and (c) Stewart platforms. The cross-beam or ‘Maltese cross’ design is arguably the most common. This consists of an outer frame connected to a central platform by three or more elastic beam members. The most popular arrangement comprises four beams arranged in a planar cross shape, as illustrated in Figure 2.9. Six DOF load components induce combinations of axial deformation, in-plane and out-of-plane bending and torsion in the members, which can be measured by strain transducers on their surfaces. Cross-beam sensors can achieve good decoupling and high sensitivity, but typically demonstrate low stiffness as the members undergo beam bending. Both three and six DOF cross-beam designs have featured in the literature.

Fontana *et al.* (2012) described a cross-beam sensor to measure F_x, F_y and F_z, with 16 ERSGs on the upper and lower beam surfaces connected into four Wheatstone bridges. Three DOF cross-beams employing FBGs have been presented by Fernandez Fernandez *et al.* (2001)

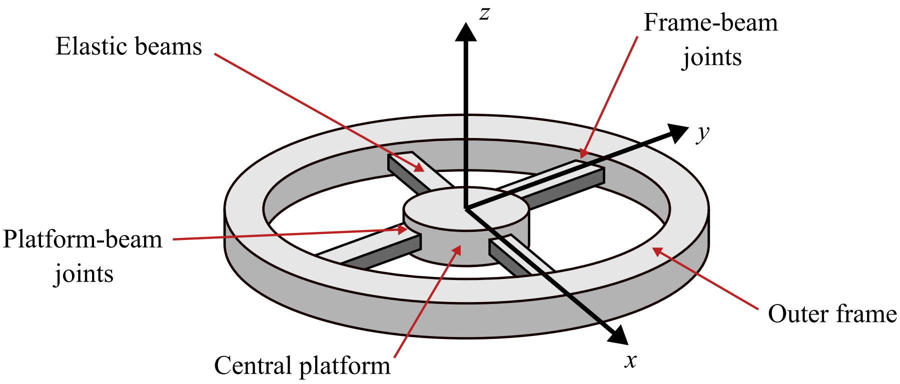

Figure 2.9 Illustration of a conventional cross-beam force sensor body showing the salient features

and Xiong *et al.* (2018). Both designs feature FBGs mounted to the upper and lower beam surfaces and achieve temperature compensation by forming the sensor outputs as the difference between two FBG wavelength shifts. Six DOF cross-beam force sensors are more complex, typically requiring strain-sensing elements on all sides of the elastic members (Gorinevsky *et al.*, 1997). Chao and Yin (1999) presented a six DOF sensor using a conventional cross-beam, to measure the reaction load on a human foot. There are a number of drawbacks to the conventional cross-beam design, which uses solid beams and rigid joints. Principally, the use of rigid joints has been shown to reduce measurement isotropy and result in a high degree of coupling between the sensor outputs (Liu and Tzo, 2002).

A wide range of more complex six DOF cross-beams have been presented to improve sensor performance. The use of compliant elements in the outer frame has featured frequently in the literature to make the frame-beam joints flexible. Scheinman (1969) documented one of the earliest designs of this type for robotic wrist force sensing using thin flexures machined into the outer frame. Huang *et al.* (2018) presented numerical analysis of a flexible jointed cross-beam intended for instrumentation with 16 FBGs. Introducing flexible joints can act to increase sensitivity, improve isotropy and minimise coupling between sensor outputs, but this comes at the cost of lower stiffness. Similar effects have been observed in designs which instead modify the compliance of the cross-beam members, such as the use of parallel plate beams (Kim, 2007) and forming 'grooves' in the beams (Kim *et al.*, 2013). A number of dual-cross beam designs have also been presented, which consist of a vertical assembly of two cross-beams each tasked

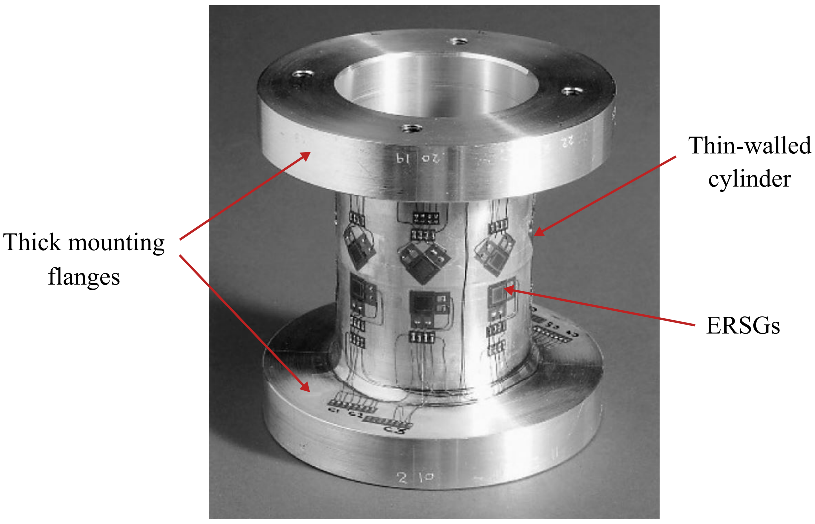

Figure 2.10 Column-type force sensor presented by Byrne and Houlsby (2005) featuring a hollow cylindrical sensor body instrumented with ERSGs on the external surface

with measuring a specific three DOF load combination (e.g. Kim *et al.*, 1999). The sensor structures are significantly more complex in these designs.

By contrast, the column multi-axis force sensor design has received less attention in the literature. These sensors consist of a single prismatic element, which is fixed at one end and free to deflect and rotate at the other. Loads applied to the sensor at the free end induce a strain field in the sensor body, which is measured by various combinations of strain transducers bonded to the outer surface. The most commonly-adopted column-type design features a hollow cylinder between two thick mounting flanges, such as in Figure 2.10. The benefits of column-type sensors including simplicity, robustness and high axial stiffness. The main disadvantages are poor measurement isotropy, low sensitivity to axial force and coupling between the measurements of lateral forces and moments.

The earliest column-type designs were presented for biomechanics applications. Cunningham and Brown (1952) presented a plate supported by four load cells for the measurement of human gait. The columns were tubular cylinders, machined from a solid bar, with ERSGs mounted on the outside surface. Berme *et al.* (1975) presented a reduced-length design to facilitate inclusion within the pylon of a prosthesis. Instead of deriving the lateral forces using the difference in bending moment at two axial positions, the shear forces were measured directly using strain gauges orientated ±45° to the cylinder axis. Byrne and Houlsby (2005) and later

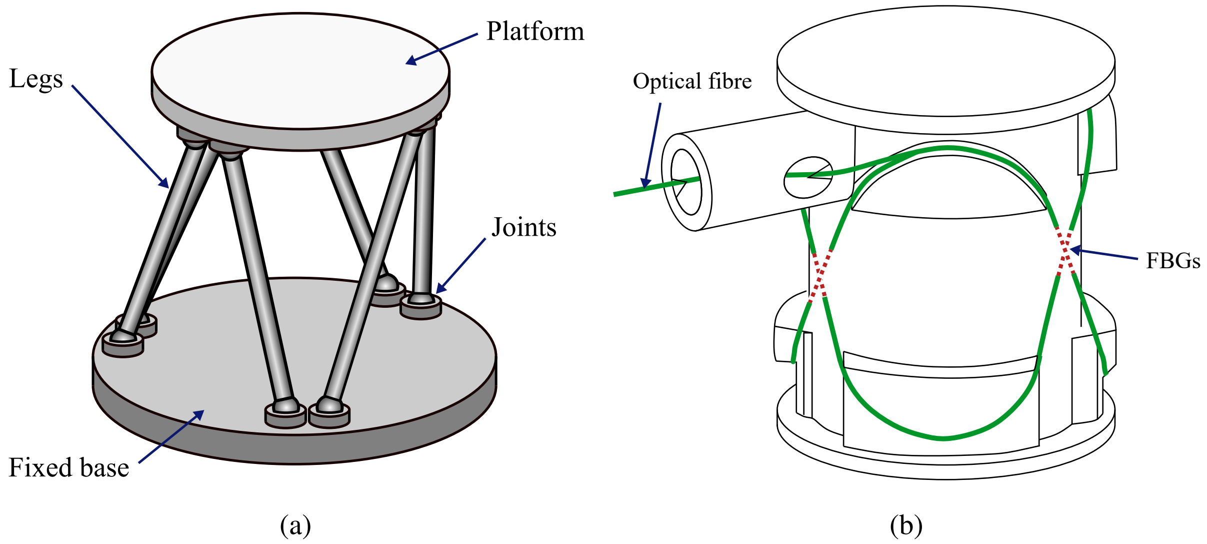

Figure 2.11 Stewart platform sensors: (a) Illustration of a Stewart platform sensor structure, with salient features, (b) Design proposed by Müller *et al.* (2009) with free-spanning FBGs

Bienen *et al.* (2006) used a column-type load cell for the measurement of six DOF loading applied to a model foundation on sand (see Figure 2.10). The outer surface of the cylinder was instrumented with 32 ERSGs connected into six full Wheatstone bridge circuits. Van der Laag (2016) extended this design to develop a large column sensor employing both ERSGs and FBGs. A total of 32 and 14 FBGs were bonded to both the outer and inner cylinder surfaces respectively. Arithmetic operations, referred to as 'digital Wheatstone bridges', were performed on the outputs of two or more FBGs to achieve load and temperature isolation.

Finally, Stewart platforms have also been shown to be effective as multi-axis force sensors. These structures consist of a rigid platform which is connected to a fixed base by six legs, as shown in Figure 2.11a. In sensor applications, the legs are formed from elastic members which can be instrumented to measure load-induced axial deformations. To implement a six DOF mechanism, the Stewart platform requires one spherical joint and either a universal or another spherical joint on each leg (Kang, 2001). When employed as a force sensor, the same joint configuration is required to ensure the leg deformations remain purely axial. Stewart platform sensors generally have the characteristics of high stiffness and load capacity, through distributing axial loading in parallel over all six of the legs.

Early Stewart platform sensors featured ball and socket joints between the legs and the platform and base. A number of designs have been documented with different sensitive elements, including single-axis force sensors (Romiti and Sorli, 1992), springs with LVDTs (Kang, 2001) and ERSGs (Dwarakanath *et al.*, 2001). These designs typically suffer from hysteresis, non-linearity and repeatability issues due to clearances and friction in the mechanical joints. Later designs typically use flexible joints, such as that used by Seibold *et al.* (2005), in which the sensor body is monolithic and the ends of the legs are machined to a thinner cross-section to mimic a spherical joint. These show improved performance over mechanical joints, but significantly increase the complexity of the structure. Stewart platform-inspired designs have also been proposed with FBG strain sensing. Müller *et al.* (2009) and Kim and Lee (2016) presented designs using free-spanning, pre-tensioned FBGs in place of the legs, with a separate central structure to support the platform (Figure 2.11b). Both designs did not consider temperature compensation, despite the experimental results of Kim and Lee (2016) confirming the outputs to be temperature dependent.

2.5 Summary

The literature highlights both the importance and the complexity of SSI during the construction of monolithic open caisson shafts, as well as the dearth of dedicated research into the problem. Despite skin friction on the external SLSI playing a critical role during sinking, the underlying mechanisms concerning friction development are poorly understood. Research pertaining to displacement piles and pipe jacking provide some insight, however fundamentally different SSI can develop due to differences in structure geometry and installation processes. Although the lubricated elemental interface testing has demonstrated the potential for friction reductions, case studies show the difficulties in achieving effective bentonite lubrication in sands in practice. Due to the significant remaining uncertainties and risks, it is clear there is scope for further research into caisson frictional behaviour in sands.

Furthermore, there is difficulty in accurately estimating the resistance at the base of the caisson wall, as many salient caisson-specific features are not captured by conventional bearing capacity calculations. Recent laboratory-scale testing has provided some insight into the influence of the cutting face inclination angle and roughness in sands, although the parameter space has not been studied comprehensively and the impact of simplifying assumptions, such as the presence of the cutting shoe, have not been explored. Whilst Royston *et al.* (2022b) provided a detailed numerical parametric study and associated design method for undrained soils, similar work has not been undertaken for the bearing capacity in cohesionless soils.

The measurement of contact stresses is an important means of gaining valuable insight into soil-structure interface behaviour. Installing sensors within full-scale projects allows detailed data to be captured, which can be used to improve understanding of the construction processes and provide real-time feedback of site conditions. However, recent field monitoring attempts on underground construction SLSIs have been critically limited by current sensor technology. Contact stress sensors installed in both caisson shafts (Royston, 2018) and pipejacked tunnelling (Phillips, 2023) showed a high degree of sensor failure, which was attributed to water ingress and EMI. These sensors also have high unit costs in the region of £1500 for commercial three-axis force sensors to £2900 for bespoke SSCS sensors. Deploying a comprehensive contact stress monitoring scheme at present is therefore very expensive and comes with a high risk of providing little useful output.

The review of existing SSCS sensors highlighted clear limitations of the current technology. There are a paucity of sensors in the literature capable of measuring frictional stress and very few designs provide a means of determining effective normal stress. The bespoke Stroud cell designs deliver high quality solutions, but their principal limitation for construction monitoring applications is the insufficient robustness of electrical-based gauging. Whilst the proposed sensors of Talesnick *et al.* (2014) and Talesnick and Ringel (2022) demonstrate very high quality results, they remain unproven in field monitoring applications. The requirement for a compressed air supply and the reliance on a very high precision LVDT are likely intractable in these environments. There is clear motivation for research into the development of new robust and lower-cost contact stress sensor technology.

Optical strain sensing in the form of FBGs is showing increased adoption in a wide range of fields and has the potential to address the issues faced by electrical sensors. The decreasing cost of FBGs is making them increasingly attractive for instrumentation in demanding conditions and therefore a good candidate for employment in underground construction monitoring applications. The review of multi-axis load cells has highlighted the merits of different candidate designs. Complex Stewart platform and cross-beam structures are less suited for FBG instrumentation, whereas the simplicity and robustness of the column-type sensor shows promise for adaptation into a new FBG-based SSCS sensor.

Chapter 3

Multi-axis force sensing using FBGs

3.1 Introduction

Multi-axis force sensors provide measurements of force and moment components in multiple spatial directions. A plethora of designs have been proposed in the literature, with the vast majority comprising electrical strain measurement techniques on complex sensor structures. The reliance on conventional electrical gauging has restricted deployment of these sensors in applications with high risk of water exposure or high levels of EMI. Furthermore the complex designs and labour-intensive gauging process drive up sensor cost, limiting widespread adoption beyond high-cost industries. Moving to optical strain measurement in the form of FBGs could overcome many of the limitations faced with electrical systems.

This chapter describes a new framework for using FBGs in multi-axis force sensor design, mitigating some of the key challenges faced in the literature. A simplistic sensor structure is coupled with the use of a machine learning model to form the mapping between the FBG strain measurements and force outputs. A general outline of the framework is provided and it is then applied to investigate a column-type six DOF sensor as an exemplar. A numerical study is used to evaluate potential sensor performance and to explore different instrumentation strategies. A physical prototype sensor instrumented with FBGs is then presented, demonstrating how the new approach is used in practice. This work was undertaken as a prerequisite for the development of a new SSCS sensor using FBGs in Chapter 4.

3.2 Problem definition

Figure 3.1 shows an illustrative force sensor with the notation adopted in this thesis for the general set of applied three-dimensional (3D) force and moment components. Convention defines the x and y axes in the plane of the sensor and the z axis in the out-of-plane direction. Therefore F_z and M_z denote axial force and torsional moment respectively, F_x and F_y denote mutually orthogonal lateral forces and M_x and M_y denote mutually orthogonal lateral moments. The actions on the sensor may be assembled into a vector $\boldsymbol{f}$ which, in the general six DOF case, can be defined as:

$$\boldsymbol{f} = \begin{bmatrix} F_\mathrm{x} & F_\mathrm{y} & F_\mathrm{z} & M_\mathrm{x} & M_\mathrm{y} & M_\mathrm{z} \end{bmatrix}^\mathrm{T} \tag{3.1}$$

The deformation induced in the sensor structure is captured by measured outputs, u_i, formed from the signals of one or more individual strain transducers on the sensor (e.g. resistance change with ERSGs, wavelength shifts for FBGs). These can be assembled into a vector, $\boldsymbol{u}$:

$$\boldsymbol{u} = \begin{bmatrix} u_1 & u_2 & u_3 & \dots & u_\mathrm{n} \end{bmatrix}^\mathrm{T} \tag{3.2}$$

where n is the total number of measurands. To obtain predictions of unknown applied loads, the relationship between $\boldsymbol{u}$ and $\boldsymbol{f}$ is required. In traditional multi-axis force sensors, this relationship is described by a sensor compliance matrix, $\boldsymbol{C}$, which is defined as:

$$\boldsymbol{u} = \boldsymbol{C}\boldsymbol{f} \tag{3.3}$$

where $\boldsymbol{C}$ is the Jacobian matrix of $\boldsymbol{u}$ with respect to $\boldsymbol{f}$ (Bayo and Stubbe, 1989; Bicchi, 1992). In practice, the components of $\boldsymbol{C}$ are determined experimentally by calibrating the sensor under each load component in turn (e.g. Berme *et al.*, 1975; Byrne and Houlsby, 2005). The matrix $\boldsymbol{C}$ in Equation 3.3 is subsequently inverted to allow the loads to be determined as linear combinations of the measured strain signals.

In addition to the applied loads, a sensor will typically be subjected to ambient temperature variation, ΔT. This is important as the outputs of strain measurement devices (e.g. ERSGs, FBGs) are typically affected by temperature variation. In practice, most conventional force

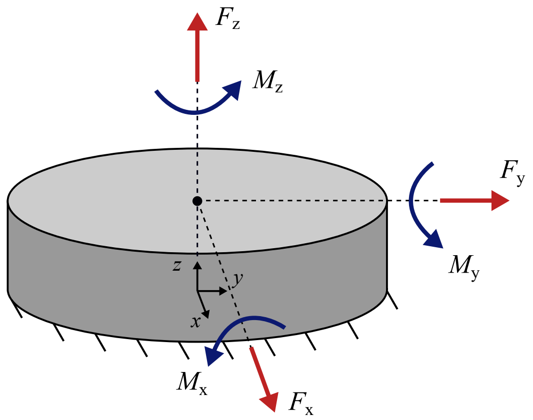

Figure 3.1 3D Cartesian coordinate system adopted for force sensor analysis, showing a general set of six DOF force and moment components

sensors are designed such that the measurands in Equation 3.2 are intended to be temperature independent (e.g. half or full Wheatstone bridges with ERSGs). This means ΔT is typically not included in $\boldsymbol{f}$ in Equation 3.1.

3.3 Fibre Bragg gratings

3.3.1 Overview

An FBG is a type of optical reflector that is created within the core of a single-mode optical fibre. An example of a typical array of FBGs is shown Figure 3.2, alongside illustrations of the FBG structure and spectral response. FBGs are created by illuminating a short region of fibre with a spatially varying laser, which inscribes a periodic modulation of the refractive index of the fibre core (Hill and Meltz, 1997). The resulting structure is a grating of length, l, typically between 2 and 10 mm, formed from thousands of grating periods of length Λ.

When a broadband spectrum of light is incident on an FBG, a narrow band of the spectrum is reflected in the fibre through coherent scattering at the grating index boundaries (Figure 3.2; Othonos, 1997). The reflected spectrum, commonly referred to as a 'peak', is characterised by the Bragg wavelength, λ_B, which is defined by:

$$\lambda_\mathrm{B} = 2n_\mathrm{eff}\Lambda \tag{3.4}$$

where n_eff is the mode effective refractive index (Hill and Meltz, 1997).

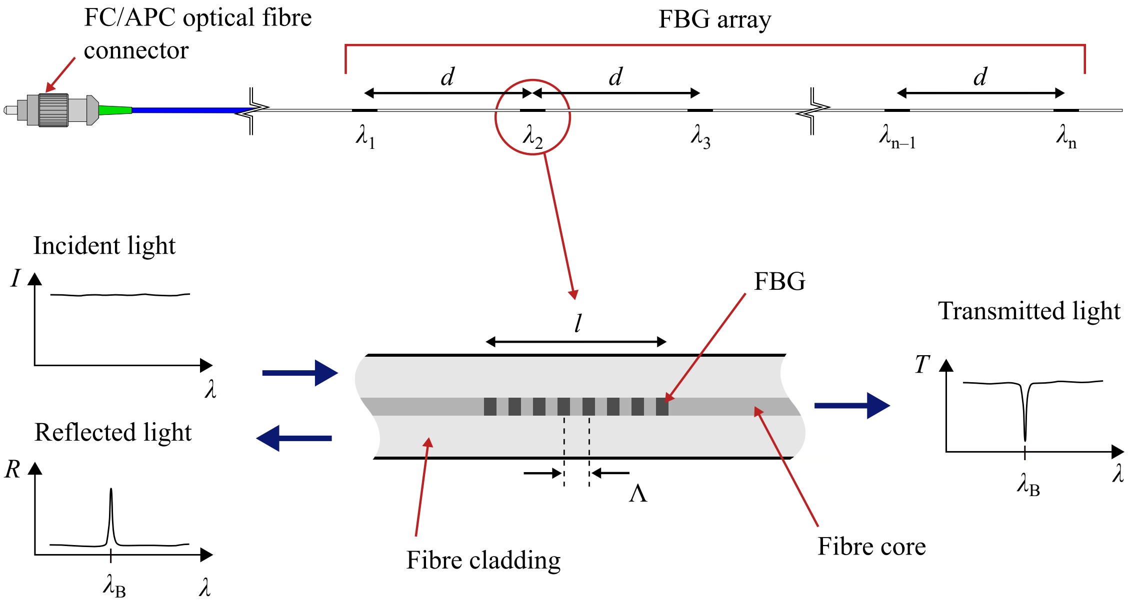

Figure 3.2 Illustration of a typical FBG array in an optical fibre, with detail showing indicative FBG structure and spectral response (not to scale)

An FBG can be exploited as a sensing element by using an optical interrogator to analyse changes in the measured peak reflected wavelength, λ_{p}, when the FBG is exposed to mechanical strain and/or temperature change. The shift in peak wavelength, $\Delta\lambda_{\mathrm{p}}$, induced by axial strain ε and a simultaneous temperature change ΔT is commonly expressed as:

$$\frac{\Delta\lambda_{\mathrm{p}}}{\lambda_{\mathrm{p}}} = (1 - P_{\mathrm{e}})\,\varepsilon + (\alpha + \zeta)\,\Delta T \tag{3.5}$$

where P_{e} is the photo-elastic coefficient of the fibre and α and ζ are the thermal expansion and thermal-optic coefficient of the fibre respectively. The strain and temperature sensitivities of a typical FBG with a peak wavelength of 1550 nm are approximately 1.2 pm/$\mu\epsilon$ and 14.2 pm/°C respectively (Othonos, 1997). When an FBG is bonded to or embedded within a structure, additional strain is applied due to differing thermal expansion of the fibre and structure. A modified form of Equation 3.5 accounting for this effect is given by Magne *et al.* (1997) as:

$$\frac{\Delta\lambda_{\mathrm{p}}}{\lambda_{\mathrm{p}}} = (1 - P_{\mathrm{e}})\,\varepsilon + (\alpha + \zeta + (1 - P_{\mathrm{e}})\,(\alpha_{\mathrm{s}} - \alpha))\,\Delta T \tag{3.6}$$

where α_{s} is the coefficient of thermal expansion of the structure. Equation 3.6 is valid for a free boundary condition, where the structure is free to expand and contract with temperature.

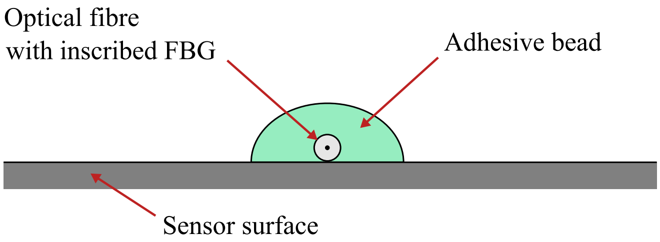

Figure 3.3 Illustration of a cross-section through an optical fibre bonded to the surface of a sensor structure (not to scale)

FBG-based sensing systems commonly exploit wavelength division multiplexing to allow arrays of multiple FBGs to be created on a single optical fibre (as shown in Figure 3.2). Each grating is inscribed with a distinct Bragg wavelength and at a different position along the fibre, typically with a uniform physical centre-centre spacing, d. An optical interrogator emits a broad spectrum of light into the fibre and uses peak detection algorithms to identify and monitor all of the connected FBGs, using their unique reflected peaks. This allows a large number of measurements to be obtained by each channel of an interrogator and can greatly simplify the connectivity of a multi-axis sensor compared to an equivalent electrical system.

In this thesis, all studies are performed using a Micron Optics HYPERION si255 optical interrogator. All of the FBG arrays used have peak wavelengths in the range 1460–1620 nm and a spectral spacing of 3–4 nm, to ensure adjacent peaks do not become indistinguishable as they are shifted under the action of strain and/or temperature. The FBGs used for sensor development in this thesis are draw tower gratings (DTGs) provided by FBGS International. The production of DTGs involves simultaneously drawing the optical fibre, writing the gratings and coating the fibre. Compared to conventional strip and recoat FBG manufacturing process, DTG production leads to a reduced unit cost and maintains the strength of a continuous fibre. When combined with the use of a low bend-loss fibre, this enables easier handling and tighter manipulation of the fibre, which is beneficial for the instrumentation of relatively compact multi-axis sensors.

3.3.2 FBG sensor strain measurement

To provide a measurement of the mechanical strain induced in a sensor structure under applied loadings, FBGs are bonded onto an exposed surface of the sensor. This bond is required to

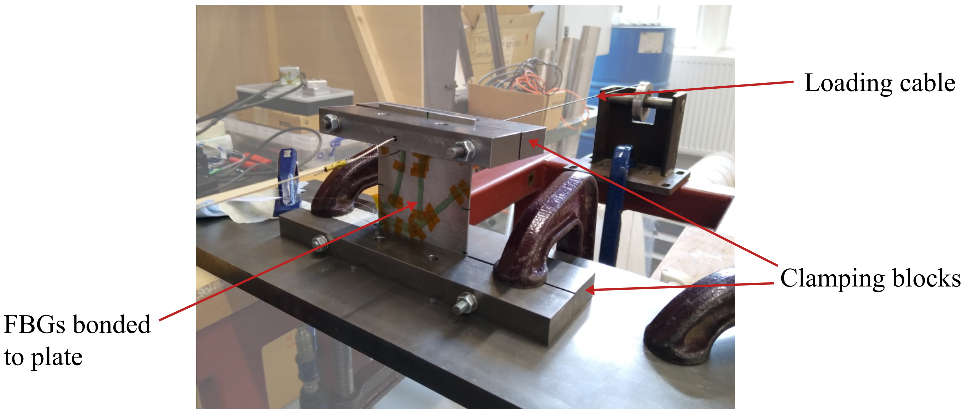

Figure 3.4 Set up of the cantilever bending test instrumented with FBGs

effectively transfer the mechanical strain and to remain stable over time. A two-part acrylic adhesive (3M Scotch-Weld DP8810NS) is used for this purpose, under recommendation from the experience of fibre optics specialists. An illustration showing a section through a bonded FBG is shown in Figure 3.3. The fibre is placed in direct contact with the sensor surface, which has been lightly abraded with fine sandpaper and degreased. Prior to bonding, the length of fibre containing each FBG is aligned by applying a small tensile pre-strain, to ensure the fibre remains straight during deformation. Each FBG is manually bonded in place by covering the full grating length with a bead of adhesive.

To assess the ability of FBGs to provide accurate strain measurements, a simple cantilever bending test was first performed. The test set up is shown in Figure 3.4, comprising a 2 mm × 76 mm × 76 mm aluminium plate held rigidly between two sets of clamping blocks. The plate was instrumented on one side with a DTG supplied by FBGS International, aligned approximately with the cantilever axis (0°). The opposite side was instrumented with three FBGs supplied by City University, London: one placed axially (0°) and two others placed offset at angles of 15° and 45°. The FBGs were bonded to the plate using the procedure outlined above; each FBG was placed under a small tensile pre-strain (between 0–300 pm shift) to ensure straightness.

The plate base clamps were bolted to a rigid loading frame and lateral loads were applied to the 'tip' clamps using weights, via a cable and pulley system. Load increments were applied between ±102.6 N in one load-unload cycle. The FBG peak wavelength responses are shown in Figure 3.5; all four FBGs demonstrate a high degree of linearity across the load range,

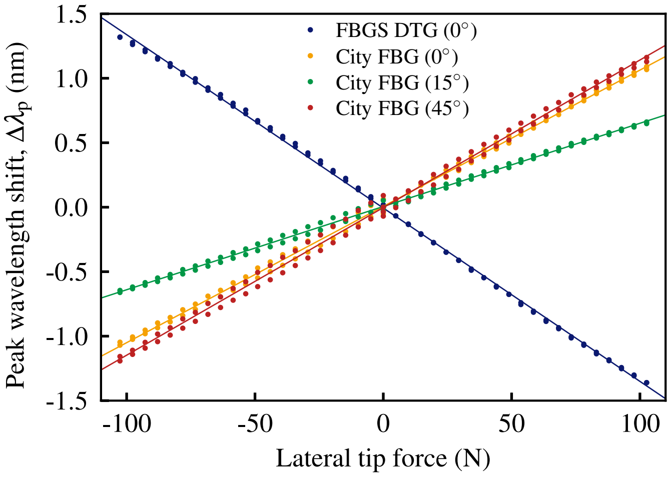

Figure 3.5 Raw peak wavelength shift data for the four FBGs on the cantilever test

indicating good strain transfer even in compression beyond the applied pre-strain. Furthermore, there appears to be good repeatability of the measurements, with only slight hysteresis noticeable with the City FBGs. It is noteworthy that these data are not compensated for temperature, so some variation may be attributable to ambient temperature variation during the loading. The axial FBGS and City FBGs undergo a wavelength shift of 1318 pm and 1231 pm respectively under full load (102.6 N). If temperature is assumed constant, using Equation 3.6 with a typical FBG gauge factor of $1 - P_e = 0.78$ gives an estimated strain of 1105 $\mu\epsilon$ and 1009 $\mu\epsilon$ in the FBGS and City FBG respectively. Beam theory estimates of the strains at the FBG locations were calculated as 1100 $\mu\epsilon$ and 1040 $\mu\epsilon$ respectively. Although approximate, this indicates close agreement with the strains predicted by the FBG measurements and gives confidence in the adopted procedures for FBG bonding in sensor applications.

3.4 Machine learning framework

3.4.1 Motivation

The ‘traditional’ approach to multi-axis force sensing involves forming algebraic combinations of strain transducer signals to produce the sensor outputs in Equation 3.2. The most common implementation of this is using ERSGs combined in Wheatstone bridge circuits. This improves sensor sensitivity, achieves temperature compensation and, in some instances, can be used to isolate individual load components. However, this process requires a large number of strain measurements (typically a minimum of between two and four times the number of output DOF, for half and full bridge circuits) to be mounted in specific positions on the sensor structure.

Attempts have been made to apply similar principles using FBGs in force sensors (e.g. Fernandez Fernandez *et al.*, 2001; Van der Laag, 2016; Xiong *et al.*, 2018), but this has limitations. Firstly, performing arithmetic operations on two or more FBG measurements does not achieve an increase in sensitivity, like with ERSGs. The individual strain transducers must be very accurately positioned to achieve temperature compensation and avoid cross-coupling. This is often intractable with FBGs, due to the physical limitations of manipulating the individual FBGs within an array on a single continuous optical fibre. These difficulties are magnified on sensors with complex geometry or higher output DOF, which require more FBGs. Furthermore, the large number of strain transducers required increases sensor cost, which is particularly relevant for FBGs given their comparatively high unit cost.

3.4.2 Overview

Instead of 'manually' determining the individual linear relationships between the strain transducer outputs and the applied load components (c.f. terms in matrix $\boldsymbol{C}$ in Equation 3.3), the entire inverse mapping can be determined automatically by a multi-output linear regression (LR) machine learning model. The output predicted by a single-output LR model, $\hat{f}$, for a set of n input features u_{i} can be defined as:

$$\hat{f} = b + w_1 u_1 + w_2 u_2 + \ldots + w_{\mathrm{n}} u_{\mathrm{n}} \tag{3.7}$$

where w_{i} and b are the coefficients and intercept of the linear fit respectively. A multi-output LR model extends this to jointly predict a vector of m outputs, $\hat{\boldsymbol{f}}$, as:

$$\hat{\boldsymbol{f}} = \boldsymbol{b} + \boldsymbol{W}\boldsymbol{u} \tag{3.8}$$

where $\boldsymbol{u}$ is a vector of n input features, $\boldsymbol{b}$ is a vector of m intercept values and $\boldsymbol{W}$ is a $m \times n$ matrix of coefficients.

The application of the machine learning approach to multi-axis force sensing is outlined in Figure 3.6. The sensor LR model takes an input vector of n strain measurements, $\boldsymbol{u}$, which comprise the peak wavelength shifts of the FBGs bonded to the sensor structure, $\Delta\lambda_\mathrm{i}$:

$$\boldsymbol{u} = \begin{bmatrix}\Delta\lambda_1 & \Delta\lambda_2 & \Delta\lambda_3 & \dots & \Delta\lambda_\mathrm{n}\end{bmatrix}^\mathrm{T} \tag{3.9}$$

The model returns a vector of $m = 7$ predicted sensor outputs, $\hat{\boldsymbol{f}}$, comprising the full six DOF load components and also temperature change, ΔT:

$$\hat{\boldsymbol{f}} = \begin{bmatrix}F_\mathrm{x} & F_\mathrm{y} & F_\mathrm{z} & M_\mathrm{x} & M_\mathrm{y} & M_\mathrm{z} & \Delta T\end{bmatrix}^\mathrm{T} \tag{3.10}$$

The values in Equation 3.9 are shifts in FBG peak wavelengths determined relative to a predefined ‘zeroing state’, which is recorded after sensor installation under zero applied loading. This approach is common for all load cells, to mitigate the influence of any differences in mounting. To implement the sensor model, only the coefficients matrix $\boldsymbol{W}$ in Equation 3.8 is required.

A linear model is adopted under the assumption of there being a linear relationship between the FBG peak wavelengths and the applied loads. This reflects the expectation that: a) the sensor structure will undergo linear elastic deformation, and b) the FBG strain dependence is known to be linear, both from theory (Equation 3.6) and experimental results (Figure 3.5). Nevertheless, the proposed framework is not limited to linear models. It can be readily applied using alternative data-driven models, such as higher order polynomial-based models or even neural networks, to handle possible measurement non-linearities (e.g. non-linear sensor material behaviour).

The main novelty of this approach is that the LR model is trained to identify the relationship between ΔT and $\boldsymbol{u}$ directly, rather than attempting to manipulate the FBG signals to produce temperature-independent measurands (i.e. ‘Wheatstone bridge’-type algebraic combinations or using a separate strain-free FBG). Although this requires a temperature calibration to be performed, the framework therefore does not rely on strict positioning of the individual strain transducers to achieve effective temperature compensation. This helps to simplify the instrumentation process by allowing the FBG positions to be altered to meet the physical constraints imposed by the optical fibre. Furthermore, when compared to using traditional algebraic com-

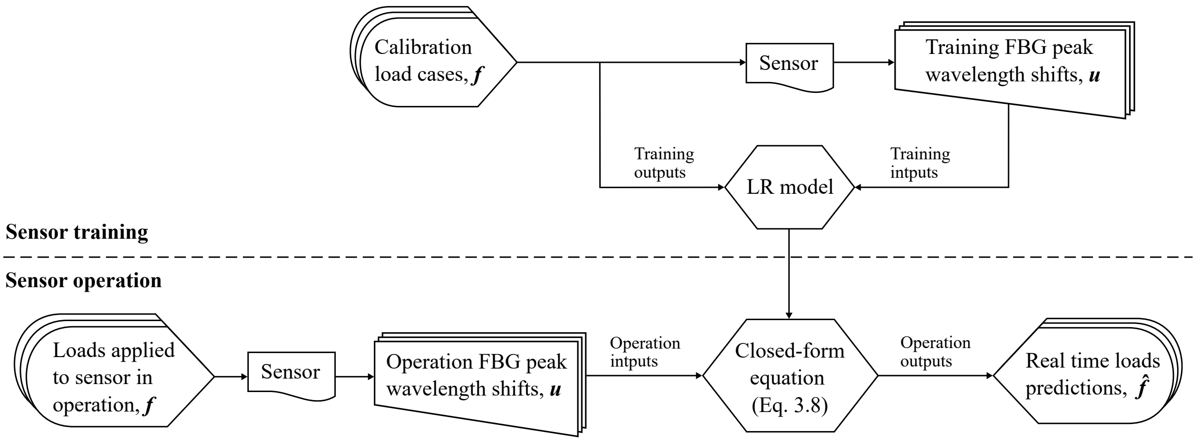

Figure 3.6 Flowchart showing the implementation of the proposed machine learning framework to multi-axis force sensing in practice

binations, a significant reduction in the number of FBGs can be achieved. Theoretically a minimum of seven FBGs on the sensor body is required to derive the six independent load components and temperature change in $\boldsymbol{f}$ ($n = m = 7$).

3.4.3 Training procedure

The sensor LR model is trained using samples of applied force/moment components and the corresponding measured peak wavelength shifts of the FBGs on the sensor. This 'training dataset' can be provided by similar tests to conventional sensor calibration tests (i.e. increments of the individual load components). Whilst not a strict requirement, this is practically desirable as isolated load cases are straightforward to achieve in a laboratory setting using dead weight. In addition, data must be provided for the model to determine the temperature dependence of the FBGs. This can be achieved through exposing the sensor to different ambient temperatures using, for example, a thermal water bath or environmental chamber. The intention is for the trained sensor LR model to generalize beyond the limited set of training load cases, to accurately predict on varied and combined load cases in operation. The minimum number of calibration load case measurements required to train the sensor LR model is equal to the number of FBGs on the sensor, as this creates a determined system. In practice a larger number of measurements are typically used, to provide more information and to allow interrogation of the individual FBG responses.

The training process determines the coefficients matrix $\boldsymbol{W}$ by minimising the sum of squared differences between the target outputs $\boldsymbol{f}$ and their corresponding model-predicted values $\hat{\boldsymbol{f}} = \boldsymbol{W}\boldsymbol{u}$. More advanced linear models can be created through regularization, by adding penalisation terms into the least squares cost function. Examples include ridge regression (Hoerl and Kennard, 1970), which can reduce the size of the terms in $\boldsymbol{W}$, and lasso regression (Tibshirani, 1996), which can perform feature selection by reducing the number of non-zero terms in $\boldsymbol{W}$. Despite the potential advantages, other models have been extensively tested for this problem, using both numerical and experimental data, and were found to have no benefit over ordinary least squares linear regression.

3.5 Numerical simulation of sensor framework

3.5.1 Column-type force sensor

The framework is first explored in this chapter via a numerical study of a six DOF column-type force sensor. This forms an initial proof of concept of the framework and is used to assess the impact of strain transducer positioning on the sensor structure on the potential sensor performance. The column-type design was highlighted in Chapter 2 as being well suited to FBG instrumentation due to the large exposed continuous gauging surface. However, the framework is not limited to this specific sensor structure and it can be readily applied to other designs, particularly those with a degree of flexibility in where the strain transducers can be located.

The sensor described by Byrne and Houlsby (2005) in Figure 2.10 is a good example of

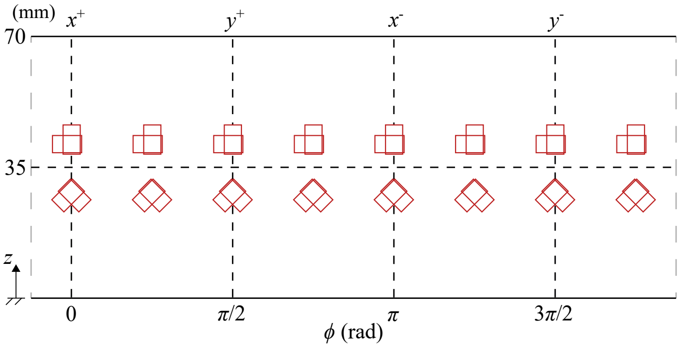

Figure 3.7 External surface of the column-type sensor documented by Byrne and Houlsby (2005) showing the layout of 32 ERSGs in overlapping pairs

a conventionally instrumented column-type force sensor. It consists of a thin-walled cylinder with thick end flanges machined from aluminium alloy. The outer surface is instrumented with 32 ERSGs in a layout shown in Figure 3.7, which are connected in six full Wheatstone bridge circuits. The gauges are positioned at the octant locations around the circumference and in overlapping pairs orientated at 0°, 90° and ±45° to the cylinder axis, corresponding to maximum induced strain under each load component. Axial force, F_z, and the lateral moments, M_x and M_y, are determined by ERSGs oriented 0° and 90° to the cylinder axis, measuring the strain induced under axial compression and bending respectively. Lateral forces, F_x and F_y, are determined using ERSGs orientated ±45° to the cylinder axis to measure shear strain. Torsional moment, M_z, is also measured via gauges at ±45°, measuring the shear strain induced by torsion.

3.5.2 Numerical sensor model

A closed-form model was developed to simulate the response of the cylindrical sensor structure to six DOF loading and uniform temperature change (see Figure 3.8). This type of model allows rapid investigation of different instrumentation configurations, using a large number of load cases. The sensor structure is approximated as a thin-walled cylinder of length L and inner and outer radii of R_i and R_o respectively. Adopting a 3D Cartesian coordinate system as in Figure 3.1, the cylinder has a circular cross-section in the xy plane, a fixed end at $z = 0$ and the six load components applied to the free end at $z = L$. Using the thin-wall assumption (i.e. the radial stress is taken as zero), the stress-state at any location is defined by three components as shown in Figure 3.9a: circumferential stress σ_{11}, axial stress σ_{22}, and shear stress τ_{12} (where $\tau_{21} = \tau_{12}$ due to symmetry). Euler-Bernoulli beam theory is used to estimate the stresses induced in the cylinder wall under each load component, assuming the cylinder remains elastic:

$$\sigma_{11} = 0 \tag{3.11}$$

$$\sigma_{22} = \frac{F_\mathrm{z}}{A} + \frac{M_\mathrm{x} y}{I} - \frac{M_\mathrm{y} x}{I} - \frac{F_\mathrm{x}(L-z)x}{I} - \frac{F_\mathrm{y}(L-z)y}{I} \tag{3.12}$$

$$\tau_{12} = \frac{M_z r}{J} - \frac{F_\mathrm{x}\sin(\phi)}{\pi t R_\mathrm{avg}} + \frac{F_\mathrm{y}\cos(\phi)}{\pi t R_\mathrm{avg}} \tag{3.13}$$

where r is the radial position within the cylinder wall, defined by $r = \sqrt{x^2 + y^2}$; ϕ is the angular position in the xy plane from the positive x axis, defined by $\phi = \tan^{-1}(y/x)$; R_{avg} is the average cylinder radius, defined by $R_{\mathrm{avg}} = (R_{\mathrm{o}} + R_{\mathrm{i}})/2$; t is the cylinder wall thickness, defined by $t = R_{\mathrm{o}} - R_{\mathrm{i}}$; A, I and J are the cylinder cross-sectional area, second moment of area and polar second moment of area respectively.

The strain field induced by the applied loads can be determined from the stress components described in Equations 3.11–3.13 using plane-stress Hooke's law. The cylinder is also assumed to expand linearly in the axial and circumferential directions when exposed to a uniform temperature change, ΔT. Therefore, the total strain-state due to the combined effect of thermally- and mechanically-induced strain can be defined as:

$$\varepsilon_{11} = \frac{1}{E}(\sigma_{11} - \nu\sigma_{22}) + \alpha_{\mathrm{s}}\Delta T \tag{3.14}$$

$$\varepsilon_{22} = \frac{1}{E}(\sigma_{22} - \nu\sigma_{11}) + \alpha_{\mathrm{s}}\Delta T \tag{3.15}$$

$$\gamma_{12} = \frac{1}{G}\tau_{12} \tag{3.16}$$

where ε_{11}, ε_{22} and γ_{12} are the circumferential, axial and shear strain in the cylinder wall

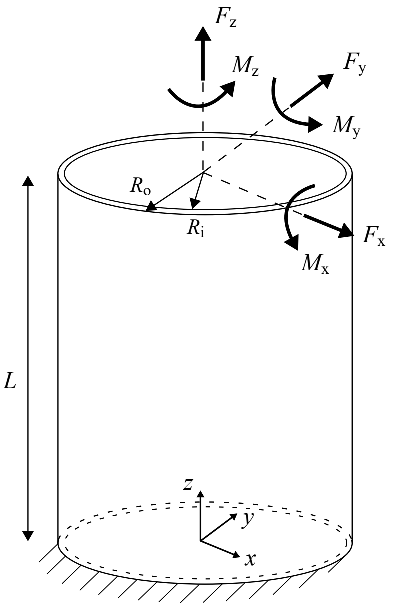

Figure 3.8 Schematic of the analytical model of the column-type force sensor

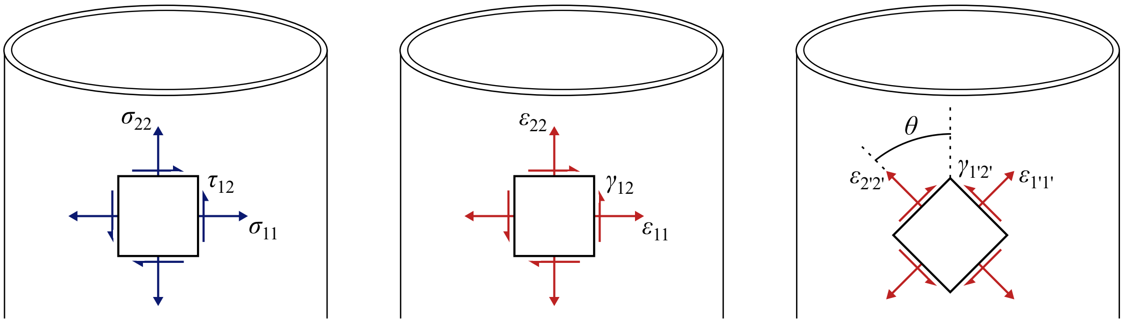

(a) (b) (c)

Figure 3.9 Outputs defined at a point on the cylinder surface for the analytical model: (a) stress state, (b) strain state, and (c) rotated strain state

respectively (Figure 3.9b); E, ν, G and α_s are the Young's modulus, Poisson's ratio, shear modulus and coefficient of thermal expansion of the cylinder material respectively. The strain in any orientation on the cylinder is obtained by rotating the strain state using:

$$\varepsilon_{2'2'} = \frac{\varepsilon_{11} + \varepsilon_{22}}{2} - \frac{\varepsilon_{11} - \varepsilon_{22}}{2}\cos(2\theta) - \frac{\gamma_{12}}{2}\sin(2\theta) \tag{3.17}$$

where θ is the rotation angle relative to the cylinder axis and $\varepsilon_{2'2'}$ is the direct strain in the rotated state (see Figure 3.9c). The analytical model (Equations 3.11–3.17) can be interrogated to obtain the strain measured by 'virtual strain transducers' in any position and orientation on the cylinder surface for a set of applied loads and temperature change.

The performance of the analytical model is validated through comparisons with 3D FEA performed using the commercial software Abaqus/Standard (Simulia, 2020). A cylinder was created using 3D eight-node linear brick elements, as shown in Figure 3.10a. The cylinder is modelled as linear elastic, with a 'built-in' boundary condition on the base and a rigid plane defined on the top surface, to simulate the influence of the thick mounting flanges. The geometric and material parameters documented by Byrne and Houlsby (2005) are adopted for model validation and all subsequent analyses in this chapter (see Table 3.1). Further details of an analogous FEA model and the corresponding surface strain extraction process are provided in Sections 4.3.2–4.3.3.

A single combined load case $\boldsymbol{f} = [250\ \text{N}, 250\ \text{N}, 500\ \text{N}, 25\ \text{Nm}, 25\ \text{Nm}, 25\ \text{Nm}, 10\ °\text{C}]^{\text{T}}$

was selected for validation. The response of the structure is shown in Figure 3.10b with FEA-predicted contours of maximum principal strain. For the purpose of model comparison, six 50 mm strain distributions on the cylinder outer surface are considered (see Figure 3.11). The results of this exercise are presented in Figure 3.12, where very close agreement between the analytical and 3D FEA predictions can be observed. The responses under each individual load component have also been investigated, which demonstrate comparable agreement. Only minor deviations are evident towards the top and bottom boundaries due to edge effects not captured by the analytical model. Nevertheless, over the central region of interest, the analytical model provides an excellent representation of the surface strain on the sensor structure.

3.5.3 Modelling preliminaries

The validated analytical model of the column-type sensor is used to provide synthetic data for this numerical study, as shown in Figure 3.13. The inputs to the sensor LR model are strains from a layout of 'virtual strain transducers' defined at specific points on the cylinder external surface, determined using Equation 3.17. Each point measurement is defined by an axial position, z_i, circumferential position, ϕ_i, and orientation angle, θ_i, as shown in Figure 3.14. A layout of n strain measurements on the cylinder surface is represented by an $n \times 3$ matrix, $(\boldsymbol{z}, \boldsymbol{\phi}, \boldsymbol{\theta})$. The LR model outputs are the load combinations and temperature changes provided to the analytical model in Equations 3.11–3.16. Although the model-predicted strains could be converted to FBG

Table 3.1 Geometric and material parameters adopted for the column-type sensor model numerical study, as documented by Byrne and Houlsby (2005)

Parameter	**Value**
Outer radius, R_o (mm)	27.5
Wall thickness, t (mm)	0.475
Cylinder length, L (mm)	70
Young's modulus, E (GPa)	72
Shear modulus, G (GPa)	27.1
Coefficient of thermal expansion, α_s (K^{-1})	24×10^{-6}

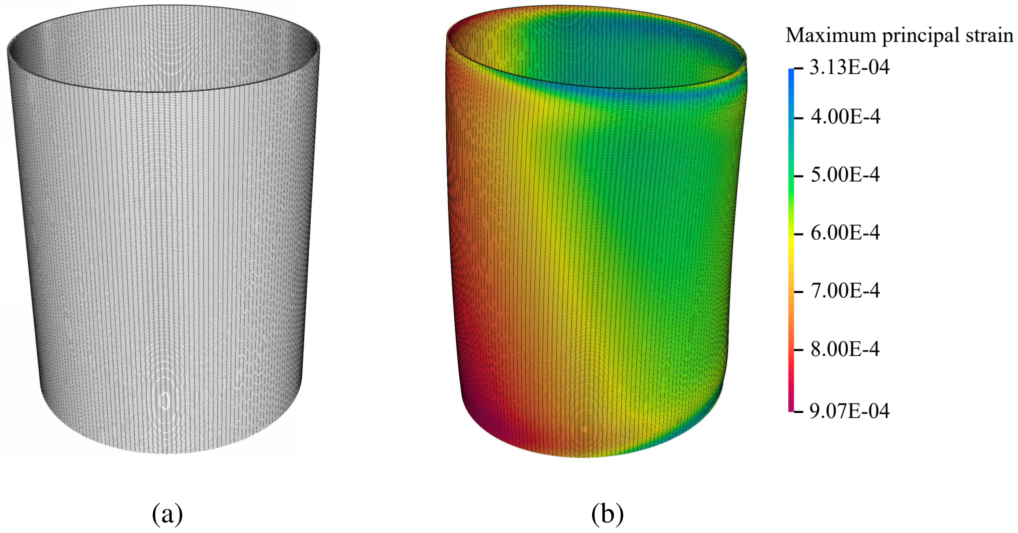

Figure 3.10 3D FEA of the column-type force sensor structure: (a) undeformed mesh, and (b) deformed mesh with contours of maximum principal strain for the combined actions $\boldsymbol{f} = [250\text{ N}, 250\text{ N}, 500\text{ N}, 25\text{ Nm}, 25\text{ Nm}, 25\text{ Nm}, 10\text{ °C}]^{\mathrm{T}}$

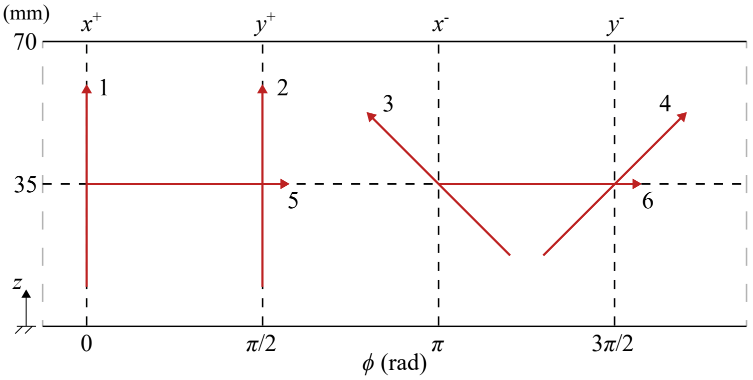

Figure 3.11 Six strain distributions on the cylinder external surface used for validation of the analytical model using 3D FEA

'peak wavelength shifts', using Equation 3.6 with assumed sensitivity values, this has not been applied here as it would simply be a linear scaling of the data.

To simulate the resolution of experimentally-obtained measurements, Gaussian white noise with zero mean and standard deviation of five is superimposed on the analytically-predicted strain values. This noise level was selected to be conservative, to provide a robust and comprehensive assessment of sensor performance. The Hyperion si255 was assessed to show noise with mean magnitude corresponding to approximately 2.0 $\mu\epsilon$. The noise level selected gives a mean magnitude over a large number of samples of 4.0 $\mu\epsilon$.

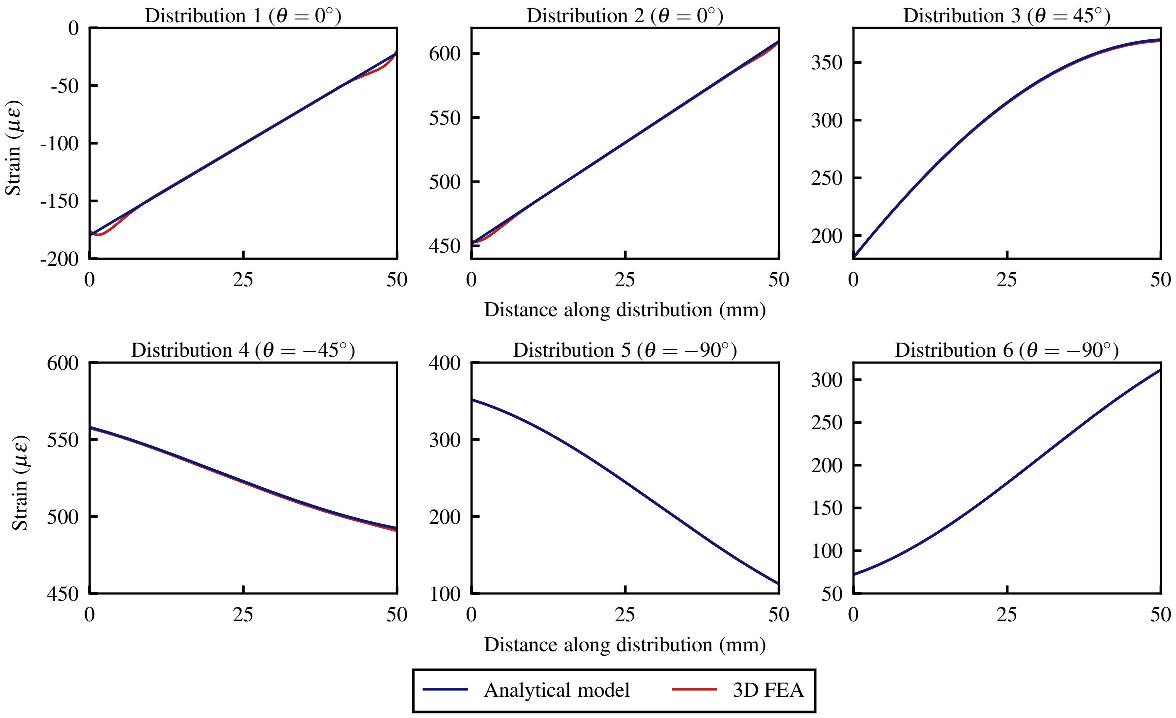

Figure 3.12 Strain distributions for validation of the analytical model against 3D FEA. The distributions on the cylinder external surface correspond with the positions in Figure 3.11, under actions $\boldsymbol{f}$ = [250 N, 250 N, 500 N, 25 Nm, 25 Nm, 25 Nm, 10 °C]$^{\mathrm{T}}$

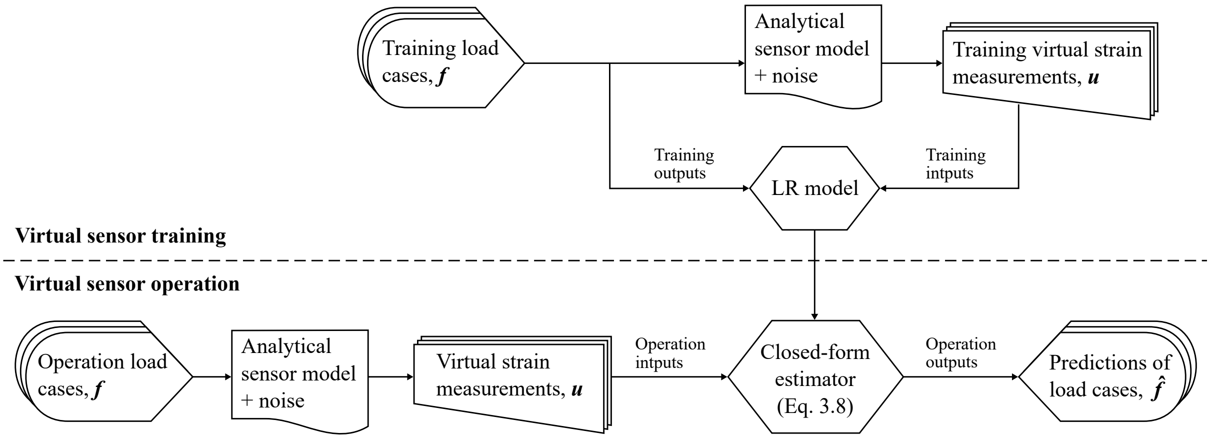

Figure 3.13 Flowchart outlining the numerical study of the proposed machine learning framework, using synthetic data from the column-type sensor analytical model

The 'training' dataset adopted for the numerical study contains 70 examples comprising increments of the individual load components and temperature change applied independently (see Table 3.2). Although not required for the machine learning methods, this simulates conventional calibration procedures typically used in practice. To ensure robustness to potential temperature variations during calibration, ΔT is varied randomly between ±5 °C in these datapoints. The

Table 3.2 Load component and temperature values used to generate training (calibration) and testing (operation) datasets for the numerical simulation of the column-type sensor

	$\boldsymbol{F}_\mathrm{x}$	$\boldsymbol{F}_\mathrm{y}$	$\boldsymbol{F}_\mathrm{z}$	$\boldsymbol{M}_\mathrm{x}$	$\boldsymbol{M}_\mathrm{y}$	$\boldsymbol{M}_\mathrm{z}$	$\boldsymbol{\Delta T}$
Range	± 250 N	± 250 N	± 500 N	± 20 Nm	± 20 Nm	± 20 Nm	± 15 °C
Training data (70 examples)	10 inc.	0	0	0	0	0	Random
	0	10 inc.	0	0	0	0	Random
	0	0	10 inc.	0	0	0	Random
	0	0	0	10 inc.	0	0	Random
	0	0	0	0	10 inc.	0	Random
	0	0	0	0	0	10 inc.	Random
	0	0	0	0	0	0	10 inc.
Testing data (1000 examples)	Random	Random	Random	Random	Random	Random	Random

inc. = increments, spaced evenly between range limits

trained LR model is then used to predict on a 'testing' dataset of previously unseen load cases. For this purpose, 1000 samples comprising random combinations of all seven output variables are used (see Table 3.2). The coefficient of determination, R^2, between the model predicted outputs and the target outputs of this testing dataset is used as the performance metric. This onerous testing provides a robust numerical assessment of output decoupling and temperature independence and simulates conditions that might be encountered in sensor operation. This was undertaken to provide a rigorous appraisal of the predictive performance of the trained sensor LR model and its ability to generalize.

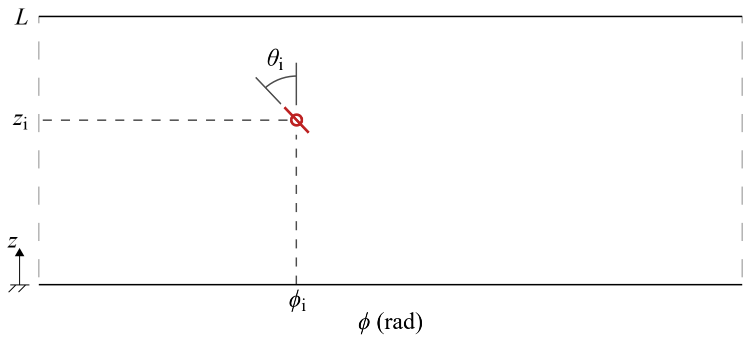

Figure 3.14 Parameters defining the position and orientation of each FBG or 'virtual strain measurement' on the cylinder sensor structure external surface

3.6 Instrumentation strategies assessment

3.6.1 Optimised layout

Three different instrumentation schemes have been considered in the numerical study of the machine learning framework: (a) an 'optimised' layout, (b) 'redundant' layouts, and (c) 'repeating pattern' layouts. The optimised approach seeks to identify an optimum layout of the minimum number of strain measurements required to predict the output variables ($n = m = 7$). Although numerous optimisation algorithms exist (e.g. grid search, random search, and evolutionary algorithms), Bayesian optimisation is adopted here for its efficiency, robustness to noisy data, and its widespread use in practical domains (Shahriari *et al.*, 2016). Bayesian optimisation is an iterative algorithm that is powered by two key components: a probabilistic surrogate model for the objective function being minimised and an acquisition function. The probabilistic surrogate model typically employs Gaussian processes to approximate the objective function, using the inputs and their associated outputs. The acquisition function then uses the predictive distribution of the surrogate model to determine where to sample next in the input space. Acquisition functions determine the utility of candidate locations by trading off exploration of uncertain locations in the input space and exploitation of a known optimal location. The surrogate model is then updated to include the output corresponding to the new input and the process is repeated iteratively. At the end of the iterations, the input space would have been efficiently searched to identify an optimal set of inputs.

For this study the optimisation space contains 21 variables, which are the three positional parameters of the seven strain measurements, (z_i, ϕ_i, θ_i). These variables are allowed to vary continuously within the ranges $0.2L \leq z_\mathrm{i} \leq 0.8L$, $0 \leq \phi_\mathrm{i} < 2\pi$, and $-\pi/2 < \theta_\mathrm{i} \leq \pi/2$. In each Bayesian iteration, a candidate layout is selected and an LR model is trained and tested using the datasets in Table 3.2. The optimisation process seeks to minimize the objective function $C(\boldsymbol{z}, \boldsymbol{\phi}, \boldsymbol{\theta}) = (1 - R^2)$, where R^2 is the coefficient of determination based on the testing dataset and averaged across all seven output variables. The measurement layout which provides the minimum C after 1000 Bayesian iterations is taken as the optimised solution. Figure 3.15 shows

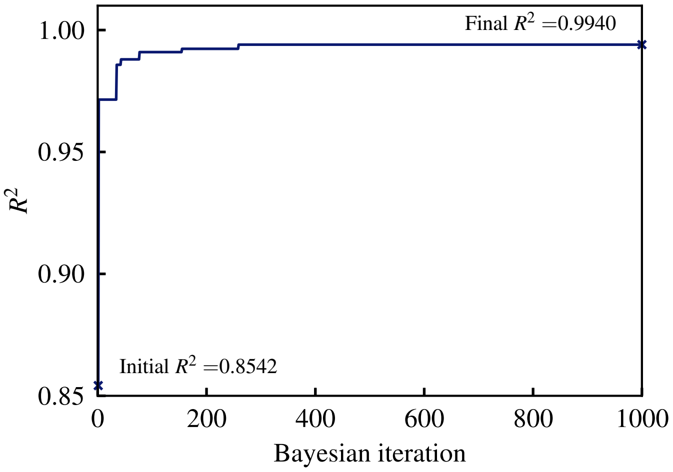

Figure 3.15 Convergence of the Bayesian optimisation process in selecting the layout of strain measurements in Figure 3.16, via minimization of the cost function $C = 1 - R^2$

an example optimisation process where it can be seen that the accuracy increases in a stepwise manner, as the cost function is only reduced after a better candidate solution is found.

The output of the instrumentation layout optimisation process is shown in Figure 3.16, alongside the multitude of candidate layouts explored. The identified layout was found to be dependent on the initial random selection of $\boldsymbol{z}$, $\boldsymbol{\phi}$ and $\boldsymbol{\theta}$, however the optimisation target (overall R^2 value) was found to be relatively insensitive to the initial parameters. This is due to the presence of numerous local minima for $C(\boldsymbol{z}, \boldsymbol{\phi}, \boldsymbol{\theta})$ in the 3D parameter space, meaning there are many possible measurement layouts that achieve similarly high performance. Characteristics that are common to layouts with very high R^2 values include distribution of the measurements around the cylinder circumference and the inclusion of a wide range of different orientation

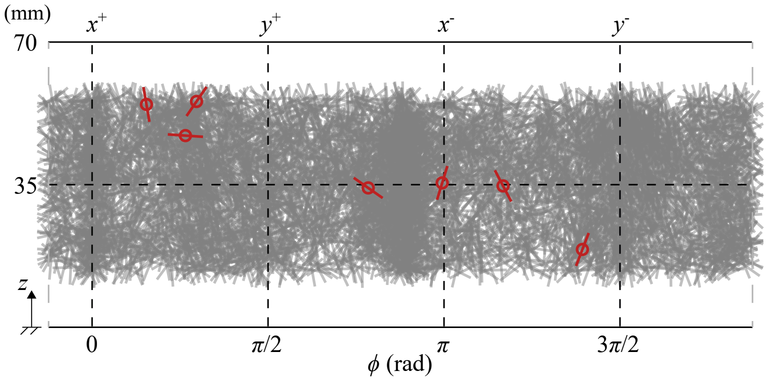

Figure 3.16 Layout of seven strain measurements on the cylinder external surface determined using the Bayesian optimisation process. The grey lines correspond to candidate solutions explored during the optimisation

Table 3.3 Summary of the predictive performance of the different instrumentation approaches considered in the numerical study

Output	Optimised layout (Figure 3.16)		Redundant layout (Figure 3.18)		Pattern layout (Figure 3.21)	
	R^2	Accuracy (%)	R^2	Accuracy (%)	R^2	Accuracy (%)
F_x	0.9901	2.35	0.9966	1.33	0.9917	2.09
F_y	0.9899	2.36	0.9949	1.64	0.9945	1.70
F_z	0.9887	2.47	0.9945	1.74	0.9828	3.11
M_x	0.9935	1.85	0.9980	1.03	0.9980	1.04
M_y	0.9987	0.84	0.9978	1.10	0.9965	1.38
M_z	0.9976	1.13	0.9984	0.89	0.9981	0.99
ΔT	0.9996	0.45	0.9998	0.33	0.9994	0.58
Average	0.9940		0.9971		0.9944	

Accuracy values = mean of the absolute differences between the LR model-predicted outputs and their target values in the testing dataset, expressed as a percentage of the corresponding range in Table 3.2

angles. The layout in Figure 3.16 also shows close grouping of certain measurements and spacing over the axial range, but these characteristics have been observed to be less critical to achieving good performance. Furthermore, similar to the design of Byrne and Houlsby (2005) (c.f. Figure 3.7), the optimisation process orients the majority of the transducers at close to 0°, 90° or ±45°, which correspond to maximum induced strain under different load components.

The performance of this layout is shown in Figure 3.17, which compares the LR model-predicted outputs against their target values in the combined load cases in the testing dataset. The corresponding R^2 and mean accuracy values for each output component are summarised in Table 3.3. It can be seen that the machine learning approach provides very good agreement for all seven outputs whilst using only the minimum number of measurements ($n = 7$). In particular, excellent force and moment predictions are obtained despite large simultaneous temperature fluctuations. The predictions of the moments are noticeably better than the force components; this is a result of higher strains induced by these components, which is a characteristic of the column-type design. Whilst it is not surprising that the outputs can be predicted from a set of only seven measurements, the numerical results indicate that high accuracy and minimal cross-

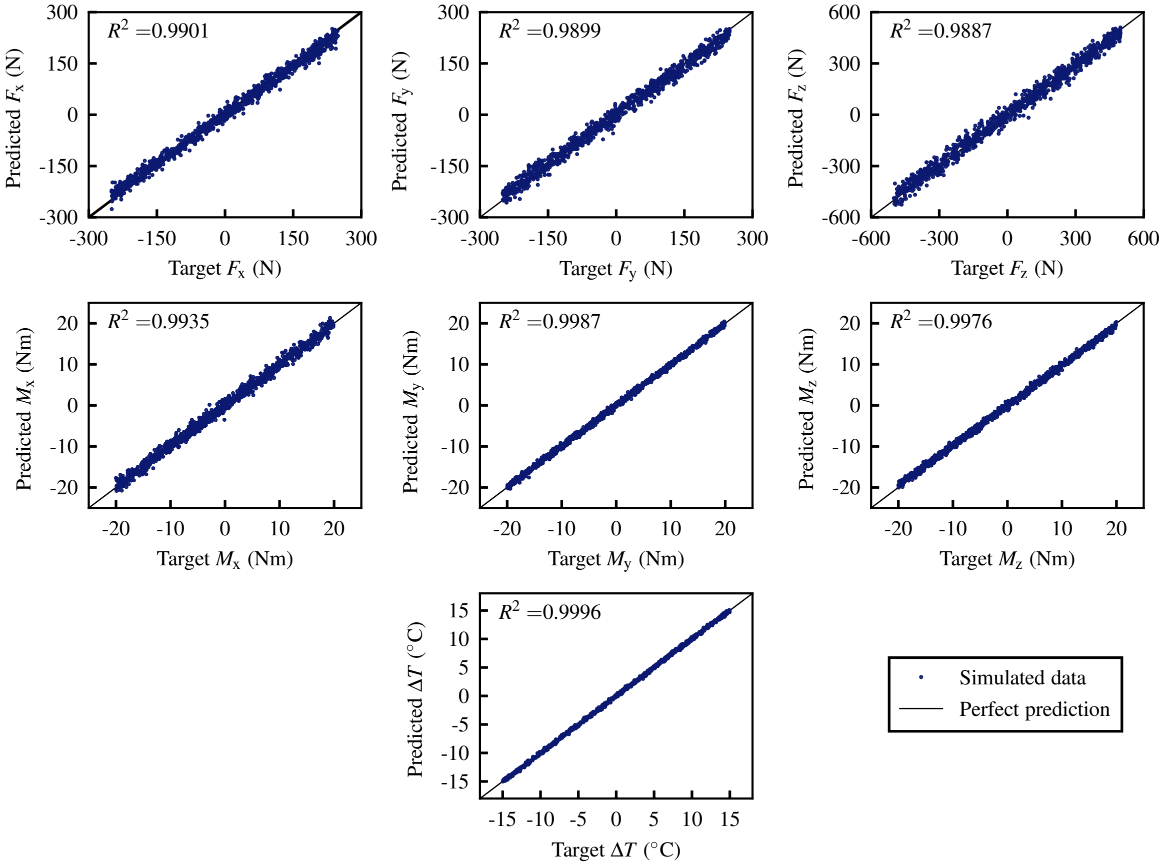

Figure 3.17 Comparison between the LR model predictions and the target output variables in the testing dataset for the optimised layout of seven strain measurements determined using Bayesian optimisation (Figure 3.16)

coupling can be achieved without the need for a large number of transducers. The agreement in Figure 3.17 and the corresponding values in Table 3.3 are also significantly affected by the conservative level of noise in this study; the accuracy in practice will show further improvement.

3.6.2 Redundant layout

Rather than identifying a specific instrumentation scheme, an alternative approach is to introduce measurement redundancy by using $n > m = 7$. Although using more FBGs would increase sensor cost, it provides the LR model with more information and therefore can allow relaxation of the constraints on transducer positioning. Stochastic layouts are explored here as an extreme case, in which each strain measurement can take any value of (z_i, ϕ_i, θ_i) within the ranges defined in Section 3.6.1. Layouts were considered for $7 \leq n \leq 11$ measurements, which corresponds to $\mathrm{DOF} \leq n \leq \mathrm{DOF} + 4$. For each value of n, 1000 stochastically selected layouts were analysed

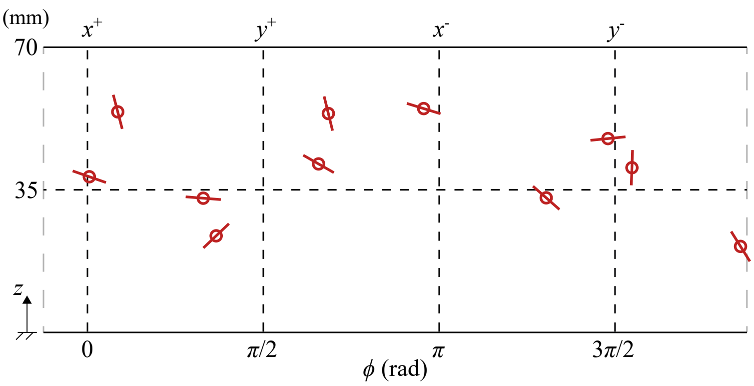

Figure 3.18 Stochastically-generated layout of eleven strain measurements on the cylinder external surface that demonstrated the highest R^2 value

to assess potential sensor performance.

The results of this exercise are presented in Table 3.4. The likelihood of achieving $R^2 \geq 0.99$ for the 1000 randomly generated instrumentation layouts significantly increases with the level of redundancy. When no redundancy is used ($n = m = 7$) very few candidate layouts achieve $R^2 \geq 0.99$, as the LR model is often provided with insufficient information to accurately determine the outputs. As the number of strain measurements increases the results show that the machine learning approach has a high likelihood of achieving very good sensor performance, even in the extreme case of using randomly placed instrumentation. As n is increased, the mean R^2 increases and the standard deviation decreases. When using a redundancy of four ($n = m + 4 = 11$), these factors combine to close the gap between the mean and maximum R^2 values, meaning a large proportion of the random layouts achieve high performance. The max R^2 values shows only minor improvement with redundancy but, as demonstrated in Figure 3.17,

Table 3.4 Results of the redundant approach based on 1000 stochastic strain transducer layouts for different values of n; σ = Standard deviation

Number of strain measurements, n	**Likelihood of $R^2 \geq 0.99$**	R^2		
		Mean	σ	**Max**
7 (DOF)	0.008	0.8949	0.0578	0.9922
8 (DOF + 1)	0.065	0.9439	0.0472	0.9954
9 (DOF + 2)	0.268	0.9711	0.0299	0.9960
10 (DOF + 3)	0.483	0.9830	0.0184	0.9970
11 (DOF + 4)	0.612	0.9870	0.0144	0.9971

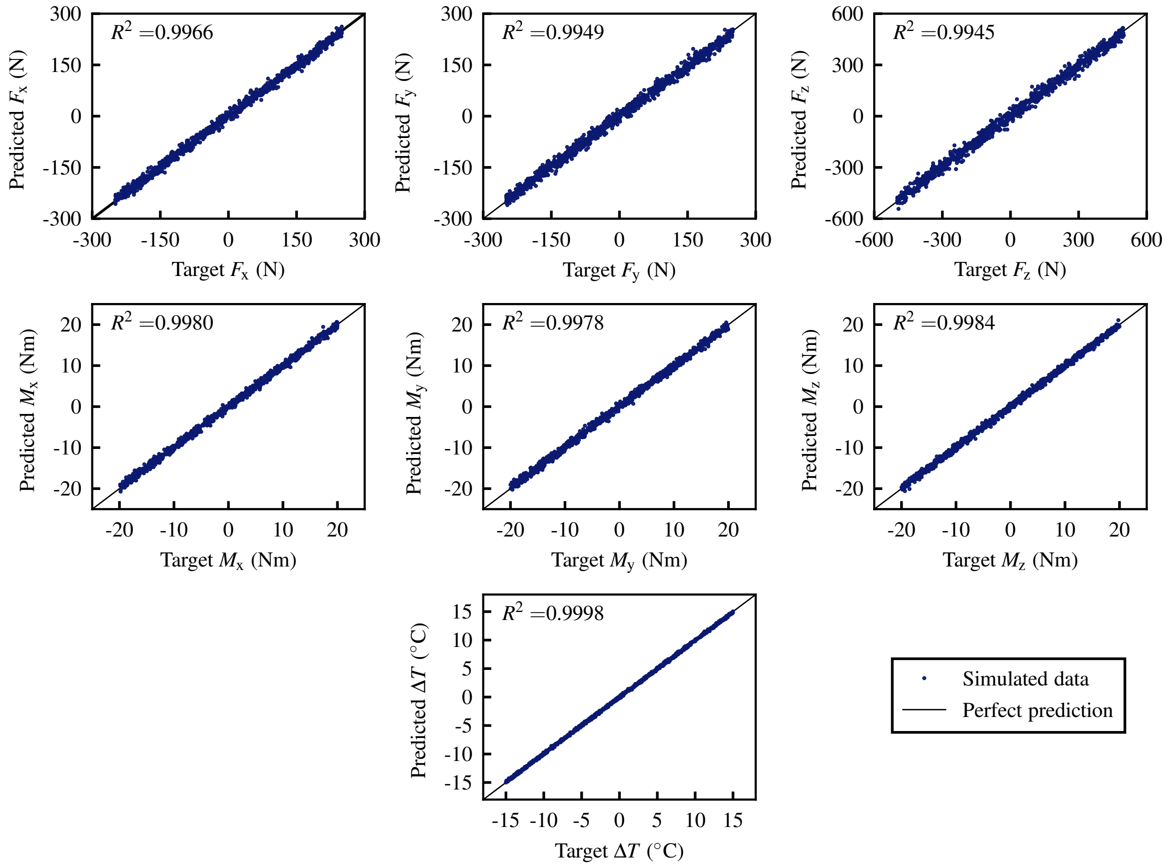

Figure 3.19 Comparison between the LR model predictions and the target output variables in the testing dataset for the randomly generated redundant layout of eleven strain measurements shown in Figure 3.18

it is possible for certain layouts to achieve high accuracy with no redundancy.

By way of example, the layout that achieved the maximum overall R^2 value with $n = 11$ strain measurements is shown in Figure 3.18. The performance using this layout to predict on the testing dataset is shown in Figure 3.19 and summarised in Table 3.3. Compared to the optimised approach with $n = 7$, these results highlight marked improvement in the prediction accuracy in all but one of the seven output variables. The use of redundancy can therefore achieve excellent performance, whilst potentially simplifying the instrumentation process by allowing greater flexibility in FBG positioning. Although this requires more transducers than the optimised approach, the total number is still significantly less than typically used in a conventionally gauged six DOF sensor (e.g. Byrne and Houlsby, 2005; Figures 2.10 and 3.7).

3.6.3 Repeating pattern layouts

Whilst the layouts considered thus far demonstrate strong ‘theoretical’ sensor performance, they are not amenable to convenient implementation with FBGs in practice. For example, achieving the ‘optimised’ layout in Figure 3.16 requires placing several FBGs very close together. The optical fibre spanning between the FBGs would need to overlap on the sensor surface, interfering with the FBG bonding. The high degree of variability in both the FBG angles and their relative positions is also not well suited to FBG arrays with uniform d. Although this could be overcome with a mixed-spacing FBG array, this would be bespoke to a specific design, increasing overall sensor cost. Furthermore, placing FBGs near to the cylinder end flanges is undesirable as they inhibit the access needed to easily manipulate and route the fibre.

To overcome these limitations, an alternative ‘intermediate’ approach is to consider placing the FBGs in a systematic repeating pattern. The aim is to create a low complexity layout that is designed to meet the constraints of the optical fibre, whilst still delivering very good performance. This produces ‘snake-like’ patterns in which the fibre passes back and forth over the sensor structure at different orientation angles. The layouts comprise straight regions, containing the FBGs, and corners or ‘pivots’, where the orientation angle of the fibre is changed.

A series of preliminary patterns were explored by instrumenting 3D printed sensor prototypes with optical fibre containing no FBGs. This facilitated qualitative assessment of instrumentation feasibility. From observations in Section 3.6.1, layouts were sought that achieve a range of orientation angles and position the FBGs near the sensor axial midplane, whilst critically accommodating uniform FBG spacing, d, on the fibre. For this exercise, patterns containing $n = 8$ FBGs were considered; the use of low redundancy is a balance between providing the LR model with additional information and limiting the layout complexity.

A candidate solution that was highlighted as potentially implementable is shown in Figure 3.20a. The cylinder is divided into six circumferential sections of width $\pi R/3$ and there are three different orientation angles of the eight FBGs, $\theta_{\mathrm{i}} = 0, \ \pm a_0$. At this stage, the ‘pivots’ are treated as sharp angles (i.e. no consideration of fibre bend radius) but the distance between each FBG is uniform, given by $d = \pi R/3 \sin(a_0)$. In this configuration, parameters R, d and

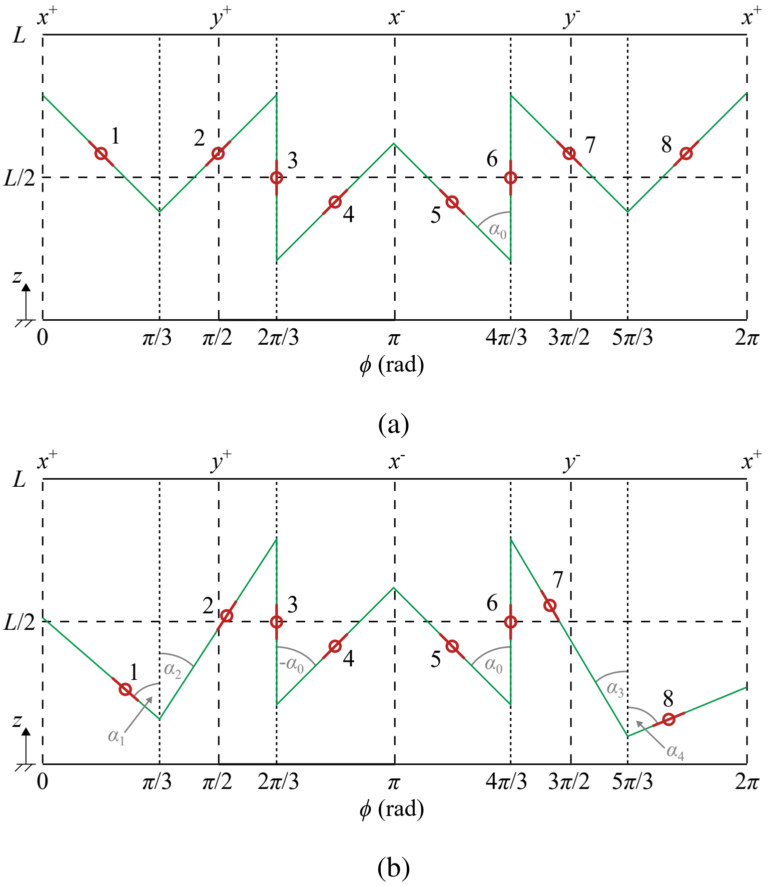

Figure 3.20 Initial candidate layout of eight FBGs on the cylinder external surface in a repeating pattern: (a) uniform orientation angles, (b) differing orientation angles. The green line represents an indicative optical fibre

a_0 cannot be chosen independently. A numerical assessment of this layout using the procedure outlined in Section 3.5.3, with $a_0 = 35°$ and $d = 50\,\text{mm}$, returned an overall R^2 value on the testing dataset of 0.9820. The significantly worse prediction compared to the other approaches can be attributed to the limited set of FBG orientation angles used.

A progression of this pattern is to incorporate different orientation angles, such as shown in Figure 3.20b. The angles of FBGs 1, 2, 7 and 8 (a_1, a_2, a_3 and a_4 respectively) can now vary independently of FBGs 4 and 5 ($\pm a_0$). To assess the selection of these orientations, a grid search was performed over 4375 combinations in the following parameter space: $30° \leq a_0 \leq 60°$ in 5° increments, $30° \leq a_{1,2,3,4} \leq 90°$ in 15° increments and $z_\text{i} = L/2$ for all FBGs. Although this temporarily neglects the constraint of uniform d on a continuous fibre, it was necessary to reduce the search space. One of the solutions from the grid search with both a very high R^2 value (0.9955) and a feasible combination of angles was $a_0 = 60°$ and $a_{1,2,3,4} = 30°$. This

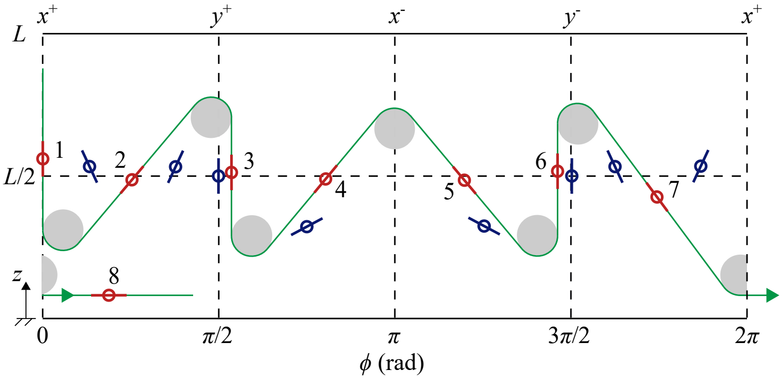

Figure 3.21 Practically implementable 'pattern' layout of eight FBGs on the cylinder surface with modifications to increase LR model performance. The blue markers indicate the intended FBG positions prior to accounting for the physical constraints

Table 3.5 Parameters defining the position and orientation of the eight FBGs on the cylinder sensor in the pattern layout in Figure 3.21

FBG	z_i/L	ϕ_i (rad)	θ_i (°)
1	0.56	0.00	0.0
2	0.49	0.80	-40.1
3	0.51	1.69	0.0
4	0.49	2.53	-39.8
5	0.48	3.77	39.8
6	0.52	4.59	0.0
7	0.43	5.48	36.4
8	0.08	0.59	90.0

is a significant improvement in performance compared to that of Figure 3.20a and is closely comparable to both the optimised and best redundant layouts considered.

The selected pattern requires alteration for implementation in practice. The constraint of a uniform $d = 50$ mm is re-introduced and smooth curves are included at the pivot locations, to accommodate the fibre minimum bend radius. For low bend-loss fibre, a radius of 6 mm is recommended to keep the surface strain below 1% (FBGS, 2022). The fibre layout can then be manually adjusted to minimise changes on the FBG positions, however this typically has a negative impact on sensor performance. For the cylinder geometry defined in Table 3.1, this requires spreading FBGs 4 and 5 circumferentially to accommodate $a_0 = \pm 60°$, and reducing $a_{1,2,3,4}$ to fit in the remaining space. This results in less variation in the different FBG responses and thus less information provided to the LR model. To mitigate this effect, the pattern can

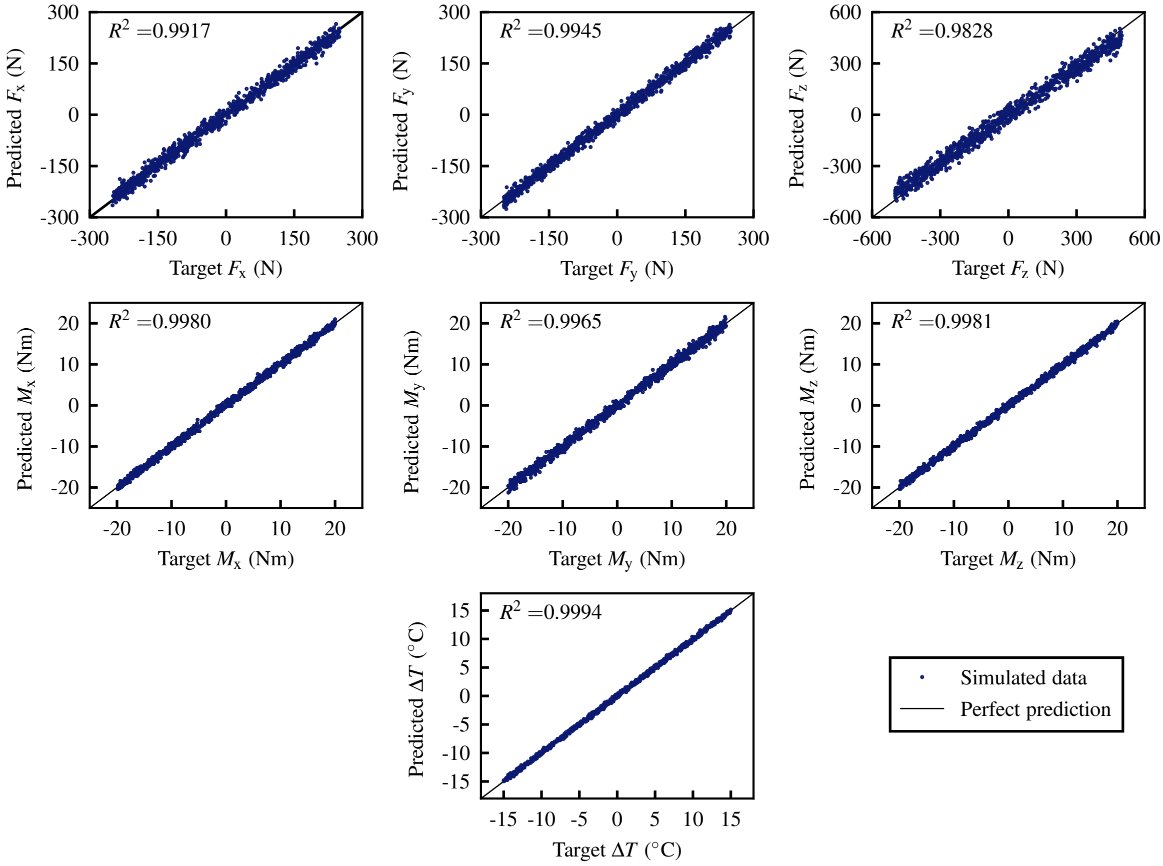

Figure 3.22 Comparison between the LR model predictions and the target values of the output variables using the testing dataset for the regular pattern layout modified for implementation with eight FBGs (shown in Figure 3.21)

be manually modified to accommodate the smooth curves, whilst maintaining a range of FBG orientations. An example is shown in Figure 3.21 and details of the FBG positional variables are given in Table 3.5. This was informed by the desirability of orientation angles close to 0°, 90° and ±45°, which was observed in Figure 3.16 and the design of Byrne and Houlsby (2005). FBGs 1 and 8 are oriented at 0° and 90° respectively, which provides more circumferential space to increase the orientation angle of FBGs 2 and 7. Although FBG 8 now sits beyond the circumferential position of FBG 1, the position is such that there is no fibre overlapping required.

The predictive performance of an LR model trained with this layout is shown in Figure 3.22 and the corresponding metrics are summarised in Table 3.3. The final practical repeating pattern layout achieves closely comparable performance to both the optimised and redundant approaches. Whilst the best random redundant approach shows slightly improved performance, this layout is not implementable and utilises three additional FBGs. Whilst further redundancy could be incorporated into the pattern layout, this increases sensor cost and would start to inhibit the instrumentation feasibility on the compact sensor body. Overall, the numerical results demonstrate that the framework is robust and can achieve very good performance, even when using an instrumentation configuration governed by the practical constraints of using FBGs.

3.7 Practical implementation

To verify practical implementation of the framework, a physical prototype of the exemplar sensor was developed in the laboratory, as shown in Figure 3.23. A thin-walled column sensor structure was machined from 6061-T6 aluminium alloy to the dimensions given in Table 3.1. This was instrumented with an array of eight DTGs with $d = 50$ mm and λ_p =1540–1564 pm, in the layout outlined in Figure 3.21. The sensor was calibrated by dead weight using the procedures detailed in Section 4.4.3.1. A total of 75 loadcases were applied to the sensor, over the ranges defined in Table 3.2. Lateral moments, M_x and M_y, were applied using a constant F_z load at different offsets from the sensor central axis. Similarly, M_z was applied by constant F_x loading offset from the sensor centreline. An additional 12 data points were obtained for temperature calibration using a thermal water bath. During all calibration stages, a reference temperature measurement was provided by a TP-01 FBG temperature sensor, supplied by FBGS International.

The calibration load cases and the corresponding induced FBG peak wavelength shifts were assembled into a dataset that was used to train an LR model for the prototype sensor. The

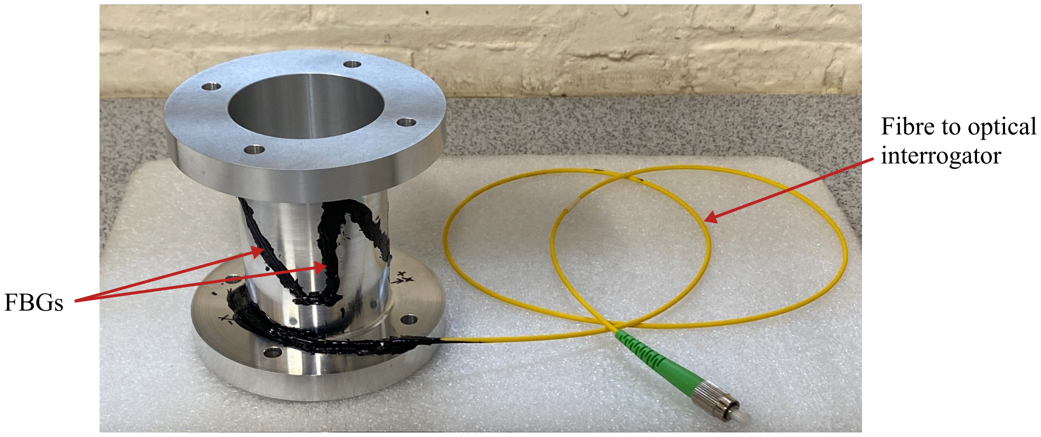

Figure 3.23 Prototype of the exemplar column-type sensor instrumented with eight FBGs using the layout in Figure 3.21

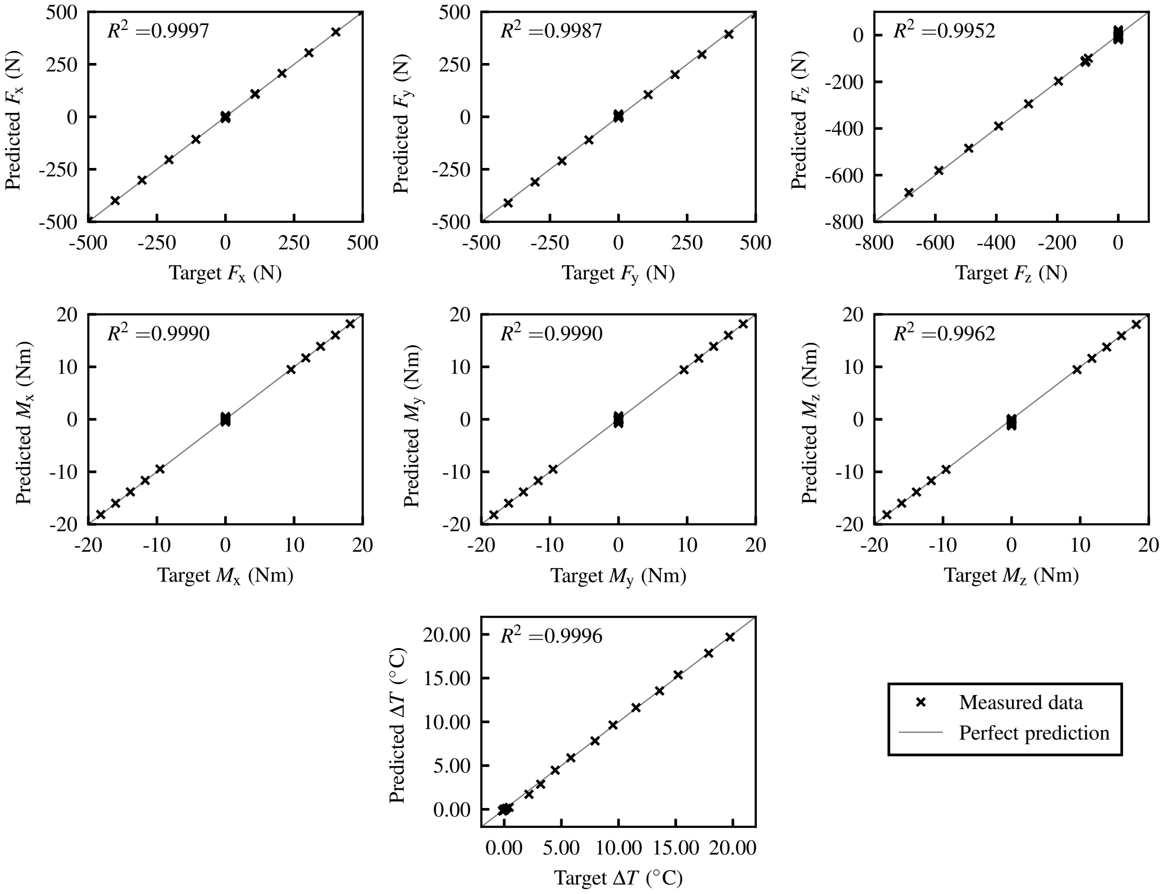

Figure 3.24 Comparison between the physical prototype sensor LR model predictions and the target values of the output variables on the the calibration dataset. The target values are the actions applied in practice.

performance of this model predicting on the training dataset is shown in Figure 3.24. Excellent predictions are observed for all outputs, with individual component R^2 values of between 0.9952 and 0.9997. Low cross-talk is apparent between the outputs for these calibration load cases, with a maximum value of 2.37% (expressed as a percentage of the corresponding applied maximum range in Figure 3.24). This is observed to occur in the F_z component under F_y application, due to the lower sensitivity of the sensor in the axial direction (see Table 3.7). In particular, the prediction of temperature change and the compensation of the force/moment outputs against temperature change is handled very well by the LR model.

The coefficients matrix for the prototype sensor LR model is given in Table 3.6a. The cell colouring highlights the relative contributions of each FBG to each individual output component. The equivalent coefficients matrix trained from the numerical simulation data is

Table 3.6 Sensor LR model coefficients matrices: (a) Physical prototype (Figure 3.23), (b) Numerical simulation (Figure 3.21). The values are truncated to two decimal points and the cell colouring is determined from the value magnitude relative to cells in the corresponding row.

(a)

	$\Delta\lambda_1$	$\Delta\lambda_2$	$\Delta\lambda_3$	$\Delta\lambda_4$	$\Delta\lambda_5$	$\Delta\lambda_6$	$\Delta\lambda_7$	$\Delta\lambda_8$
F_x	4.23×10^2	-6.90×10^2	6.77×10^2	-4.74×10^2	-4.87×10^2	5.91×10^2	-7.88×10^2	7.96×10^2
F_y	-1.80×10^2	8.07×10^2	-1.35×10^2	-6.55×10^2	6.26×10^2	6.53×10^1	-5.64×10^2	-2.42
F_z	6.32×10^2	-1.70×10^3	2.10×10^3	5.99×10^2	6.28×10^2	2.39×10^3	-9.84×10^2	-3.46×10^3
M_x	-1.06×10^1	3.46×10^1	2.93×10^1	-2.90×10^1	3.63×10^1	-3.08×10^1	-2.88×10^1	-3.85
M_y	-5.65×10^1	8.32	-9.22	4.26×10^1	4.10×10^1	-3.91	1.64×10^1	-3.98×10^1
M_z	-5.30	3.12×10^1	-1.83×10^1	2.42×10^1	-2.49×10^1	1.89×10^1	-2.75×10^1	2.49
ΔT	2.44	7.52	5.80×10^{-2}	4.04×10^{-1}	-9.23×10^{-1}	-1.87	4.12	2.45×10^1

(b)

	$\Delta\lambda_1$	$\Delta\lambda_2$	$\Delta\lambda_3$	$\Delta\lambda_4$	$\Delta\lambda_5$	$\Delta\lambda_6$	$\Delta\lambda_7$	$\Delta\lambda_8$
F_x	5.55×10^2	-7.73×10^2	4.93×10^2	-3.88×10^2	-4.55×10^2	3.75×10^2	-7.29×10^2	9.23×10^2
F_y	1.67	6.55×10^2	-4.09×10^1	-6.49×10^2	6.08×10^2	8.20×10^1	-6.19×10^2	-3.78×10^1
F_z	2.19×10^2	-4.63×10^2	1.66×10^3	2.41×10^1	4.30×10^2	2.36×10^3	-8.96×10^2	-3.34×10^3
M_x	6.45×10^{-1}	2.18×10^1	3.13×10^1	-2.13×10^1	2.14×10^1	-3.07×10^1	-2.15×10^1	-1.50
M_y	-5.62×10^1	1.08×10^1	4.06×10^{-1}	3.09×10^1	3.43×10^1	6.08	7.64	-3.39×10^1
M_z	3.52×10^{-1}	2.94×10^1	-1.55×10^1	2.14×10^1	-2.28×10^1	1.68×10^1	-2.77×10^1	-1.89
ΔT	4.05	9.82×10^{-1}	9.53×10^{-1}	2.23	3.33×10^{-1}	-2.54	2.97	1.72×10^1

given in Table 3.6b. To enable a comparison with the prototype sensor, the strain outputs of the numerical sensor model in Section 3.5.2 were transformed into indicative peak wavelength shifts using Equation 3.6 using typical FBG parameters. The maximum FBG sensitivities for the prototype sensor are also given in Table 3.7, alongside the corresponding numerical simulation predicted values. Although there are clear numerical differences, the physical and numerical coefficients matrices are both similar in form, indicated by the closely comparable cell colouring. This demonstrates very similar weighting of the same FBGs in both approaches. Furthermore the output component sensitivities also match relatively well, in particular F_z and the three moment components. This exercise gives confidence that numerical simulation during sensor design can provide a reliable representation of physical behaviour in practice. The differences in the coefficient values and sensitivities can be largely attributed to the conversion of the numerical strain outputs to peak wavelength shifts being highly approximate, as well as slight differences in FBG position compared to the planned layout. The greater differences in F_x and F_y sensitivities can be attributed to greater mounting flange thickness in the prototype sensor.

Table 3.7 FBG sensitivities of the prototype column sensor in Figure 3.23 and the corresponding sensitivity estimated from the numerical simulated sensor outputs

Component	Maximum FBG sensitivity	Numerical simulation predicted sensitivity
F_x	0.697 pm/N (FBG 2)	0.556 pm/N
F_y	0.751 pm/N (FBG 6)	0.583 pm/N
F_z	0.201 pm/N (FBG 1)	0.206 pm/N
M_x	15.6 pm/Nm (FBG 3)	15.1 pm/Nm
M_y	13.3 pm/Nm (FBG 1)	15.2 pm/Nm
M_z	9.90 pm/Nm (FBG 7)	9.65 pm/Nm
ΔT	28.8 pm/°C (FBG 5)	38.2 pm/°C

3.8 Comparison to traditional instrumentation scheme

To further emphasise the benefits of the proposed framework, the equivalent of a ‘traditional’ instrumentation scheme using FBGs was also conceptualised for the column sensor. In this approach, the FBGs are placed in specific locations on the sensor structure and outputs are formed from arithmetic combinations of the FBG wavelength shifts (analogous to a Wheatstone bridge with ERSGs). The number of FBGs, their layout and the combinations were chosen to maximise sensitivity and minimize the cross coupling between the sensor outputs. The resulting layout is shown in Figure 3.25, consisting of 14 FBGs mounted at 0°, 90° and ±45° to the cylinder axis at the quarter points around the circumference and four axial heights, z_{1-4}. The sensor outputs corresponding to six load components are determined from the FBG fractional wavelength shifts as:

$$O_{F_x} = \frac{\Delta\lambda_7}{\lambda_7} - \frac{\Delta\lambda_6}{\lambda_6} + \frac{\Delta\lambda_{14}}{\lambda_{14}} - \frac{\Delta\lambda_{13}}{\lambda_{13}} \tag{3.18}$$

$$O_{M_x} = \frac{\Delta\lambda_5}{\lambda_5} - \frac{\Delta\lambda_{12}}{\lambda_{12}} \tag{3.21}$$

$$O_{F_y} = \frac{\Delta\lambda_3}{\lambda_3} - \frac{\Delta\lambda_2}{\lambda_2} + \frac{\Delta\lambda_{10}}{\lambda_{10}} - \frac{\Delta\lambda_9}{\lambda_9} \tag{3.19}$$

$$O_{M_y} = \frac{\Delta\lambda_8}{\lambda_8} - \frac{\Delta\lambda_1}{\lambda_1} \tag{3.22}$$

$$O_{F_z} = \frac{\Delta\lambda_1}{\lambda_1} - \frac{\Delta\lambda_4}{\lambda_4} + \frac{\Delta\lambda_8}{\lambda_8} - \frac{\Delta\lambda_{11}}{\lambda_{11}} \tag{3.20}$$

$$O_{M_z} = \frac{\Delta\lambda_6}{\lambda_6} - \frac{\Delta\lambda_7}{\lambda_7} + \frac{\Delta\lambda_{14}}{\lambda_{14}} - \frac{\Delta\lambda_{13}}{\lambda_{13}} \tag{3.23}$$

where λ_i and $\Delta\lambda_i$ are the initial peak wavelength and the corresponding shift for the ith FBG respectively, where $i = 1 - 14$, as defined in Figure 3.25. The strain at each FBG (evaluated using

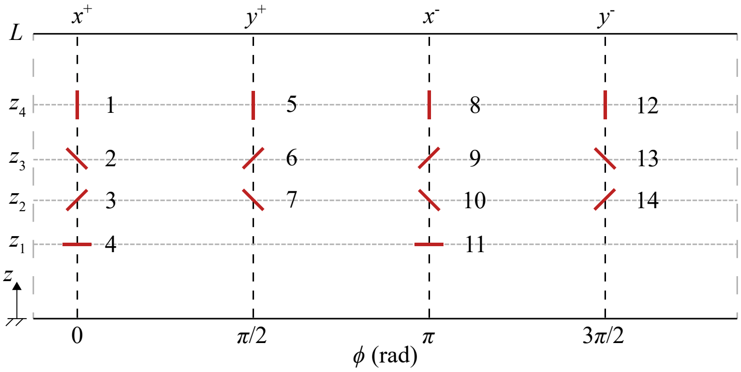

Figure 3.25 Layout of FBGs on the external surface of a column sensor in a ‘traditional instrumentation approach

Equations 3.11–3.17) and temperature change can be subbed into Equation 3.6 to determine the estimated peak wavelength shift for each FBG.

Evaluating the six outputs in Equations 3.18–3.23 using the corresponding normalised wavelength shifts results in the matrix equation given in Equation 3.24. This shows that the outputs are fully temperature compensated in theory and there are only three cases of cross-coupling. This is broadly comparable to the form of the calibration matrix of the Byrne and Houlsby (2005) sensor, with only one additional term arising due to the axial spacing of the FBGs to avoid overlapping. This approach uses more FBGs than has been considered in the framework in Section 3.6 (14 = DOF + 7 redundancy), but is still considerably less than the 32 ERSGs in the Byrne and Houlsby (2005) design.

$$\begin{bmatrix} O_{\mathrm{F_x}} \\ O_{\mathrm{F_y}} \\ O_{\mathrm{F_z}} \\ O_{\mathrm{M_x}} \\ O_{\mathrm{M_y}} \\ O_{\mathrm{M_z}} \end{bmatrix} = \frac{2\,(1-P_\mathrm{e})}{E} \begin{bmatrix} \frac{2(1+\nu)}{\pi R t} & 0 & 0 & 0 & 0 & 0 \\ 0 & \frac{2(1+\nu)}{\pi R t} & 0 & 0 & 0 & 0 \\ 0 & 0 & \frac{1+\nu}{A} & 0 & 0 & 0 \\ 0 & -\frac{R_\mathrm{o}(L-z_4)}{I} & 0 & \frac{R_\mathrm{o}}{I} & 0 & 0 \\ \frac{R_\mathrm{o}(L-z_4)}{I} & 0 & 0 & 0 & \frac{R_\mathrm{o}}{I} & 0 \\ 0 & \left(\frac{R_\mathrm{o}(1-\nu)}{I}\right)\left(\frac{z_3-z_2}{2}\right) & 0 & 0 & 0 & \frac{2R_\mathrm{o}(1+\nu)}{J} \end{bmatrix} \begin{bmatrix} F_\mathrm{x} \\ F_\mathrm{y} \\ F_\mathrm{z} \\ M_\mathrm{x} \\ M_\mathrm{y} \\ M_\mathrm{z} \end{bmatrix} \tag{3.24}$$

Despite this, achieving the very specific layout of FBGs required in Figure 3.25 is likely infeasible. Positioning four FBGs at different orientation angles along a single axial line presents a significant challenge, particularly when using an FBG array with uniform spacing.

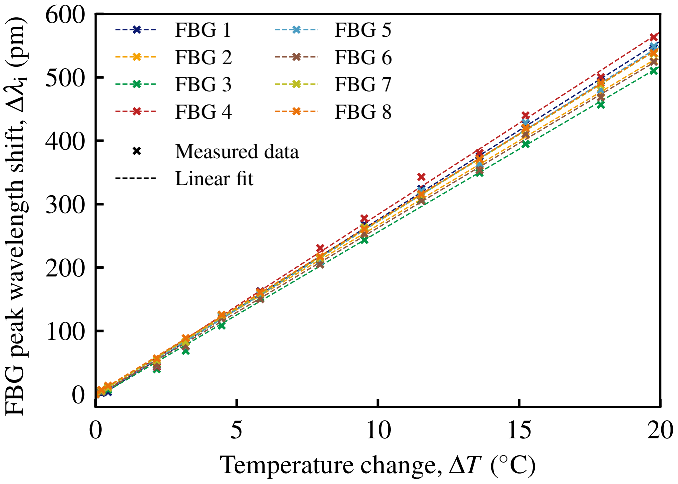

Figure 3.26 Temperature calibration data for the prototype column sensor in Figure 3.23, illustrating the differing temperature dependence of the individual bonded FBGs

The length and diameter of the cylinder structure would likely have to greatly increase compared to the geometry in Table 3.1, which would be undesirable in many applications. Furthermore, bonded FBGs can display varied temperature dependence, as illustrated using the prototype sensor calibration data in Figure 3.26. Relying purely on arithmetic operations, which assume identical FBG thermal behaviour, in this case will likely result in temperature dependence in the force/moment outputs.

3.9 Summary

This chapter has introduced a new framework for using FBGs in multi-axis force sensors. The approach is to utilise a simple sensor structure with a ‘snake-like’ layout of optical fibre. A machine learning model, namely multi-output LR, is adopted to automatically determine a mapping between the FBG measurements and the force/moment sensor outputs. A numerical study was undertaken to evaluate the performance of the new approach, using a column-type six DOF force sensor as a demonstrator. This was subsequently validated by implementing the framework with a physical prototype sensor. The key findings from the study are as follows:

a) The numerical investigation of different instrumentation strategies provided important insights into FBG placement. The optimised approach showed that excellent sensor performance can be achieved using the same number of measurands as the sensor output degrees of freedom, which is a significant reduction compared to traditional instrumentation approaches. Bayesian optimisation was demonstrated to be highly capable and efficient at exploring a large search space. In contrast, an extreme case of stochastic strain transducer positioning highlighted the opportunity of increasing the flexibility of the transducer positioning for the sake of minor measurand redundancy. This was exploited in the use of a repeating ‘snake-like’ pattern, which facilitated feasible implementation with optical fibre. These factors are of major benefit in the adoption of FBGs, given their multiplexed nature and relatively high unit cost.

b) The combination of a machine learning training process with explicit temperature calibration was shown to be an effective means of achieving thermal compensation of the force/moment outputs. This removes the need for specific arithmetic combinations of FBG outputs or the provision of a strain free FBG, as well as accounting differences in individual FBG responses after bonding.

c) The use of a basic prismatic design dramatically reduces the complexity of manufacturing the sensor structure. Coupled with the reduction in the number of strain transducers and the practical fibre layout design, the sensors can also be easily and quickly instrumented with FBGs. These factors lead to significant time and cost savings during sensor manufacture, when compared with comparable electrical strain gauged designs. Furthermore both the numerical and physical trials have demonstrated the training data required is no more onerous to obtain than traditional sensor calibration tests.

d) A numerical ‘virtual-twin’ model was shown to be a useful tool for simulating the sensor structure behaviour during design. The analytical model developed in this chapter provided an expedient means of rapidly considering a large number of load cases, to rigorously assess the instrumentation strategies. The model showed excellent agreement with 3D FEA results and compared favourably with the physical prototype sensor.

e) Although the cylindrical column design has obvious benefits when using FBGs, the framework is not limited to this exemplar design. Furthermore, the LR model can be readily replaced with more complex, non-linear models, opening opportunities for new, innovative measurement applications.

Chapter 4

Development of a new soil-structure contact stress sensor for underground construction applications

4.1 Introduction

This chapter describes the development of a new sensor for measuring the contact stresses at a soil-structure interface. This addresses the need for new sensing technology, highlighted by critical sensor failure in recent field monitoring projects (Phillips, 2023; Royston, 2018). The design employs FBG strain sensing in conjunction with the data-driven framework introduced in Chapter 3, with the aim of creating a multi-axis contact stress sensor that is both economical and suitably robust for deployment in underground construction applications. The proposed design is capable of measuring total normal stress and bi-directional interface shear stresses. A novel sensor structure and operating principle are also incorporated to allow for potential concurrent measurement of pore water pressure, for determination of interface effective normal stress.

The sensor concept is first introduced, before giving an overview of a prototype sensor developed for laboratory testing. Details of the sensor structure and instrumentation design are provided, followed by describing key aspects of the manufacture and calibration procedures for the example sensor. The performance of the new sensor is then assessed though a series of validation tests, covering both total stress and effective stress measurement. Versions of the developed sensor are subsequently deployed in the laboratory testing described in Chapter 5, to measure contact stresses at lubricated concrete-sand interfaces.

4.2 Sensor concept

4.2.1 Novel operating principle

The proposed contact stress sensor design centres around the use of FBGs in place of conventional electrical strain gauging. The benefits of optical strain measurement are particularly advantageous in construction monitoring applications. Critically, the immunity of the sensing system to both EMI and damage through water exposure eliminates the sources of previous sensor failure. The wavelength-encoded measurement of FBGs allows for robust communication over long distances and high resolution is possible with modern interrogation systems. Furthermore, the ability to multiplex a large number of FBGs on a single fibre reduces the amount of cabling and connections, which significantly reduces the time and complexity of sensor installation.

The multi-axis force sensor considered in Chapter 3 serves as a good candidate for development into a new SSCS sensor. The columnar design has a high axial stiffness, helping to limit the effect of sensor compliance on the soil stress state, and the prismatic shape is ideally suited to instrumentation with optical fibre. The sensor would be installed in the structure surface (as in Figure 1.7), with a solid ‘face’ at one end of the column exposed to direct contact with the soil. In this configuration, the sensor provides a measurement of total normal stress, σ_{n}, as the sensor face is exposed to loading from both the soil matrix and pore water. To determine the effective normal stress at the interface, this approach would still rely on the installation of an additional PT to measure the local pore pressure.

Instead, a novel operating principle has been developed for the SSI sensor to directly measure pore pressure. The proposed solution is to actively allow pore water from the soil to enter the region around the sensor body. This is achieved by pre-filling the cavity around the sensor with fluid and surrounding the sensing face with a porous element, which permits water flow but blocks soil particles. When pore pressure develops at the soil-structure interface, the pressure is transferred via the fluid into distributed loading on the sides of the column sensor and any underside area of the sensor face (see Figure 4.1a). This lateral fluid loading induces additional deformation of the thin walls, which can be measured by the bonded FBGs. The contact stresses

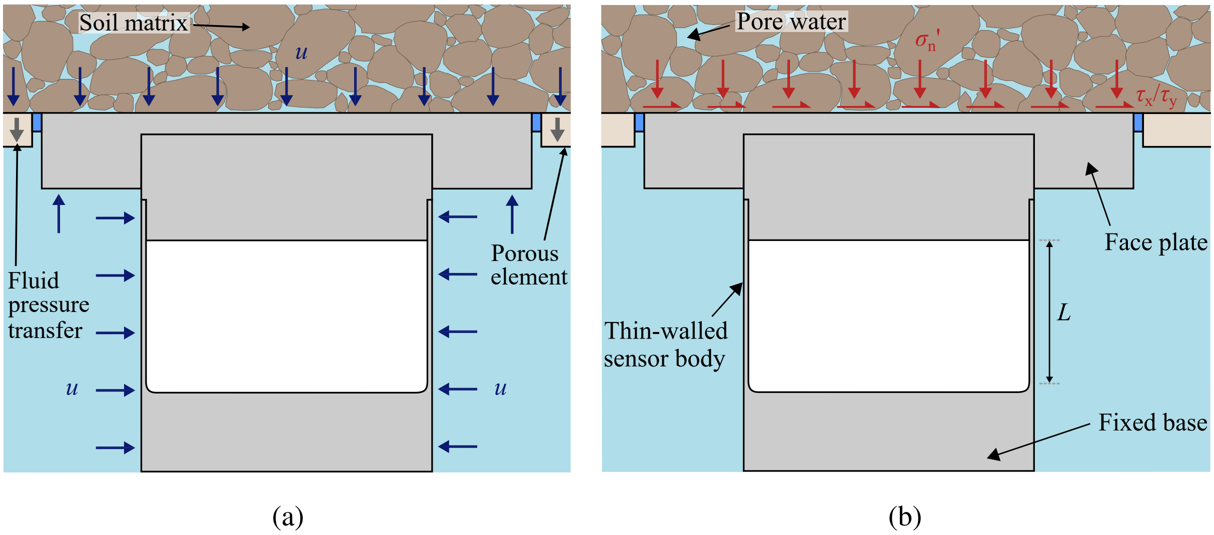

Figure 4.1 Section showing the stresses on the proposed sensor: (a) Pore water pressure transferred through a porous element and fluid inside the housing, (b) Contact stresses from the soil matrix. The pore pressure measurement is used to calculate σ_n' using Equation 4.2.

from the soil matrix, comprising the effective normal stress and potentially two orthogonal shear stress components, act only on the sensing face (see Figure 4.1b). The additional deformation mechanism from the fluid loading enables the sensor to provide a measurement of pore pressure, which is then used to determine the effective normal stress at the interface.

4.2.2 Progression of machine learning framework

The framework introduced in Chapter 3 can be directly applied to the new sensor design. Instead of explicitly using the contact stresses, the sensor can be considered using the same concentrated force and moment components defined in Figure 3.1. When used to measure total stress, F_x, F_y and F_z are produced by the bi-directional shear stress components, τ_x and τ_y, and the total normal stress, σ_n, acting on the sensor face respectively (c.f. Figure 1.7).

The contact stresses can also lead to moment loading on the sensor face. Lateral moments, M_x and M_y, can arise from non-uniform normal stress on the sensor face, and axial moment, M_z, can be caused by non-uniform shear stresses. Whilst the moment components are not of primary interest and should remain relatively small in use, the contact stress outputs need to remain invariant to any moment loading. Furthermore, as seen in Chapter 3, the outputs of the proposed sensor should also remain unaffected by any ambient temperature variation. Therefore, the LR model for the proposed sensor must also include the moment components, M_x, M_y and M_z, and temperature change, ΔT, and these variables must be calibrated for.

The LR model takes an input vector comprising peak wavelength shifts of n number of FBGs bonded to the sensor structure, $\Delta\lambda_\mathrm{i}$ (Equation 3.9). To measure effective normal stress, incorporating the pore pressure, u, is straightforward, as it simply forms an additional output variable. In this case, the sensor LR model produces a vector of $m = 8$ predicted outputs, $\hat{\boldsymbol{f}}$:

$$\hat{\boldsymbol{f}} = \begin{bmatrix} F_\mathrm{x} & F_\mathrm{y} & F_\mathrm{z} & u & M_\mathrm{x} & M_\mathrm{y} & M_\mathrm{z} & \Delta T \end{bmatrix}^\mathrm{T} \tag{4.1}$$

Additional calibration steps are therefore required to ensure u is captured in the model training dataset. In operation, τ_x and τ_y are determined by dividing F_x and F_y respectively by the sensor face area, A_f. The effective normal stress, σ'_n, can be determined from outputs F_z and u using:

$$F_\mathrm{z} = -\sigma'_\mathrm{n} A_\mathrm{f} - u\left(A_\mathrm{f} - A_\mathrm{u}\right) \tag{4.2}$$

where A_u is the sensor face underside area. The negative in Equation 4.2 is due to the difference in direction between F_z in Figure 3.1 and the compression-positive convention for normal stress.

4.2.3 Sensor structure

The hollow cylindrical sensor structure considered in Chapter 3 is not optimal for this new measurement application. Firstly, the open-ended design requires sealing at both the base and top flanges, to prevent fluid entry into the centre of the column. Secondly, a cylinder has very high stiffness to external pressure loading acting radially on the circular cross-section. This would lead to poor sensitivity due to the low strain induced per unit pressure. For example, the hoop strain induced under 100 kPa external pressure on a cylinder with parameters from Table 3.1 was calculated as only $-54\,\mu\varepsilon$, using a thick-walled cylindrical pressure vessel solution.

The proposed solution is a novel sensor structure, comprising a short length of thin-walled hollow square box-section. This structure behaves broadly similar to cylindrical column under the action of the contact stresses. However, when exposed to distributed external pressure, the walls of the box-section undergo a plate bending-type deformation, as illustrated in Figure 4.2.

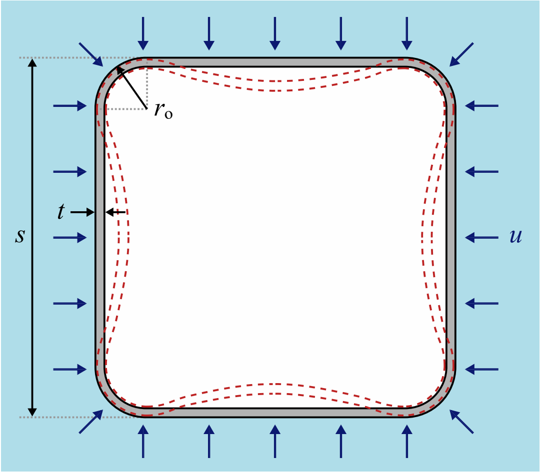

Figure 4.2 Illustration of a plan cross-section through the proposed sensor structure, showing indicative deformation under external pressure loading

The plate bending deformation results in much higher induced surface strain and therefore greater sensitivity to pore pressure. The use of a square cross-section ensures the same structural characteristics in the two orthogonal directions (x and y). The corners of the box are also rounded to remove the sharp internal corners and smooth the outer surface, which improves the machinability of the structure and facilitates instrumentation of the outer surface with a continuous optical fibre.

This structure can be viewed as a modified column-type design and therefore inherits many of the beneficial features of the original cylinder, including ease of manufacture, large smooth gauging surface and high axial stiffness. The sensitivity to each of the load components can be tuned by careful selection of the box geometry parameters, including side width s, wall thickness t and corner outer radius, r_o (see Figure 4.2) and wall axial length, L (see Figure 4.1b). For example, the influence of u can be modulated by altering r_o.

4.2.4 Design features

A detailed view of the components of the proposed contact stress sensor is shown in Figure 4.3 and a section through the assembled sensor installed at a soil-structure interface is shown in Figure 4.4. The sensor structure comprises the thin-walled square box-section, which sits between a solid base and top cap. The top cap is bolted to a face plate that is exposed to direct contact with the surrounding soil, whilst the base acts as a fixed mounting point. A single optical fibre containing an array of n number of FBGs is bonded to the outer surface of the sensor structure. The sensor body (comprising the structure and FBG instrumentation) is bolted via its base inside a stiff external housing, which is embedded into the structure at the interface.

For effective stress measurement, a porous 'ring' is mounted around the sensor face, into a rebate in the housing. This provides a flow path for pore water into the housing around all sides of the sensor. A thin strip of silicone sealant is inserted between the sensor face plate and the ring, to accommodate the small lateral displacements of the sensor face under load. Conveyance of the pore water pressure onto the sensor body requires the cavity within the housing to be pre-filled with an incompressible fluid. Bleeding ports are included in the base of the housing to enable filling and effective saturation of the sensor. For total stress measurement, the porous ring is replaced with a metal equivalent and the cavity around the sensor body is left dry.

There are several additional developments compared to the column design in Chapter 3. Firstly the large external mounting flanges are removed, such that the outer surface of the box

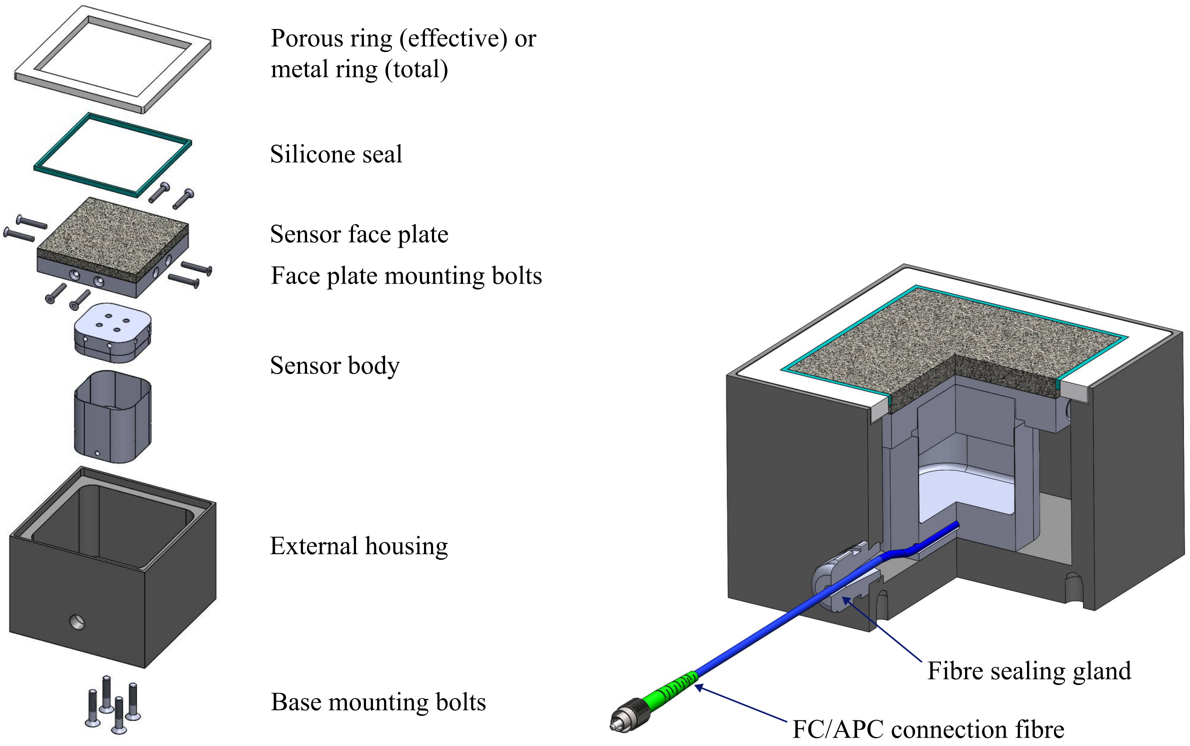

(a) (b)

Figure 4.3 New contact stress sensor design: (a) Exploded view showing individual components, (b) Complete assembled sensor with internal cut-out. FBGs omitted for clarity

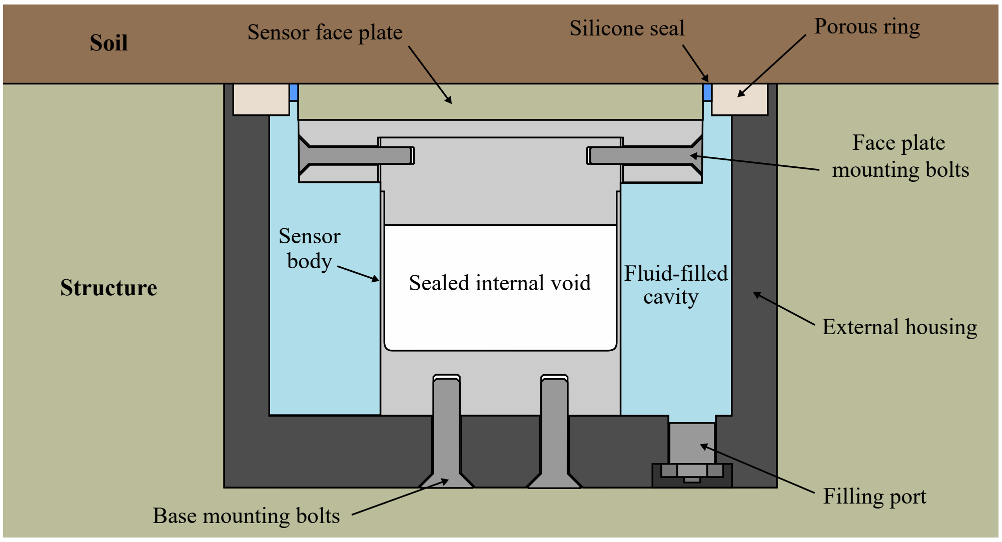

Figure 4.4 Section through the proposed sensor installed at a soil-structure interface, illustrating the effective stress measurement set up. Fibre omitted for clarity

walls continues flush into the base and top cap. This greatly simplifies the instrumentation process, as it improves access to the wall surface for bonding the FBGs. In combination with this, a removable face plate is used, which has a larger area than the sensor body. This results in greater force being applied to the sensor under a given contact stress and therefore achieves higher sensitivities (strain per unit contact stress). This is particularly critical for normal stress measurement, due to the high axial stiffness of the sensor. The face plate is designed to bolt into the side of the top cap (see Figure 4.4). This allows the face plate to closely match the interface roughness of the structure interface, with no obstruction on the face from bolt heads. This also conveniently aids sensor calibration, as different face plates can be mounted to the sensor to allow accurate application of specific load components (see Section 4.4.3).

The novel operating principle requires a sealed void inside the sensor body to create a pressure differential from the housing cavity. To achieve this, the sensor structure is implemented in two parts: the sensor base and thin-walled section are machined as a single piece, with a separate top cap (see Figure 4.3a). A short length of reduced cross-section is machined into the underside of the top cap, which ‘mates’ inside the hollow box-section with a bonded interference fit. This joint facilitates a strong rigid connection (for load transfer) and a watertight seal (to prevent fluid entering the internal void). Furthermore, the sensor base mounting is implemented as threaded blind holes, to ensure no additional paths for water ingress are created.

4.3 Design of sensor for laboratory testing

4.3.1 Problem definition

To assess the proposed design, sensors were designed and built for use in laboratory-scale experiments. The purpose of the sensors is for contact stress measurement in a lubricated concrete-sand interface, simulating the large-strain frictional sliding typically encountered in pipejacked tunnelling or caisson sinking. Whilst this application is primarily concerned with unidirectional shearing, thus not fully exploiting the capabilities of the sensors, the harsh lubricated interface conditions make it a good candidate for deployment of optical-based sensors.

The overall sensor is constrained to fit in a maximum 125 × 125 × 100 mm volume. The sensor is designed for the maximum expected working loads of the testing apparatus, which are outlined in Table 4.1. Shear stress will only be applied in one direction in the experimental testing, but the sensors are designed for equal loading in both orthogonal directions for generality and due to the sensor symmetry. To determine the design stress values, a factor of safety (FS) of 2.5 is applied to the maximum expected values. A relatively large FS is applied due to potential for buckling of thin walls, particularly under pressure loading, and the potential uncertainty in the fixity of the box walls at the bonded joint.

4.3.2 Numerical modelling methodology

Unlike with the cylindrical sensor, it was not feasible to develop a simple analytical model of the rounded-corner box structure. The stocky aspect ratio, non-standard geometry and the more complex loading mean that beam-theory approaches no longer give a good representation of

Table 4.1 Contact stresses for design of sensors for laboratory testing

Stress component	Maximum expected value (kPa)	Design value (kPa; FS = 2.5)
Effective normal stress, σ'_n	100	250
Pore water pressure, u	100	250
Frictional shear stress in direction of loading, τ_x	60	150

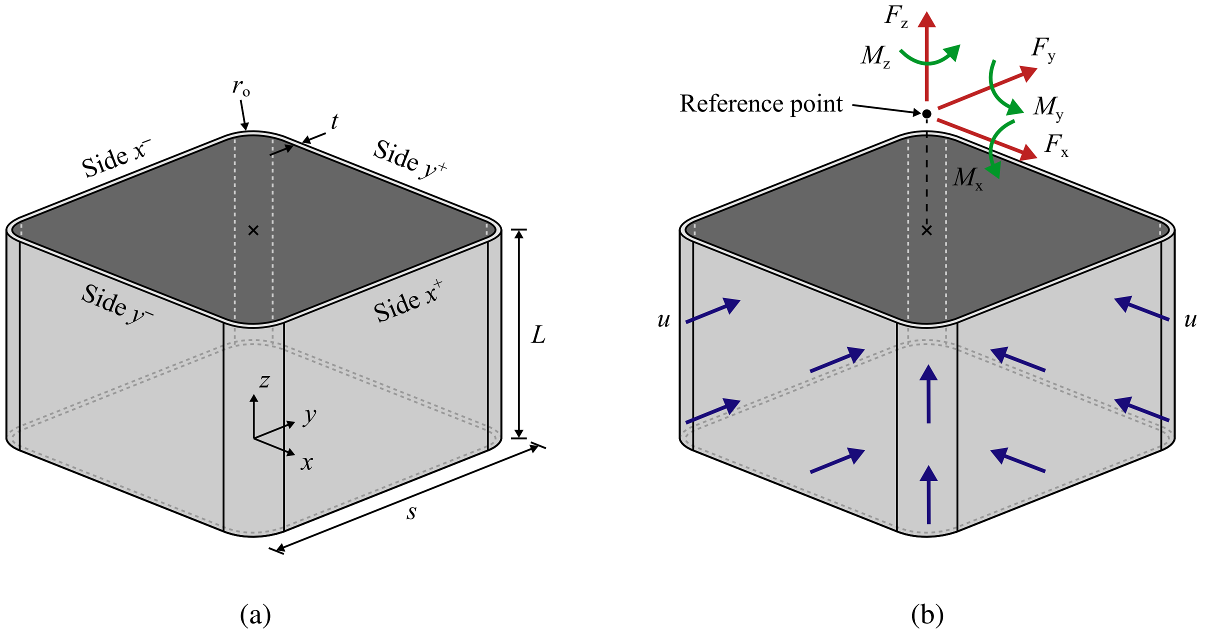

Figure 4.5 Schematic of the 3D FEA of the box sensor structure: (a) Geometry, (b) Loading

sensor behaviour under load. As a result, 3D FEA was adopted to model the new sensor structure. The 3D FEA was performed using the commercial software Abaqus/Standard (Simulia, 2020). The modelled structure comprises a thin-walled square box of length L, side width s and wall thickness t, with the corners rounded to an outer radius of r_{o}. This approach models only the deformable, thin-walled portion of the sensor structure. The solid sensor base is approximated as a fixed boundary condition (zero displacement and rotation) on the bottom surface of the box walls. The connection to the solid top cap is approximated by defining the top surface of the walls as a rigid plane, by tying the nodes to a central reference point.

The sensor material is treated as linear elastic, defined by Young's modulus, E, Poisson's ratio, ν, and coefficient of thermal expansion, α_{s}. The model is meshed with C3D8R elements (eight node linear brick with reduced integration). The mesh comprises uniform layers through the wall thickness (see Figure 4.6), with an approximate element size in the outer surface of $0.5 \times 0.5 \times 0.05$ mm (height, width, depth). The contact stresses on the sensor face are modelled by applying six concentrated force and moment components to the central reference point (Figure 4.5b). This is offset 32 mm axially from the top surface of the box, to account for the thickness of the sensor face plate. The values of the applied forces are calculated from the specified load case of σ'_{n}, τ_{x}, τ_{y} and u, based on a sensor face area, A_{f}. The fluid pressure is

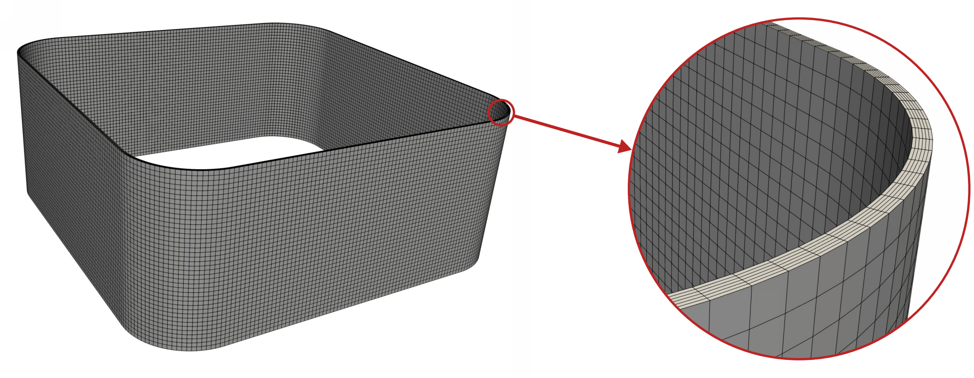

Figure 4.6 3D FEA mesh of the sensor box-section wall, comprising 89280 elements. Detail shows the thin elements through the wall thickness to improve surface strain evaluation

modelled by applying a compressive distributed load, u, onto the outer surface of the box. In addition to the mechanical loading, a uniform temperature change is also applied to the structure.

4.3.3 Synthetic data generation

The outputs of the 3D FEA calculations are used to create ‘synthetic data’, comprising the strains experienced by FBGs bonded at specific positions on the structure. An overview of the synthetic data generation process is given in Figure 4.7. This is executed as a fully automated process in Python, which generates and runs a large number of Abaqus FEA calculations for various load cases, then extracts and processes all outputs.

Strain distributions on the outer surface of the box are first extracted from the outputs of each FEA calculation. The local 2D strain state is defined by three components: the ’in-plane’ lateral and axial strain components, ϵ_{11} and ϵ_{22} respectively, and an ’in-plane’ shear strain, γ_{12} (see Figure 4.8). The global 3D Cartesian strain outputs and coordinates are extracted at the integration points of the elements that make up the outer surface of the box. On the flat sections of the walls, the correct global strain components corresponding to the local in-plane directions are selected (these are different on each side of the box). For elements which lie within the rounded corners, the global strains are transformed into a cylindrical coordinate system (centred on each corner’s axis), before selecting the appropriate components. The extracted values on all four sides and corners are then assembled to produce ’continuous’ distributions of the strain components ϵ_{11}, ϵ_{22} and γ_{12} around the outer surface of the box.

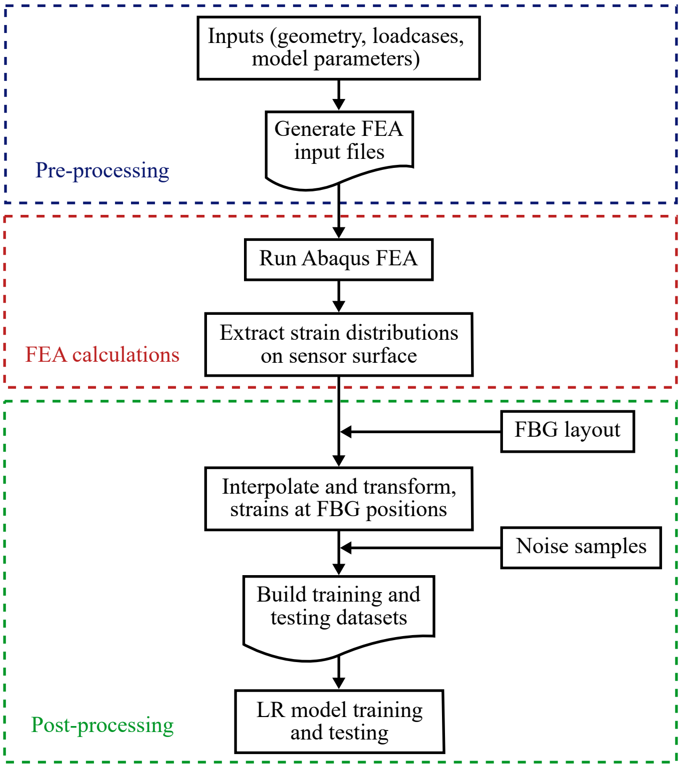

Figure 4.7 Process of generating synthetic data for LR model assessment of the box sensor design using 3D FEA

A set of 2D strain distribution FEA outputs is shown in Figure 4.9, for an example box sensor under the application of normal stress and uniaxial shear in the x direction. The extraction process produces continuous strain distributions and the expected deformation behaviour is observed. For example, the axial strain, ϵ_{22}, is compressive on the x^+ side and tensile on the x^- side due to the shear loading, and there is an overall shift towards compression due to the application of normal stress. The high mesh density gives good resolution in the distributions and the very thin

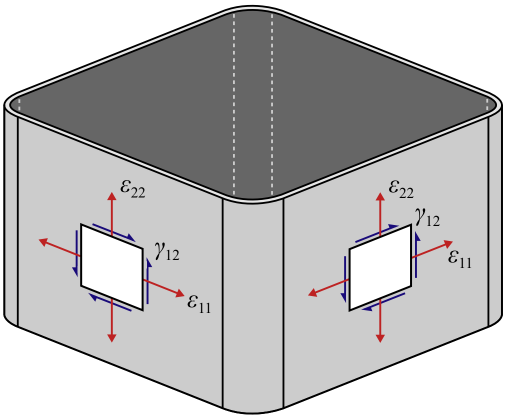

Figure 4.8 Definition of the 2D strain state on the outer surface of the box sensor

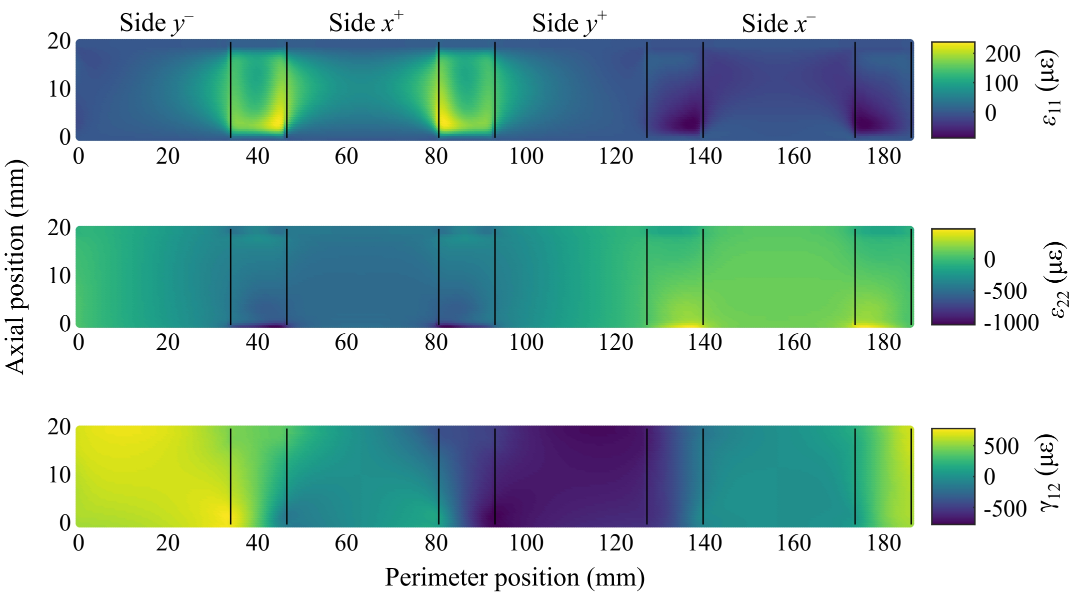

Figure 4.9 Distributions of strain components on the outer surface of an example box sensor extracted from 3D FEA results with $\sigma'_n = 100\,\mathrm{kPa}$ and $\tau_\mathrm{x} = 60\,\mathrm{kPa}$. Material properties from Table 4.2a; $s = 50\,\mathrm{mm}$, $L = 20\,\mathrm{mm}$, $r_\mathrm{o} = 8\,\mathrm{mm}$, $t = 0.3\,\mathrm{mm}$

element thickness through the wall ensures the strain in the outer elements' integration points are a good approximation of the wall surface strain.

Similar to the column sensor in Chapter 3, each point measurement representing an FBG is defined by an axial position, z_i, perimeter position, p_i, and orientation angle, θ_i, as shown in Figure 4.10. The strain components ϵ_{11}, ϵ_{22} and γ_{12} at each measurement location are determined from the extracted 2D strain distributions using 2D linear interpolation. The strains are then transformed using Equation 3.17 to give the strain in the direction of the FBG orientation. For each FEA calculation, the strain interpolation and transformation procedure is performed for each of the n number of measurements representing the layout of FBGs on the sensor. This overall process is repeated for a large number of FEA calculations under different load cases, the outputs of which are assembled to form the synthetic datasets for LR model training and testing.

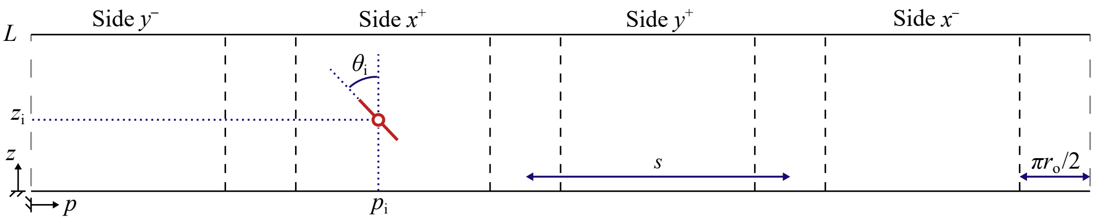

Figure 4.10 Parameters defining the centre position and orientation of each FBG or 'virtual strain measurement' on the box sensor 'rolled-out' external surface

4.3.4 Structure and instrumentation design

4.3.4.1 Overview

Design of the sensor structure was performed using 3D FEA calculations under specific load cases, considering each individual component and combinations of normal effective stress, pore pressure and biaxial shear stress. For structural design, loads derived from the factored contact stresses in Table 4.1 are used. To assess the FBG layout, 3D FEA calculations are performed to populate synthetic training and testing datasets. Similar load cases to Table 3.2 are used, except over different load ranges and with the addition of pore pressure cases. The applied loads are based on the unfactored contact stresses in Table 4.1, to simulate sensor operation. The same noise as used in Chapter 3 is also superimposed on the extracted FEA output strains.

The forces applied to the sensor are a function of the contact stresses and the sensor face area, A_f. For the experimental testing, A_f was fixed at $90 \times 90\,\mathrm{mm}$. This is a compromise between maximising the face area within the available space in the experimental setup, whilst ensuring sufficient gap around the face for the porous disc. For sensor design, a range of ± 20 Nm is considered for all three moment components and a temperature change of ± 15 °C. These limits were deemed acceptable for laboratory testing applications, where no large contact stress gradients or large changes in ambient temperature are expected.

The material adopted for the sensor structure is 7075-T6 aluminium alloy. Sensors have been traditionally machined from 'Dural' (e.g. Martin, 1994; Sheil *et al.*, 2018a; Stroud, 1971), for a

Table 4.2 Parameters adopted for laboratory testing sensor design

(a) Material

Parameter	**Value**
Young's modulus, E (GPa)	71.7
Poisson's ratio, ν	0.33
Yield strength, σ_y (MPa)	430
Coefficient of thermal expansion, α_s (/K)	23.6×10^{-6}

(b) Geometry (revised design)

Parameter	**Dimension (mm)**
Face area, A_f	90×90
Thin-wall length, L	26
Box side width, s	53.5
Wall thickness, t	0.3
Corner outer radius, r_o	15

high yield strength (up to 270 MPa) and low stiffness. 7075-T6 is an aluminium-zinc alloy that has one of the highest yield strengths available (typically 430–480 MPa). A high yield strength is beneficial in sensor applications, as it enables higher sensitivities to be achieved whilst ensuring the structure remains elastic. This is particularly critical for external pressure loading, as the bending of the box walls causes high stresses to develop. The sensor material properties are given in Table 4.2a.

Design of the sensor structure concerns selecting the geometry parameters s, t, L and r_o. The simple prismatic nature of the structure means altering the sensor response to the individual load components independently is intractable. The structure also cannot be designed fully in isolation of the FBG instrumentation. The key instrumentation details include the number of FBGs, n, the FBG length, l, the FBG spacing, d, and the FBG positioning on the sensor structure.

4.3.4.2 Initial prototype design

An initial prototype sensor was developed with geometry defined by $s = 50\,\text{mm}$, $L = 20\,\text{mm}$, $t = 0.3\,\text{mm}$ and $r_\text{o} = 8\,\text{mm}$. The parameter values were selected based on the following criteria:

- Ensuring the structure remains elastic under the design load combinations
- Maximising the sensitivity to each load component and, where possible, balancing the sensitivity to different load components
- Minimising the deflection of the sensor face
- Ensuring good compatibility with the designed optical fibre layout
- Maintaining the machinability of the structure.

The parameters s, t and r_o define the box cross-sectional area (see Figure 4.2) and therefore govern both the sensor stiffness and the size of the outer surface for gauging. A value of $r_\text{o} = 8\,\text{mm}$ was selected for the prototype, to ensure the 6 mm minimum bend radius is not exceeded during fibre routing (FBGS, 2022). A box size of 50 × 50 mm offers a good compromise between the axial and lateral force sensitivities, and was empirically found to be well suited to a 50 mm FBG spacing. The main limitation on the performance of this sensor design is the stiffness under normal stress. For a given s, r_o and E, the axial strain induced per unit normal stress can only be increased by reducing the sensor wall thickness, t. The value of t also critically influences the sensitivity and capacity of the sensor under all other load components. When using 7075-T6 material, 3D FEA design checks showed that, t can be reduced until practical considerations become the limiting factor. A value of $t = 0.3$ mm was found to be the minimum that could be feasibly achieved with conventional machining.

Compared to the design in Chapter 3, the sensor aspect ratio (axial length:plan dimension) is significantly decreased. The length of the deformable walls, L, is reduced to limit the sensor face deflection for a given induced strain. This minimises the influence of the sensor compliance on the interface soil stress state. For load cell-type contact stress sensors, there is always a trade-off between sensitivity and minimisation of sensor compliance. Decreasing L also benefits the manufacture of the thin-walled component, by reducing the deflections and vibrations during machining and allowing stiffer tooling to be used. This allows thinner walls to be achieved for improved sensitivity, without requiring expensive advanced techniques, such as electric discharge machining. The adopted value of $L = 20$ mm maximises these benefits whilst ensuring the influence of edge effects on the FBGs are limited.

The initial prototype was designed to be instrumented with a uniform array of FBGs with $l = 8$ mm and $d = 50$ mm. For effective stress measurement, the sensor requires a minimum of $n = 8$ strain measurements. The instrumentation design framework described in Section 3.6 was applied to the box sensor. Firstly, the Bayesian optimisation procedure was used to consider an optimised layout of FBGs. The centre point axial positions and orientation angles of the 'virtual' FBGs were allowed to vary continuously in the ranges $0 + l/2 \leq z_i \leq L - l/2$ and $-\pi/2 < \theta_i \leq \pi/2$ respectively. The perimeter positions, p_i, were constrained to ensure two measurements per box side, to mimic likely physical implementation. For the candidate layout in

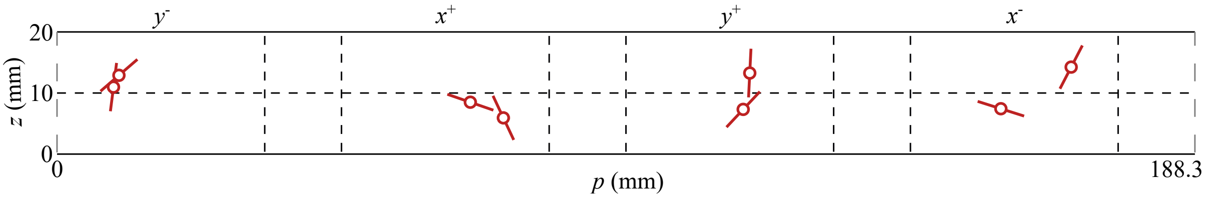

Figure 4.11 Layout of eight strain measurements on the prototype box sensor external surface determined using the Bayesian optimisation process

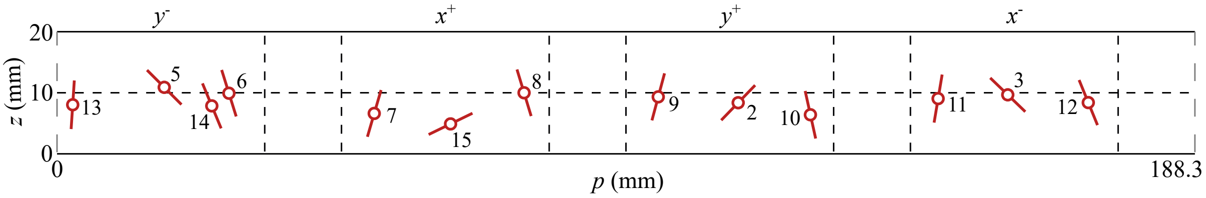

Figure 4.12 Pattern layout of fifteen FBGs on the external surface of the box sensor adopted for the initial prototype. FBGs 1 and 4 are positioned on the sensor base (not shown)

each Bayesian iteration, the strain extraction process described in Section 4.3.3 is applied to the FEA calculations for the 80 training cases and 1000 testing cases introduced in Section 4.3.4.1.

The resulting layout selected after 1000 Bayesian iterations is shown in Figure 4.11. An LR model trained with data corresponding to this layout produced an overall R^2 value on the testing dataset of 0.9964, with maximum and minimum component R^2 values of 0.9995 and 0.9859 with τ_x and σ_n respectively. The layout includes clear selection of orientations close to 0° and ±45°, which correspond to maximum induced strain under different load components. The FBGs also appear to be grouped in close-proximity pairs, however this arrangement would be clearly unachievable in practice.

A practically implementable layout was then developed using a repeating ‘snake-like’ fibre pattern. The selected layout of fifteen FBGs, shown in Figure 4.12, was developed iteratively using physical models concurrently with numerical simulation. The box shape poses much greater constraint on FBG positioning, due to the corners and the reduced axial length. The use of significant redundancy is required to achieve sufficient scope in selecting the FBG positions, enabling the fibre to wrap twice around the sensor structure. Key features include eight FBGs with $\theta_\mathrm{i} < 15°$ (6–13), three FBGs at $\theta_\mathrm{i} = 45°$ (2, 3 and 5) and two FBGs at $\theta_\mathrm{i} = 90°$ located on the sensor base (1 and 4; not shown in Figure 4.12). This configuration aids in maximising the sensitivity to normal and shear stresses, whilst allowing the fibre to be routed effectively.

The numerically simulated performance of this layout is shown in Figure 4.13. The LR model demonstrates good predictions of all eight outputs for the random load combinations in the FEA testing dataset, including pore pressure. With both the layout in Figure 4.12 and that determined by Bayesian optimisation (Figure 4.11), the least accurate predictions are obtained for the normal stress. This is attributable to the axial stiffness of the structure and is expected to

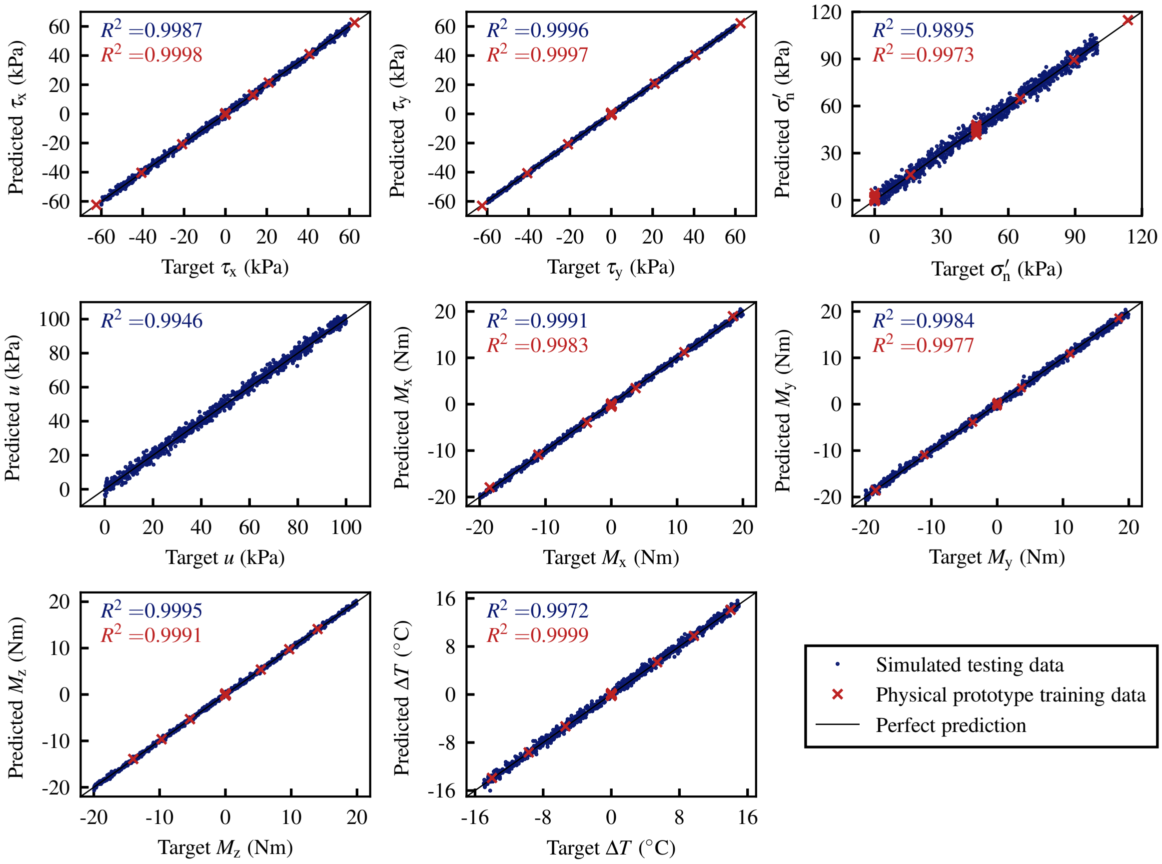

Figure 4.13 Comparison between the predicted and the target testing dataset outputs from numerical simulation with the sensor layout in Figure 4.12. Training results from a physical prototype of this initial sensor design are also overlaid for comparison (total stress only)

improve in practice, due to the conservative noise values applied to the simulated data.

4.3.4.3 FBG birefringence

A physical prototype of the initial sensor design was implemented in the laboratory, based on the parameters introduced in Section 4.3.4.2 and the FBG layout shown in Figure 4.12. The sensor was created using the instrumentation process detailed in Section 4.4.2 and a training dataset for this sensor was created using the calibration procedures described in Section 4.4.3.1. The total stress results for this physical prototype are overlaid in Figure 4.13 in red. The results demonstrate that a high quality sensor can be implemented in practice with the adopted approach. In particular, very high R^2 values are observed for the prediction of both lateral contact stress components and temperature in the training data.

Although the initial prototype design demonstrated good performance for total stress mea-

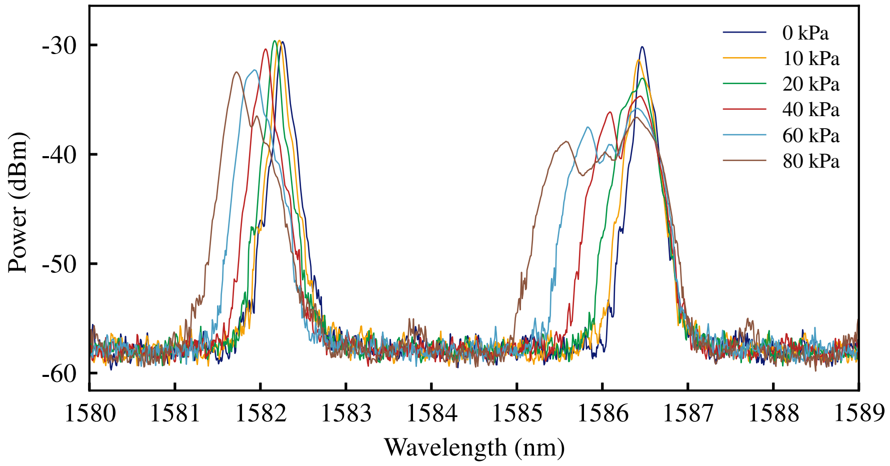

Figure 4.14 Example of spectral responses of two FBGs from the physical prototype of the initial sensor design in Section 4.3.4.2 under external fluid pressure loading

surement, it was found to be unable to measure pore pressure effectively in practice. Figure 4.14 shows the spectral responses of two FBGs on the prototype when subjected to external pressure. The FBG with an initial peak wavelength of 1586.5 nm shows a significant drop in reflectivity, combined with a broadening and eventual splitting of the peak for $p \geq 40$ kPa. The FBG peak at 1582.3 nm remains intact with only a minor drop in reflectivity. This spectral separation behaviour is a result of FBG birefringence (Emmons *et al.*, 2009). It is primarily caused by strain non-uniformity along the FBG, which results in the individual gratings of the FBG deforming differently and thus reflecting varying wavelengths. Whilst this phenomenon is entirely reversible, it presents a critical limit on the peak detection algorithms.

A limitation of the numerical modelling methodology in Section 4.3.3 is that each FBG is treated as a point strain measurement. To explore the influence of birefringence, the strain extraction and interpolation process was modified to consider a series of collinear points spaced uniformly along a length representing an FBG. This allows an estimation of the distribution of strain that each FBG will be exposed to on the outer surface of the sensor.

The FEA-predicted strain distributions for the initial design under 100 kPa external pressure are shown in Figure 4.15a, which correspond to the FBG layout in Figure 4.12. Significant strain inhomogeneities are apparent, with the greatest difference being 1034 $\mu\epsilon$ along the length of FBG 7. Larger distributions are experienced by FBGs spaced far from the sensor's axial midplane, due to the gradients as the surface strain changes form compressive to tensile near the

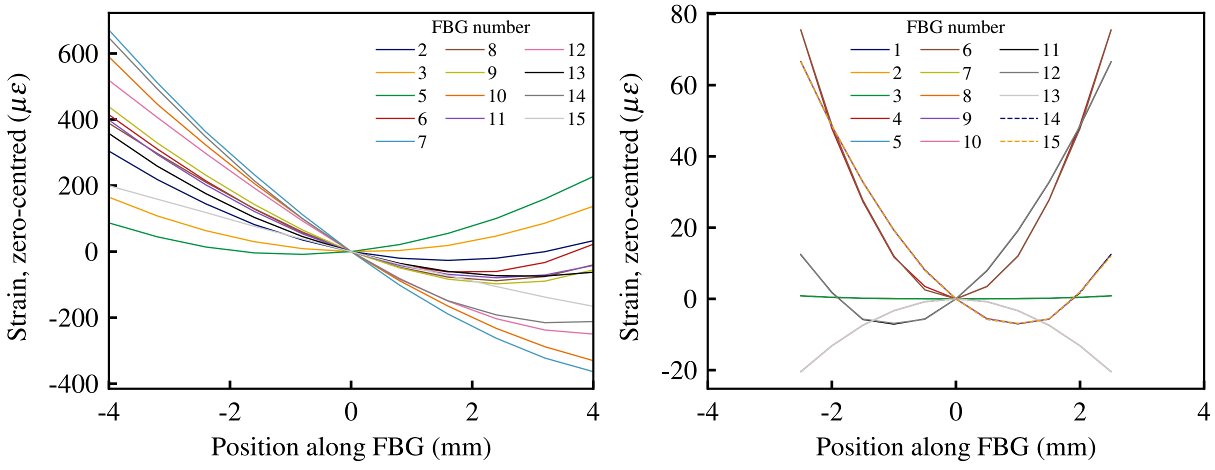

(a) (b)

Figure 4.15 FEA-calculated strain distributions for the sensor FBGs under 100 kPa external pressure loading: (a) Initial prototype (Figure 4.12), (a) Revised design (Figure 4.16). Distributions are zero-centred by subtracting the central strain for each FBG

edges. The corresponding distributions were also extracted from FEA calculations under the maximum F_z, F_x and M_x loading, which showed greatest FBG strain differences of 18.7, 60.0 and 31.4 $\mu\epsilon$ respectively. The significantly larger strain distributions induced by pore pressure gives an indication as to why spectral issues were not experienced with total stress loading.

4.3.4.4 Revised sensor design

The prototype sensor design was modified to address the limitations faced with pore pressure measurement, including changes to both the sensor structure and the instrumentation layout. The selected geometry for the revised design is given in Table 4.2b and the corresponding FBG layout is illustrated in Figure 4.16. This design was developed following a sensitivity analysis to assess potential improvements to the uniformity of strain in the FBGs under pressure loading.

Firstly, the FBG length l was reduced to 5 mm, which reduces the strain range that each FBG is exposed to in regions with high strain gradients. The drawback of using shorter FBGs is a decrease in the FBG reflectivity (the height and definition of the peak), but this was not found to be critical in this application. Secondly, the wall axial length, L, was increased by 6 mm, which moves the transition to tensile surface strains further away from the sensor axial midplane. The increase to L is only minor, to limit the increase in sensor face deflection and

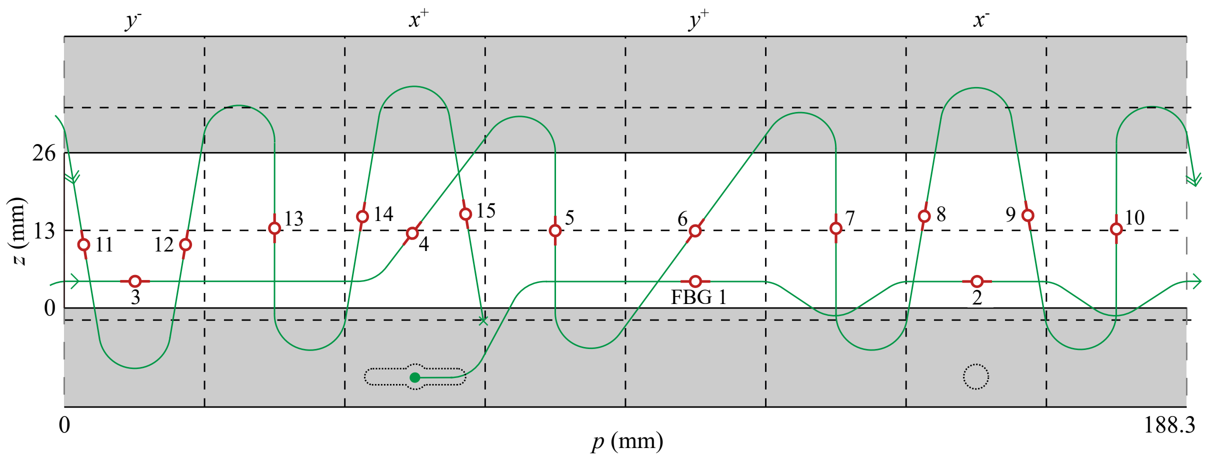

Figure 4.16 Layout of fifteen FBGs on the sensor surface for the revised design, including the optical fibre path (green line)

maintain the machinability of the structure. The wall thickness, t, remains unchanged at 0.3 mm in the revised design. Whilst increasing t would reduce the magnitude of strain induced through bending under pressure, it would cause a significant reduction in the sensitivity to all other load components, which is particularly critical to normal stress measurement.

The wall width, s and the corner radius, r_o, have a larger impact on the overall design, including the FBG layout. The adopted solution is to increase r_o to 15 mm and s to 53.5 mm. The influence of r_o is interesting; increasing r_o for a given s reduces the lateral size of the flat wall panels (i.e. the shape becomes closer to a cylinder). This greatly reduces both the magnitude and gradients of strain induced via bending under pressure, whilst having minimal impact on the other load components. However this change significantly reduces the available wall surface for FBG instrumentation. Increasing s is undesirable as it increases the compliance of the walls to bending and the box cross-sectional area, reducing the sensitivity to other load components. A minor increase in s was adopted to keep the perimeter of the box the same as the initial prototype (188.3 mm), to maintain good compatibility with the 50 mm FBG spacing.

To accommodate the reduction in the flat wall surface area, the FBG layout was modified by now also placing FBGs on the rounded corners. These were restricted to being oriented axially ($\theta = 0°$) along the centre of the corners, to avoid any undesirable influence of fibre bending. When combined with the redundancy of using fifteen FBGs, this approach allows much greater freedom in the positioning of the FBGs. The revised layout is shown in Figure 4.16 and

Table 4.3 Parameters defining the position and orientation of the fifteen FBGs on revised sensor design (Figure 4.16)

FBG	z_i (mm)	p_i (mm)	θ_i (°)
1	5.0	105.9	90.0
2	5.0	152.9	90.0
3	5.0	11.8	90.0
4	13.0	58.8	-37.5
5	13.0	82.3	0.0
6	13.0	105.9	-37.5
7	13.0	129.4	0.0
8	15.4	144.2	-9.5
9	15.4	161.7	9.5
10	13	176.5	0.0
11	10.6	3.0	9.5
12	10.6	20.5	-9.5
13	13.0	35.3	0.0
14	15.4	50.1	-9.5
15	15.4	67.6	9.5

summarised in Table 4.3. Undesirable features from the previous layout (Figure 4.12) were eliminated from the design. These include the congested region around FBGs 5, 6 and 14, which was difficult to instrument, and repositioning FBGs 1 and 4 from the sensor base. The layout was also carefully manipulated to ensure all angled FBGs are located in close proximity to the axial midplane, where the strain gradients under pressure loading are minimum.

The FEA-predicted strain distributions for the revised design under 100 kPa pressure loading are plotted in Figure 4.15b. The maximum difference in strain experienced by an FBG along its length is now 75 $\mu\epsilon$ (in FBGs 4 and 6). This represents over an order of magnitude reduction (factor of 13.7) compared to the analogous distributions in Figure 4.15a for the initial design. An LR model was trained for the revised sensor design and used to predict on a synthetic testing dataset, derived from 3D FEA calculations under 1000 random combined load cases. The predictions are plotted in Figure 4.17. Comparable performance to the initial prototype in Figure 4.13 can be observed, with improvement in both normal stress and pore pressure.

4.4 Sensor implementation

4.4.1 Sensor assembly

The sensor structure is machined from solid aluminium alloy 7075-T6 stock. The two parts of the structure (see Figure 4.19a) are bonded together using Bostik Born2bond™ structural

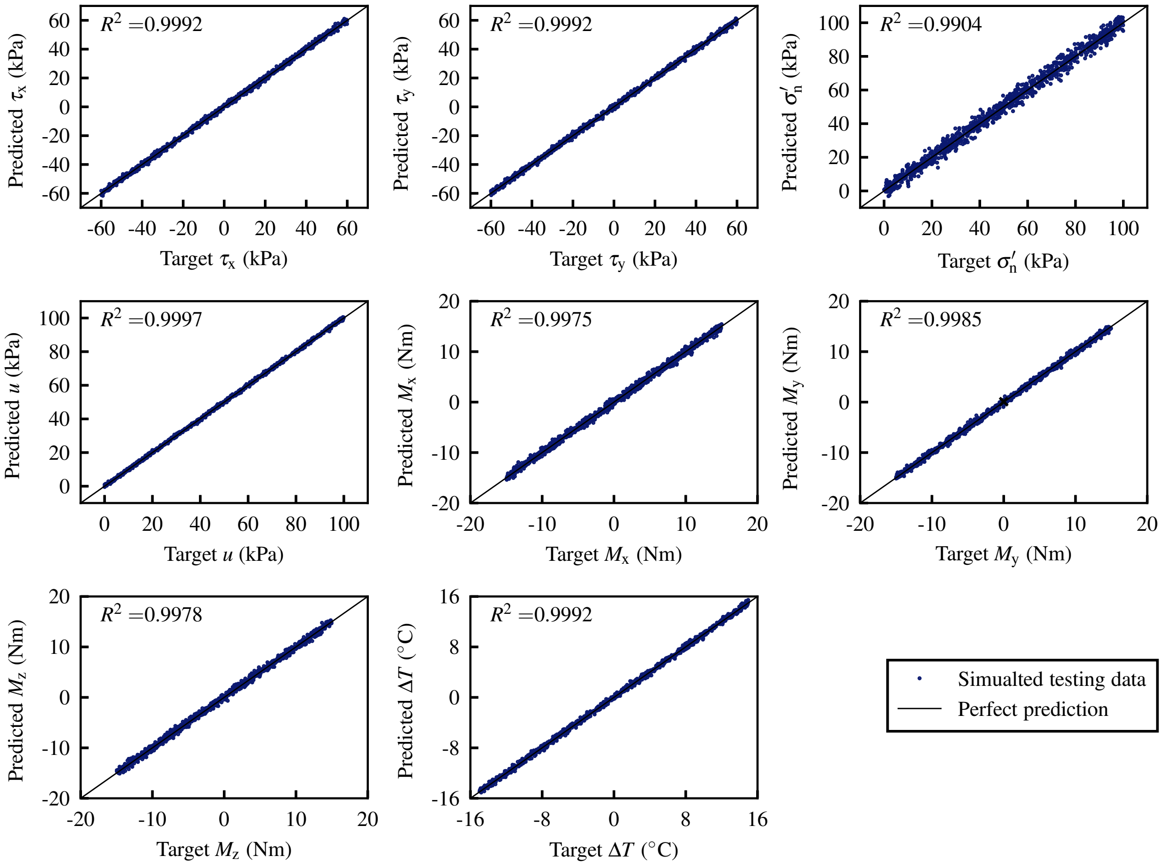

Figure 4.17 Comparison between the LR model predications and the target output values in the testing dataset generated using 3D FEA of the revised sensor design (based on the parameters in Table 4.2 and the FBG layout in Figure 4.16)

cyanoacrylate adhesive. This has excellent adhesion to aluminium and is capable of providing the structural load transfer between the sensor face and the deformable thin walls, and the gap-filling needed to seal the central sensor void from fluid entry.

The face plate is a separate machined aluminium piece that attaches into the side of the sensor body top cap using eight M4 bolts. This can be used directly for soil contact or it can be used as a mounting plate for a facing material. The laboratory testing sensors developed for this research feature a concrete face bonded to the mounting plate, as shown in Figure 4.18a. The face was cast using a 3D printed mould with sieved aggregate, to accurately produce the 8 mm thick 90 × 90 mm square shape. This approach results in a uniform sensor face that closely matches the surface roughness of the interface material. This overcomes the need to apply often assumed roughness factor conversions, to estimate the stresses on the overall structure from interface contact stress sensor measurements.

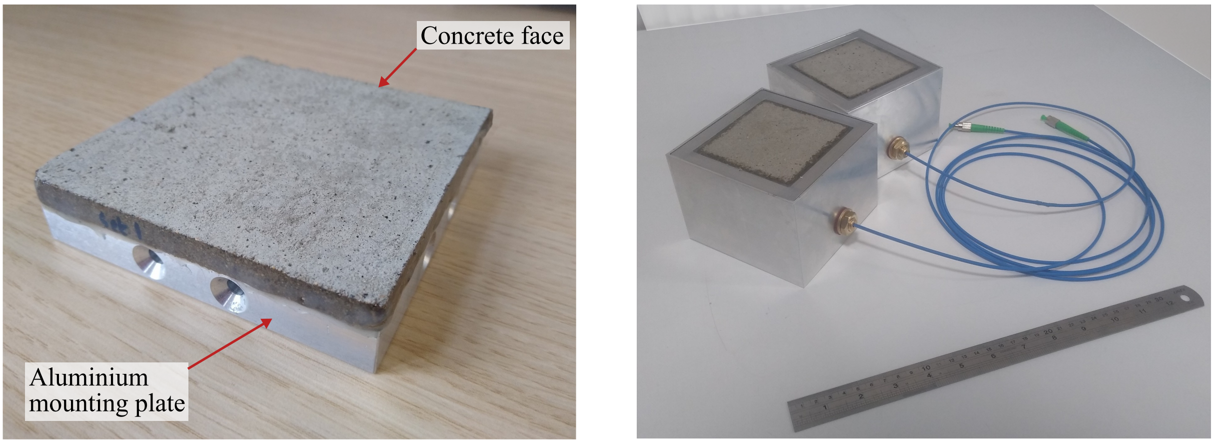

(a) (b)

Figure 4.18 Sensor assembly: (a) Concrete sensor face plate, (b) Two assembled total stress sensors for use in laboratory testing

After the sensor body is instrumented (see Section 4.4.2), it is bolted into the housing using four M6 countersunk bolts. The porous or metal ring is then fitted onto the housing around the sensor face plate and held in place with adhesive. The 1.5 mm gap around the sensor face is then filled with a bead of silicone sealant, which seals the housing whilst allowing face displacement to occur. Two of the fully assembled sensors are shown in Figure 4.18b prior to installation in the laboratory testing apparatus described in Chapter 5.

4.4.2 FBG instrumentation

The sensor body is instrumented with a single optical fibre containing the uniform array of $n = 15$ FBGs with $l = 5\,\text{mm}$ and $d = 50\,\text{mm}$. The FBGs are bonded onto the deformable thin-walled section of the structure, using the procedures detailed in Section 3.3.2. To position the FBGs in the intricate layout pattern in Figure 4.16, a novel fibre mounting process was developed. The concept involves the use of guide pieces, referred to as ‘pivots’. These small circular supports are temporarily mounted in specific locations to the sensor surface. The fibre is then ‘strung’ around the pivots and lightly tensioned, pulling the fibre into direct contact with the sensor surface and holding it in a fixed layout. The pivots form the curved arcs in the fibre pattern in Figure 4.16 and the FBGs are located on the straight lines of fibre spanning between adjacent pivots. Provided the pivots are accurately positioned and the first FBG is located accurately,

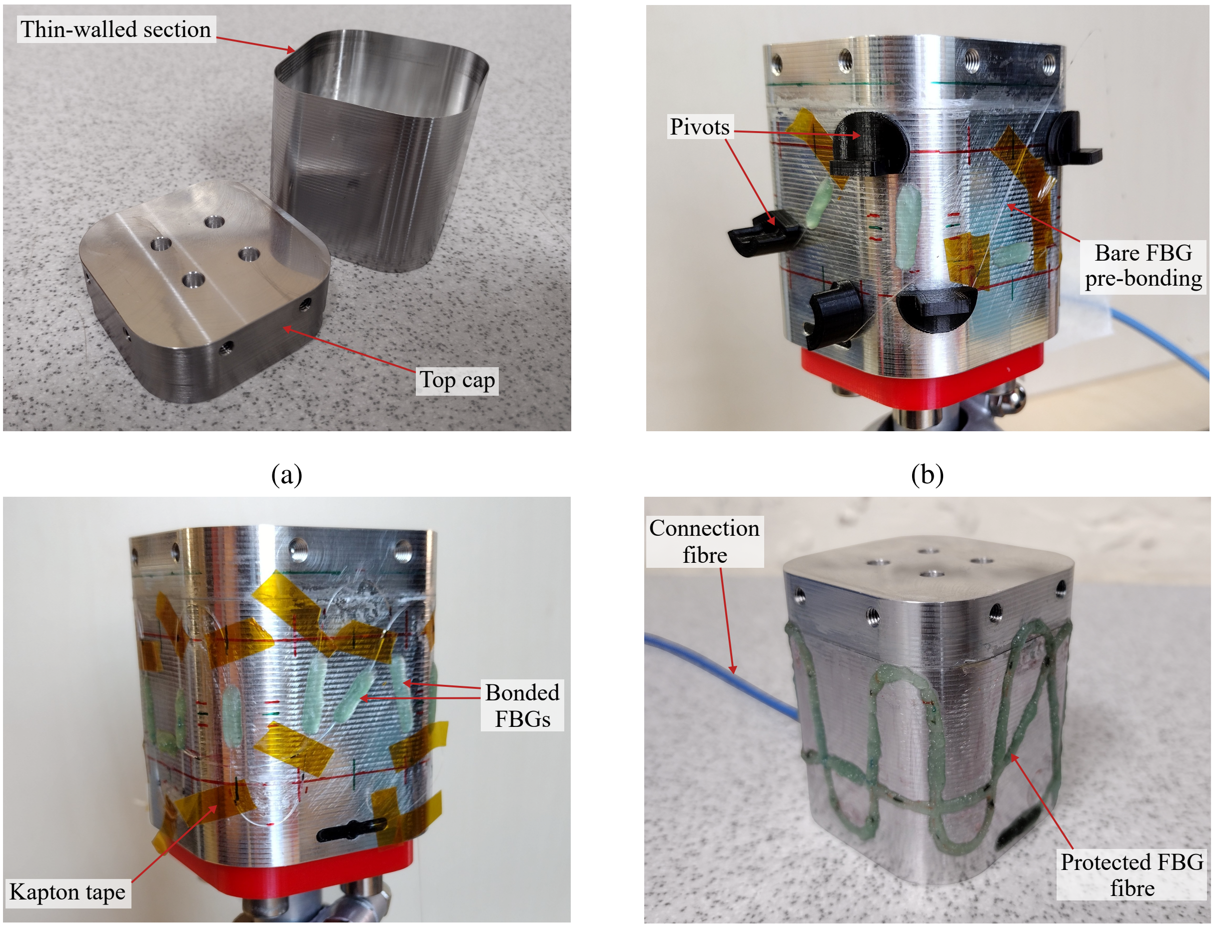

(a) (b) (c) (d)

Figure 4.19 Assembly and instrumentation of sensor: (a) Sensor structure prior to top cap bonding, (b) Positioning of FBGs using 3D printed 'pivots', (c) FBGs bonded to sensor, (d) Finished sensor body

the FBGs in between the pivots will sit very close to their designed positions. Compared to manually positioning and bonding each FBG sequentially, this approach dramatically reduces the overall instrumentation time and improves repeatability.

To instrument the box structure, small bespoke 3D printed pieces were used to form the pivots (see Figure 4.19b). The circular shape ensures the minimum bend radius of the fibre is not exceeded. To aid with FBG bonding, the inner surface of the pivots was designed to sit flush against the sensor and a 45° chamfer is used on the pivot edge, which creates a 'channel' that pulls the fibre into the sensor surface. The fibre is temporarily held in place around the pivots using Kapton tape, whilst two-part acrylic adhesive (3M Scotch-Weld DP8810NS) is applied to the FBGs to permanently bond them to the sensor structure. After the adhesive is cured,

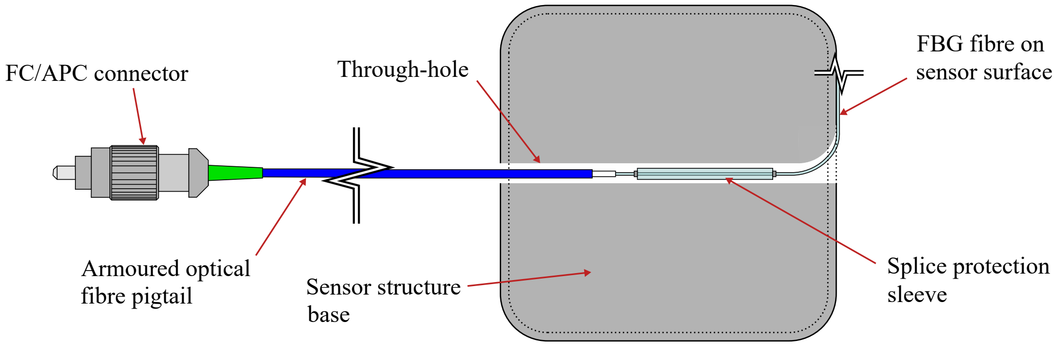

Figure 4.20 Illustration showing detail of optical fibre connectivity to the sensor

the temporary pivots are removed (Figure 4.19c) and the remaining exposed fibre is covered in adhesive for protection (Figure 4.19d).

To connect the sensor to an optical interrogator, the FBG fibre is fusion spliced to a single-mode optical fibre pigtail with an FC/APC connector. For improved durability, a 3 mm diameter armoured fibre was used, featuring a helical stainless steel tape surrounded by a layer of aramid and stainless steel mesh. The splice was formed using a Fujikura 41S splicer with an FH-FC-30 clamp fitted, which enables the splice to be formed very close to the end of the armoured fibre. The splice is protected using a 20 mm heat-shrink protection sleeve, before embedding the optical joint inside a through-hole in the solid sensor base, as shown in Figure 4.20. This procedure gives full protection to the FBG fibre and the weakened region around the splice, whilst minimising obstruction to the gauging surfaces. At the end of the through-hole, a smooth radius channel is formed in the sensor base to allow the FBG fibre to transition smoothly onto the sensor surface.

The 3 mm diameter fibre comes out of an opening in the sensor housing. To achieve a watertight pass-through, an M16 Lapp SKINTOP® MS-M gland is used (see Figure 4.3b). The large size gives a sufficient opening to accommodate the FC/APC connector. A Lapp SKINTOP® DIX-M gland insert is used to provide a strong seal against the relatively thin fibre. This insert was modified to allow installation from the side of the pre-connectorised fibre. This approach gives flexibility as it allows the entire sealing gland assembly to be fitted to a sensor after assembly, which cannot be achieved with a standard 3 mm cable gland.

4.4.3 Sensor calibration

4.4.3.1 Methods

Calibration involves subjecting the sensor to specific controlled actions in the laboratory. These tests are used to assemble a dataset of known input-output samples for training the sensor LR model. See Table 4.4 for a summary of the applied actions. In all cases, calibration is performed by applying at least 10 approximately uniform increments, up to ±10% beyond the expected working range. Prior to calibration, the sensor is subjected to three load and unload cycles over the maximum range for each action. This is recommended to strain-cycle the gauges and sensor material to remove hysteresis effects (Bransby, 1972) and is required in load cell calibration standards (e.g. ISO, 2011). Calibration is conducted in three distinct stages: a) force/moment components, b) temperature, and c) pore water pressure. For total stress measurement, only stages a) and b) are required. The prototype sensor in Chapter 3 was also calibrated using the same procedures as described here.

For each calibration data point, the peak wavelengths of the fifteen FBGs on the sensor body, λ_i, are measured. For each set of calibration tests, an initial data point is also recorded with no applied action, giving a set of zeroing wavelengths, $\lambda_{0,\mathrm{i}}$. The FBG peak wavelengths are then converted to wavelength shifts by subtracting the corresponding zeroing value, $\Delta\lambda_\mathrm{i} = \lambda_\mathrm{i} - \lambda_{0,\mathrm{i}}$.

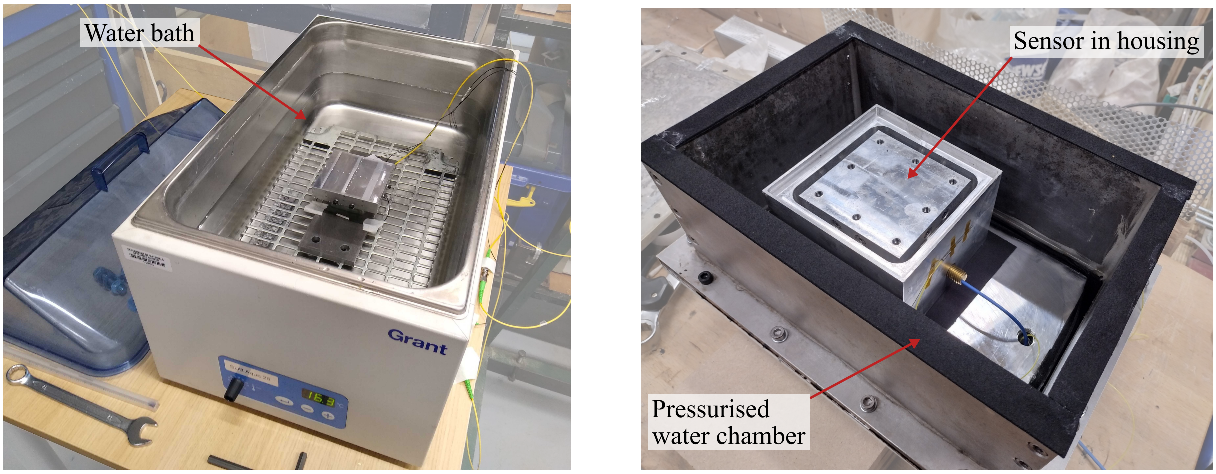

(a)

(b)

Figure 4.21 Sensor calibration: (a) Applying temperature increments in a thermal water bath, (b) External water pressure calibration

Table 4.4 Summary of the sensor calibration process

Load component	**Calibration range**	**Additional loads applied** [a]	**Maximum FBG sensitivity**
F_x	± 550 N		−1.06 pm/N (FBG 6)
F_y	± 550 N		0.958 pm/N (FBG 4)
F_z	−1150 N		0.604 pm/N (FBG 11)
M_x	± 22.5 Nm	$F_z = -450$ N	20.2 pm/Nm (FBG 11)
M_y	± 22.5 Nm	$F_z = -450$ N	18.6 pm/Nm (FBG 9)
M_z	± 22.0 Nm	$F_x = -145$ N	15.9 pm/Nm (FBG 4)
u	± −110 kPa		14.5 pm/kPa (FBG 15)
ΔT	−8–14 °C [b]		48.7 pm/°C (FBG 12)

[a] Ambient temperature change can occur during all tests; [b] relative to 20 °C ambient temperature

The $\Delta\lambda_i$ values form the inputs in the LR model training data. This procedure is important as it accounts for variations in the absolute FBG peak wavelengths caused by installation effects, such as bolting and sensor orientation, which change multiple times throughout calibration. In operational use, a set of zeroing wavelengths are measured post-installation of the sensor.

Firstly, thermal calibration is performed with the sensor fully submerged in a temperature-controlled water bath, as shown in Figure 4.21a. Calibration was performed over an operating range of 12–34 °C in approximately 2 °C increments. To provide an accurate measure of the bath temperature, an FBG temperature probe (FBGS TP01) is mounted directly adjacent to the sensor. The temperature bath corresponds to free boundary conditions on the sensor, as in Equation 3.6. In practice the boundary conditions on the sensor and therefore the thermal response may change under the application of the other load components. The influence of these effects are beyond the scope of this research.

In addition to explicitly calibrating for temperature dependence, any changes in ambient temperature during the other calibration tests will cause thermal-induced wavelength shifts. The temperature probe is therefore left in place during all other calibration tests, to provide a reference temperature measurement. These measurements are included in all training data, enabling the LR model to effectively account for the influence of temperature.

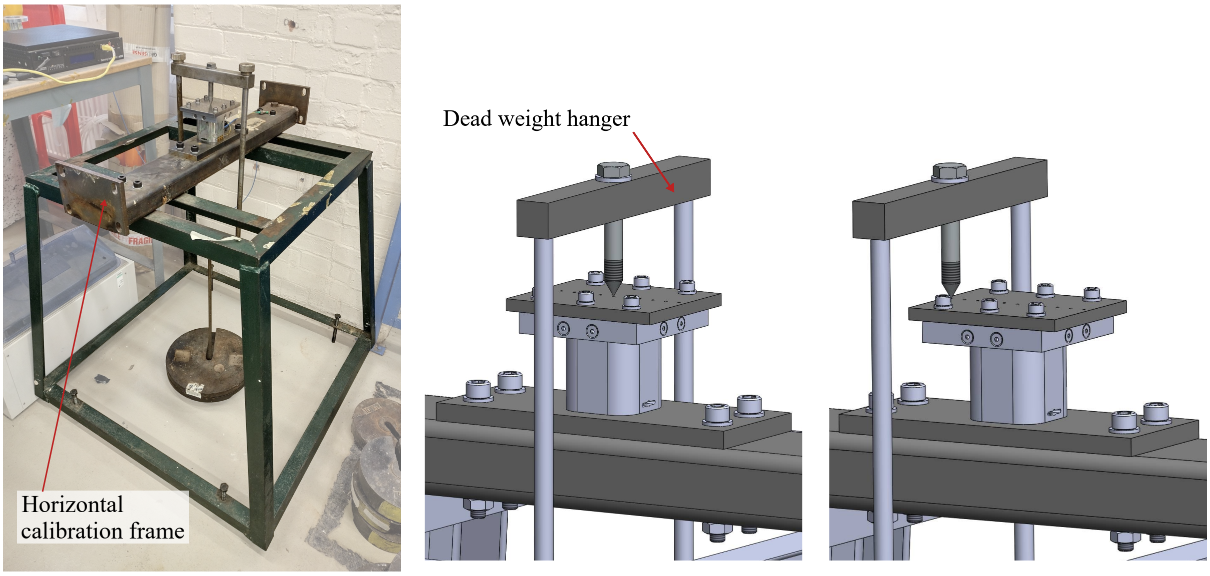

(a) Horizontal configuration (b) F_z (c) M_x or M_y, with F_z

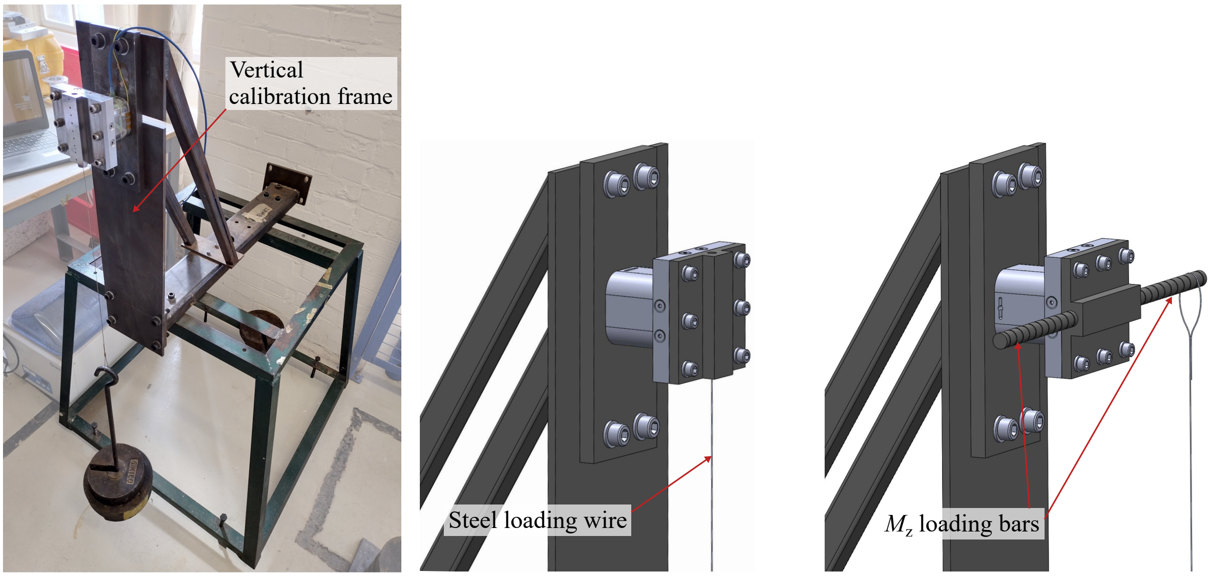

(d) Vertical configuration (e) F_x or F_y (f) M_z, with F_x or F_y

Figure 4.22 Sensor calibration for force and moment components, showing the two mounting configurations and the four different load application methods used

Sensor calibration under force/moment components is performed using dead weights, as shown in Figure 4.22. A custom calibration frame allows the sensor to be mounted horizontally (Figure 4.22a) or vertically (Figure 4.22d), for application of different load components:

- Axial force, F_z, is applied with the sensor mounted horizontally, using a dead weight loading hanger. The load is applied to the sensor using a conical pin through a machined indent at the centre point of the calibration face plate (see Figure 4.22b). This ensures the force application is accurate and repeatable, and minimises any off-axis loading. The sensor was only calibrated under compressive axial force, under the assumption that the sensor face will not be subject to tensile normal stress.

- Lateral moments, M_x and M_y, are achieved by applying the loading hanger offset from the sensor face centre point (see Figure 4.22c). The calibration face plate features indents that are machined at 10 mm offset increments, up to ± 50 mm. The axial force is offset in the y direction to apply M_x, before rotating the sensor and applying offsets in the x direction to apply M_y. The constant axial force applied in these tests is accounted for in the LR model by including it the training dataset.
- Lateral forces, F_x and F_y, are applied with the sensor mounted vertically, as shown in Figure 4.22e, to avoid the use of pulleys. The load is applied using dead weights through a steel wire, which is fixed into the side of a calibration face plate. The wire is coincident with the plane of the sensor face during operation, ensuring that the lateral forces closely replicate the shear stresses. The sensor is calibrated in both directions by rotating the sensor 180° on the frame, before rotating 90° to calibrate the orthogonal force.
- Axial moment, M_z, is applied using a constant F_x or F_y force positioned offset from the sensor centreline (see Figure 4.22f). Dead weight is applied via a steel wire hanging on a pair of horizontal steel bars. A series of notches are machined into the bars at 10 mm increments between 50 and 150 mm from the centreline, to accurately locate the wire. The constant lateral force applied is also included in the training dataset.

External fluid pressure calibration is performed by placing the sensor in a sealed pressure chamber (see Figure 4.21b). The sensor was mounted within its housing and with a face plate fitted, to ensure the same loading configuration as in operation. The chamber is filled with water and pressure is applied using the laboratory compressed air supply. A regulator was used to control the pressure increments applied and a PT was fitted on the air line to provide an accurate measurement of the applied pressure (see Section 4.5.3).

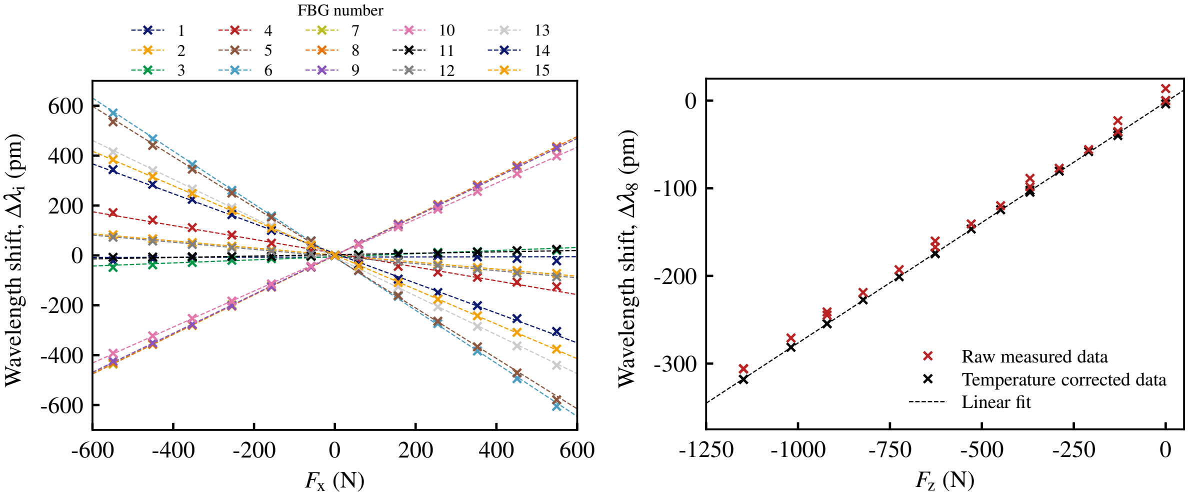

(a) (b)

Figure 4.23 Example calibration results: (a) F_x application, (b) Single FBG under F_z application showing the influence of ambient temperature variation

4.4.3.2 Results

An example of the FBG wavelength shift data from F_x calibration of the sensor is shown in Figure 4.23a. Excellent linearity of the FBG responses is seen in all cases. A maximum peak response of $-1.06\,\mathrm{pm/N}$ is demonstrated by FBG 6 during this loading. This is attributable to its positioning at $-45°$ on the y^+ sensor wall, where the induced strain under the lateral force is expected to be largest. This gives confidence in the FBG bonding and the behaviour of the sensor body. A broadly similar response is seen under the other applied actions and a summary of the maximum responses is given in Table 4.4.

To illustrate the importance of the reference temperature measurement, Figure 4.23b shows an example of the response of a single FBG during a load-unload cycle of F_z calibration. The raw peak wavelength shift data do not return to zero after unloading and this is attributable to temperature change during F_z application. To demonstrate this, a linear fit between the sensor FBG and the reference FBG was formed during temperature calibration and used to ‘correct’ the raw F_z data for the simultaneous temperature change. Excellent linear behaviour and no zero-drift is shown in Figure 4.23b for these temperature-corrected data. During F_z calibration the reference FBG recorded only 0.45 °C temperature change, which indicates the importance of temperature measurement during calibration, as even very minor temperature changes influence

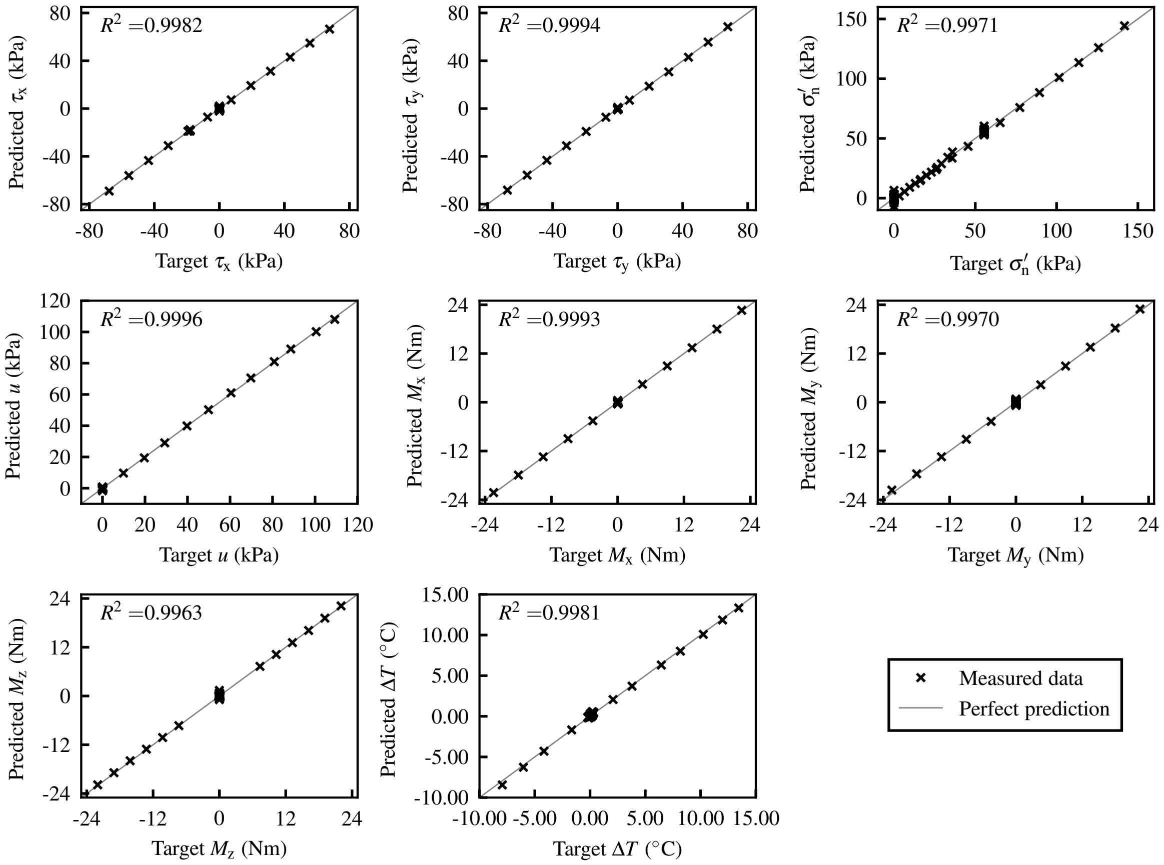

Figure 4.24 Comparison between the prototype sensor LR model predications and the applied actions in the calibration data for effective normal stress measurement

the resulting gradient. It should be noted that this manual compensation process is not undertaken in practice; the raw wavelength shift data are provided to the LR model, which determines the temperature dependence automatically.

The applied calibration actions and the corresponding measured peak wavelength shifts are assembled into a dataset for training the sensor LR model. The performance of the trained model predicting on the training dataset is shown in Figure 4.24. Very good predictions are observed for all outputs, with individual component R^2 values of between 0.9963 and 0.9996. The worst performance is seen with pore water pressure and effective normal stress, however the predictive performance is still very good. The maximum cross-talk (difference between predicted and target outputs, expressed as a percentage of corresponding range in Table 4.4) observed was 3.47%, which occurred in σ'_n during M_y loading. The calibration results show that the framework outlined in Chapter 3 can extend to determine all eight component outputs,

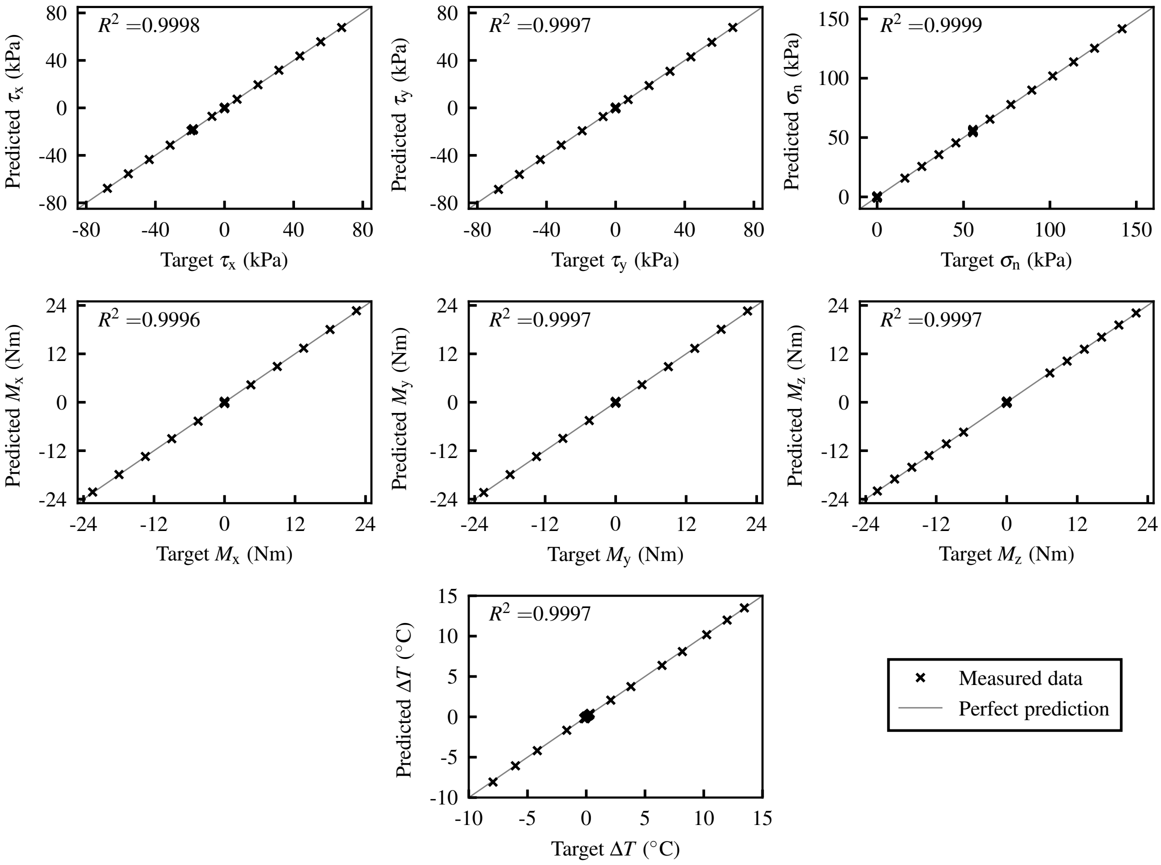

Figure 4.25 Comparison between the prototype sensor LR model predications and the applied actions in a reduced calibration dataset for the simpler total normal stress measurement case

handling the additional complexity of pore pressure loading.

For comparison, an LR model was also trained for the simpler total stress sensor case. This comprises using the same training data but only considering seven component outputs (no pore pressure loading). The performance of the trained LR model predicting on the corresponding reduced training data is shown in Figure 4.25. This mode of operation shows excellent performance across all components. There is notable improvement, particularly in the normal stress prediction. This is to be expected, as there is less complexity in loading on the sensor and fewer outputs for the LR model to capture. In general, the sensor performance is also improved over the prototype column in Chapter 3, which is likely attributable to the greater FBG responses under all load components in Table 4.4, compared to Table 3.7.

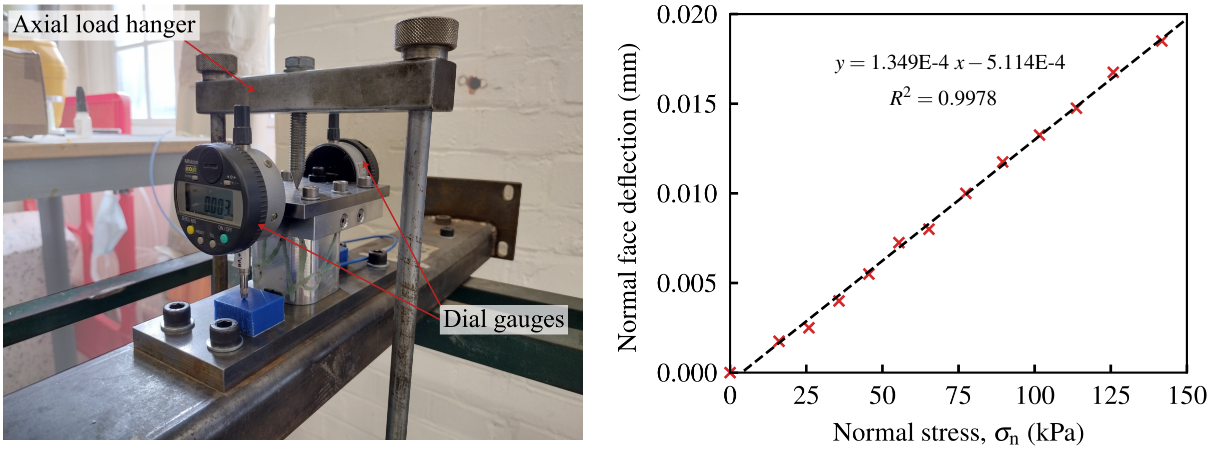

(a) (b)

Figure 4.26 Sensor face deflection under total normal stress application: (a) measurement set up, (b) results

4.5 Sensor validation

4.5.1 Sensor normal compliance

The sensor compliance under normal stress application was assessed using axial dead weight application (F_z in Figure 4.22b). The axial deflection of the sensor face was measured using two dial gauges (Mitutoyo 543 12.7 mm, 0.001 mm resolution) rigidly bolted on opposite sides of the face plate (Figure 4.26a). These react off of the calibration base plate close to the sensor body, limiting any influence from calibration frame compliance on the measurements. The sensor face deflection is calculated as the average of the two dial gauge readings.

The stress-deflection results are shown in Figure 4.26b. The response is highly linear over the applied stress range, confirming the linear elastic behaviour of the sensor structure. The experimental results can be interpolated to the design normal stress of 100 kPa, showing a face deflection of 0.0139 mm. Compared to the sensor 90 mm × 90 mm face, the results give a deflection:length ratio of 1:6454 at the maximum expected normal stress. This is exceeds both the commonly referenced recommendation of 1:2000 (Waterways Experiment Station, 1944) and also the more stringent 1:5000 recommended by Weiler Jr. and Kulhawy (1982).

Talesnick *et al.* (2014) claims that sensor compliance must be eliminated entirely to achieve accurate measurements of soil normal pressures. Whilst it is clear that sensor compliance

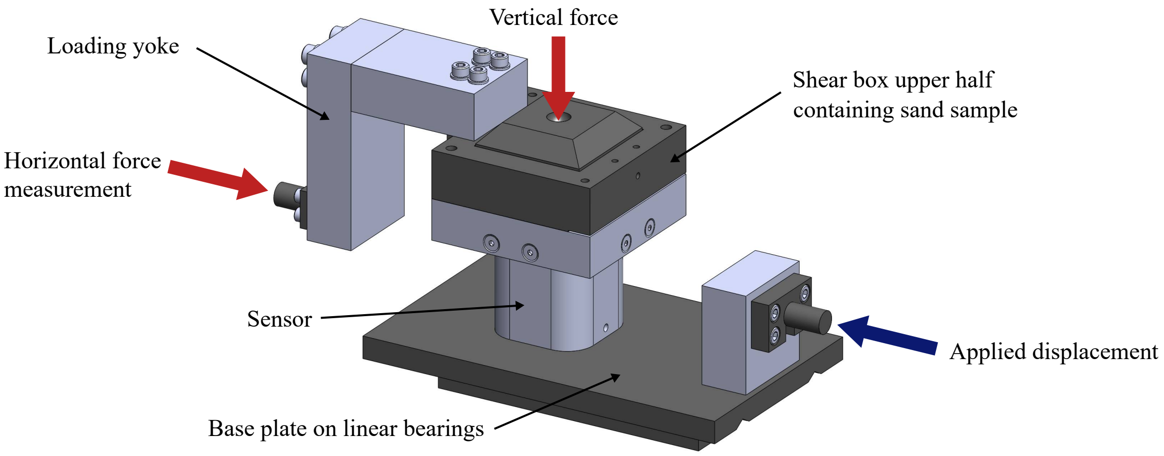

Figure 4.27 Illustration of the direct interface shear test set up for sensor validation

influences the interface stress state, the observations of Talesnick *et al.* (2014) are for relatively small diameter diaphragm-type sensors. The face deflection ratio of the present sensor exceeds that of typical Cambridge-type SSCS designs (Bransby, 1972), which have a more closely comparable deflection mechanism and have provided reliable measurements for a range of applications (e.g. Martin, 1994; Sheil *et al.*, 2018a). Null-gauging technology, such as that of Talesnick *et al.* (2014), represents a high performance option, but there are significant limitations to application in underground construction. These include the requirement for a compressed air feed and several ancillary components at each sensing location (see Figure 2.7a), the potential impact of EMI on null pressure determination, and the reliance on additional sensors for shear stress measurement (e.g. Talesnick and Ringel, 2022). The sensor technology presented in this thesis represents a compromise between sensing accuracy and the practical benefits of using fibre optics, including robustness and simplified connectivity.

4.5.2 Direct interface shear testing

To validate the sensor under similar loading to its intended application, a series of direct interface shear tests were performed. Tests were conducted using a modified shear box apparatus, in which the sensor replaces the lower half of a conventional direct shear box, as shown in Figure 4.27. The carriage is replaced by a stiff base plate, which is translated along the original linear bearings by the apparatus drive unit. The sensor is bolted to this base plate and a machined aluminium face plate is fitted, to which the original upper half of the direct shear box attaches using the

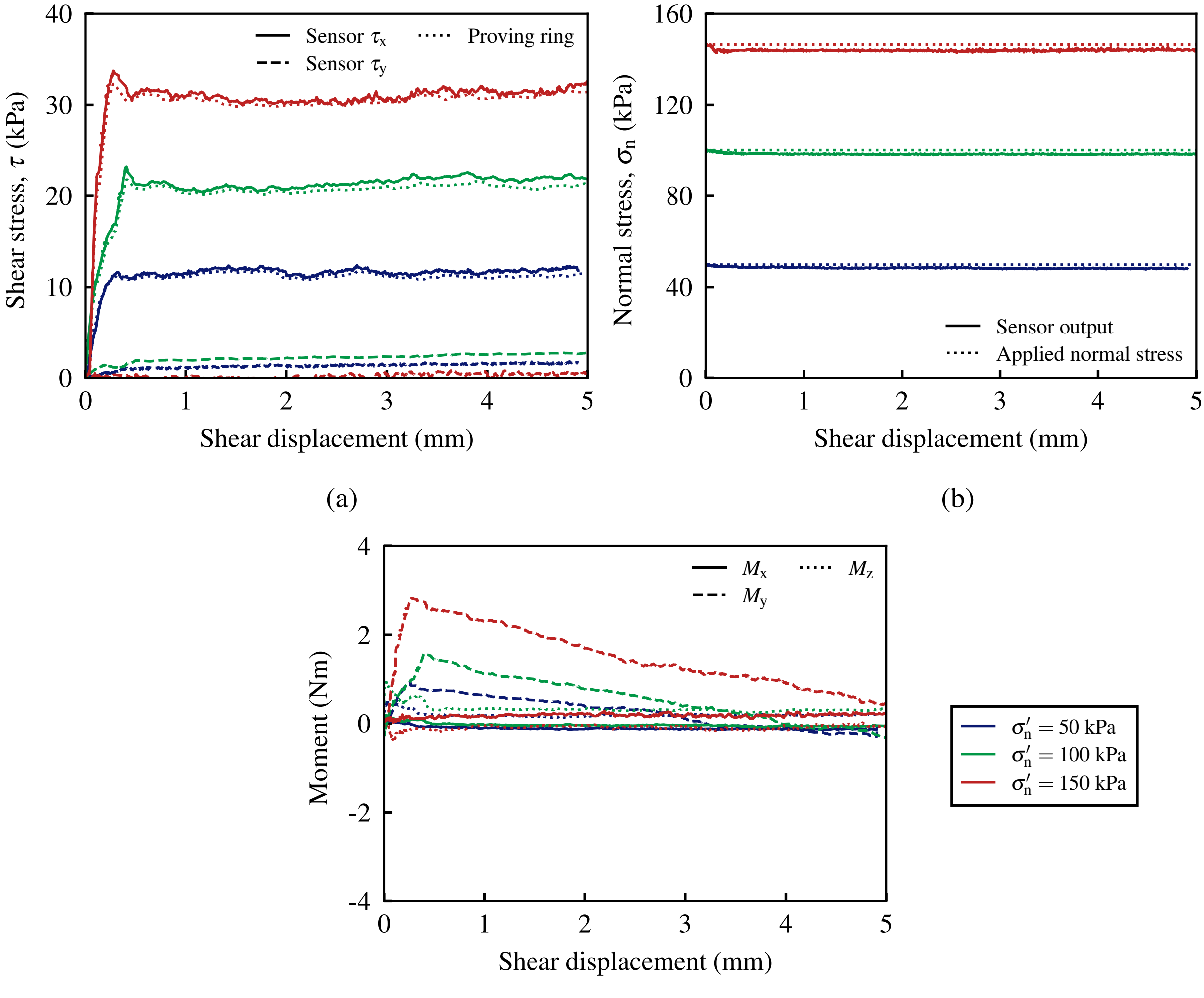

(a)

(b)

(c)

Figure 4.28 Sensor validation using direct interface shear tests, with shearing in the x direction: (a) shear stresses (b) normal stress, (c) moment components. The colour legend applies to all subfigures, whereas the linestyles are defined in the individual subfigures

securing and raising bolts. An extended loading yoke is fitted to maintain the connection to the horizontal 50 lb proving ring, facilitating measurement of the shearing force.

A 60 × 60 × 20 mm 'half' soil sample is prepared directly onto the sensor face and normal stress is applied by a dead-weight loading hangar. The normal stress is constant during shearing, due to the sample area remaining constant as it is translated over the larger 90 × 90 mm sensor face. All tests were performed using Leighton Buzzard (LB) 14/25 sand, details of which are provided in Section 5.3.1. Tests were performed at three normal stress levels (50, 100, 150 kPa) on dense sand samples of relative density, D_R, of 0.88 ± 2.5%. Although the maximum normal stress is greater than applied during sensor calibration, the resulting force is lower due to the

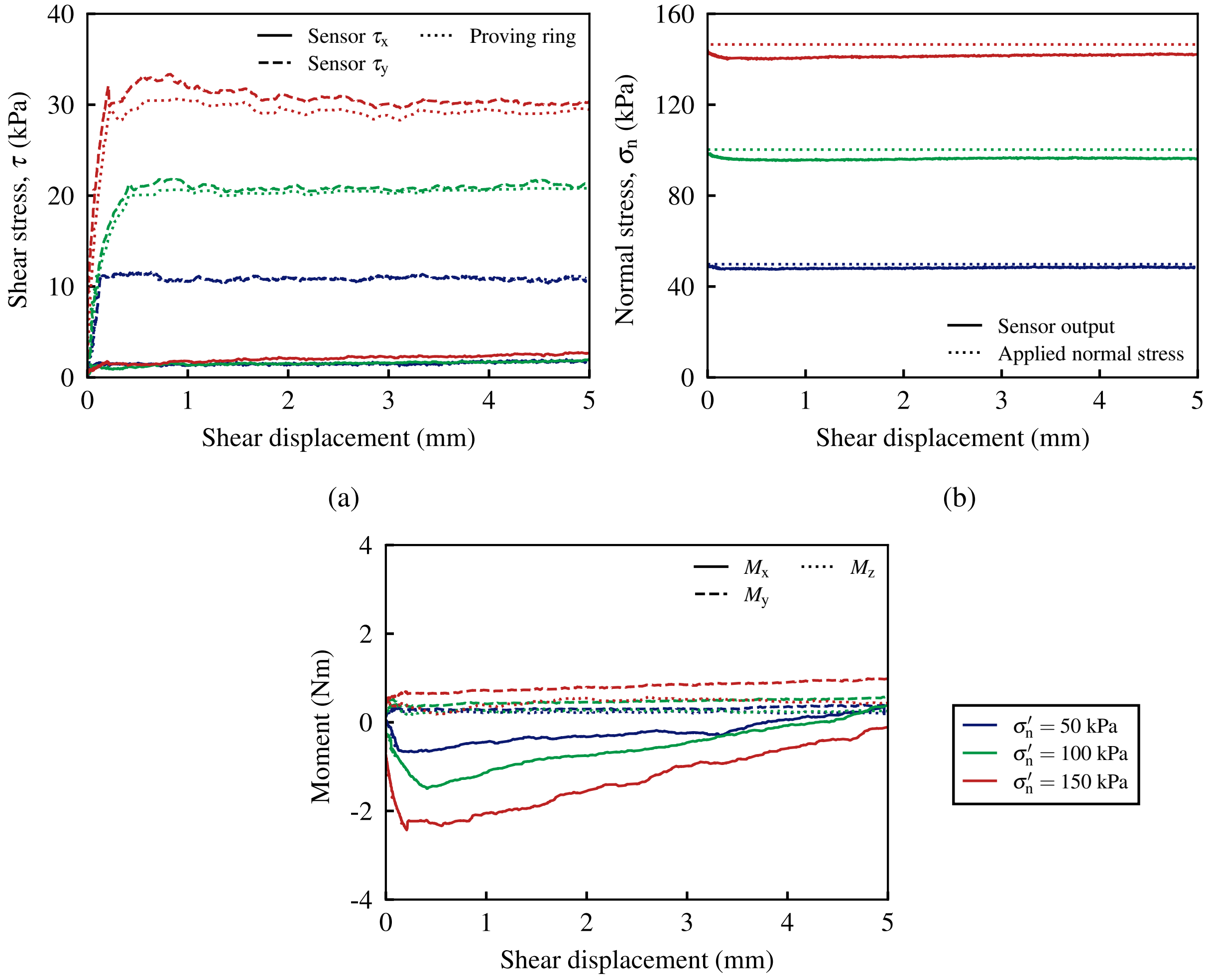

(a) (b)

(c)

Figure 4.29 Sensor validation using direct interface shear tests, with shearing in the *y* direction: (a) shear stresses (b) normal stress, (c) moment components. The colour legend applies to all subfigures, whereas the linestyles are defined in the individual subfigures

stress only being applied over a portion of the sensor face.

The results from a set of tests with shearing parallel to the sensor *x* axis are presented in Figure 4.28. An equivalent set of results for shearing in the orthogonal *y* axis direction are shown in Figure 4.29. There is good agreement between the sensor normal stress output and the constant applied normal stress in both sets of tests (Figures 4.28b and 4.29b). There appears to be excellent agreement at zero displacement, with only slight under-prediction developing as shearing occurs. This is most apparent at 150 kPa when shearing parallel to the sensor *y* axis.

The shear stress outputs show very good agreement between the sensor outputs and the force measured by the horizontal proving ring (Figures 4.28a and 4.29a). A very minor over-prediction

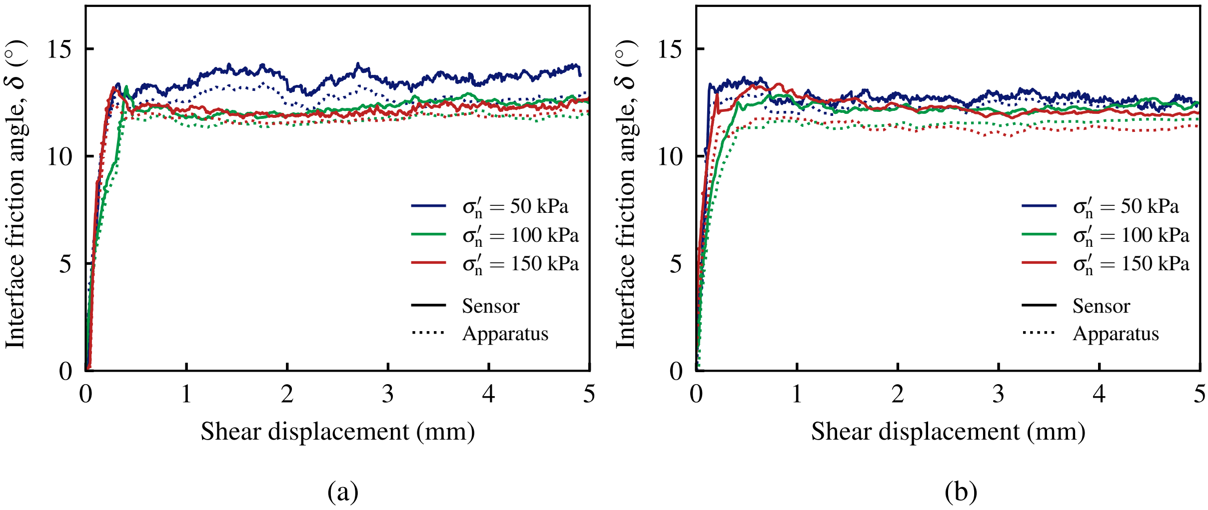

Figure 4.30 Comparison between the interface friction angle, δ, determined by the direct interface shear apparatus and the contact stress sensor: (a) x direction tests, (b) y direction tests

is observed in all cases, which may be attributable to frictional losses in the apparatus affecting the proving ring measurement. Figures 4.28a and 4.29a also plot the sensor shear stress outputs perpendicular to the direction of shear (τ_y and τ_x respectively). In all tests these remain close to zero, as expected. However, a small, approximately linear increase with shear displacement can be observed. This may be attributable to cross-talk, but is also likely influenced by slight misalignment of the sensor within the apparatus.

The three moment component outputs from the sensor during shearing parallel to the x axis are shown in Figure 4.28c. The magnitude of the M_x and M_z outputs are low in all tests, whilst the M_y component rapidly increases then linearly decreases with displacement. This behaviour is entirely expected from the loading. The initial rise is caused by the moment applied to the sensor by the loading yoke, as it experiences F_x reaction from the proving ring. The subsequent decrease in moment occurs as the normal stress application becomes offset from sensor centreline with continued shearing. Analogous behaviour can be observed during tests parallel to the y axis in Figure 4.29c. The reverse of the direction of M_x in Figure 4.29c compared to M_y in Figure 4.28c is due to the adopted sign convention.

Plots of the sand-aluminium interface friction angle, δ, are presented in Figure 4.30. Good agreement is observed between the values determined from the sensor outputs and the apparatus, especially considering these outputs are formed by dividing two signals. This gives confidence in using the sensor outputs for their intended purpose of measurement at a frictional soil-structure interface. The greatest deviation is seen with 50 kPa test in the x direction. This is likely due to the low magnitude of the forces involved in this test (only approximately 40 N of shear force), as some difference is also apparent in the δ plot determined from the apparatus proving ring.

4.5.3 Effective stress measurement

Further tests were performed to assess the sensor's ability to concurrently measure pore pressure and effective normal stress. This loading can be conveniently explored with the sensor placed in a modified triaxial apparatus, as shown in Figure 4.31. Applying shear force in additional to normal stress and pore pressure was not deemed practically feasible for this research.

The sensor body was fitted to the base pedestal and enclosed within the triaxial cell. Axial force, representing normal effective stress, is applied to the sensor face plate by the loading frame through the ram. The applied ram load is measured using a vertical proving ring. The triaxial cell is sealed and saturated with water. The optical fibre is passed out of the cell using the same sealing gland as present on the sensor housing. External pressure, equivalent to the loading on the sensor by fluid in the housing, is applied by pressurising the water in the cell using the

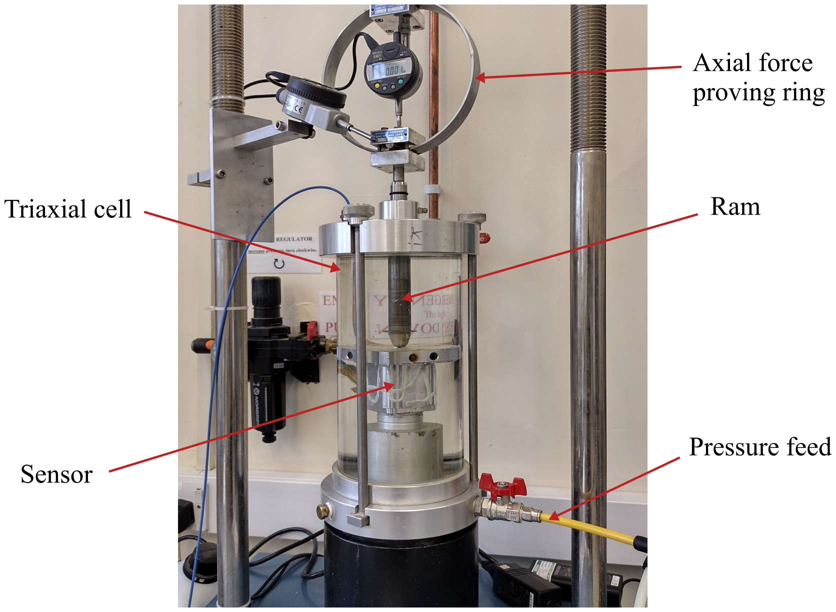

Figure 4.31 Modified triaxial testing apparatus applying effective normal stress and external fluid pressure to the sensor

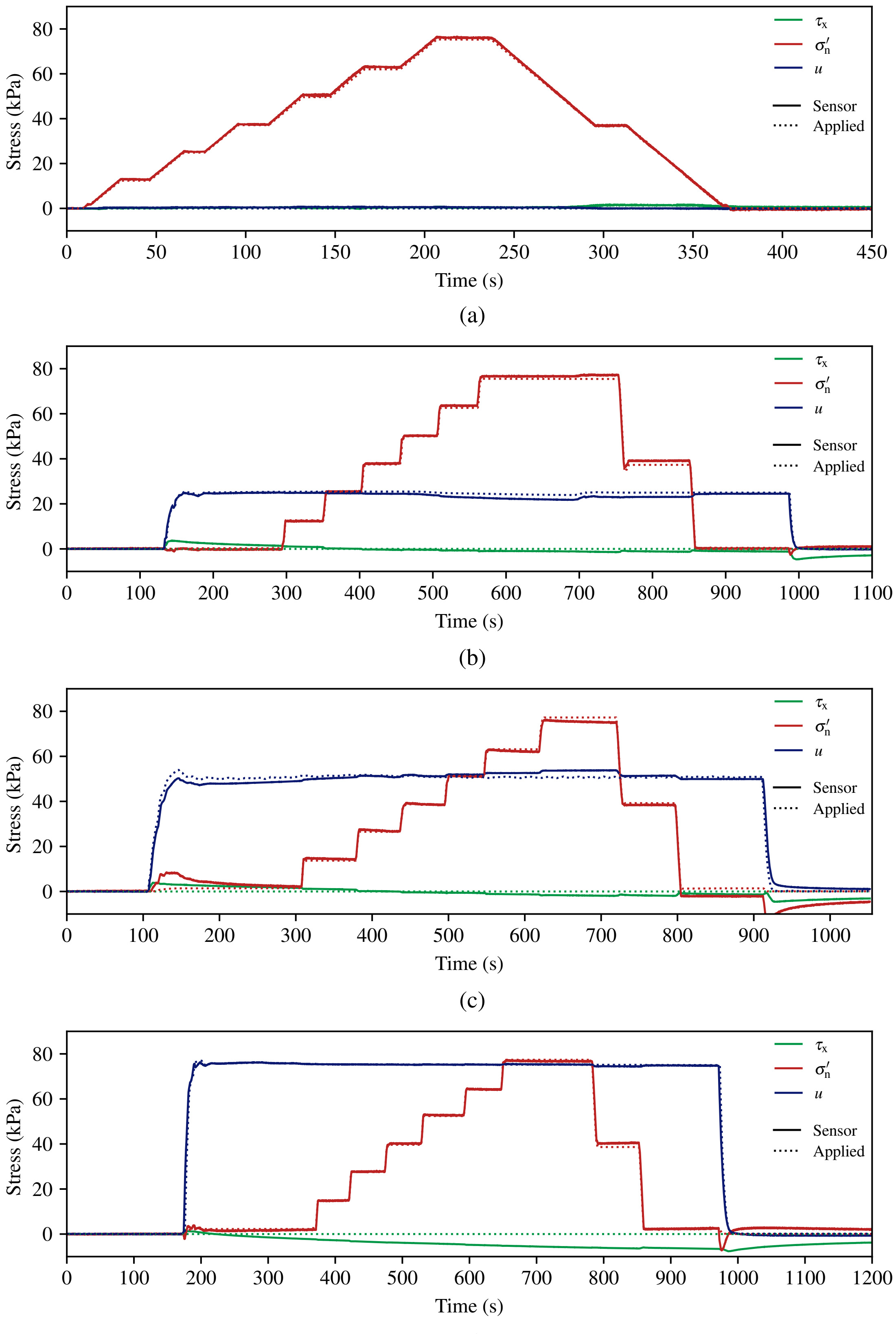

(a)

(b)

(c)

(d)

Figure 4.32 Sensor validation for effective normal stress measurement using triaxial apparatus: (a) $u = 0$ kPa, (b) $u = 25$ kPa, (c) $u = 50$ kPa, (d) $u = 75$ kPa. Outputs for σ'_n and u are processed using HLM laboratory compressed air supply. The applied pressure, was measured using a 1 bar PT (Omega PX 309-015GV) with a National Instruments (NI) NI-9237 strain bridge input module. Each test comprised applying a constant pressure using an air regulator, before applying increments of the ram load by manually displacing the loading frame. Four tests were undertaken at u = 0, 25, 50, 75 kPa; in each test, axial force increments of approximately 100 N up to 600 N were applied, before unloading back to zero and removing the pressure.

The raw sensor outputs in these tests demonstrated significant apparent cross-coupling between σ_n' and u. To account for this behaviour and improve sensor performance, a hierarchical linear model (HLM) has been adopted, in which a second 'layer' of least-squares linear regression is added after the primary sensor LR model. For these tests, the F_z and u outputs of the sensor LR model in Equation 4.1 are extracted to form the inputs to a subsequent LR model. This model is trained on additional calibration data, comprising combined F_z and u load cases. Although this is a simplification, it is reasonable as the influence of u was observed to be significantly less on the other measured output variables.

Figure 4.32 plots the sensor outputs from the four triaxial apparatus tests, with HLM processing applied. Excellent predictions of σ_n' are observed across the applied load range at all four applied u values, with a maximum deviation of 2.5% at u = 50 kPa when σ_n' = 75 kPa (Figure 4.32c). Very close agreement between the measured and applied σ_n' values also still occurs for the case of zero applied u (Figure 4.32a). Furthermore, good predictions of the constant applied u are observed throughout the σ_n' increments, with a maximum deviation of 5% from the applied value in the u = 50 kPa test. Improved agreement is seen in tests with applied u of 25 and 75 kPa (Figure 4.32b and 4.32d respectively). In the u = 50 and 75 kPa tests (Figures 4.32c and 4.32d respectively), time-dependent behaviour is observed during the rapid application and removal of the pressure. Although the response is seen to decay with time, there is also some non-zero return apparent. Similar behaviour is not observed under total stress loading, suggesting it is caused by either the high strain induced by the plate bending mechanism or the influence of the water on the sensor. Ongoing tests in the laboratory indicate that this is linked to viscoelastic behaviour of the glues adopted.

4.6 Summary

This chapter has documented the development of a new SSCS sensor using optical measurement in the form of FBGs. The framework outlined in Chapter 3 was applied to facilitate the sensor instrumentation and extended to explore a novel means of measuring effective normal stress. The design and prototyping of an exemplar sensor was described, before providing details of the manufacture and calibration procedures. Validation tests investigating the sensor performance have also been presented. The following points summarise the key outcomes:

a) The new sensor design provides multi-axis contact stress measurement, including normal stress and bi-directional interface shear stresses. This is well suited to complex frictional interfaces, such as seen with caisson sinking and pipejacked tunnelling. The validation tests performed give confidence in the sensor's ability to provide accurate contact stress measurements in a typical soil-interface shear application.

b) The new sensor design harnesses many of the inherent benefits of FBGs. These include the wavelength-encoded optical communication, which gives immunity of the system to EMI and damage through water ingress, and the use a single lightweight cable and connector, which significantly simplifies installation on site. These will be particularly beneficial in field monitoring applications, helping to address the critical points of failure in previous instrumentation case studies.

c) Measurement of effective normal stress has also been explored with the new sensor, through the use of a novel sensor structure and operating principle. The ability of the sensor to respond to pore pressure loading was demonstrated by numerical simulation and physical prototype calibration. Validation tests performed in the triaxial apparatus provided a useful proof-of-concept of this measurement. Further work is required to optimise the model and calibration procedures, as well as practical considerations for applying the approach.

d) The instrumentation design process used synthetic data provided by extracting and interpolating FBG strains from a large number of 3D FEA calculations. This demonstrates the ability to extend the 'virtual twin' sensor design approach introduced in Chapter 3 to a wider range of more complex sensor structures.

e) Physical prototyping of the sensor highlighted the important limitation of FBG birefringence under pressure loading. This is likely to be a common issue faced in developing packaged sensors with FBGs, particularly when seeking miniaturisation. It is recommended to estimate the distributions of strain that FBGs may be exposed to, rather than just centre point values. In this study, this approach was used to inform careful structural and instrumentation design to overcome the issue.

f) The use of novel 3D printed 'pivots' enabled quick and repeatable implementation of the desired FBG layout. This procedure mitigates many challenges faced with instrumenting a small sensor structure with continuous optical fibre and requires significantly less skill and time compared to conventional electrical strain gauging.

Despite the potential benefits of the novel effective stress operating principle, further work is required to address challenges in its use. However, the total stress configuration has been demonstrated to offer a robust, high quality and easily implementable measurement solution. The total stress sensors are a good candidate for direct replacement of existing electrical-based contact stress sensors in construction applications and are utilised in laboratory testing of caisson-soil interface friction in Chapter 5.

Chapter 5

Laboratory testing of caisson-soil friction in sand

5.1 Introduction

This chapter presents a series of laboratory-scale experiments considering the development of friction on open caisson shafts during sinking. Although previous field monitoring efforts have provided some important insights into full-scale behaviour, there are typically additional complexities and unavoidable site-specific influencing factors, such as the presence of ancillary structures. Furthermore, observations are limited to the particular site conditions and there is no opportunity for parametric analysis. Laboratory testing enables detailed insight and assessment of frictional mechanisms, as the conditions at the soil-structure interface can be carefully controlled and varied. The testing in this chapter focuses on dense sand, in which difficulties concerning high friction and ineffective lubrication have been highlighted in previous case studies (Abdrabbo and Gaaver, 2012; Royston *et al.*, 2022a).

This chapter first describes the development of the new experimental apparatus used for this testing, including key details to closely replicate the SLSI around an open caisson shaft. The experimental methods are then outlined, including the sand properties, sample preparation process and test procedures. A series of experimental results are then presented, considering the influence of over-cut creation and interface lubrication. Detailed measurements of the interface stresses are obtained using the sensors described in Chapter 4, as well as visual observations of the sand and lubricant behaviours.

5.2 Testing apparatus

5.2.1 Overview

The experimental testing presented in this chapter is performed using a novel large displacement interface shear apparatus. This was developed collaboratively with B. M. Phillips, who deployed the apparatus in a horizontal configuration for analysis of pipejacked tunnelling (Phillips, 2023). In this research, the apparatus is used in a vertical configuration to simulate SLSI on the external surface of large diameter open caisson shafts during sinking. For completeness, an overview of the main features of the apparatus for caisson testing is provided in this thesis; further description of the broader design decisions and details are provided in Phillips (2023).

Figure 5.1 shows a simplified section through the testing apparatus, comprising a series of interconnected ‘test pieces’ that are passed vertically though a tank containing a prepared soil sample. The interface between the test pieces and the soil sample simulates the interface between a ‘strip’ of caisson wall and the surrounding soil during shaft sinking. The test pieces are able to deliver lubricant at the interface via an injection system and each test piece is instrumented

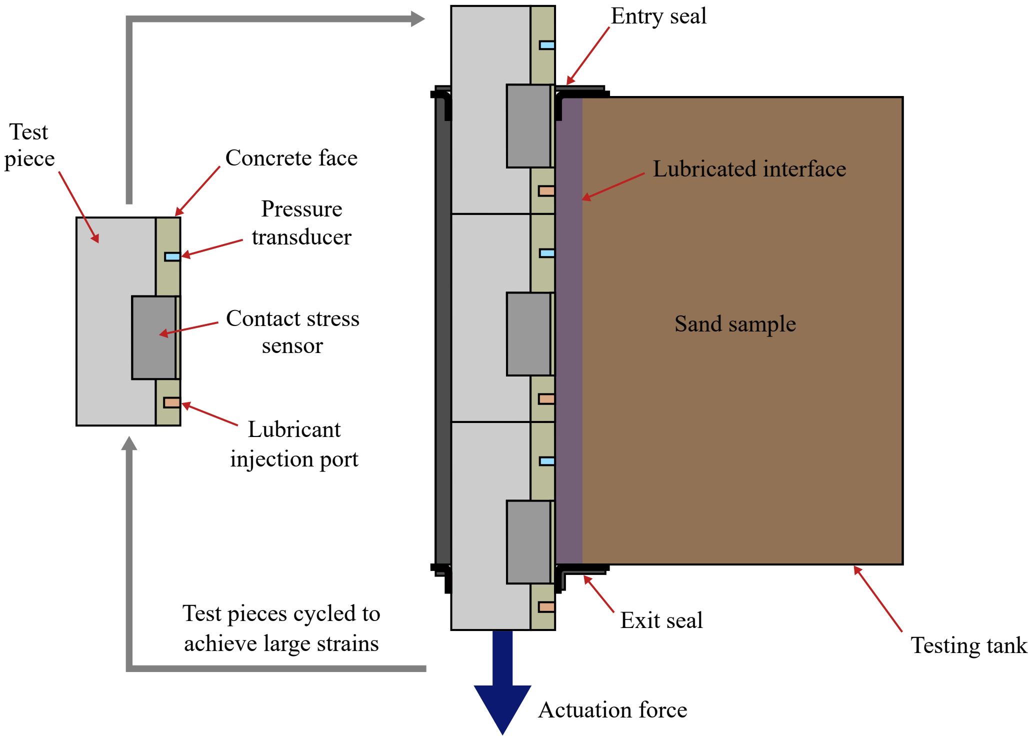

Figure 5.1 Simplified schematic illustration of a section through the testing apparatus

to measure local interface stresses and fluid pressures. The test pieces pass into and out of the testing tank through entry and exit seals on the top and bottom sides of the tank respectively (see Figure 5.1). As a test piece exits the tank, it is disconnected and recycled to the top of the string. This process is repeated, allowing large interface shearing behaviour to be achieved.

Although strictly an axisymmetric problem, the caisson-soil interface is tacitly approximated as plane-strain for these analyses. This allows isolation of the interface mechanics and simplifies the complex lubricant delivery process. This approach also allows larger scale testing than would be possible with an axisymmetric setup within the laboratory constraints. This interface condition is more closely representative of large diameter caissons, which are more likely to encounter high frictional resistance during sinking due to the larger external surface area. Royston (2018) demonstrated that the plane-strain assumption is reasonable for the large diameters typically used in practice.

5.2.2 Testing tank

The testing tank is a cuboid constructed using 10 mm thick steel plate (Figure 5.2a). This is assembled by bolting the individual panels to steel PFC section bracing members, which act to minimise lateral deflections of the tank walls during testing. The tank is raised approximately 1 m above the floor on a support frame comprising eight steel SHS columns. The tank is sealed using 1.5 mm thick neoprene gaskets, which are compressed by the bolted connections. On one side of the tank, two 30 mm thick perspex windows are installed in openings in the steel wall panels, to allow viewing of the test piece-soil interface during testing (see Figure 5.2b).

The internal dimensions of the tank are given in Figure 5.2a and the overall height of the testing apparatus is 2.85 m. The tank length is limited to 1000 mm due to height constraints below the laboratory gantry crane. Sufficient clearance is needed above the tank to load and connect the test pieces prior to actuation, and below the tank to remove the test pieces as they leave the exit seal. The tank was designed to be square in profile and a relatively large width of 500 mm was selected to ensure any boundary effects from the tank walls are limited over the central region where local interface stress measurements are made. With the test pieces in

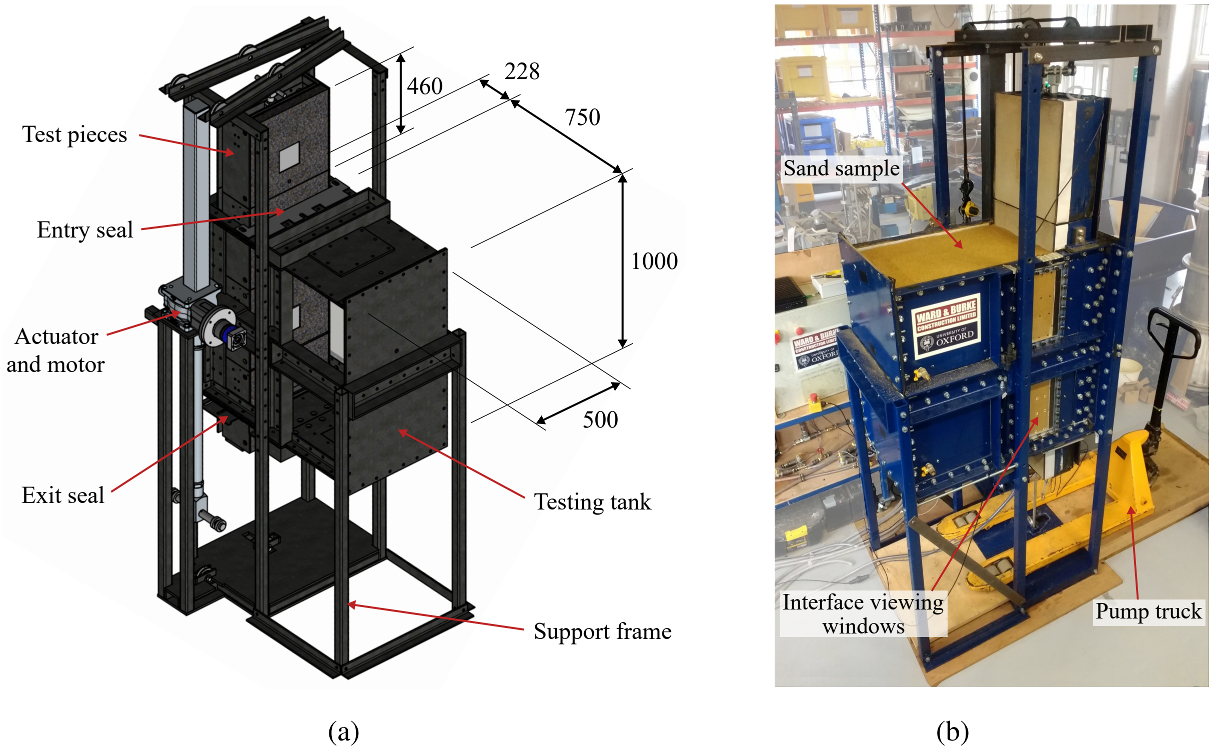

Figure 5.2 Testing apparatus: (a) Isometric 3D model view (tank side panels and ropes not shown), (b) Photo of apparatus pre-testing with a prepared sand sample. Measurements are for test piece and internal dimensions of testing tank (in mm)

place, the tank is able to accommodate a maximum soil sample volume of 1000×750×500 mm. Phillips (2023) performed column apparatus tests with the same sand and lubricant used in this chapter, to determine that the 750 mm soil sample depth (normal to the interface) is sufficient to ensure no boundary effects from the tank on the lubricant penetration.

At the entry and exit openings in the testing tank, bespoke seals can be installed around the test pieces. These limit loss of interface lubricant from the tank and to enable lubricant pressurisation, whilst allowing the test pieces to pass into and out of the tank. Sections through the tank seal assemblies are shown in Figure 5.3. The primary sealing component in both assemblies is a 10 mm thick neoprene sheet with openings cut-out for the test pieces to pass through. The openings are 15 mm smaller than the test dimensions to ensure contact on all surfaces of the test pieces and the corners are cut with smooth radii to prevent tearing. The current seal arrangement is likely to be insufficient for testing saturated materials, which was beyond the scope of this research.

The neoprene seal is clamped onto the test pieces by adjustable ‘fish plates’. These are

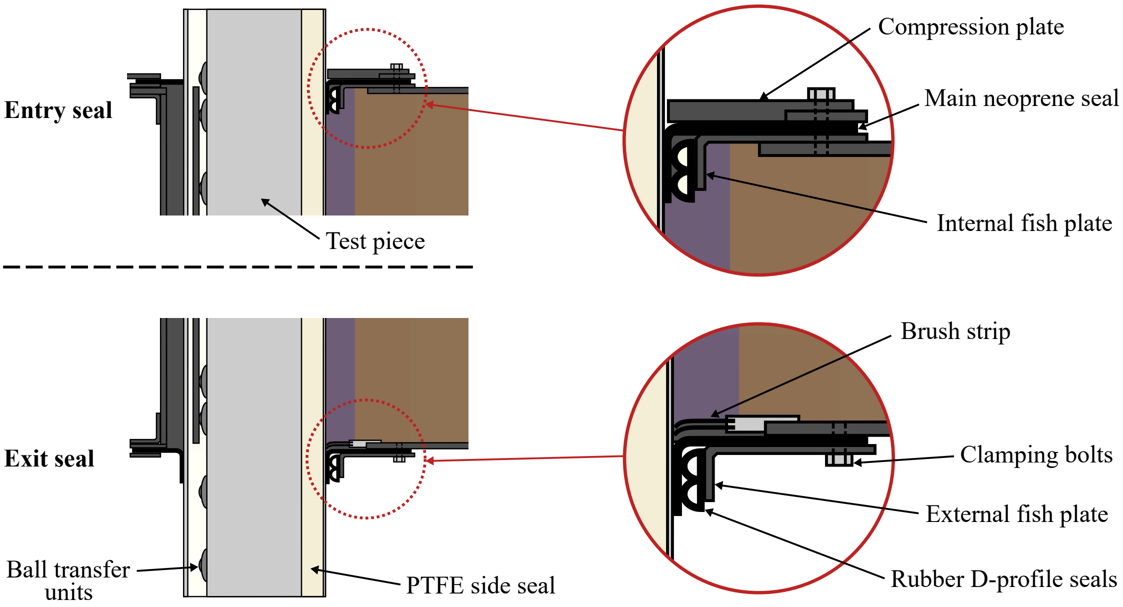

Figure 5.3 Sections through the entry and exit seal assemblies of the testing tank, including details of the salient components

lengths of steel 90° angle section with slotted bolt holes, which are tightened down to compress the seal prior to testing. To distribute the clamping pressure over the surface, two 'D-profile' rubber seal strips are bonded to the underside of each fish plate. At the entry seal a fish plate is present on the inside the tank against the test piece face surface; at the exit seal there are fish plates on the outside of the tank against the test piece face and both side surfaces of the test piece. To prevent the neoprene from inverting at the entry seal under the internal lubricant pressure, an external compression plate is also fitted. Furthermore, two 50 mm deep stiff brush strips are installed inside the exit seal, to limit the amount of sand reaching the neoprene seal.

Additional sealing is required at the sliding interface between the sides of the test pieces and the tank walls. A 50 mm wide strip of 0.5 mm thick PTFE is bonded to either side of the testing tank, on top of a layer of 3.0 mm thick neoprene foam. These strips are positioned flush with the test piece surfaces and run continuously along the full height of the tank. Matching strips of PTFE and neoprene are also attached to the sides of the test pieces. The PTFE-PTFE contact creates a low friction sliding interface, whilst the neoprene layers compress the two PTFE strips together, creating a seal along the length of the tank.

To minimise friction between the soil sample and tank boundaries, a 0.5 mm thick PTFE lining is bonded to the sides and base of the testing tank. Preliminary testing was performed on a more advanced lining design as documented by Brachman *et al.* (2001), comprising two layers of PTFE lubricated with grease. Whilst this configuration demonstrated very low friction in interface direct shear tests, it was found to be incompatible with interface lubrication, as the pressurised slurry tended to flow into the lubricated layer. A single layer of PTFE bonded to the tank walls was adopted for this testing as a compromise.

All test results presented in this chapter are conducted in a simplified ‘open-tank’ configuration, with the tank lid and entry seal removed, as shown in Figure 5.2b. This configuration simulates low-stress conditions, which are applicable to sinking relatively close to ground level. An added benefit is that it significantly reduces the complexity of the experimental setup.

5.2.3 Actuation system

The test pieces are pulled downwards through the testing tank by a 100 kN linear screw system (Zimm ZE100-SL-TR), with a 9 mm lead and an integrated 36:1 gear ratio. This is driven by an 80 mm 750 W servo motor (Applied Motion J0750-302-5-000) coupled with a 20:1 ratio planetary gearhead (Wittenstein NP025S-MF2-20-1). The whole system is driven by an Applied Motion SV2B5-Q-DE digital servo drive. The actuation system and the support frame for the testing apparatus was designed for a maximum required actuation force of 50 kN, with a 900 mm effective stroke length and a maximum actuation rate of 50 mm/min (see Phillips, 2023).

All experimental tests in this chapter were performed at a rate of 25 mm/min. This was informed by the field monitoring of Royston *et al.* (2022a) during construction of a 32 m ID, 20 m deep caisson in dense sand. A total of 19 distinct sinking movements were observed by the level detection system, as shown in Figure 5.4. An approximate sinking rate was determined by identifying a start and end point for each movement and applying a linear fit. An average sinking rate over all movements greater than 250 mm was determined to be 23.5 mm/min.

The actuation system operates in tension by pulling the string of test pieces downwards through the tank. The actuation force is applied to the test pieces using a 12 mm diameter high-modulus polyethylene rope strop, through two 96 mm diameter aluminium pulleys mounted on roller bearings in the stiff base plate of the support frame (Figure 5.5a). This configuration

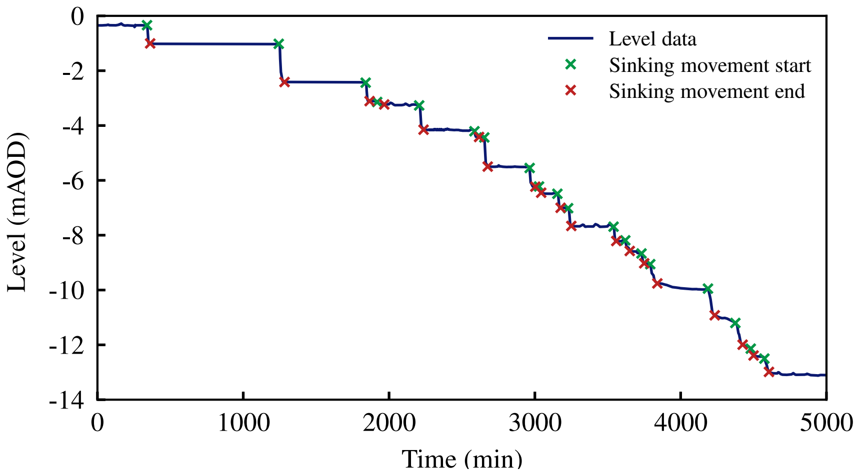

Figure 5.4 Field monitoring data of Royston *et al.* (2022a) showing caisson level during construction, with sinking movements identified for determination of average sinking rate

allows the actuator to be mounted alongside the tank (as in Figure 5.1), thereby achieving a significant reduction in the overall height of the rig. The ‘actuation’ rope attaches to the leading test piece through a 5 kN S-type tension/compression load cell (Force Logic FSB-5T), referred to as the lead axial load cell, which provides a measurement of the total applied actuation force.

Despite the benefits of the actuator configuration, there is a risk that the string of test pieces could fall through the tank under their self-weight (approximately 500 kg) if there is insufficient friction from the interface and seals. To provide safe operation, a novel ‘continuous-loop’ actuation procedure was developed, as illustrated in Figure 5.5. The actuator is also connected directly to the trailing test piece by a ‘counterbalance’ rope system. A set of two ropes are used, to clear the motor housing (Figure 5.5b), which pass through a series of pulleys mounted at the top of the support frame. The main actuation rope and the counterbalance ropes therefore form a continuous loop with the test pieces. A pair of 0.5 tonne ratchet lever hoists are included within the counterbalance ropes to pre-tension the system, such that continuous support is provided to the test pieces and any sudden slipping is prevented. As the actuator retracts, the jacking rope pulls the test pieces downwards, whilst the counterbalance ropes move upwards by an equal amount to allow the advance to occur. The counterbalance system is connected to the uppermost test piece by a 1 kN S-type tension/compression load cell (Applied Measurements DBBSM-1000kg), referred to as the counterbalance axial load cell. This allows the actuation force to be determined by subtraction from the lead axial load cell.

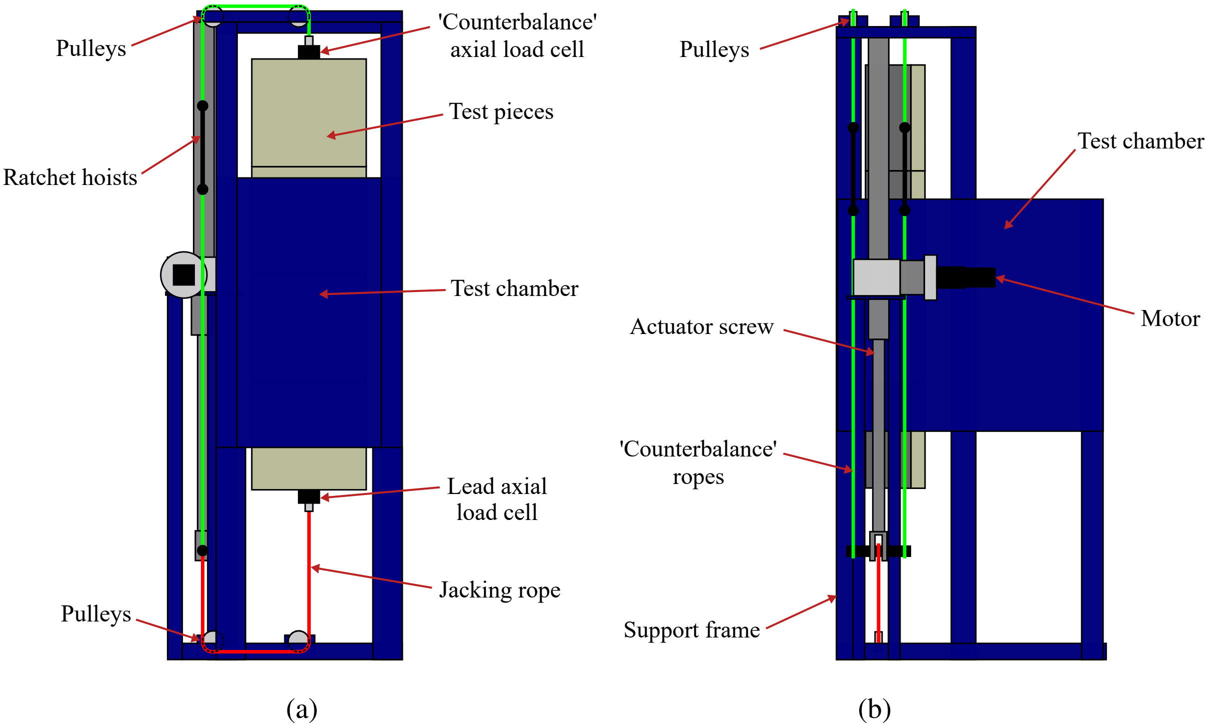

Figure 5.5 Schematic of the test apparatus actuation system showing the test piece counterbalance system: (a) front view, (b) side view

Each actuator movement consists of the length of one test piece (approximately 460 mm). After each advance, the actuation and counterbalance systems are disengaged and the weight of the test pieces is temporarily supported by a set of fixed ‘stop blocks’. The test piece exiting the tank is supported by a hydraulic lifter whilst it is disconnected (see Figure 5.2). The counterbalance system is retracted and moved to allow the free test piece to be loaded back at the top of the rig by the gantry crane. Once the test pieces and the actuation systems have been reconnected, the stop blocks are removed and the next advance is performed. This process is repeated to achieve large shearing displacement.

5.2.4 Instrumented caisson test pieces

5.2.4.1 Overview

The caisson wall is represented by a string of four interconnecting test pieces, labelled TP1–4. An example test piece is shown in Figure 5.6a. These comprise 460 mm tall × 494 mm wide × 228 mm deep boxes welded from 10 mm thick steel plate. When joined together, the steel

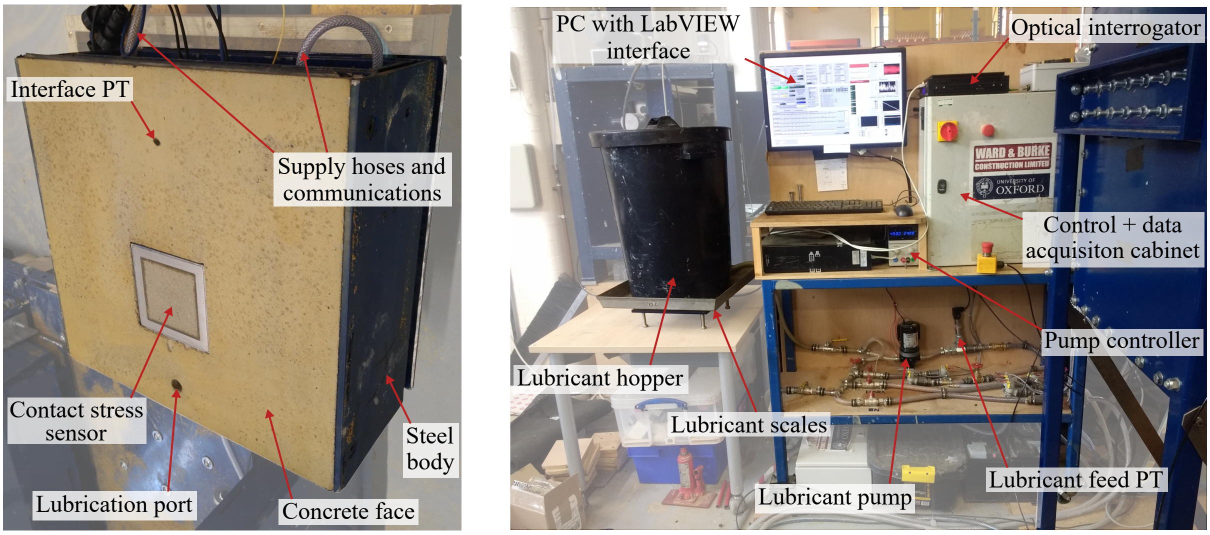

(a)

(b)

Figure 5.6 Photographs of the testing apparatus: (a) a ‘caisson’ test piece prior to installation, (b) the main control, data acquisition and lubrication system components

bodies form a continuous internal box-shaped void. This houses all of the control, sensor and lubrication systems for the test pieces, as well as the inter-test piece physical connection. To guide and align the test pieces vertically, eight M30 ball-transfer units are fitted to the back of each test piece, which ride on 45 mm wide steel guide rails welded to the tank side walls, as shown in Figure 5.3.

The test pieces are joined using an internal connection structure illustrated in Figure 5.7. The connection comprises two 20 mm diameter steel rods, which thread into an internal wall in the lower test piece. These rods are attached to a rectangular joining bar, which is also bolted to a 5 kN S-type tension/compression load cell (Force Logic FSB-5T). The upper test piece bolts directly down into this load cell, pulling the two test pieces together. Three of these connection structures are required to join the four test pieces together. When fully assembled, the test pieces are isolated from one another by the S-type load cells at either end. These are referred to as the internal axial load cells and they allow the net axial force on each test piece to be determined. The top and bottom edges of the test pieces mate with a spigot and socket joint. A neoprene gasket is inserted into the socket, which is compressed by the spigot as the central connection structure is pre-tensioned. This joint helps with aligning the test pieces and acts to seal the central void from fluid entry.

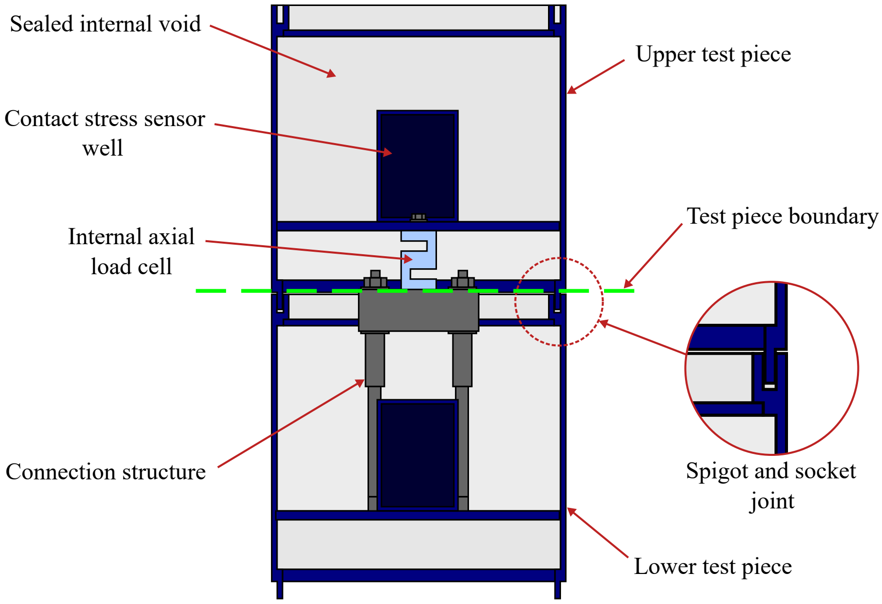

Figure 5.7 Schematic illustration of a section through two test pieces, showing the internal connection. The lubrication system and communication cables are not shown, for clarity

5.2.4.2 Concrete interface

To faithfully simulate the exterior surface of a caisson in practice, the faces of the test pieces were created out of concrete. A 50 mm thick face was cast in a recess within the front of the steel test pieces, using a greased MDF mould with a mix of 0.55:2.5:1 water, sand (Jewsons fine aggregate) and cement (Hanson Multicem). Casting the faces in-situ ensures the fit of the concrete and achieves a flush surface finish across the entire test piece face. The concrete is held in place by four M10 countersunk bolts in the sides of the test piece, allowing the face to be removed for installation of interface instrumentation. A sheet of wire mesh was cast into the face, to prevent cracking during removal and re-installation.

To assess the suitability of the interface material, the surface roughness of concrete samples was assessed using an Alicona G4 optical profilometer. This produced representative 3D images of the concrete surface (see Figure 5.8), as well as performing surface profile assessments. The mould material, casting method and concrete mix for the samples were identical to that used for the test piece faces. A total of 60 surface profiles were taken over four separate samples, which were assessed to give a mean roughness, R_a, of 18.9 µm, with a standard deviation of 4.4 µm. This is in good agreement with R_a values documented by Staheli *et al.* (2006) for wet-cast

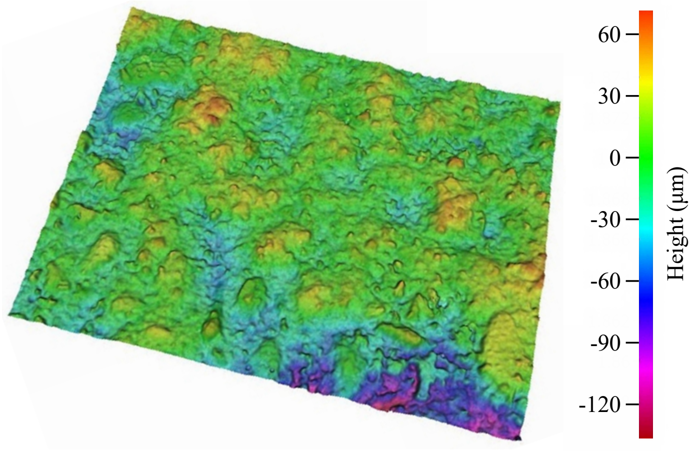

Figure 5.8 Example of the optical profilometer surface roughness assessment on a sample of the test piece concrete interface material

concrete jacking pipes (24.8 µm) and interface testing samples used by Reilly and Orr (2017) (22.8 µm). This was deemed acceptable for consideration of caisson friction, as the RC wall casting methods used in industry have similarities to wet-cast jacking pipes and caisson-specific data are not available in the literature.

Direct interface shear tests were performed to assess the sand-concrete interface friction angle, δ. The lower half of a conventional direct shear box was replaced with a 90×90 mm sample of concrete. Samples of the same sand used in this study (see Section 5.3.1) were prepared in the original shear box upper half on top of the concrete. Tests were performed at two normal stress levels (σ'_n = 50 and 100 kPa) on sand samples prepared at two relative densities, D_R: Dense (D_R = 0.86 ± 3%), and Medium (D_R = 0.56 ± 8%). Concrete pipes have been observed in industry to have increased surface roughness after jacking, due to abrasion from the surrounding soil (Phillips, 2023). A similar effect is expected for caisson shafts, although direct observation or measurement of the surface is not possible after sinking. To assess the influence of this surface degradation, tests were performed on two types of concrete samples: a) 'as-cast' (Figure 5.9a) and b) after six prior 6 mm direct interface shear tests with dense sand samples at 100 kPa applied normal stress (Figure 5.9b). Interface friction angles at critical state of 31.1° and 33.9° were calculated for the as-cast and degraded surfaces respectively. Compared to the measured critical state friction angle for the sand, ϕ'_{cs}, of 33.2° (see Section 5.3.1), these values correspond to strength reduction factors of 0.94 and 1.02 respectively. Due to the repeated

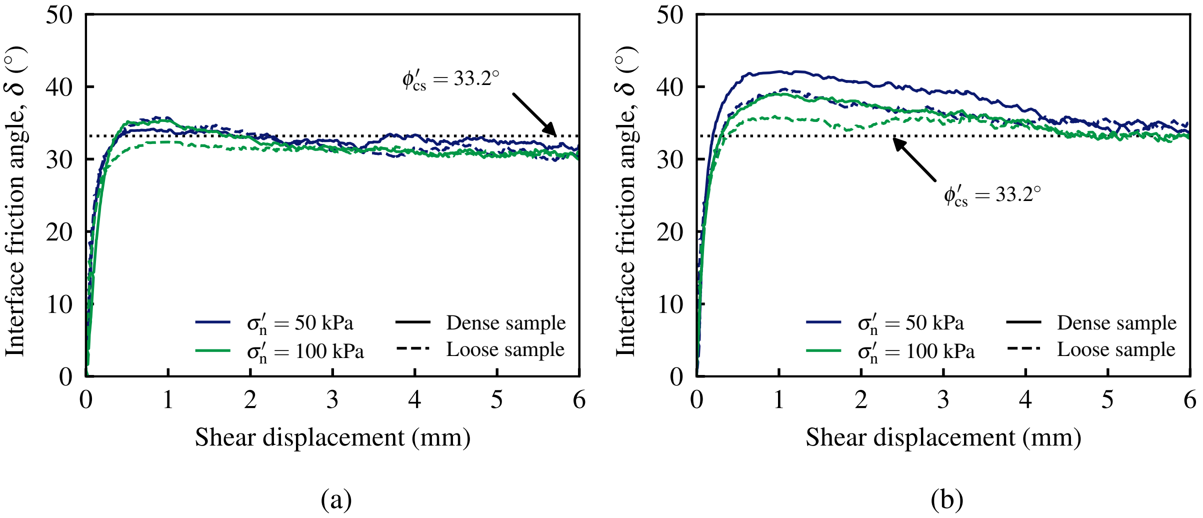

Figure 5.9 Direct interface shear test results of LB 14/25 sand on concrete samples: (a) ‘as-cast’ surface, (b) concrete surface after repeated shearing

cycling of the test pieces through the testing apparatus, it is expected that the concrete interface in practice will resemble the degraded sample and is therefore taken to be fully rough.

5.2.4.3 Interface stress measurement

Each test piece was fitted with a contact stress sensor at the centre of the concrete face, to measure the local interface stresses. Two test pieces (TP1 and TP3) were fitted with the optical SSCS sensors described in Chapter 4, which were developed bespoke for this apparatus. These sensors provide measurement of total normal stress, vertical shear stress, transverse shear stress and three orthogonal moment components. The sensors were designed for a maximum expected loading in the apparatus of 100 kPa normal stress and 60 kPa shear stress. The other two test pieces (TP2 and TP4) were fitted with SSCS sensors created from commercial three-axis load cells (Interface 3A120-2KN). These provide measurements of the three orthogonal shear stress components (total normal, vertical shear, transverse shear). This gives an opportunity to compare and validate the new optical sensors.

The contact stress sensors bolt into a ‘well’ formed in the centre of the steel test piece structures (Figure 5.7). A 125 × 125 mm opening cast into the concrete allows the face of the sensors to sit flush with the concrete surface. All four of the sensors are fitted with an 8 mm thick concrete face plate, which is cast using the same procedure as the test piece surfaces (see Section 4.4.1). This ensures a fully uniform sensor face that closely matches the surface roughness of the overall structure interface. The communications fibres and cables sit within the internal void of the test pieces and are sufficiently long to pass down through the entire apparatus. This allows the exiting test piece to be disconnected, whilst eliminating the need for electrical and optical connections to be made within the test pieces.

5.2.5 Lubrication system

A bespoke system was implemented to deliver lubricant to the soil-structure interface from within the test pieces. This was designed to replicate the lubrication system typically used for caisson sinking in industry. Each test piece features a 1/2” port cast into the centre of concrete surface, 50 mm above the leading edge (see Figure 5.6a). To control lubricant delivery from individual test pieces, each port comprises a 1/2” pneumatically actuated ball valve operated by the laboratory compressed air supply. The airflow to each valve is controlled by a NAMUR solenoid valve, which is activated via a USB-controlled relay in the control cabinet. A photo of the set up is shown in Figure 5.6b and an overview of the system is given in Figure 5.10.

The lubricant is pre-mixed (as detailed in Section 5.3.3) and stored in a central hopper. A set of ‘scales’ beneath the hopper was created using three Applied Measurements DBBSMM 25 kg miniature S-beam load cells, to continuously measure the mass of the hopper. This is used to determine the flow rate of lubricant into the testing apparatus. The lubricant is delivered to the test pieces by a high-pressure diaphragm pump (Xylem Flojet Triplex), providing up to 8 bar outlet pressure at a maximum flow rate of 5.4 l/min. A programmable DC power supply capable of delivering 0–5 A at 0–30 V (Tenma 72-2710) was used to power the pump. Both the current and voltage of the power supplied to the pump are programmable from PC via a serial interface. To measure the pressure of the pumped lubricant, a 0–7 bar PT (Wika Model A-10) is installed in the supply downstream of the pump (see Figure 5.6b). A single lubricant and compressed air supply hose feeds all four test pieces, which are joined by interconnecting hoses. These use quick-release non-return valves, to allow disconnection during test piece cycling.

All lubricated tests in this chapter were performed using volume-controlled delivery (i.e.

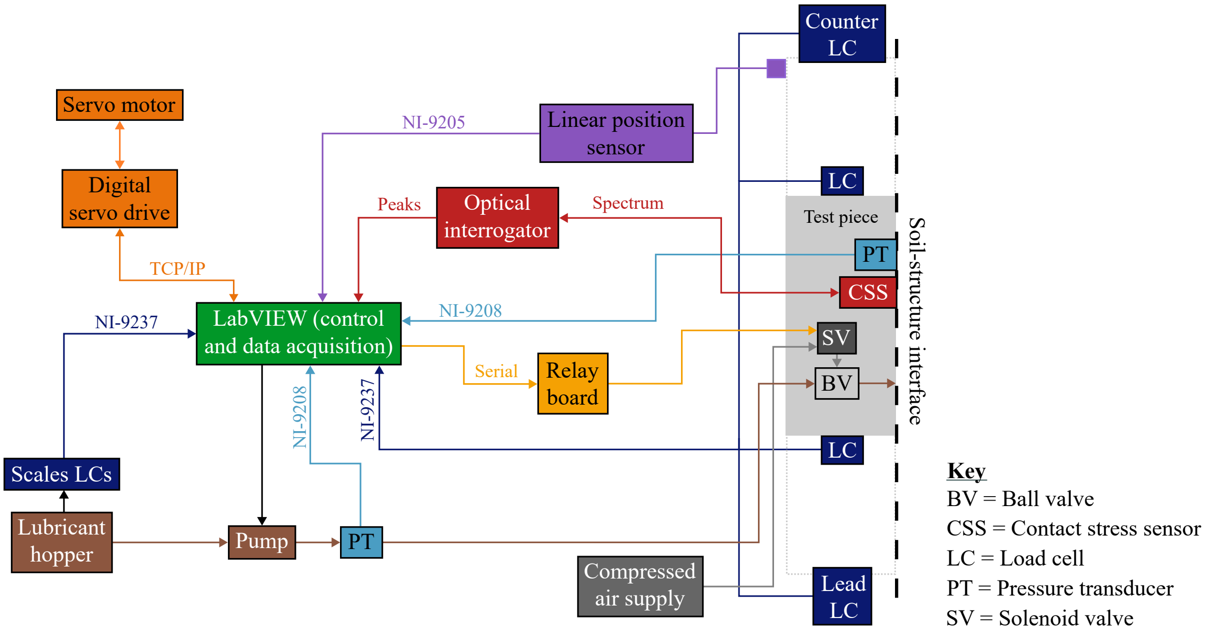

Figure 5.10 Overview of control, data acquisition and lubrication systems for the testing apparatus, showing the key components and their connectivity. Only one of the four test pieces is shown, for clarity

constant lubricant injection rate). This reflects the approach typically adopted in industry (e.g. Royston, 2018). During a test, the desired port and a target lubricant flow rate are specified. A PID control loop is used to set the pump voltage, based on the error between the target flow rate and the value measured from the hopper scales. Testing documented by Phillips (2023) determined the system capable of supplying between 400 and 3000 g/min of 6% bentonite slurry to within ± 3% of the target value. To provide a measurement of the lubricant pressure at the soil-structure interface, another 0–7 bar PT (Wika Model A-10) is installed into the concrete surface of each test piece (see Figure 5.6a). This is fitted with a filter element to prevent sand entry into the sensor, which is pre-saturated with glycerine prior to testing.

5.2.6 Control and data acquisition

The control of the actuation and lubrication systems and all data acquisition for the testing apparatus are managed by a Windows PC through an NI LabVIEW interface. An overview of key components and their connectivity is given in Figure 5.10 and a photo of the setup is shown in Figure 5.6b. The control system operates at a typical frequency of 5 Hz, with a data acquisition rate of 1 Hz.

A summary of all sensors used in the testing apparatus is provided in Table 5.1. Data from all electrical sensors is acquired using an 8 slot NI CompactDAQ chassis (cDAQ-9189) with appropriate modules. All load cells are full Wheatstone bridge mV/V type and are connected to NI-9237 strain bridge input modules. Each bridge is excited by a constant 10 V supplied by the module. All PTs used in this testing apparatus are 4–20 mA output. They are excited by a constant 24 V DC power supply (Chinfa AMR2-24) and are logged using an NI-9208 current input modules. The displacement of the test pieces during the advances was measured accurately using an 800 mm long Temposonics® G-Series non-contact linear position sensor, connected to an NI-9205 16-Bit voltage input module. The sensor waveguide is rigidly mounted to the apparatus support frame; the position cart is attached to the uppermost test piece via an aluminium arm, which is removed and reconnected after each advance.

Table 5.1 Summary of sensors used in the laboratory testing apparatus

Sensor name	**Brand/model**	**Data acquisition**	**Measurement purpose**
Optical contact stress sensor (x2)	Bespoke (see Chapter 4)	Micron Optics HYPERION si255 optical interrogator	Local interface stresses on test piece surface
Electrical contact stress sensor (x2)	Interface 3A120-2KN	NI-9237 Bridge DAQ module	Local interface stresses on test piece surface
Lead axial load cell (x1)	Force Logic FSB-5T	NI-9237 Bridge DAQ module	Global actuation force applied to front of test piece string
Internal axial load cells (x3)	Force Logic FSB-5T	NI-9237 Bridge DAQ module	Determination of net axial force on each test piece
Counterbalance axial load cell (x1)	Applied Measurements DBBSM-1000kg	NI-9237 Bridge DAQ module	Global counterbalance force applied to test piece string
Test piece displacement sensor	Temposonic G-Series	NI-9205 ±10 V, 16-Bit Voltage Input DAQ module	Displacement and displacement rate of test pieces
Lubricant scale load cells (x3)	Applied Measurements DBBSMM-25kg	NI-9237 Bridge DAQ module	Lubricant mass/flow rate
Lubricant supply PT (x1)	Wika Model A-10 (0-7 bar)	NI-9208 ±20 mA Current Input DAQ module	Pressure of pumped lubricant supply
Interface PT (x4)	Wika Model A-10 (0-7 bar)	NI-9208 ±20 mA Current Input DAQ module	Fluid pressure at soil-test piece interface

5.3 Experimental procedures

5.3.1 Sand properties

Leighton Buzzard (LB) sand is used for all tests in this chapter, provided by Aggregate Industries from Garside Sands. Specifically the 14/25 grading is used, which is a coarse, uniformly graded silica sand that has been used extensively in physical modelling in the geotechnical group at the University of Oxford (e.g. LeBlanc *et al.*, 2010; Richards *et al.*, 2020; Schnaid, 1990). Although the index and mechanical properties of LB 14/25 sand are well-documented in the literature, further characterisation tests were undertaken as newly supplied sand was used in this study. A summary of the measured LB 14/25 sand properties is given in Table 5.2.

Figure 5.11 shows particle size distribution (PSD) tests performed on the supplied sand, using the dry sieving method described in BS 1377-2:1990 (BSI, 1996). Tests were performed using sieve apertures defined in BS 1377-2:1990 (BSI, 1996) and BS ISO 3310-1:2016 (BSI, 2016). The effective particle sizes determined from the BS ISO 3310-1:2016 test are given in Table 5.2, where d_{10}, d_{30}, d_{50}, d_{60} are the effective particle sizes at which 10, 30, 50 and 60% of the sample are finer than respectively. The low coefficient of uniformity ($C_\mathrm{U} = d_{60}/d_{10}$) and coefficient of curvature ($C_\mathrm{Z} = d_{30}^2/d_{60}d_{10}$) values in Table 5.2 indicate that the sand is poorly graded, consisting of relatively uniformly sized particles. The values agree closely with tests by

Table 5.2 LB 14/25 sand properties

Property	**Value**
Particle sizes, d_{10}, d_{30}, d_{50}, d_{60} (mm)	0.65, 0.77, 0.89, 0.95
Coefficient of uniformity, C_U	1.44
Coefficient of curvature, C_Z	0.96
Minimum dry unit weight, γ'_min (kN/m^3)	14.22
Maximum dry unit weight, γ'_max (kN/m^3)	17.00
Maximum void ratio, e_max	0.834
Minimum void ratio, e_min	0.566
Particle specific gravity, G_s	2.66
Critical state angle of friction, ϕ'_cs (°)	33.2

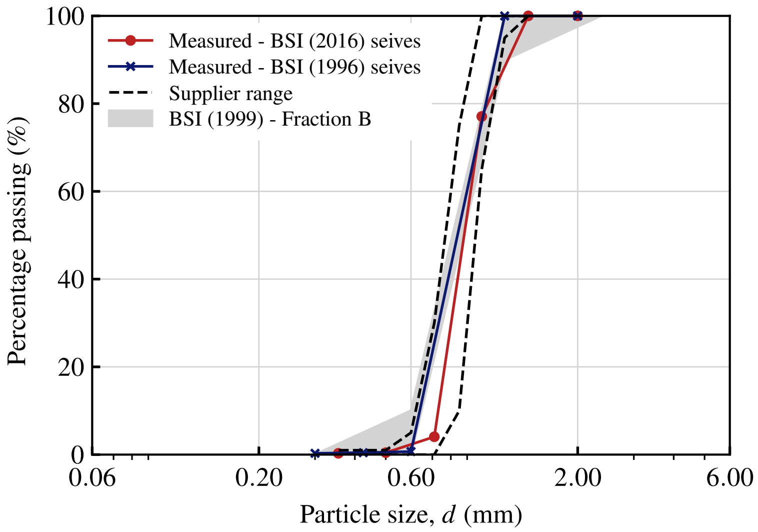

Figure 5.11 Measured PSD curves for the LB 14/25 sand used in this thesis/study

White (2020) and also more broadly with values documented in the literature for 14/25 sand.

The density of a sample of granular material is typically characterised in terms of its relative density, D_R, which can be defined as:

$$D_\mathrm{R} = \left(\frac{\gamma'_\mathrm{max}}{\gamma'}\right)\frac{\gamma' - \gamma'_\mathrm{min}}{\gamma'_\mathrm{max} - \gamma'_\mathrm{min}} \tag{5.1}$$

where γ' is the sample dry unit weight and γ'_min and γ'_max are the minimum and maximum dry unit weight for the soil respectively. The limiting unit weights in Table 5.2 for the LB 14/25 sand in this study were measured using the methods described in BS 1377-4: 1990 (BSI, 2002). The measured values agree closely with values documented by Lunne *et al.* (2019) using the BS 1377-4: 1990 methods ($\gamma'_\mathrm{min} = 14.28\,\mathrm{kN/m^3}$ and $\gamma'_\mathrm{max} = 17.11\,\mathrm{kN/m^3}$) and other studies using comparable sand (e.g. White, 2020). However, the magnitudes of γ'_min and γ'_max can be significantly dependent on the adopted test method. Comparisons to other data should be made with caution, as the variations in the limiting unit weights can lead to large uncertainty in the resulting calculated D_R values (Lunne *et al.*, 2019).

A series of direct shear tests were performed to assess the critical state friction angle, ϕ'_cs, of the LB 14/25 sand. Tests were performed at three normal stress levels ($\sigma'_\mathrm{n} = 50, 100, 150\,\mathrm{kPa}$) on sand samples of two densities: Dense ($D_\mathrm{R} = 0.88 \pm 6\%$) and Medium ($D_\mathrm{R} = 0.55 \pm 3\%$). Sample density is determined from measurements of global sample mass and volume. The vertical and

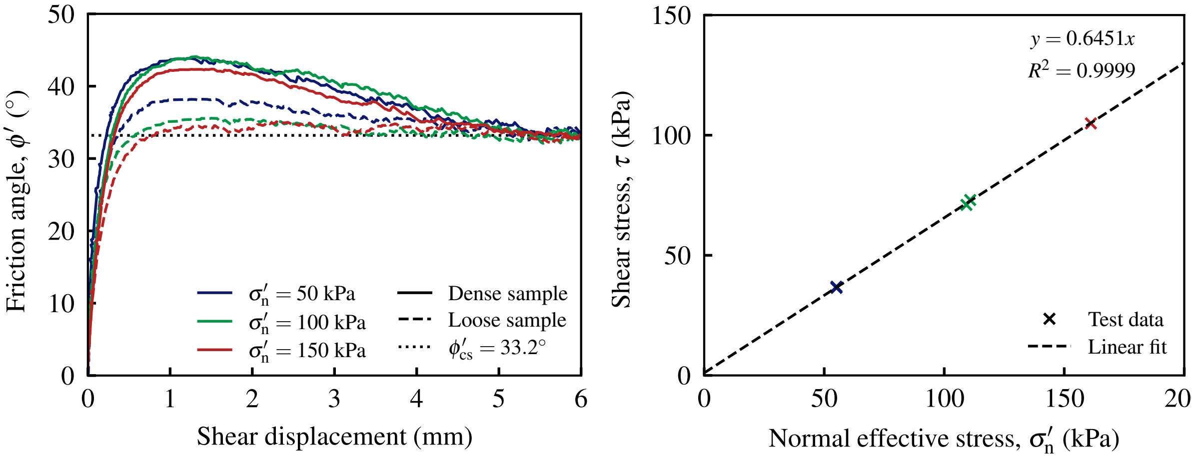

(a) (b)

Figure 5.12 Direct shear testing of LB 14/25 sand: a) Combined results, b) ϕ'_{cs} assessment

horizontal loads in each test were processed to determine the effective normal and shear stresses, σ'_n and τ respectively, as well as friction angle using $\tan\phi' = \tau/\sigma'_n$. The combined results are shown in Figure 5.12a. The normal and shear stresses at critical state were extracted for each test and a linear fit was used to determine a value of $\phi'_{cs} = 33.2°$ (see Figure 5.12b).

5.3.2 Sample preparation

Air pluviation was selected as the deposition technique to produce repeatable, homogeneous samples of dry LB 14/25 sand, at a specific relative density. This typically involves 'raining' sand from a drop-height above the sample through a flow control and dispersion mechanism. A fixed-height sand raining device was developed for the testing tank outlined in Section 5.2.2, as shown in Figure 5.13a. The apparatus comprises a hopper which is supported above the testing tank. At the base of the hopper are two perforated shutter plates with matching hole patterns; the lower plate can slide in one direction, whilst the upper plate remains fixed. The two shutter plates are initially misaligned to retain sand in the hopper, then the holes are rapidly aligned to allow pluviation into the tank to occur. The resulting 'jets' of sand from the shutter plates are further dispersed using a second 'diffuser' mesh (Schnaid, 1990).

The resulting sample unit weight, γ', is determined by the sand flow rate and the particle drop height (Richards, 2019). The design of this raining device is a compromise between ensuring a suitable hopper volume and maximising the particle drop height in the restricted space above

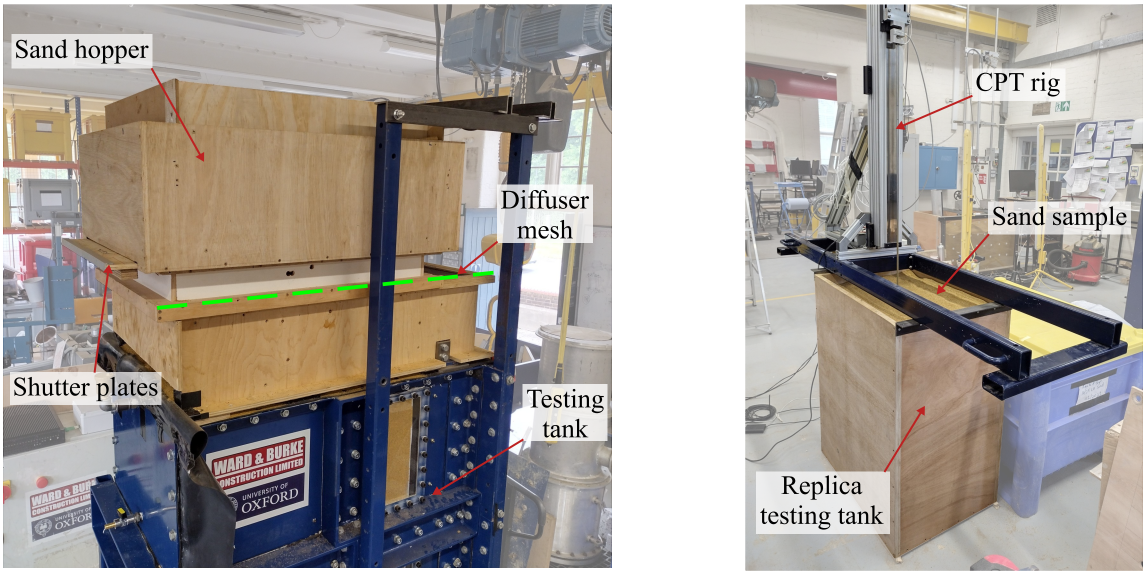

(a) (b)

Figure 5.13 Sand sample preparation: a) Sand raining device fitted to the testing tank, b) CPT assessment of a prepared sample

the tank. A minimum drop height of 325 mm was achieved below the diffuser mesh, which is located 125 mm below the shutter plates. Due to the limited volume of the sand hopper, the samples are prepared in three layers. All samples in this study were prepared using shutter plates with 20 mm diameter holes on an 80 mm centre-centre grid spacing pattern. The diffuser mesh comprised a 0.5 mm thick perforated steel sheet, with 5 mm diameter holes on a 6 mm centre-centre grid spacing. The shutter plates and diffuser mesh cover the full plan area of the testing tank (750×500 mm), to minimise any boundary effects.

Across eight samples prepared using this technique, the average sample unit weight was calculated as $\gamma' = 16.13 \pm 0.11\,\mathrm{kN/m^3}$. Using the LB 14/25 sand properties defined in Section 5.3.1, this corresponds to a mean relative density of $D_\mathrm{R} = 72\%$ with standard deviation of 3.7%, and therefore a classification as ‘dense’ according to BS EN 1997-2 (BSI, 2007). This was selected as it closely represents the conditions in recent open caisson shaft case studies with documented high friction in sands (Abdrabbo and Gaaver, 2012; Royston *et al.*, 2022a).

Cone penetration tests (CPTs) were performed to assess the homogeneity and density of the prepared samples. The CPT rig described by Mayall (2019) was used, which comprises an 8 mm diameter cone with a 60° apex angle. The cone resistance, q_c, is measured directly

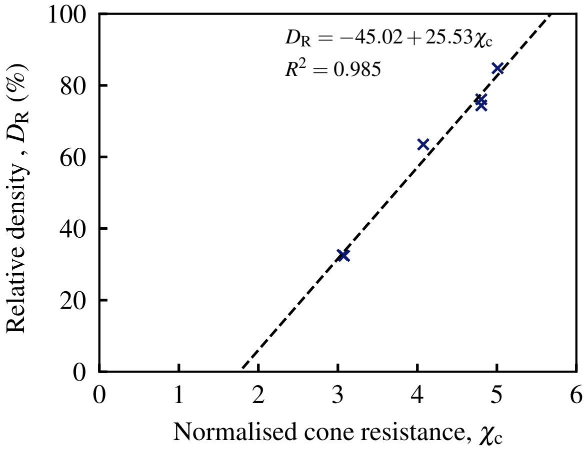

Figure 5.14 Relationship between sample relative density and representative CPT normalised cone resistance for LB 14/25 sand, with a linear fit to determine parameters for Equation 5.2

using strain gauged instrumentation within the tip of the probe. Due to height constraints above the testing apparatus, samples for CPT assessment were prepared in a replica tank of identical dimensions to that described in Section 5.2.2, as shown in Figure 5.13b. A series of six CPTs were performed in two 'virgin' prepared samples (see Figure 5.15). Four tests were spaced along the tank centreline to assess the sample homogeneity normal to the soil-structure interface (C1-4); two additional tests offset 125 mm from the centreline provide an indication of variation in the lateral direction (O1-2). The cone was penetrated at a rate of 5 mm/s to a depth of 800 mm, which corresponds to approximately 85% of the prepared sample height.

To relate the q_c data to the sample D_R, the relationship adopted by Mayall (2019) was used:

$$D_R = \rho_1 + \rho_2\chi_c \qquad \chi_c = \ln \frac{q_c/p_{ref}}{(\sigma'_v/p_{ref})^{0.5}} \tag{5.2}$$

where χ_c is the normalised cone resistance, p_{ref} is a reference stress (taken as 100 kPa) and σ'_v is the effective vertical stress. This empirical correlation is a generalised form of the relationships proposed by numerous authors in the literature (e.g. Jamiolkowski *et al.*, 1985, 2003; Schmertmann, 1976). To calibrate the fitting coefficients, ρ_1 and ρ_2, for the LB 14/25 sand in this study, samples were prepared at several relative densities (measured using global mass and volume measurements) by using different shutter plates and diffuser meshes. For each CPT the mean of χ_c is calculated from data below 120 mm penetration, to avoid the influence of alternative failure mechanisms at shallow depths (Mayall, 2019). The mean of this value over

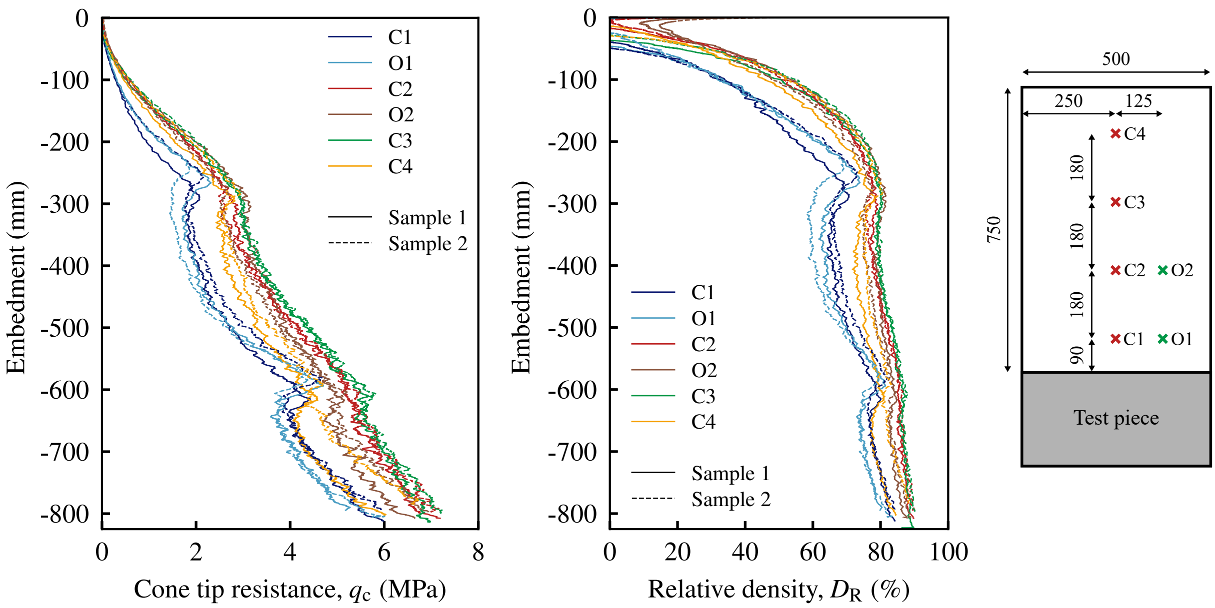

(a)

(b)

Figure 5.15 CPT results on two prepared samples of LB 14/25 sand: a) cone tip resistance, b) relative density calculated using the relationship from Mayall (2019)

the four central CPTs (C1-4) is then calculated to give a representative value, $\bar{\chi}_c$, for the soil sample. A least-squares linear regression is then performed between the global D_R and $\bar{\chi}_c$ to determine values for ρ_1 and ρ_2 in Equation 5.2. Figure 5.14 plots the data obtained from the various CPTs in this study and the corresponding linear fit.

The CPT results for the two prepared dense samples are presented in Figure 5.15. There is noticeable variation in the q_c profiles, in particular C1 and C4 display reduced resistance (Figure 5.15a). This indicates a slight reduction in D_R near the tank boundaries. Two regions of slightly increased resistance are also visible in C1 and C4 at approximately 300 and 600 mm depth, which correspond to the intersections between successive rained layers. However, the q_c profiles C2 and C3 are remarkably linear and in close agreement, showing good sample uniformity over the central region of the tank. Furthermore, there is only minor lateral variation in the sample, indicated by the close agreement between tests C1 and O1, and also C2 and O2. The fitted D_R profiles in Figure 5.15b show good uniformity over the lower 750 mm of the sample and correspond well with the calculated global D_R values. The reduction in sample density in the upper 250 mm is an artefact of the constrained minimum drop height, which is relatively low as the sand surface level rises in the testing tank. However, there is very close agreement between the corresponding CPTs in the two distinct samples, demonstrating excellent repeatability of the sample preparation.

5.3.3 Bentonite slurry

The bentonite slurry adopted as the lubricant in this testing was TUNNEL-GEL® PLUS supplied by Baroid Industrial Drilling Products. This is a widely available and commonly used lubricant for caisson sinking and microtunnelling operations in industry and thus serves as a good baseline for practical observations and future comparisons. A 6.25% mix was adopted for all tests, corresponding to a ratio of 400 L water : 25 kg bentonite powder. This represents a typical baseline mix adopted in industry (Phillips, 2023). The lubricant was prepared using a high-shear mixer to suspend and disperse the bentonite particles in the water (Praetorius and Schößer, 2017). Once mixed, the slurry was left for 24 hours for hydration of the bentonite.

5.3.4 Soil displacement tracking

To investigate the soil displacements caused by different interface conditions, particle image velocimetry (PIV) was used. A Nikon D3200 24.2 megapixel camera was used to obtain images of the interface through the lower perspex tank viewing window (Figure 5.16). The camera was mounted on a fixed tripod and photos were taken remotely, to avoid any camera movement, at fixed 30 s intervals during each advance. Two freestanding LED area lights were placed on either side of the apparatus to provide uniform illumination of the interface.

The PIV analysis was undertaken using geoPIV-RG (Stanier *et al.*, 2016). A grid of twelve 7 mm diameter black circles were drawn onto the inside face of the perspex glass to act as control points (see example photo in Figure 5.26a). Calibration of the position of these control points was performed using an accurate printed grid of 12 mm diameter circles on a 40 mm centre-centre spacing. A 310 × 100 mm region of interest is considered approximately 30 mm from the soil-test piece interface (see Figure 5.26a). This considers soil displacements approximately 10 mm from the over-cut formation, to avoid difficulties with image analysis due to the large changes that occur between consecutive images in this region.

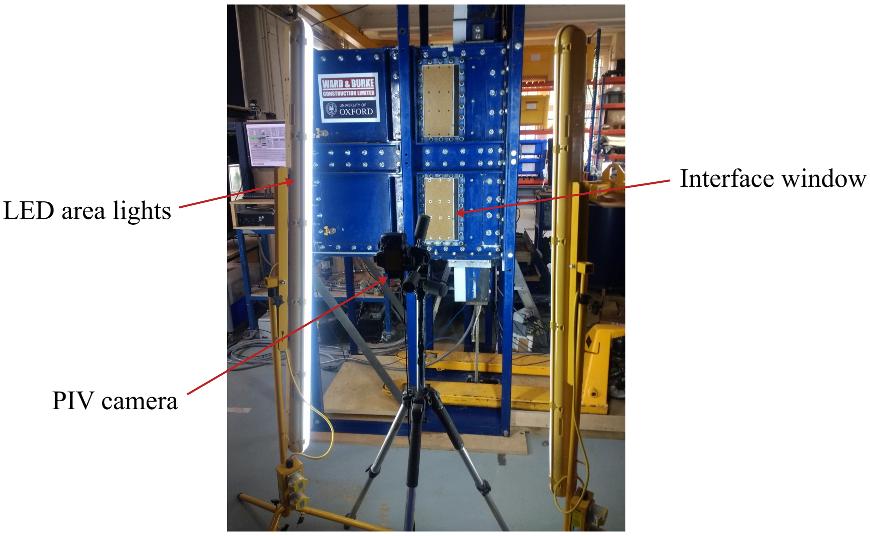

Figure 5.16 Photo showing the PIV camera set up to image the soil-test piece interface through the perspex tank viewing window

5.3.5 Testing programme

Table 5.3 provides an overview of the tests performed in this chapter, which are focused on exploring the influence of over-cut formation and interface lubrication on the development of skin friction.

Tests are conducted with two different interface conditions: a) no over-cut and b) with over-cut. When no over-cut is created, the sand sample is prepared directly against the concrete test piece surface prior to shearing. In the over-cut tests, a void is formed adjacent to the test pieces using the process illustrated in Figure 5.17. MDF over-cut ‘plates’ are fitted to the test pieces before sample preparation. These fully cover the concrete faces and are clamped in place by the inter-test piece connection, moving with the test pieces as they advance. During the first three advances, the over-cut plates pass out of the tank through the exit seal; these are removed before reattaching the test piece for subsequent advances. This process simulates the use of a cutting shoe in caisson sinking to form an external annulus through over-excavation.

The over-cut plates used in this chapter have a thickness of 20 mm. Although this is less than typically used for caisson construction (Table 2.1), it represents a compromise between faithfully recreating field conditions and practical considerations of the apparatus, namely the seal configuration. The tank seals must adjust to accommodate the reduction in thickness as the

Table 5.3 Summary of testing programme and key parameters

Test	**Lubrication** (g/min)	**Over-cut**	**Description**
1	None	0 mm	Baseline dry interface friction
2	None	20 mm	Influence of non-lubricated over-cut
3	400	0 mm	Influence of interface lubrication without over-cut formation
4	650	20 mm	Over-cut with interface lubrication (typical industry practice)

over-cut plates move forward, which is achieved by using thick neoprene and manually adjusting the fish plates. The use of a smaller over-cut would simplify the seal arrangement, however this may lead to increased shearing resistance due to inadequate bentonite surface coverage or from bentonite filtration at the interface. The influence of these effects may be reduced at low confining stress, however adopting a larger overcut facilitates comparison with future testing at higher confining stresses, where the over-cut depth will have a greater influence.

Interface lubrication is considered both with and without over-cut formation (Test 4 and 3 respectively). When no over-cut is formed, lubricant is delivered from the test piece ports directly into the sand sample. When an over-cut is formed, lubrication is injected from the port immediately behind the uppermost over-cut formation plate, as shown in Figure 5.17. Although the interface in the experimental testing represents a reduced-scale plane-strain approximation, the term ‘annulus’ is still used to refer to the lubricated void after forming an over-cut. This reflects the common terminology for caisson sinking used on-site and in the literature.

The required slurry delivery rate was calculated as a function of the interface area, the test piece advance rate, the sample porosity and the bentonite penetration distance. Using the column test results of Phillips (2023), a penetration distance of 78 mm was predicted at a slurry pressure of 30 kPa, based on the maximum normal stress observed with a non-lubricated interface (see Section 5.4.1). A lubrication rate of 382 g/min was calculated, but 400 g/min was adopted as this is the minimum the delivery system in Section 5.2.5 could reliably provide. For Test 4, additional slurry is required to ‘fill’ the volume created by the over-cut formation plates. An additional 250 g/min was calculated to provide this at the 25 mm/min advance rate. For the open tank tests in this research, the lubricant delivery rates were maintained constant throughout

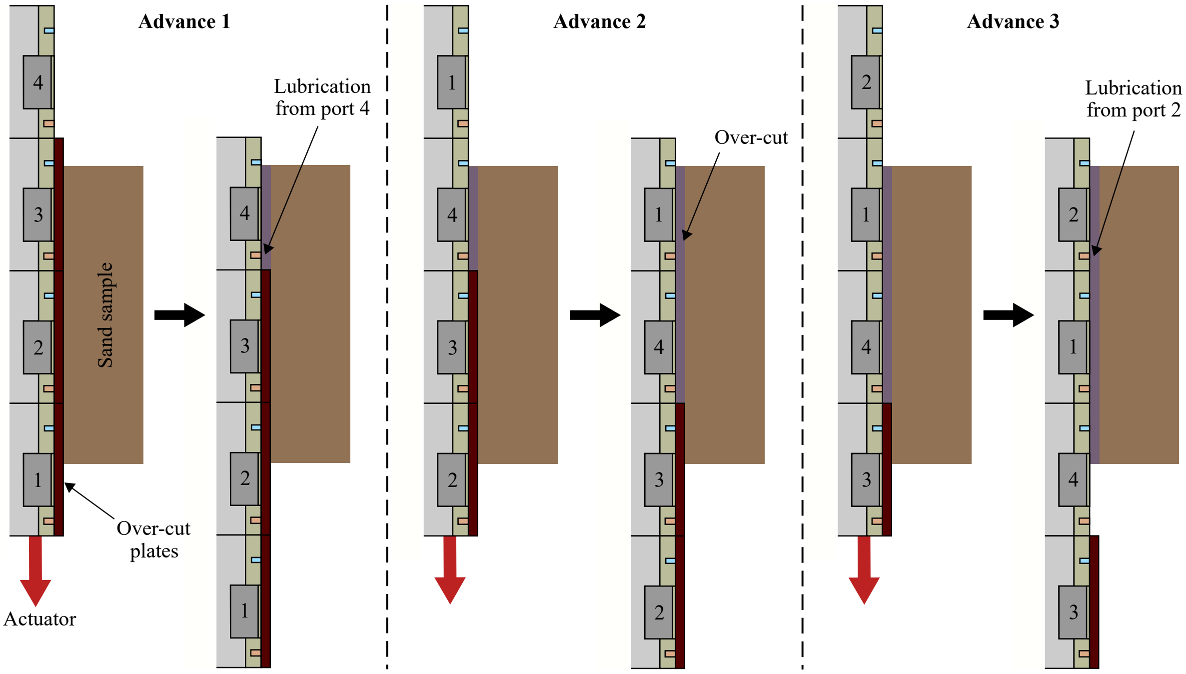

Figure 5.17 Schematic of a section through the testing apparatus during the first three advances of a test with over-cut formation

the tests. Any excess lubricant delivered to the interface appears at the sand surface, where it is drawn off to prevent any build up.

5.4 Experimental results

The data logged from all sensors during testing form continuous time series data streams. The current order of the test pieces is recorded at all points during testing, as well flags to determine when an advance movement is ‘active’ and the current advance number. By using the temposonic position sensor data and the known test piece order, the position of all test pieces and sensors relative to the testing tank can be determined. The advance ‘active’ flags then enable the data to be filtered to extract data from the individual advance movements.

5.4.1 Baseline friction

To establish baseline interface behaviour, Test 1 considers a non-lubricated interface with no over-cut formation. The primary outputs of the testing apparatus are the interface SSCS sensor measurements, namely the normal stress and the shear component parallel to the actuation direction. Figure 5.18 shows these outputs for Test 1, with the four sensor responses plotted against their position in the tank for each test piece advance. Although no time dependent effects are expected, four advances were completed for comparison of data. The solid lines show SSCS measurements in the present advance, whilst the dotted lines correspond to prior advances. This allows comparison of the interface stresses at each depth within the tank as the repeated shearing occurs. The test piece configuration at the start of each advance is also shown in Figure 5.18. Each sensor has a 'primary advance' between approximately 160 and 620 mm depth, where it is in the zone of interest within the tank for a full advance (e.g. TP4 in advance 1 in Figure 5.18). Due to boundary effects on the sensors in proximity to the exit seal, results from the lower 150 mm of the tank are omitted.

Both the shear stress (Figure 5.18a) and normal stress (Figure 5.18b) show an increase with depth in the tank, due to the increase in overburden soil. The increase is relatively linear, particularly over the upper 650 mm depth, as would be expected for a uniform soil sample. A linear least-squares fit on the sensor data between 160 and 620 mm depth suggests mean gradients of 8.7 kPa/m and 14.8 kPa/m over the four advances, for shear and normal stress respectively. This corresponds to a coefficient of lateral earth pressure of approximately $K = 0.91$. Although this is higher than typical at-rest K_0 value, it is expected for the experimental conditions. Air pluviation produces higher K values than other sample preparation methods and can result in values greater than unity at low vertical effective stresses (Chu and Gan, 2004; Northcutt and Wijewickreme, 2013).

There is a slight increase in the gradient of normal stress with depth below approximately 650 mm recorded by all four sensors. This could be an artefact of the sample preparation; a pluviation layer occurs at approximately 600 mm, which may cause an increase in density in the lower portion of the sample. However, this could also be caused by an increase in density towards the exit seal, as sand is dragged down at the interface. The higher shear stress shown by the sensor in TP1 below 700 mm is potentially caused by sensor face and the concrete test piece surface being slightly non-coplanar.

The measured interface shear stress broadly reflects the normal stress. There is close

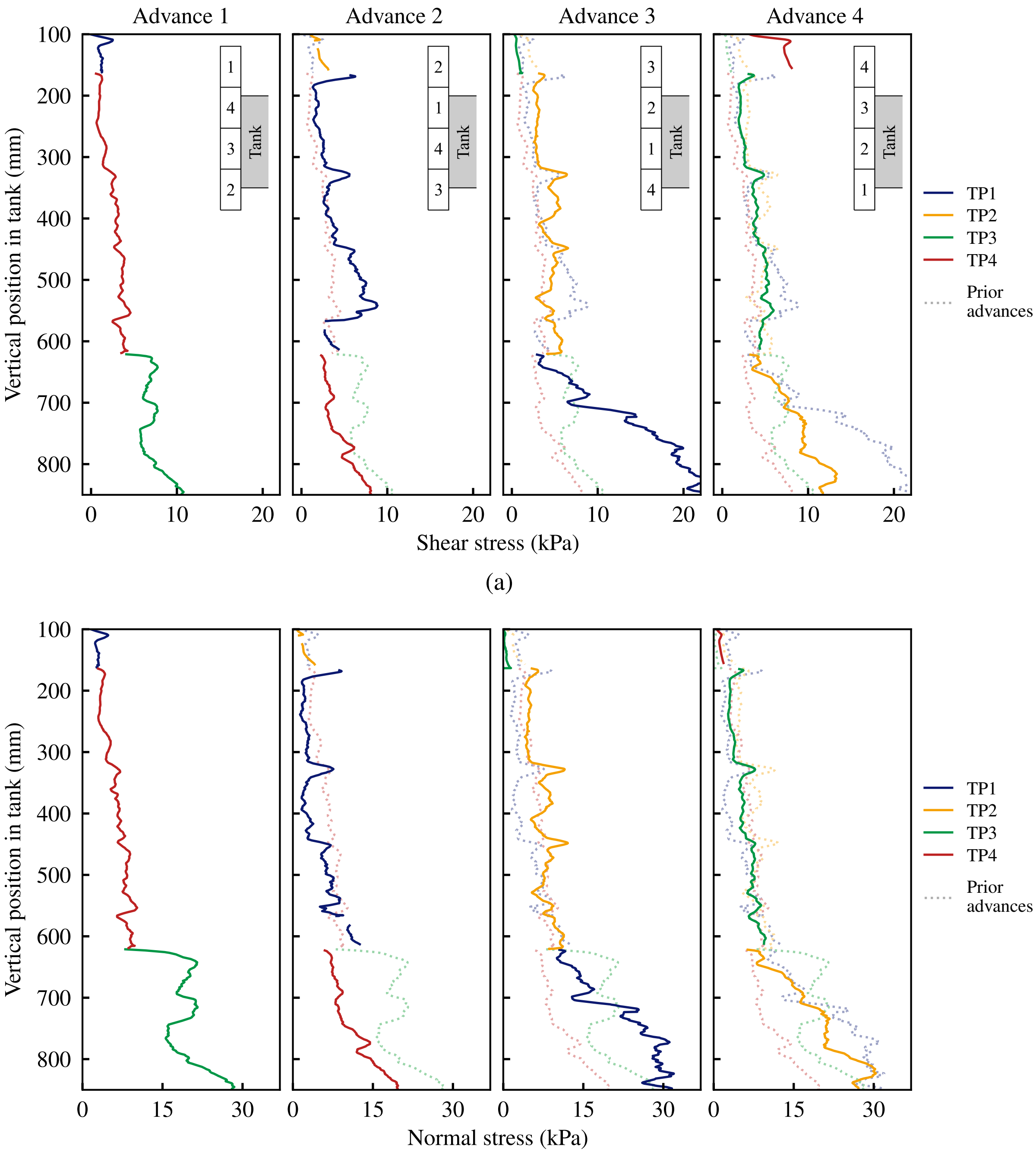

(a)

(b)

Figure 5.18 Measured interface contact stresses in Test 1 (non-lubricated, no over-cut): (a) shear stress, (b) normal stress. The solid lines are measurements in the present advance, whilst the dotted lines correspond to prior advances. The schematic inlays show the test piece configuration at start of each advance.

agreement between the SSCS measurements in the upper 650 mm of the tank, indicating that there is little to no change in friction with continued shearing. The optical SSCS sensors developed in Chapter 4 show very good agreement with their electrical counterparts. In particular, the sensor in TP3 shows excellent agreement with TP4 over advances 1 and 4, for both the shear and normal stress. Furthermore, the transverse shear stress component remains less than 1 kPa in all sensors over the advances in Figure 5.18. Considering the four SSCS sensors over their respective primary advances, the mean interface friction angle is calculated as $\delta = 32.3°$. This agrees closely with the expected interface friction measured from concrete samples in Section 5.2.4.2. These observations give confidence in the measurements obtained by the optical SSCS sensors.

As the test pieces advance through the tank, draw down of the sand surface occurs at the interface. This is likely attributed to a combination of densification of the sample and loss of sand from the tank, which is dragged through the exit seal by the concrete surface. Manual measurements were made of the sample surface profile after each advance using a laser distance meter, as well as the sand mass passing the exit seal. The measured sand drawdown profile was observed to be highly linear throughout the test. Performing a least-squares linear regression on this portion of the data after each advance showed an angle of repose of between 32.4 and 34.0° (average 33.1°), which matches very closely with the measured angle of internal friction for the sand (see Section 5.3.1). The amount of sand lost from the tank through the exit seal was relatively consistent in the four advances of Test 1, and was measured to be between 306 and 472 g. It should be emphasised that this is only a very small proportion of the overall sample mass; on average for Test 1 the lost sand represents 0.069% of the 569 kg sample.

The surface measurements were used to calculate the mean volume of the drawdown profile per advance, over the four advances (699 cm^3). The equivalent volume of sand lost was estimated as a mean of 237 cm^3, using the measured mass of the sand from the exit seal per advance and the sample global unit weight (16.2 $\mathrm{kN/m}^3$). Hence only approximately a third of the drawdown volume was accounted for by the lost sand. This contribution remained relatively constant across the four advances in this test (1.87 m total displacement). This suggests that densification of the sample is continually occurring during the test. As the shearing is concentrated at the interface, it may require many advances to reach a steady state global density, at which point any drawdown should be attributable only to sand passing the exit seal.

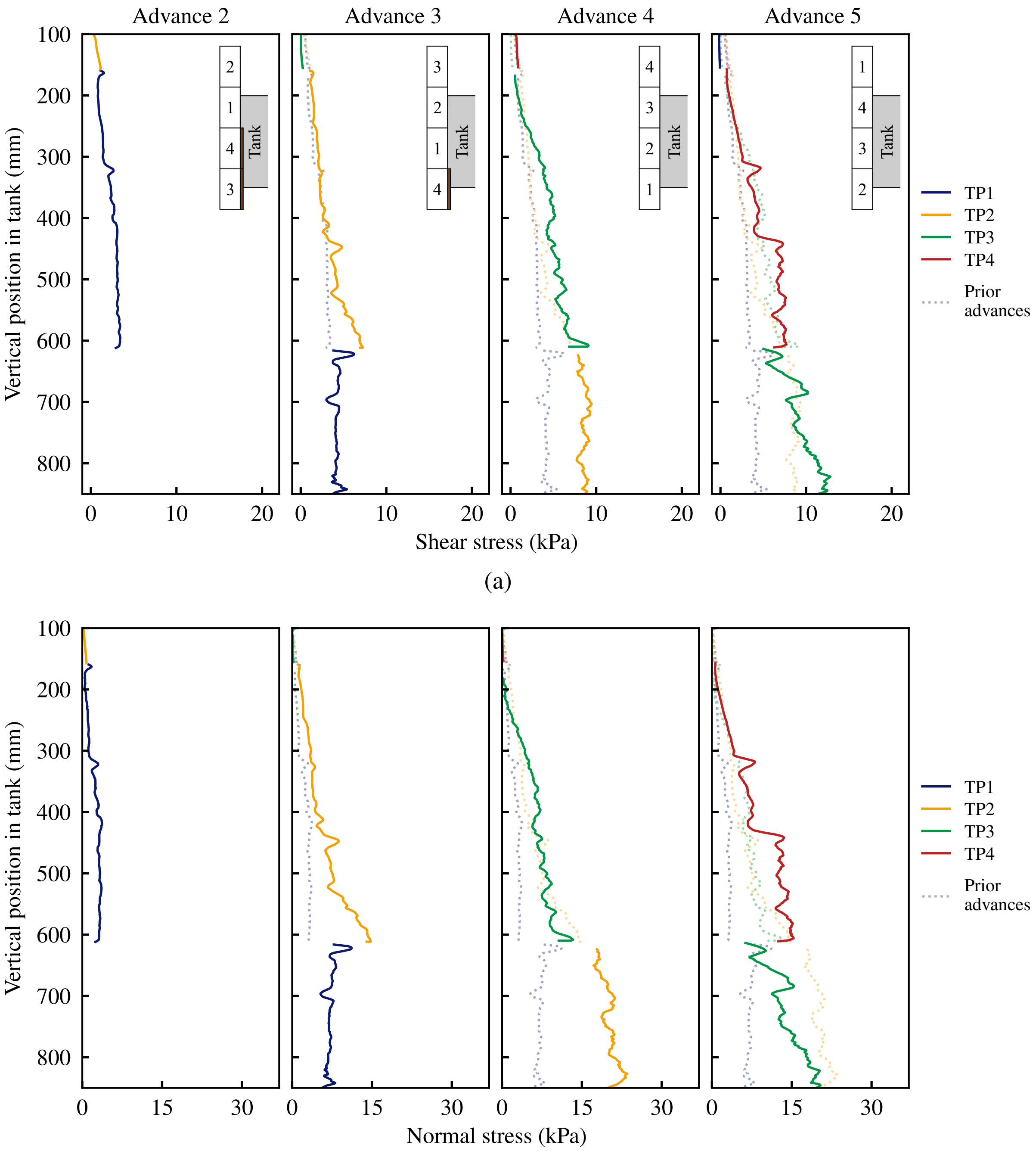

(a)

(b)

Figure 5.19 Measured interface contact stresses in Test 2 (non-lubricated, 20 mm over-cut): (a) shear stress, (b) normal stress. The solid lines are measurements in the present advance, whilst the dotted lines correspond to prior advances. The schematic inlays show the test piece configuration at start of each advance, including the over-cut plates.

5.4.2 Influence of over-cut formation

Figure 5.19 plots the four SSCS sensor measurements during Test 2, which explores the influence of over-cut formation at a non-lubricated interface. In this case, large-displacement shearing

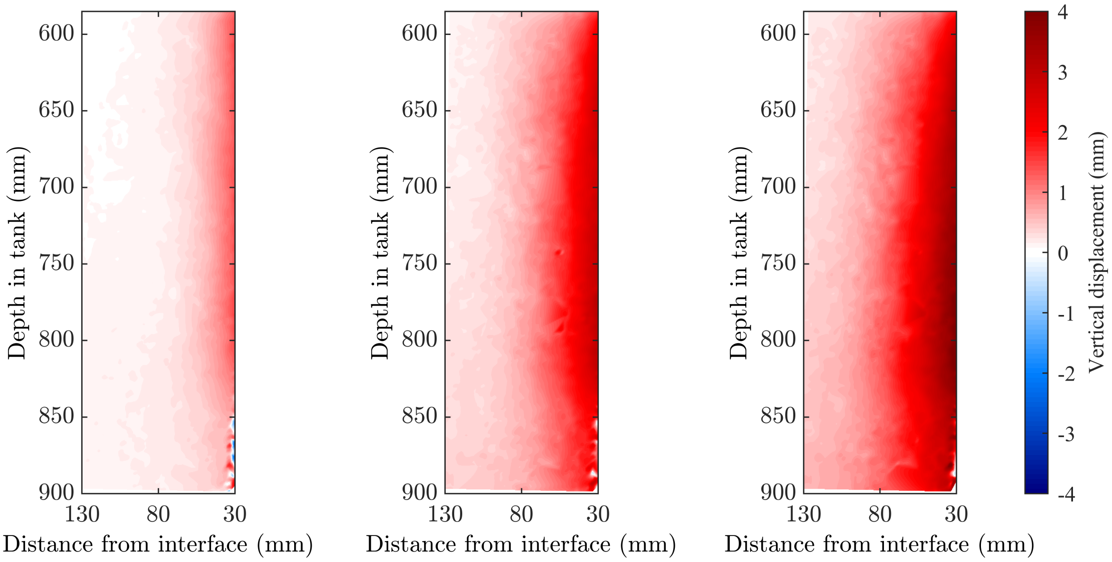

(a) Advance 1 (b) Advance 3 (c) Advance 5

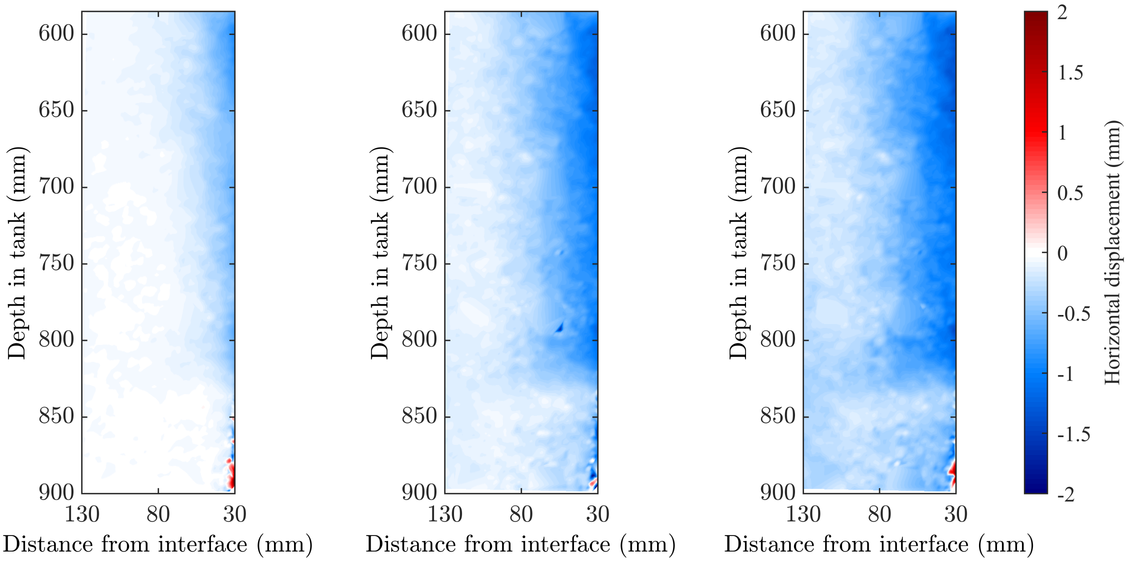

(d) Advance 1 (e) Advance 3 (f) Advance 5

Figure 5.20 Accumulated spatial vertical (a–c) and horizontal (d–f) sand displacement fields at the lower tank window after test piece advances in Test 2. Positive vertical and horizontal displacements are downwards and away the interface (left) respectively.

is required for over-cut formation using the procedure described in Figure 5.17 and to allow subsequent sand displacement to occur. Data from the SSCS sensors below the over-cut former plates are omitted from Figure 5.19 for clarity. Furthermore, advance 1 is not shown in Figure 5.19, as all three SSCS sensors within the tank are covered by the over-cut plates.

The sensor immediately after over-cut formation (TP1 in advances 2 and 3) experiences low contact stresses. Below 600 mm in advance 3, the normal and shear stresses are approximately

6.9 kPa and 4.2 kPa respectively (corresponding to $\delta = 31.3°$) and roughly constant with depth. Increased normal and shear stresses are observed by subsequent SSCS sensors after continued shearing. In TP3 in advance 4, the normal and shear stresses increase approximately linearly with depth, with gradients of 23.4 kPa/m and 15.0 kPa/m respectively (corresponding to $\delta = 32.6°$). The normal and shear stresses measured by TP2, TP3 and TP4 in advances 3, 4 and 5 respectively are relatively consistent, suggesting steady state friction is reached.

This behaviour is likely due to the movement of soil into the 'void' formed as the over-cut plates pass through the tank. To investigate this phenomenon, PIV was used to track the soil displacements. Figures 5.20a–c and 5.20d–f display the PIV-calculated vertical and horizontal soil displacement fields respectively. The adopted convention is that positive vertical and horizontal displacements are defined as downwards and away the interface respectively. After advance 1, there are only minor vertical (Figure 5.20a) and horizontal (Figure 5.20d) displacements, indicating that there is relatively little movement of the bulk soil when shearing against the over-cut plates. After advance 3, larger downwards soil displacements are observed in the region adjacent to the over-cut (Figure 5.20b), combined with smaller magnitude horizontal displacements towards the interface (Figure 5.20e). After advance 5, further downwards displacement occurs (Figure 5.20c), with only minor additional horizontal displacement (Figure 5.20f). This indicates that the over-cut is filled with sand falling primarily downwards, with the majority of displacement occurring quickly after the passing of the over-cut plates. After the 'collapse' of the annulus, the deformation is almost entirely within a narrow shear band directly adjacent to the concrete surface (not covered by PIV).

5.4.3 Influence of interface lubrication

Test 3 explores the influence of interface lubrication without over-cut formation, with bentonite slurry delivered directly into the soil sample from the test pieces, as described in Section 5.3.5. The SSCS sensor measurements during this test are plotted in Figure 5.21. The test piece inlays highlight the lubricant port activated during a given advance: solid cyan denotes initial activation, which is then switched to the hatched cyan port if appropriate. For example, in

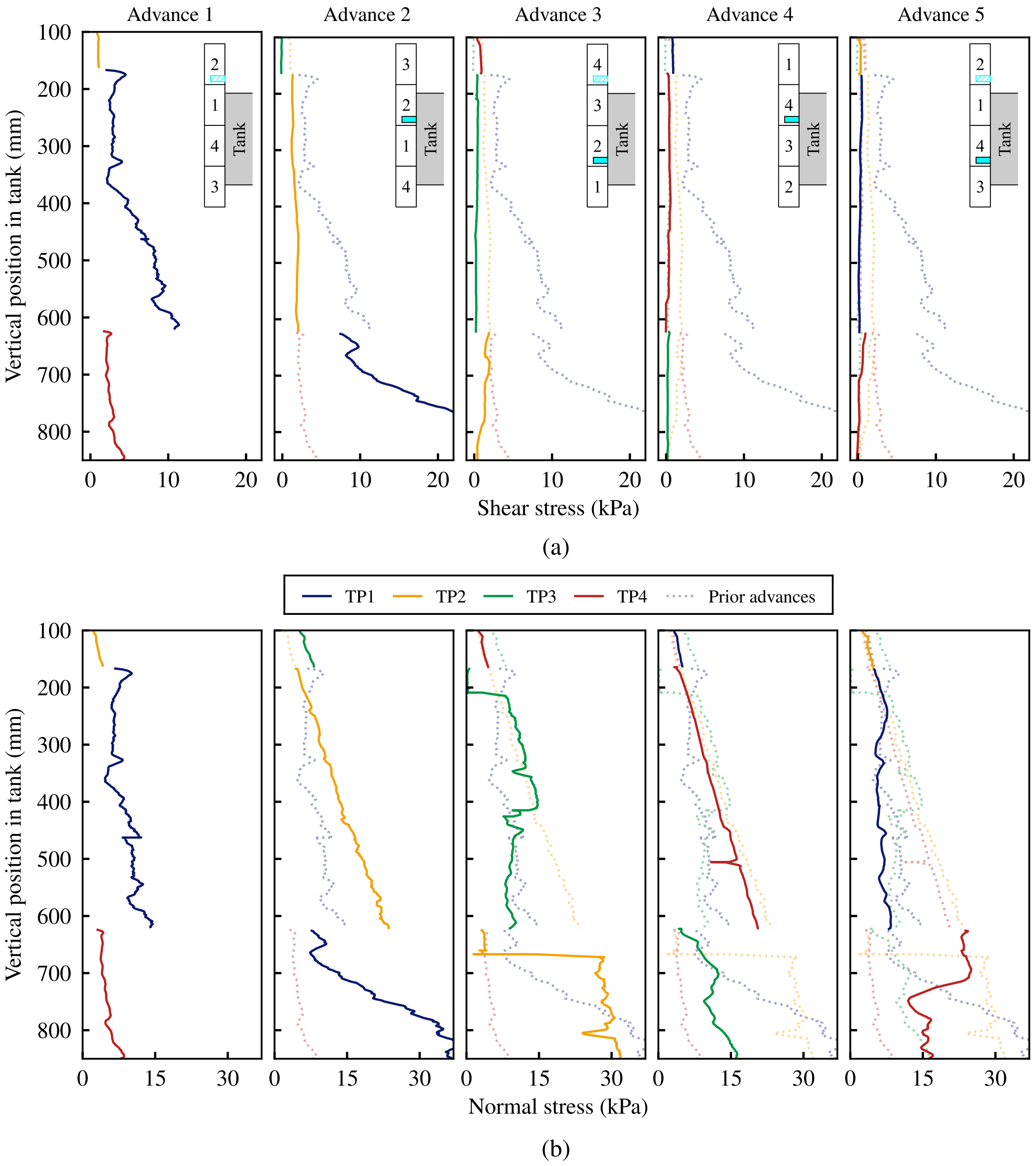

(a)

(b)

Figure 5.21 Measured interface contact stresses in Test 3 (lubricated, no over-cut): (a) shear stress, (b) normal stress. The solid lines are measurements in the present advance, whilst the dotted lines correspond to prior advances. Schematics show the test piece configuration at start of each advance, including the active lubrication port.

advance 2 only the lubricant port in TP2 is active, whereas in advance 3 the port in TP2 is active for approximately 250 mm, before switching lubrication to the port in TP4. Five advances were conducted in this test, to ensure full uniform lubricant spread across the tank depth.

The normal stress measured by TP1 prior to lubrication broadly agrees with values observed in the non-lubricated Tests 1 and 2. From advance 2 onwards, the test pieces are exposed to lubrication. This is evidenced by the highly linear normal stresses at the interface, particularly over the upper 600 mm depth within the tank (Figure 5.21b). Measurements from TP2 show a highly linear response in advances 2 and 3, over the full upper 850 mm of the tank shown. The drop in normal stress between 620 and 670 mm at TP2 in advance 3 is attributed to a temporary stoppage of the lubricant delivery system. Upon restart of the lubrication, the normal stress quickly returns to its prior level. This is also visible in the response of TP3 between 160 and 210 mm. The gradient and overall magnitude of the measured normal stresses at TP2, TP3 and TP4 are relatively consistent over advances 2–4.

In advance 3, the normal stress at TP3 shows a linear response consistent with measurements from TP2 in the prior advance until about 450 mm depth. Below this point, TP3 experiences a reduction in normal stress back to a similar magnitude as measured prior to lubrication in advance 1. The linear response of TP2 is likely attributed to lubricant delivery occurring from a port directly below the SSCS sensor. A similar response is observed in the normal stress measured by TP4 in advance 4, during active lubrication from the port in TP4. The drop in normal stress observed for TP3 in advance 3 corresponds to the point at which active lubrication is switched to the port in TP4. The reduction in normal stress is not thought to be affected by the temporary halting of lubrication from TP2, as a similar response is observed by TP1 in advance 5 after effective ‘re-lubrication’ of that region.

The progression of interface lubrication at the exit seal in Test 3 is shown in Figure 5.22. In the early stages of lubrication, a small amount of water emerged from the seal in the centre of the test pieces (Figure 5.22a). This is caused by filtration of water from the lubricant through the sand matrix under pressure at the port. This causes a region of saturated sand to occur ahead of the port (Figure 5.22b). As the active lubrication port approaches the exit seal, lubricant starts to leak downwards (Figure 5.22c), which causes a loss in support pressure. This can be seen by the drop in normal stress measured by TP4 in advance 5 below 700 mm depth (Figure 5.21b), as the lubrication port is approximately 150 mm ahead of the sensor centre point. At this point, the active lubricant port is switched to the port at the top of the tank before continuing the advance.

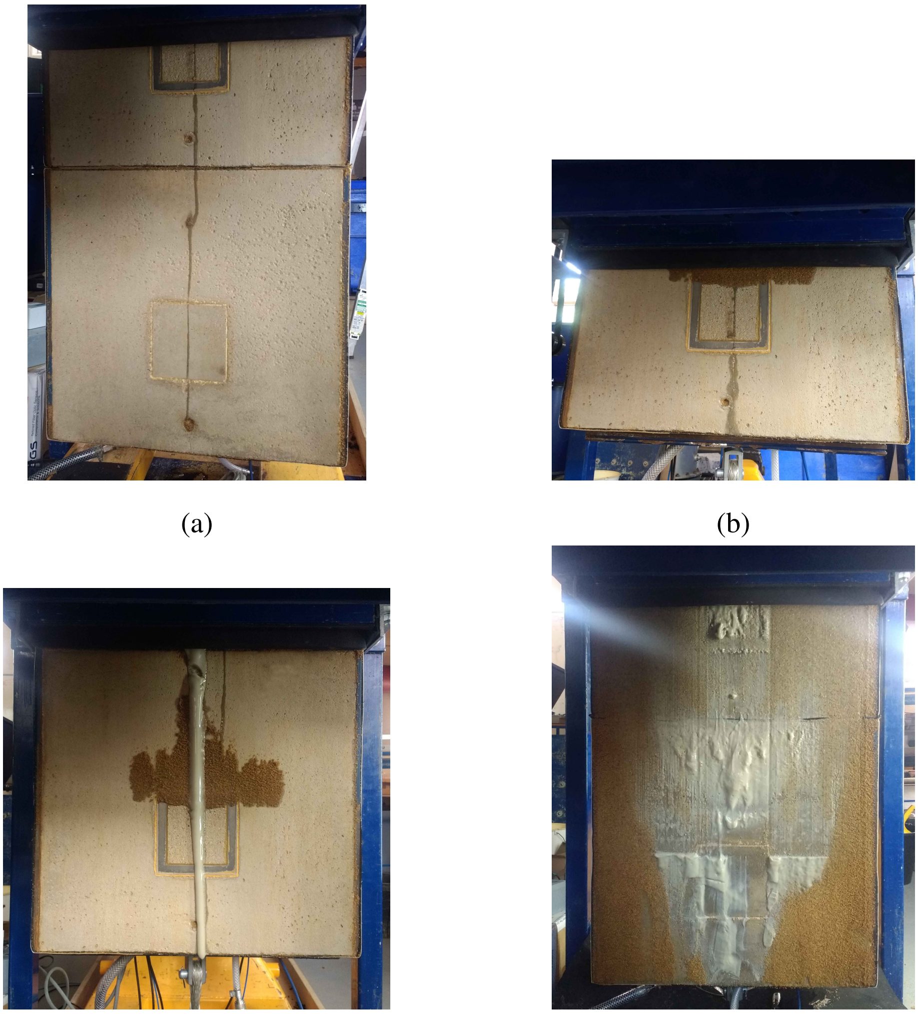

(a) (b)

(c) (d)

Figure 5.22 Lubricant showing on the test pieces exiting the tank in Test 3: (a) Water bleed, (b) Saturated sand caused by water bleed, (c) bentonite slurry emerging from port in proximity to exit seal, (d) surface after two lubriacted advances

The vertical and horizontal soil displacements fields during Test 3 are plotted in Figures 5.23a–c and 5.23d–f respectively. Significant downwards displacements are observed after the first three advances (Figure 5.23b). After advances 4 and 5, in which the lubricant has been distributed over the full tank depth, there is only very minor further downward displacement observed (Figure 5.23c). The horizontal soil displacements in Test 3 occur away from the test pieces. Interestingly, horizontal displacements occurs over the entire region considered in PIV in Test 3, with an average of 0.6 mm after advance 5 (Figure 5.23c). This horizontal displacement accumulates relatively consistently throughout the test. This indicates it is likely caused by a combination of non-lubricated soil being pushed away from the interface during

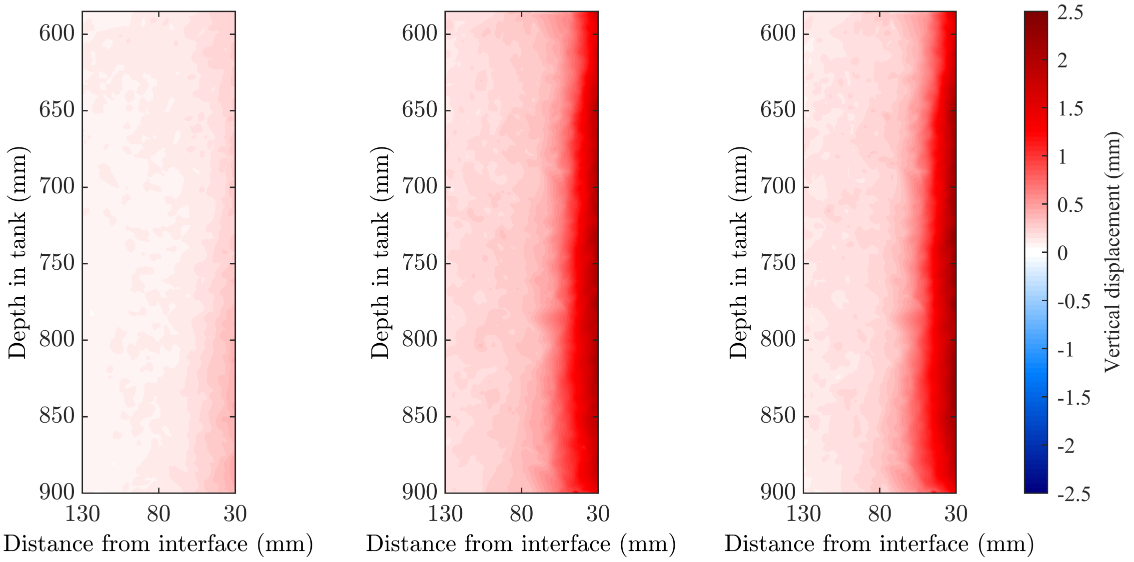

(a) Advance 1 (b) Advance 3 (c) Advance 5

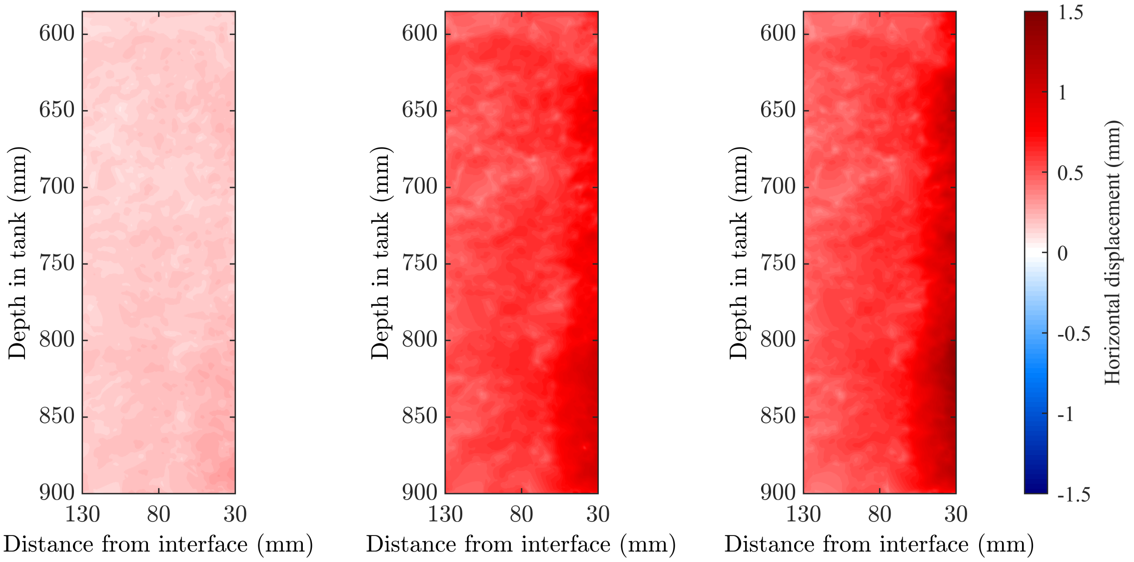

(d) Advance 1 (e) Advance 3 (f) Advance 5

Figure 5.23 Accumulated spatial vertical (a–c) and horizontal (d–f) sand displacement fields induced after test piece advances in Test 3. Positive vertical and horizontal displacements are downwards and away the interface (left) respectively.

shearing and soil movement induced by lubrication delivery. Compared with Test 2, the vertical displacements in Test 3 are lower in magnitude and concentrated in the region closer to the interface. The horizontal displacements are of similar magnitude in Tests 2 and 3, but act in the opposite direction. Furthermore, in Test 3 there is greater horizontal displacement of bulk soil over the entire region of interest compared to Test 2.

Crucially, the shear stress remains very low throughout Test 3, from advance 2 onwards

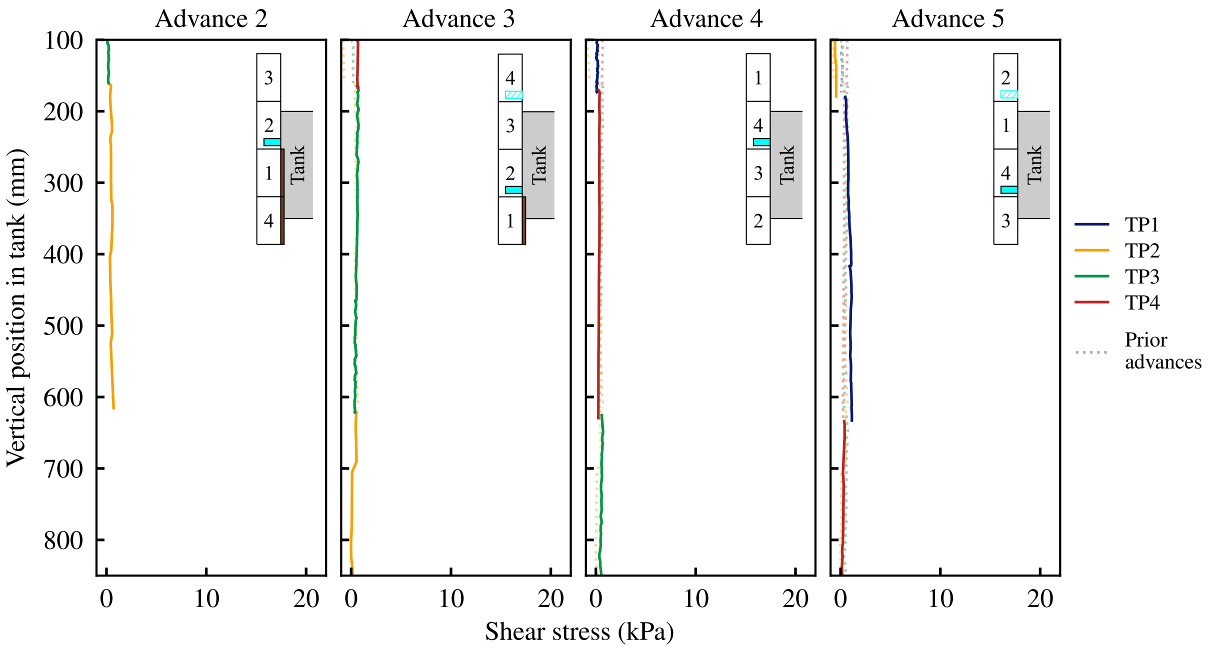

(a)

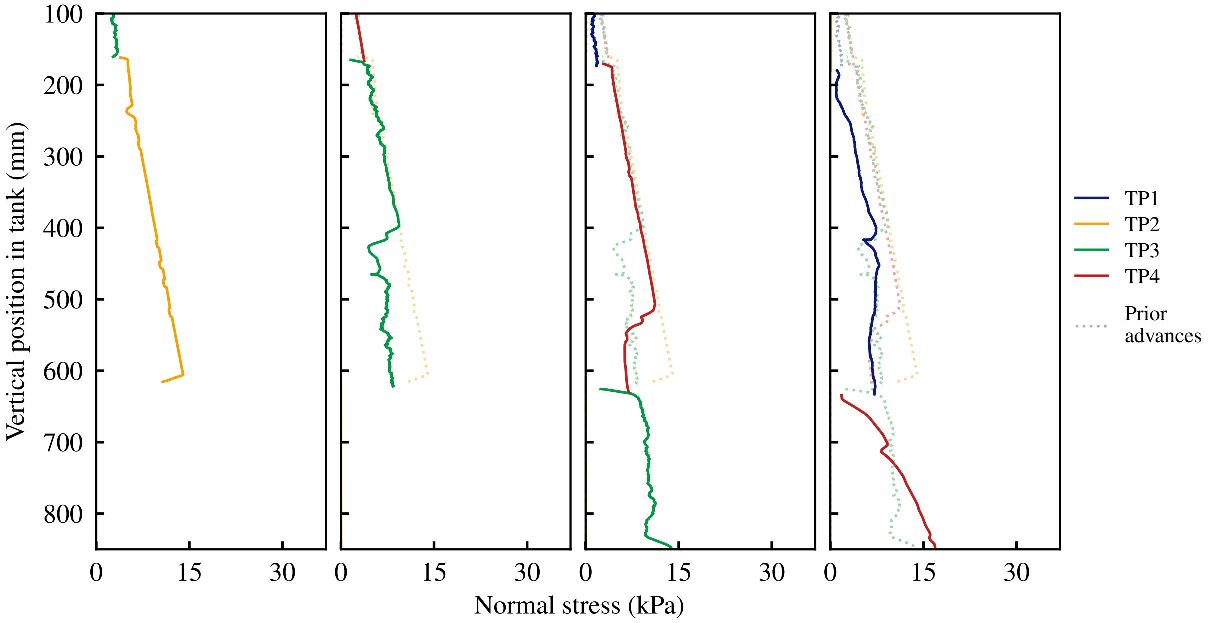

(b)

Figure 5.24 Measured interface contact stresses in Test 4 (lubricated, over-cut): (a) shear stress, (b) normal stress. The solid lines are measurements in the present advance, whilst the dotted lines correspond to prior advances. Schematics show the test piece configuration at start of each advance, including the active lubrication port.

(Figure 5.19a). Despite the reductions in normal stress occurring in advances 3 and 5, there is no noticeable corresponding increase in shear stress. This indicates that the bentonite lubrication of the interface does not require pressure to provide a reduction in shear stress in these tests.

Test 4 explores the influence of creating a lubricated ‘annulus’, through the use of the over-cut plates combined with slurry delivery at the interface. This arrangement most closely represents the desired interface condition in practice. Figure 5.24 plots the SSCS measurements during Test 4. Measurements are broadly similar to those observed for Test 3, including very low shear stresses (less then 1 kPa) and a relatively linear normal stress response in the upper 600 mm sand depth. The normal stress measurement of the electrical SSCS sensor in TP2 failed after advance 2. This is believed to be caused by damage through water or lubricant exposure during testing.

In Test 4, a lubricated ‘annulus’ was formed by the over-cut plates, with the sand supported away from the majority of the test piece surface. This was confirmed by excavation of the tank post-test. A least-squares linear fit on the normal stress measured by TP2 in advance 2 gives a gradient of 20.7 kPa/m depth.

5.4.4 Discussion and comparison of results

For comparison of the different interface conditions, Figures 5.25a and 5.25c plot the shear and normal measurements of the SSCS sensor in primary advance during advance 2 of all four tests described in this chapter. Similarly, Figures 5.25b and 5.25d plot the shear and normal SSCS measurements respectively in advance 4, which is after approximately 920 mm further shearing relative to advance 2.

In Test 2, the SSCS sensor immediately after the formation of the non-lubricated over-cut in advance 2 experiences lower shear and normal stress compared to that measured in Test 1 with no over-cut, which is emphasised in Figures 5.25a and 5.25c. By advance 4, both the shear and normal stresses have returned to similar magnitudes to in Test 1 over the tank depths considered in Figures 5.25b and 5.25d. The gradient of the stresses with depth in the tank is observed to have increased. In advance 4 of Test 2, the gradient of shear and normal stresses show an increase of 72% and 58% respectively over the values determined for Test 1 in Section 5.4.1. This indicates that increased lateral stresses and higher friction can result from the use of a dry over-cut. This is the opposite of a friction-fatigue behaviour and represents a risk for caisson construction, showing potential for increased resistance with continued shearing. This behaviour agrees with

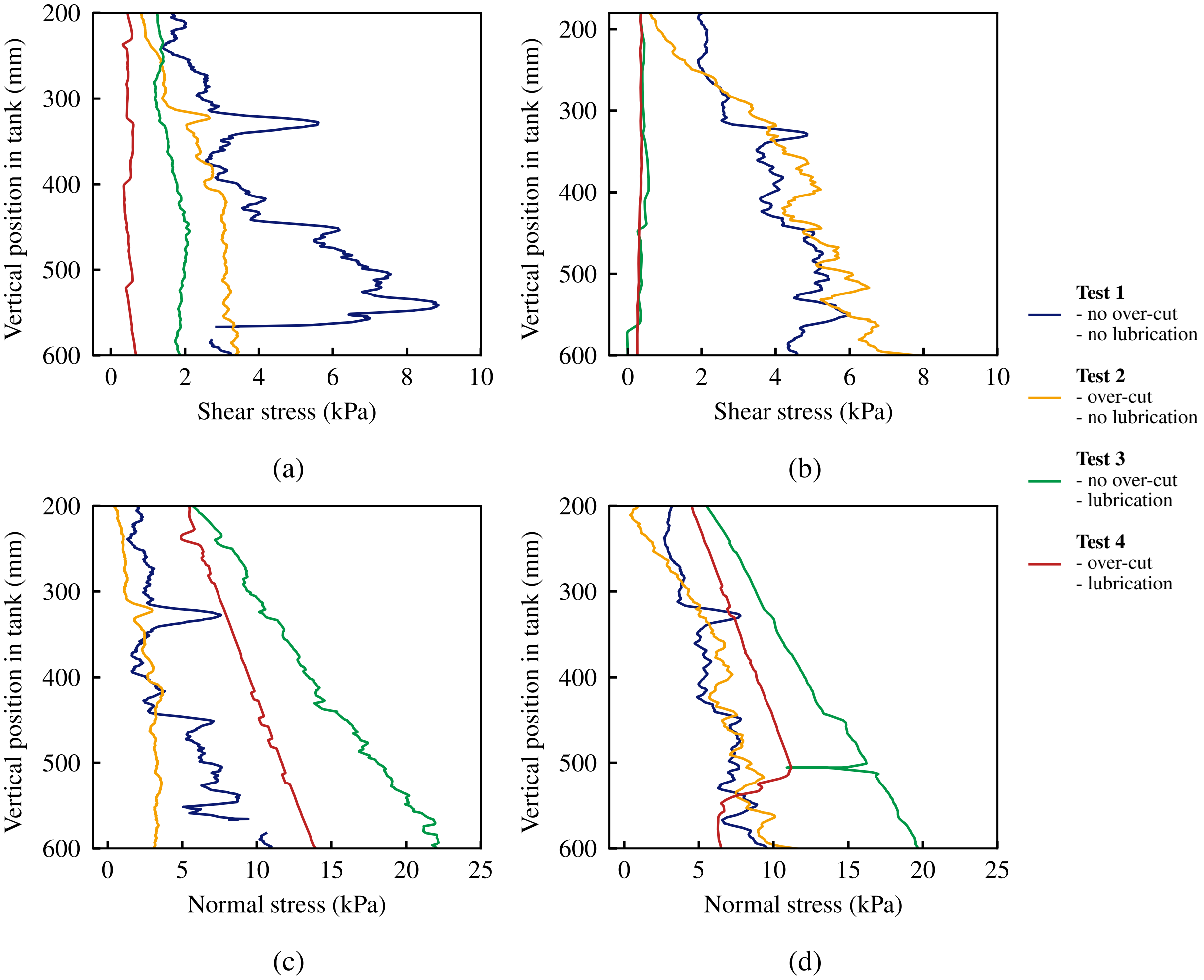

Figure 5.25 Comparison of the interface contact stress measurements during the primary test piece advances in Tests 1–4: (a) advance 2 shear stress, (b) advance 4 shear stress, (c) advance 2 normal stress, (d) advance 4 normal stress

the caisson field monitoring observations of Royston (2018) in dense sand (Figure 2.3b), where high K and friction was observed after a potential annulus collapse.

In Tests 3 (lubricated, no over-cut) and 4 (lubricated with over-cut), the normal stress is observed to be much greater than in the non-lubricated Test 1. The normal stress is greater when no over-cut is formed; linear gradients of 32.6 kPa/m and 20.7 kPa/m are calculated over advance 4 for Tests 3 and 4 respectively in Figure 5.25d. It is likely that the normal stress experienced in Test 3 is a combination of normal effective stress from soil and the lubricant pressure. The normal stress in Test 3 corresponds to an increase of approximately 17.8 kPa/m over the non-lubricated Test 1 stress. This broadly agrees with the normal stress measured in Test 4, which is attributable to lubricant pressure alone. In both Tests 3 and 4, the lubricant

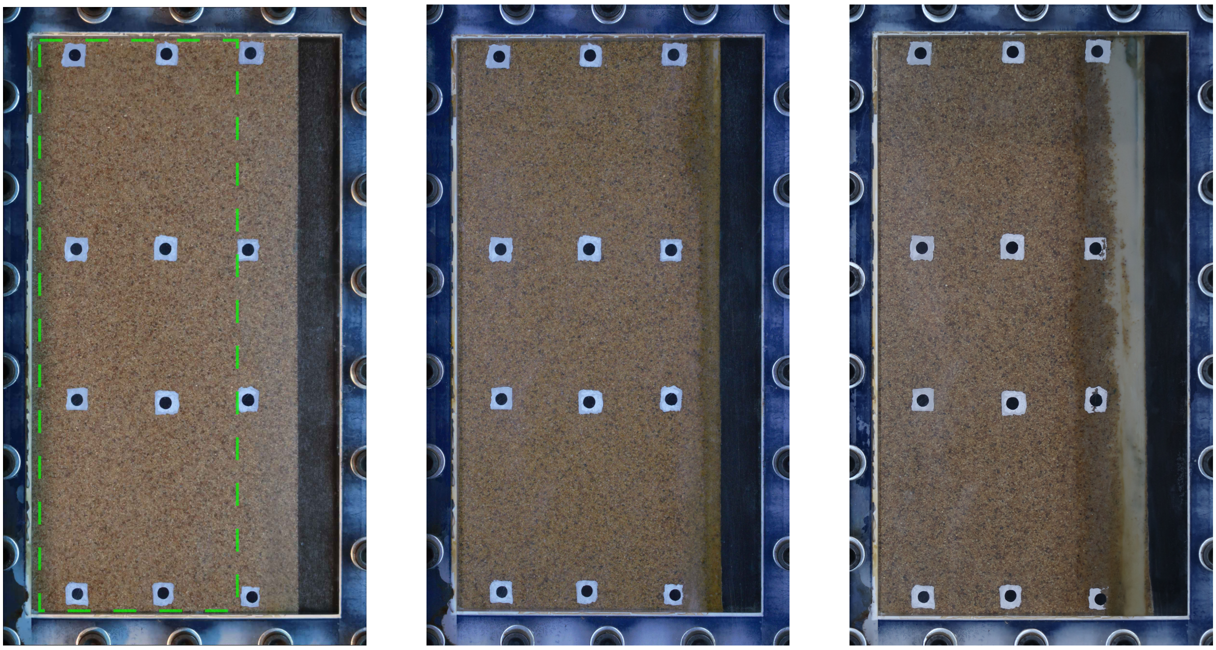
(a) (b) (c)

Figure 5.26 Photos of the test piece-sand interface after 5 advances: (a) Test 2 (also showing the region of interest used in PIV analysis), (b) Test 3, (c) Test 4

pressure is considerably greater than would be expected from pure hydrostatic support from the bentonite slurry (based on a typical bentonite unit weight of approximately $10\,\mathrm{kN/m^3}$). This is potentially attributable to locally raised 'locked-in' pressures, which the SSCS sensors are exposed to due to their proximity behind the lubrications ports.

There is very little change in shear stress between advances 2 and 4 in Test 4 in Figures 5.25a and 5.25b. This indicates lubrication is fully effective almost immediately with the formation of an over-cut. By contrast, Figure 5.25a shows that in Test 3 a marginally higher shear stress is measured in advance 2, indicating that lubrication is initially less effective when no over-cut is formed. By advance 4 in Figure 5.25b, the shear stresses in Tests 3 and 4 are very closely comparable. Although the normal stress results suggest that the slurry pressure is not supporting soil (reducing the normal effective stress) in Test 3, there is still a significant reduction in the shear stress compared to the non-lubricated Test 1 results.

Although the SSCS measurements indicate similar lubrication in Tests 3 and 4, visual observations of the interface show that this may not be representative of the whole test piece surface. This is caused by the close proximity of the lubrication ports and the SSCS sensors along the test piece centreline. Figure 5.26c shows the formation of a uniform lubricated ‘annulus’ in Test 4 over the full lateral extent of the tank. The slurry region covers approximately the same depth as the void left by the over-cut plates and there is clear internal filter cake formation. This was confirmed by excavation of the tank post-test. Only a very limited partially saturated zone was observed beyond the filter cake. The presence of this zone would be expected to increase at higher confining stresses in the soil, due to increased filtration caused by the greater lubricant pressure required to maintain annulus support (Phillips, 2023).

In Test 3, there is much less indication of interface lubrication at the tank window (Figure 5.26b). Only a thin zone containing bentonite is visible adjacent to the interface, suggesting that there is minimal pressurisation of lubricant towards the tank boundaries. This was confirmed by the exiting test piece, which shows only partially slurry coverage of the test piece surface in a ‘fan’ shape behind the active port (Figure 5.22d). This observed behaviour would be expected to occur in practice as well, in the case of discrete lubrication ports at intervals around the caisson circumference. This highlights a risk in caisson sinking when caisson-soil contact occurs, as effective lubrication may only occur in the vicinity of the actively injecting ports. For large diameter caissons, portions of the wall may still experience high friction due to limited lubricant spread.

The positioning of the SSCS sensors is such that the averaged behaviour over the full test piece surface is not captured. Instead, a comparison of the global forces acting on the four test pieces in Tests 2, 3 and 4 is shown in Figure 5.27. For each test, this comprises the lead and counterbalance axial load cell forces; the difference of these measurements gives the overall actuation force. By adding the weight of the four test pieces (480 kg), the global resistance on the test pieces can be determined, which includes contributions from the soil-concrete interface, the exit seal, the sliding side seals and the ball transfer units. The reduction in resistance observed in advance 3 in Tests 2 and 4 is due to the final over-cut plate leaving the exit seal. A similar reduction is observed in Test 3, which instead corresponds with the lubricated region of the concrete interface first reaching the exit seal. In all three tests, the global forces are relatively consistent in advances 4 and 5, suggesting steady state friction is occurring. Observed

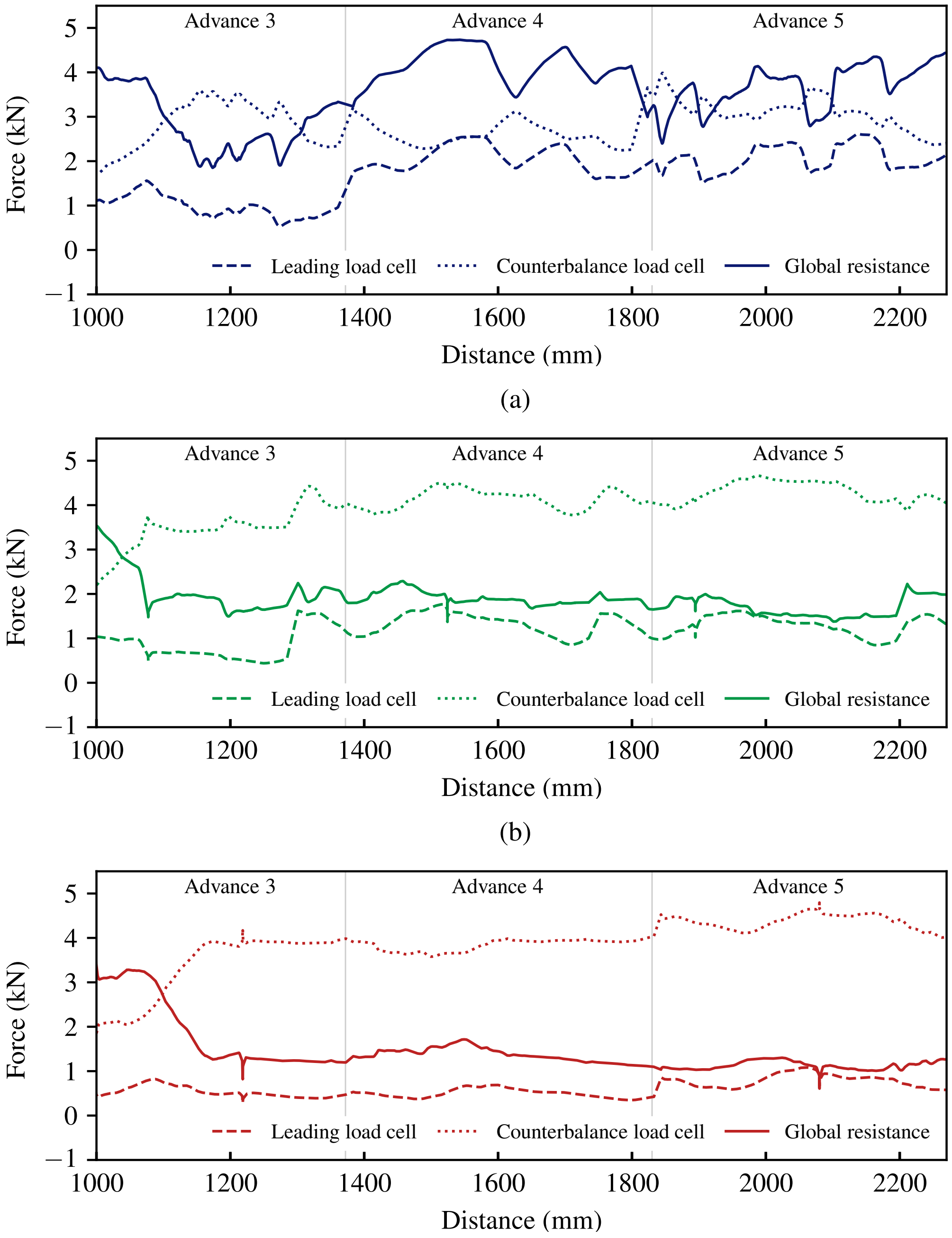

(a)

(b)

(c)

Figure 5.27 Global forces on the four test pieces: (a) Test 2, (b) Test 3, (c) Test 4

oscillations in the load cell readings, which are more pronounced in the non-lubricated Test 2, are caused by the ball transfer units interfacing with the guide rail in the tank.

In Test 2, the lead and counterbalance axial load cell readings are broadly similar, leading to a high global resistance of approximately 4 kN (Figure 5.27a). A least-squares linear fit on the shear stress in TP3 during advance 4 of Figure 5.19a indicates a gradient of 15 kPa/m depth. Integrating this over the test piece surface area exposed to sand contact in the tank gives an estimated soil-test piece frictional resistance of 3.52 kN, which corresponds well with the global observations. In Tests 3 and 4, the counterbalance load cell value is significantly higher than the leading load cell. This indicates that the displacement is largely driven by the self-weight of the test pieces, with low global resistance. The global resistance in Test 3 is marginally greater compared to Test 4, which would be expected as a result of the non-uniform lubrication of the full test piece surface.

5.5 Summary

This chapter has described a suite of laboratory-scale tests exploring the development of friction on open caisson shafts in sands. Large displacement plane strain interface shear experiments were used to consider the influence of over-cut creation and interface lubrication. The following points summarise the key outcomes:

a) The novel testing apparatus developed for this study was demonstrated to capture salient features of caisson SLSI in practice. This includes: a) faithful replication of the concrete caisson surface, b) over-cut creation, c) lubricant delivery to the soil-structure interface, and d) large interface shearing comparable to the sinking process.

b) The optical SSCS sensors developed in Chapter 4 provided vital output measurements of the interface stress state for these experiments. The new sensors provided comparable performance to high-quality conventional electrical sensors and proved to be more robust throughout testing. Failure of electrical sensors is even more likely at field-scale, due to the higher fluid pressures.

c) The soil displacements adjacent to the interface were shown to have an important influence on the observed interface stress state. Soil PIV was used to quantify this, alongside qualitative observations of the interface and test pieces, showing different mechanisms caused by over-cut creation and lubrication.

d) The use of a non-lubricated over-cut appears to show very little benefit in cohesionless soil. Sand displacements were observed to rapidly fill the over-cut void, leading to increased lateral stresses and friction compared to the baseline case. This behaviour is opposite to the friction fatigue typically observed for displacement piles and agrees with caisson field monitoring observations in the literature

e) Lubrication of the interface with bentonite slurry provides significant reduction in the skin friction. Close to zero local frictional resistance was observed with both a fully supported annulus and when effective normal stresses from the soil occur at the interface. This indicates that, at low stress levels, frictional reductions may be possible during construction even if a full annulus is not formed or if the excavation support is lost.

f) Distribution of lubricant over the soil-structure interface is greatly enhanced by the formation of annulus. Lubrication from discrete ports directly into the surrounding soil in practice may only result in localised friction reductions.

Chapter 6

Numerical modelling of caisson bearing capacity in sand

6.1 Introduction

The bearing stresses beneath the RC walls are one of the primary resistances that develop on an open caisson shaft during construction. This chapter presents the results of a suite of FELA calculations exploring the vertical bearing capacity of the tapered cutting face at the base of a caisson in sand. Salient soil and structure parameters are considered in the modelling, including the soil friction angle, the inclination and roughness of the cutting face, and the caisson external embedment depth and radius. In each case, the behaviours observed in the results are interrogated by examining the calculated soil failure mechanisms. The FELA output is subsequently used in Chapter 7 to inform the development of a new closed-form analytical approach amenable for use in routine design.

The study is then extended to explore three further aspects of interest. Firstly, the influence of soil non-associativity is assessed using FEA calculations, as FELA is restricted to considering only associated flow material behaviour. A user-defined material model and an adaptive remeshing procedure are used to obtain accurate bearing capacity predictions from the FEA. Secondly, the horizontal force that develops on the tapered cutting face during vertical penetration is explored. Thirdly, additional FELA calculations are used to assess the influence of an external cutting shoe on caisson vertical bearing capacity.

6.2 Problem definition

Figure 6.1 outlines the problem considered in this numerical study. A caisson shaft is considered embedded in homogeneous drained Mohr-Coulomb soil, with unit weight, γ', friction angle, ϕ', dilation angle, ψ' and zero cohesion, $c = 0$. The cross-section of the caisson wall is described by the cutting face taper angle, β, wall thickness, B, and internal radius, R. In this chapter the internal soil surface is assumed to always be coincident with the top of the cutting face, reflecting typical excavation of soil from inside the caisson during construction. The external embedment depth relative to the top of the cutting face is given by h, which defines the depth of overburden soil on the external side of the caisson. The interface between the cutting face and the surrounding soil is defined by roughness factor, α_f, such that the interface friction angle, δ_f, is given by $\tan\delta_\mathrm{f} = \alpha_\mathrm{f}\tan\phi'$ (Cassidy and Houlsby, 2002). Values of $\alpha_\mathrm{f} = 0$ and 1 denote a fully smooth and rough interface at the cutting face respectively.

In this chapter, it is assumed that a fully supported lubricated annulus is maintained around the caisson, meaning that no frictional stresses develop on the external surface and it can be treated as a fully smooth interface. It is acknowledged that the results of Chapter 5 and field monitoring (e.g. Royston *et al.*, 2022a) have shown this to typically not be the case for construction in sands.

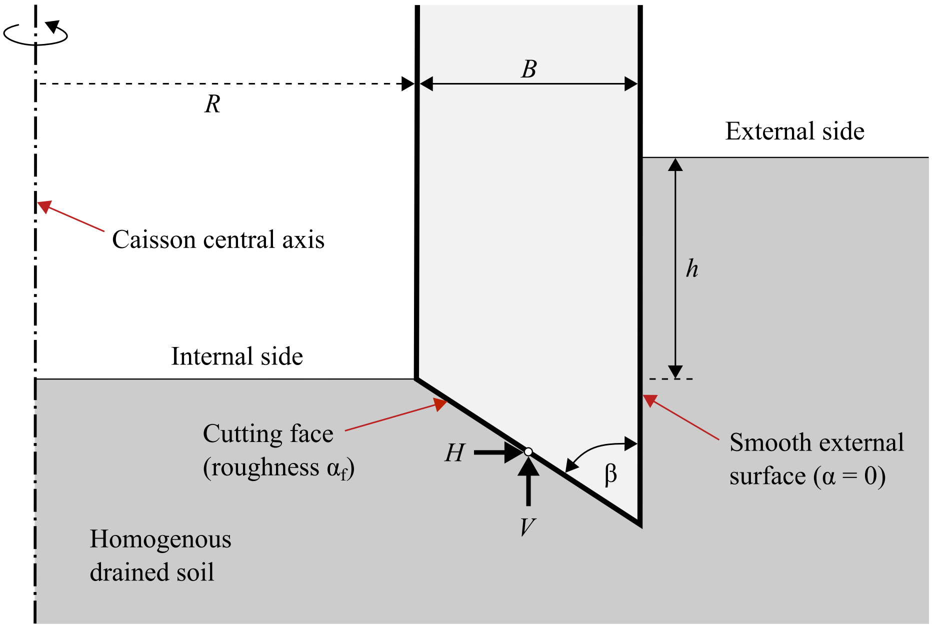

Figure 6.1 Problem definition for the caisson bearing capacity numerical study

However, this assumption isolates the bearing resistance mechanisms from the potentially highly variable external friction. A similar approach has been used in recent numerical research on caisson shafts (e.g. Chavda and Dodagoudar, 2022b; Royston *et al.*, 2022b). Furthermore, the wall section in Figure 6.1 tacitly simplifies the caisson geometry by neglecting the presence of a cutting shoe. This simplification has been used in both numerical and experimental research on caissons (e.g. Chavda and Dodagoudar, 2018; Chavda *et al.*, 2020; Royston *et al.*, 2016, 2022b). The results presented in Section 6.4 are based on this assumption, as it a) creates a practical parameter space for exploration, b) allows detailed observations of the influence of caisson features independently of the choice of cutting shoe, and c) facilitates comparison with previous studies in the literature.

The role of the shoe is to create the annulus towards reducing the soil frictional resistance, but it also widens the effective embedded width of the wall and modifies the geometry of the cutting face. Therefore, a series of additional FELA calculations are presented in Section 6.5 to explore the influence of a cutting shoe on the caisson vertical bearing capacity. For these calculations, the problem definition is modified as shown in Figure 6.2. The cutting shoe is idealised as a rectangular appendage on the external surface of the caisson and is described by the cutting shoe thickness, t, length extending ahead of the apex of the cutting face, l, and length behind the apex, l_{b}. The caisson wall section and cutting shoe are modelled as a single rigid body with interface roughness factors α_{f} and α_{s} for the cutting face and shoe surfaces respectively. It is assumed that no lateral displacement of the external soil surface above the cutting shoe occurs and no frictional stresses develop on the caisson.

Vertical and horizontal bearing forces, denoted V and H respectively, are exerted by the soil on the caisson as it penetrates vertically downwards. The results of this study are expressed in terms of a dimensionless vertical bearing capacity factor, N', defined as:

$$N' = 2\frac{V/A}{\gamma' B_{\mathrm{w}}} \tag{6.1}$$

where A and B_{w} are the embedded area and width of the footing respectively. This factor is analogous to the factor N_{γ} in conventional bearing capacity theory. For the results presented in

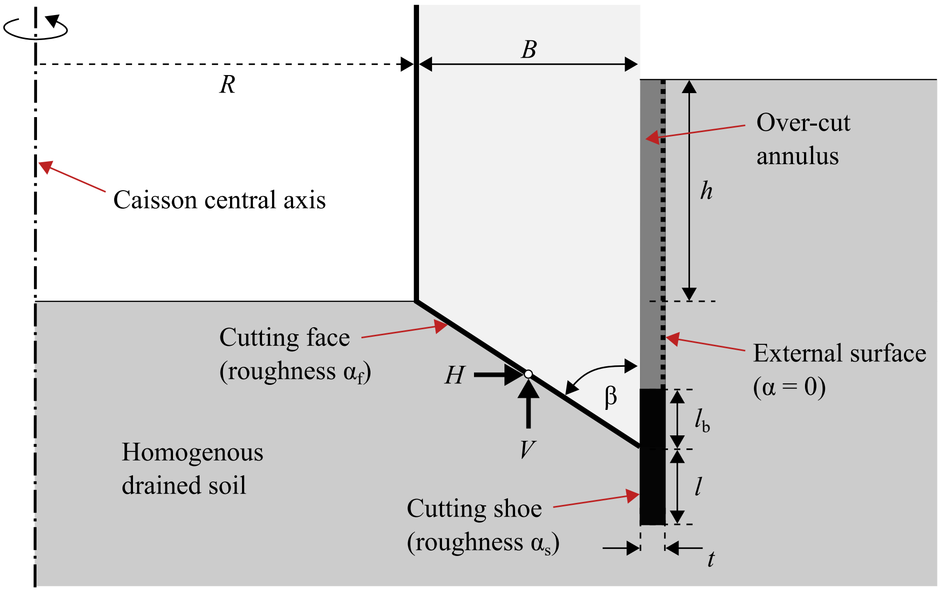

Figure 6.2 Modifications to the problem definition in Figure 6.1 for numerical analysis of the influence of an external cutting shoe on caisson vertical bearing capacity in Section 6.5

Section 6.4, the embedded width is equal to the caisson wall width ($B_\mathrm{w} = B$). For the results in Section 6.5, A and B_w are increased to account for the cutting shoe thickness (i.e. $B_\mathrm{w} = B + t$).

6.3 Numerical modelling methodologies

6.3.1 Finite element limit analysis

The majority of the numerical analyses described in this chapter are performed using the FELA software package OptumG2 (Krabbenhoft *et al.*, 2016). The soil is modelled as a 2D domain of rigid-plastic material obeying the Mohr-Coulomb failure criterion with an associated flow rule ($\psi' = \phi'$). The caisson wall section is modelled as a rigid body with an interface roughness factor of α_f on the cutting face and a fully smooth external vertical surface ($\alpha = 0$). In each analysis strict lower- (LB) and upper-bound (UB) plasticity solutions are computed, bracketing the exact collapse load. The LB analyses use triangular elements with a linear variation in stresses between corner nodes such that yield conditions are enforced at the three corner nodes. The UB analyses use triangular elements with quadratic interpolation of displacements and linear interpolation of stresses. To overcome the issue of locking under plastic flow, kinematically admissible discontinuities are allowed between the elements in upper bound limit analysis (Krabbenhoft *et al.*, 2005). Velocity discontinuities are handled in OptumG2 by including zero-thickness elements of the same type between the continuum triangle elements (Krabbenhoft *et al.*, 2016). The error between the UB and LB plasticity solutions can be defined by:

$$\text{error}(\%) = \pm \frac{\text{UB} - \text{LB}}{\text{UB} + \text{LB}} \tag{6.2}$$

Each model is initially uniformly discretised with 1000 elements, before iterating through eight rounds of adaptive mesh refinement based on the distribution of plastic shear dissipation. After several remeshing iterations, the concentration of elements in the mesh reflects the characteristics of the soil failure mechanisms. The maximum number of elements at the end of the analysis is varied depending on the size of the model, to allow a sufficiently small error to be achieved. In all analyses performed, the final error was less than ±3% and an estimate of the collapse load was obtained by averaging the final LB and UB collapse multipliers.

6.3.2 Finite element analysis

To explore the influence of soil non-associativity on caisson bearing capacity, FEA calculations are also performed in this chapter. Limit analysis approaches, including FELA, are restricted to only considering materials that exhibit an associated flow rule, where the dilation angle is equal to the friction angle, $\psi' = \phi'$ (Frydman and Burd, 1997). Calculations based on associativity remain an important reference, for example in the application of conventional bearing capacity factors in design codes. However, it is widely appreciated that associated flow does not represent realistic behaviour of frictional soils, in which ψ' is typically significantly lower than ϕ' for most practical situations. Non-associativity has been shown to have a considerable influence on foundation bearing capacity calculations. A reduction in capacity, compared to the associated flow case, has been demonstrated in a number of previous studies (e.g. Frydman and Burd, 1997; Krabbenhoft *et al.*, 2012; Loukidis and Salgado, 2009), particularly when there is a large difference between ϕ' and ψ'.

6.3.2.1 Model overview

The FEA calculations in this thesis are performed using the software package Abaqus/ Standard (Simulia, 2020). The soil is defined as a 2D domain modelled using six-node quadratic plane strain triangular elements (CPE6). The caisson section is defined using a separate body meshed with 2-node rigid elements (R2D2), which are tied to a reference node to create a rigid body. The interaction between the soil and caisson section is modelled using surface-to-surface contact with finite-sliding formulation. The normal contact behaviour is defined by the 'hard' pressure-overclosure relationship, and the shear strength of the interface is defined using classical isotropic Coulomb friction.

6.3.2.2 Soil material model

The constitutive model adopted to represent the soil behaviour in this study is linear isotropic elasticity with perfect plasticity, governed by a smooth approximation to the Mohr-Coulomb yield surface. The conventional Mohr-Coulomb criterion is widely applied in classical bearing capacity analyses, but difficulties are typically encountered when using this failure criterion in FEA. Numerical stress integration schemes can fail at stress states near to the gradient discontinuities at the tip and edges of the yield surface. To overcome these numerical difficulties, a smooth approximation to the Mohr-Coulomb criterion is used as the yield function in this study, based on that presented by Abbo *et al.* (2011). Only a brief overview of the main features of the definition of the yield criterion is given in this thesis.

A convenient form of the conventional Mohr-Coulomb criterion was provided by Nayak and Zienkiewicz (1972) using a set of three stress invariants, σ_{m}, $\bar{\sigma}$ and θ:

$$f = \sigma_{\mathrm{m}} \sin\phi' + \bar{\sigma} K(\theta) - c\cos\phi' = 0 \tag{6.3}$$

where c and ϕ' represent the cohesion and friction angle of the soil respectively. The function $K(\theta)$ controls the shape of the yield surface in the octahedral plane, which is defined for the conventional Mohr-Coulomb surface as:

$$K(\theta) = \cos\theta - \frac{1}{\sqrt{3}} \sin\phi' \sin\theta \tag{6.4}$$

In Equations 6.3 and 6.4, σ_m denotes the mean normal stress , $\bar{\sigma}$ is a measure of the deviatoric stress and θ is the Lode angle. For a particular 3D stress state defined in Cartesian axes (x,y,z) expressed in Voigt form, $\boldsymbol{\sigma} = \left[\sigma_\mathrm{xx}\ \sigma_\mathrm{yy}\ \sigma_\mathrm{zz}\ \sigma_\mathrm{xy}\ \sigma_\mathrm{yz}\ \sigma_\mathrm{zx}\right]^\mathrm{T}$, these stress invariants can be defined using the following expressions:

$$\sigma_\mathrm{m} = \frac{1}{3}\left(\sigma_\mathrm{xx} + \sigma_\mathrm{yy} + \sigma_\mathrm{zz}\right) \tag{6.5}$$

$$\bar{\sigma} = \sqrt{\frac{1}{2}\left(s_\mathrm{xx}^2 + s_\mathrm{yy}^2 + s_\mathrm{zz}^2\right) + \sigma_\mathrm{xy}^2 + \sigma_\mathrm{yz}^2 + \sigma_\mathrm{zx}^2} \tag{6.6}$$

$$\theta = \frac{1}{3}\sin^{-1}\left(-\frac{3\sqrt{3}}{2}\frac{J_3}{\bar{\sigma}^3}\right) \tag{6.7}$$

where $J_3 = s_\mathrm{xx}s_\mathrm{yy}s_\mathrm{zz} + 2\sigma_\mathrm{xy}\sigma_\mathrm{yz}\sigma_\mathrm{zx} - s_\mathrm{xx}\sigma_\mathrm{yz}^2 - s_\mathrm{yy}\sigma_\mathrm{zx}^2 - s_\mathrm{zz}\sigma_\mathrm{xy}^2$ and the deviatoric normal stress components are defined as $s_\mathrm{xx} = \sigma_\mathrm{xx} - \sigma_\mathrm{m}$, $s_\mathrm{yy} = \sigma_\mathrm{yy} - \sigma_\mathrm{m}$ and $s_\mathrm{zz} = \sigma_\mathrm{zz} - \sigma_\mathrm{m}$.

The sharp vertex at the tip of the Mohr-Coulomb surface is smoothed by a hyperbolic approximation, as shown in Figure 6.3a alongside the conventional Mohr-Coulomb criterion. This approximation results in a modified form of the Mohr-Coulomb yield function, defined by Abbo *et al.* (2011) as:

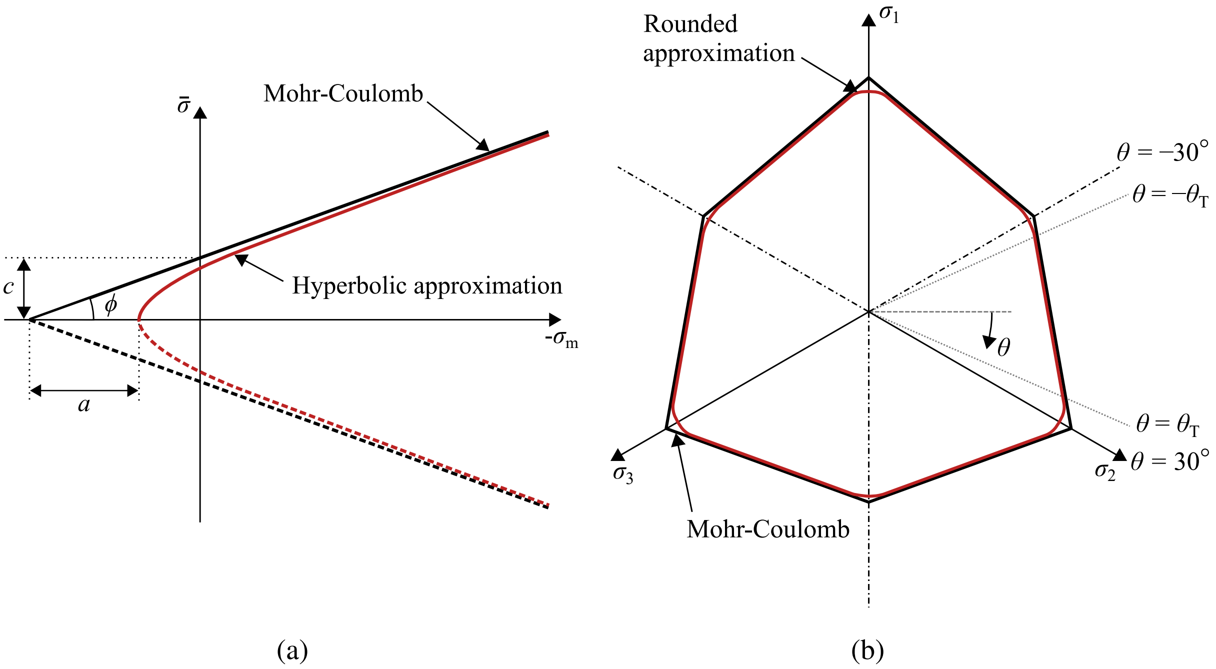

(a) (b)

Figure 6.3 Smoothed approximation to the Mohr-Coulomb criterion: (a) Meridional section, (b) Octahedral section

$$f = \sigma_{\mathrm{m}} \sin\phi' + \sqrt{\bar{\sigma}^2 K^2(\theta) + a^2 \sin^2\phi'} - c\cos\phi' = 0 \tag{6.8}$$

where a is the distance between the tip of the Mohr-Coulomb criterion and the hyperbolic approximation (see Figure 6.3a).

The edge discontinuities of the Mohr-Coulomb surface are smoothed by trigonometric rounding in the octahedral plane in the vicinity of the corners, as shown in Figure 6.3b. This is achieved by redefining the function $K(\theta)$ in Equation 6.8 (or equally in Equation 6.3) as:

$$K(\theta) = \begin{cases} A + B\sin 3\theta + C\sin^2 3\theta & |\theta| > \theta_{\mathrm{T}} \\ \cos\theta - \frac{1}{\sqrt{3}}\sin\phi'\sin\theta & |\theta| \leq \theta_{\mathrm{T}} \end{cases} \tag{6.9}$$

The form of $K(\theta)$ in Equation 6.9 is identical to the conventional Mohr-Coulomb surface (Equation 6.4) for Lode angles of $|\theta| \leq \theta_{\mathrm{T}}$, where θ_{T} is the 'transition angle'. For $|\theta| > \theta_{\mathrm{T}}$, which corresponds to stress states in the vicinity of the edge vertices, the rounding approximation is applied (see Figure 6.3b). In Equation 6.9, A, B and C are coefficients which are defined by Abbo *et al.* (2011) as:

$$A = -\frac{1}{\sqrt{3}}\sin\phi' \langle\theta\rangle \sin\theta_{\mathrm{T}} - B\langle\theta\rangle\sin 3\theta_{\mathrm{T}} - C\sin^2 3\theta_{\mathrm{T}} + \cos\theta_{\mathrm{T}} \tag{6.10}$$

$$B = \frac{1}{18\cos^3 3\theta_{\mathrm{T}}}\left(\langle\theta\rangle\sin 6\theta_{\mathrm{T}}\left(\cos\theta_{\mathrm{T}} - \frac{1}{\sqrt{3}}\sin\phi'\langle\theta\rangle\sin\theta_{\mathrm{T}}\right) - 6\cos 6\theta_{\mathrm{T}}\left(\langle\theta\rangle\sin\theta_{\mathrm{T}} + \frac{1}{\sqrt{3}}\sin\phi'\cos\theta_{\mathrm{T}}\right)\right) \tag{6.11}$$

$$C = \frac{1}{18\cos^3 3\theta_{\mathrm{T}}}\left(-\cos 3\theta_{\mathrm{T}}\left(\cos\theta_{\mathrm{T}} - \frac{1}{\sqrt{3}}\sin\phi'\langle\theta\rangle\sin\theta_{\mathrm{T}}\right) - 3\langle\theta\rangle\sin 3\theta_{\mathrm{T}}\left(\langle\theta\rangle\sin\theta_{\mathrm{T}} + \frac{1}{\sqrt{3}}\sin\phi'\cos\theta_{\mathrm{T}}\right)\right) \tag{6.12}$$

where $\langle\theta\rangle$ denotes the sign function ($\langle\theta\rangle = 1$ for $\theta \geq 0°$ and $\langle\theta\rangle = -1$ for $\theta < 0°$).

This approximation gives a smooth yield function that has both continuous first and second derivatives at all stress states, providing a robust numerical implementation. This approximation is also conservative, remaining internal to the corresponding conventional 'parent' Mohr-Coulomb surface (i.e. for given values of c and ϕ'), and quickly asymptotes to the 'parent' surface as compressive stress increases (see Figure 6.3a).

The closeness-of-fit of the approximation is governed by the selection of parameters a and θ_T. A closer match to the conventional Mohr-Coulomb criterion is achieved by setting a close to zero and θ_T close to 30°. However, values very close to these limits increase the curvature of the yield surface, which can cause numerical integration schemes to fail at stress states near to the vertices. Abbo and Sloan (1995) recommends a value of $a = 0.05c \cot\phi'$ to achieve results which are almost identical to the Mohr-Coulomb model and Abbo *et al.* (2011) suggests typical values for θ_T to be in the range $25° \leq \theta_\mathrm{T} \leq 29.5°$.

A plastic potential function is also required for the definition of material plasticity. In this model, the plastic potential is assumed to be of the same form as the yield function (i.e. Equations 6.8–6.12), except with ϕ' replaced by the dilation angle, ψ'. In the case of associated flow, the dilation angle is equal to the friction angle ($\phi' = \psi'$) and the yield function and plastic potential are the same.

The soil material model is implemented in Abaqus/Standard using a user-defined material subroutine (UMAT) written in Fortran. The adopted numerical stress integration approach is based on the explicit modified Euler scheme, with adaptive sub-stepping and error control, presented by Sloan *et al.* (2001). Details of the algorithms used are provided in Sloan *et al.* (2001) and, for brevity, are not repeated in this thesis. In this study the tolerances on the yield function evaluation and stress error ($FTOL$ and $STOL$ respectively in Sloan *et al.* (2001)) are both taken to be 1×10^{-6}.

6.3.2.3 Adaptive remeshing strategy

The discretisation of the soil domain with finite elements can be a source of inaccuracy in FEA. Errors can arise from using a coarse mesh in regions where there are large gradients in the stresses and strains. This occurs in analyses of foundations, where there are rapid changes in the direction of the displacement vectors at the corners/edges of the structure (Potts and Zdravković, 2001). More accurate modelling of the behaviour in these regions can be obtained by using smaller

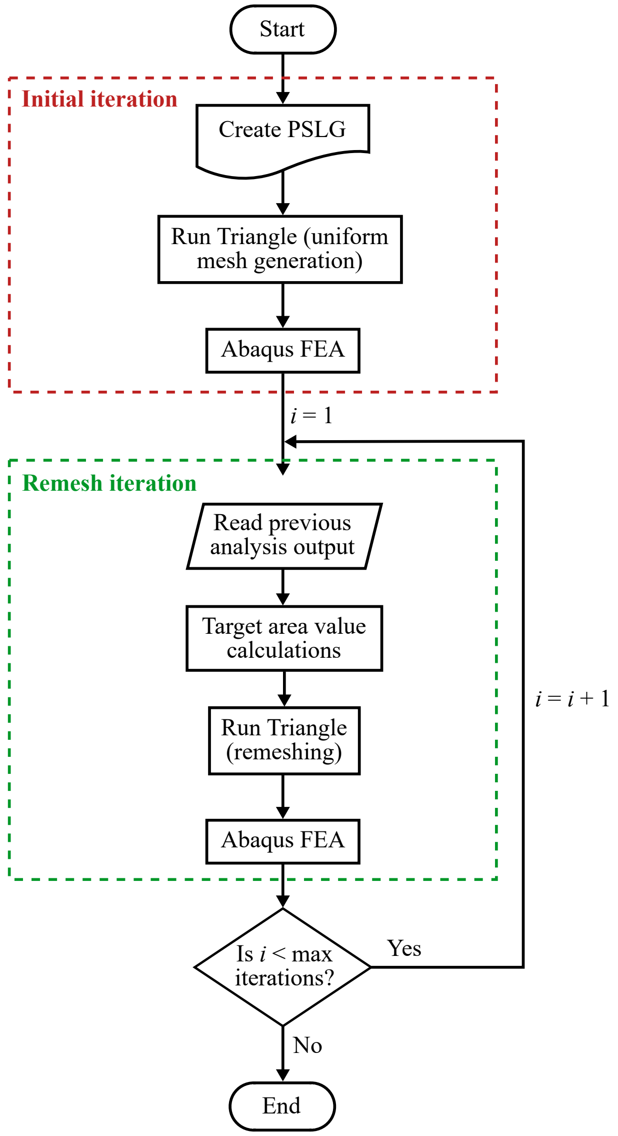

Figure 6.4 Overview of the FEA adaptive remeshing procedure

finite elements. However, using a uniform mesh for this purpose is inefficient, particularly for large problems, as this places many elements outside of the soil failure mechanism. This leads to minimal improvement in the solution accuracy but adds significant computational cost.

A more effective strategy is to concentrate smaller elements in regions of the model where they lead to the greatest improvement of the solution. One such approach is to manually increase the density of elements in certain regions of the mesh, for example near the corners of a foundation. This is straightforward but it relies on prior knowledge of where to refine the mesh, or a trial and error process, to optimise both run time and accuracy. An alternative approach is to use an adaptive remeshing procedure, in which the mesh is iteratively refined over a number of successive analyses. This allows automated and efficient improvement of the solution accuracy.

To obtain accurate bearing capacity predictions in this study, the adaptive mesh refinement procedure described in Martin (2011) is adopted, as summarised in Figure 6.4. The initial analysis starts with the creation of a planar straight-line graph (PSLG) that represents the specified geometry of the problem. The open-source program Triangle (Shewchuk, 1996, 2002) is used to generate a coarse 2D unstructured triangular mesh of the PSLG using conforming constrained Delaunay triangulation. These mesh details are extracted and incorporated into an Abaqus FEA input file. The modelling procedure then enters a series of remeshing iterations, in which the soil domain mesh is progressively refined based on the previous FEA results. The remeshing scheme in this study seeks to equalise the integral of the maximum shear strain rate over all elements in the mesh. In each iteration Triangle is called to refine the previous mesh based on calculated target element area values, before a new FEA input file is generated and supplied to Abaqus.

6.3.3 Modelling preliminaries

In all FELA and FEA calculations in this study, the soil domain is sized such that it comfortably contained the soil failure mechanism for all soil and caisson parameter combinations considered. The lateral boundaries are restrained from movement normal to the respective surface whereas the bottom boundary is restrained from movement in all directions. The following stages of analysis are adopted in the modelling:

1. Initialisation of soil stresses: This is achieved through the application of gravity in the FELA calculations. In the FEA calculations, an initial geostatic stress field is defined for the soil domain and a negative vertical body force is applied to represent the soil weight. This is applied within a ‘geostatic step’ to equilibrate the soil stresses.

2. Wished-in-place installation of a weightless, rigid caisson section of width of $B = 1$ m to an embedment depth h in drained soil with $\gamma' = 1$ kN/m^3, friction angle ϕ', dilation angle ψ'. Additional parameters used specifically in the FEA modelling include the soil Young’s modulus, $E = 5 \times 10^7$ MPa, Poisson’s ratio, $\nu = 0.3$ and rounding

parameters $a = 0.1c\cot(\phi')$ and $\theta_T = 29°$. Note that an unrealistically large E is chosen to approximate rigid-plastic soil behaviour and its value does not influence the resulting plastic collapse load (Griffiths, 1982). A small value for c (typically 5×10^{-4} kPa) is adopted for numerical stability in the FEA calculations. The footing is restrained in all degrees of freedom during this calculation phase.

3. Application of a downward load multiplier (FELA) or prescribed displacement, u (FEA), to the caisson footing until failure is achieved. During this step, only vertical movement is allowed. The treatment of the penetration problem in this way implies that the caisson behaves as a rigid body and remains vertical during the sinking process. In the FEA calculations, the displacement boundary condition is applied to the rigid body reference node and the internal forces V and H in Figure 6.1 are obtained from the reaction forces on this reference node.

6.3.4 Overview of numerical study

Section 6.4 presents the results of a suite of 6300 FELA calculations exploring the following five dimensionless parameters:

a) Soil friction angle, ϕ': 15°, 20°, 25°, 30°, 35°, 40°, 45°;

b) Cutting face taper angle, β: 90°, 75°, 60°, 45°, 30°;

c) Cutting face roughness, α_f: 0, 0.25, 0.5, 0.75, 1;

d) Dimensionless external embedment depth, h/B: 0, 2.5, 5, 7.5, 10, 15;

e) Dimensionless caisson radius, B/R: 0.5, 0.4, 0.3, 0.2, 0.1, 0 (plane strain).

The range of B/R considered extends beyond what is typical for caissons in practice, to explore behaviours at size 'limits'. Similarly, the parametric study includes a range of ϕ' beyond what is applicable to real sand for completeness. The assumption of a constant ϕ' value for each analysis case is a simplification from physical sand behaviour. The peak friction angle will vary with density and confining stress and thus can differ between the interior and exterior of the caisson due to embedment. This will have an influence on the bearing reaction force and the failure mechanisms that result in practice. Further limitations of the modelling are discussed in Section 6.6.

In addition, a limited number of FEA calculations are undertaken to explore: a) the role of soil non-associativity on the caisson vertical bearing capacity, and b) the development of horizontal reaction. Parameters specific to the FEA modelling are listed in Table 6.1. All results presented in Section 6.4 do not include a caisson cutting shoe.

Section 6.5 presents the results of an additional 950 FELA calculations exploring the influence of a cutting shoe on the caisson vertical bearing capacity. The calculations in this section are all conducted with $\beta = 45°$, reflecting the most common design practice in industry (Fischer *et al.*, 2004; Royston *et al.*, 2016). The parameter space outlined in Table 6.2 is used to first investigate the influence of including a cutting shoe on the vertical bearing resistance of a shallow, plane strain inclined footing ($h/B = 0$, $B/R = 0$). These analyses consider a smooth cutting shoe ($\alpha_s = 0$), to isolate the geometric effects of shoe inclusion from any frictional contribution. The influence of dimensionless cutting shoe thickness, t/B, and extension length, l/B, are considered in turn. The ranges of t/B and l/B considered in Table 6.2 are selected to cover the shoe geometries described in case studies in the literature (see Table 2.1).

Additional FELA calculations are subsequently undertaken to investigate the influence of a cutting shoe with different interface roughness, α_s. These are considered over a range of dimensionless embedment depths, h/B, and caisson radii, B/R. For these analyses, a 'typical' cutting shoe defined by $t/B = 0.07$ and $l/B = l_b/B = 0.25$ is used, derived from industry experience within the Oxford research group.

Table 6.1 Parameters adopted for the FEA calculations exploring soil non-associativity and horizontal reaction force. $h/B = 0$ and $B/R = 0$ in all analyses.

Parameter	**Value**
Cutting face taper angle, β	90°, 75°, 60°, 45°, 30°
Cutting face roughness, α_f	0, 0.25, 0.5, 0.75, 1.0
Soil friction angle, ϕ'	10°, 20°, 30°, 40°
Soil dilation angle, ψ'	ϕ', $\phi'/2$, $\phi'/4$

Table 6.2 Parameters adopted in the FELA calculations of the influence of cutting shoe geometry on caisson vertical bearing capacity (in Sections 6.5.1 and 6.5.2)

Parameter	**Value**
Soil friction angle, ϕ'	15°, 20°, 25°, 30°, 35°, 40°, 45°
Cutting face taper angle, β	45°
Cutting face roughness, α_f	0, 1
Dimensionless embedment, h/B	0
Dimensionless caisson radius, B/R	0 (plane strain)
Cutting shoe roughness, α_s	0
Dimensionless shoe thickness, t/B	0 (no shoe), 0.05, 0.1, 0.15, 0.2
Dimensionless shoe length, l/B	0, 0.1, 0.2, 0.3, 0.4

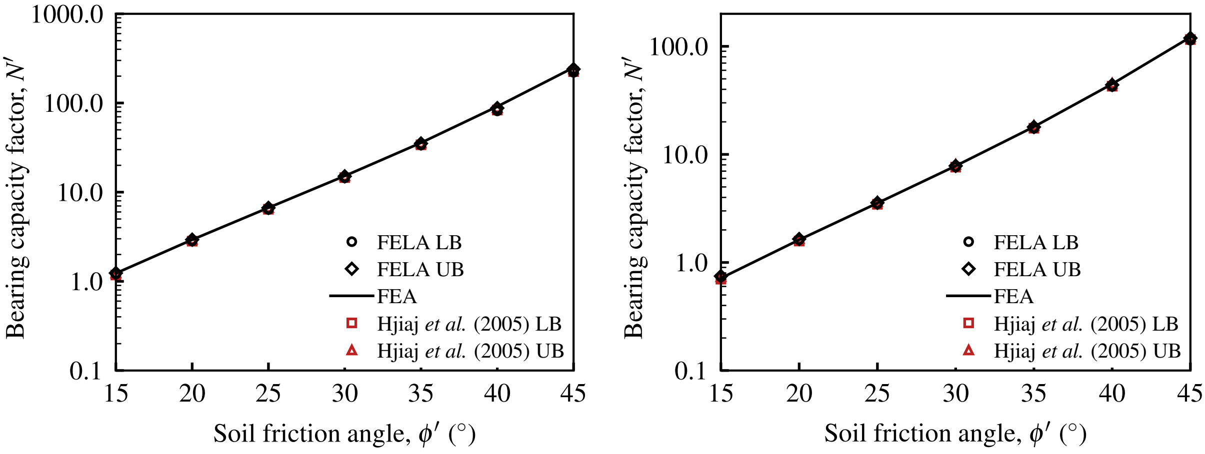

(a) $\alpha_\mathrm{f} = 1$ (b) $\alpha_\mathrm{f} = 0$

Figure 6.5 Validation of present FELA and FEA bearing capacity calculations through comparisons to FELA solutions previously documented by Hjiaj *et al.* (2005) for a flat strip footing ($\beta = 90°$ and $h/B = 0$) with: (a) a rough interface and (b) a smooth interface; $\psi' = \phi'$

6.3.5 Validation of methods

A validation exercise was performed to confirm that the adopted FELA and FEA modelling procedures produce adequate results for the vertical bearing capacity of a surface strip footing with no applied ground surface pressure. Figure 6.5 plots the FELA- and FEA-calculated values of N' (as defined by Equation 6.1) as a function of ϕ'. FELA solutions reported by Hjiaj *et al.* (2005) are also plotted for comparison. It can be observed that the present FELA and FEA

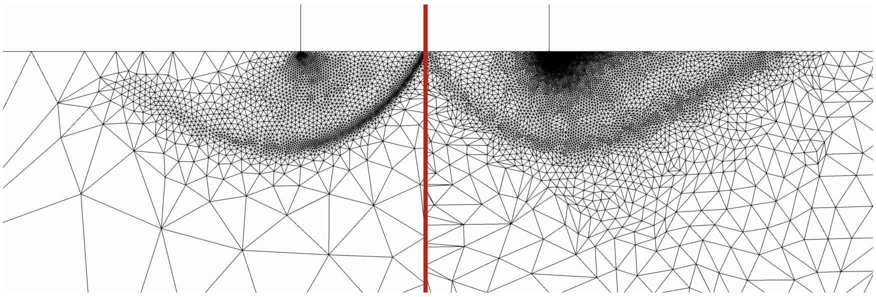

Figure 6.6 Exemplar finite element meshes for a smooth strip footing on soil with $\phi' = 30°$ and $\gamma' = 1\,\mathrm{kN/m^3}$ after adaptive remeshing: left side shows FELA UB analysis (based on shear dissipation rates), right side shows FEA (based on maximum principal strain rates); $\psi' = \phi'$

solutions are in excellent agreement with the Hjiaj *et al.* (2005) solutions for both a rough footing (Figure 6.5a) and smooth footing (Figure 6.5b), giving confidence in the present results.

Figure 6.6 compares an example mesh generated using the custom FEA adaptive remeshing strategy described by Figure 6.4 with the mesh generated using the FELA adaptive meshing implementation in OptumG2. It can be qualitatively observed that both meshes are in good agreement. After several iterations of adaptive refinement, the elements become increasingly concentrated in regions where the intensity of shearing is greatest. This results in velocity discontinuities appearing as dark bands of high density of small elements, regions of diffuse plastic shearing undergo intermediate levels of refinement and rigid blocks remain largely unrefined (Martin, 2011). Figure 6.7 also considers the performance of the FEA adaptive remeshing scheme. Figure 6.7a shows the FEA-calculated values of N' converge closely to the FELA LB and UB as the total number of elements increases. When the same analyses are performed with a uniform mesh using approximately the same number of elements, much poorer bearing capacity solutions are produced. Five adaptive iterations are adopted for the FEA calculations in this study. Further mesh refinement only produces a minor improvement in solution accuracy but this comes with a significant increase in computational effort (Figure 6.7b).

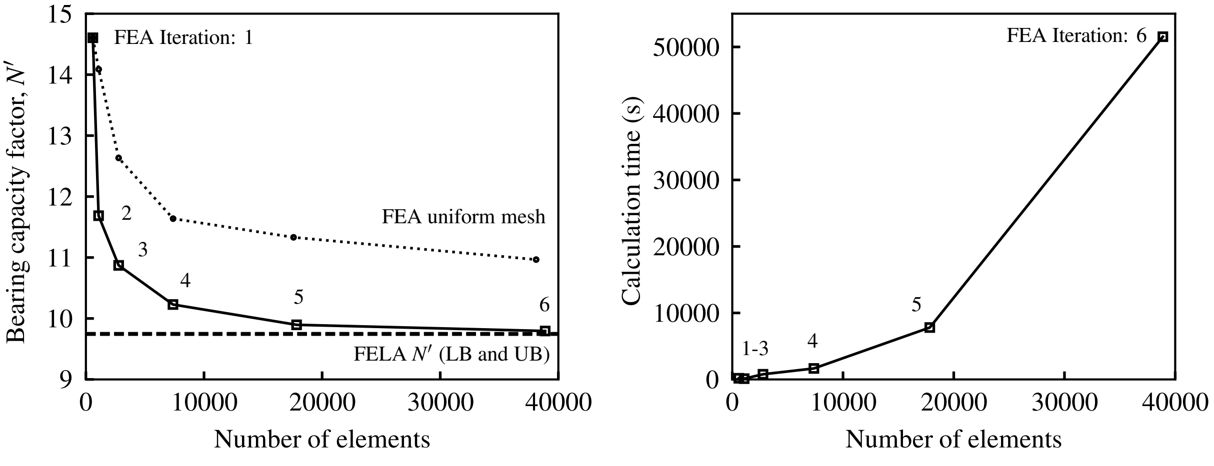

(a) (b)

Figure 6.7 Evaluation of FEA adaptive remeshing using the example of a smooth $\beta = 45°$ caisson footing ($h/B = 0$, $B/R = 0$, $\psi' = \phi'$): (a) N' convergence, (b) computation time

6.4 Numerical results

6.4.1 Influence of cutting face taper angle

The FELA-calculated influence of β on N' for a shallow footing ($h/B = 0$) is presented in Figure 6.8 considering both a rough ($\alpha_\mathrm{f} = 1$) and smooth ($\alpha_\mathrm{f} = 0$) cutting face and values of ϕ' ranging between 15° and 45°. Considering first the results for $\alpha_\mathrm{f} = 1$ (Figure 6.8a), a reduction in β causes an increase in N' for all values of ϕ' where an approximately log-linear relationship can be observed. These data are re-plotted in Figure 6.8b except that values of N' have been normalised by the corresponding flat footing values, $N'_{\beta=90°}$. It can be seen that the gradient of $N'/N'_{\beta=90°}$ with respect to β is a function of ϕ' and that β has less of an influence on the vertical bearing capacity for high-ϕ' soil.

Similar observations may be deduced from the corresponding figures for $\alpha_\mathrm{f} = 0$ (Figures 6.8c and 6.8d). In this case, there is greater non-linearity in the relationship between $N'/N'_{\beta=90°}$ and β. Interestingly, a reduction in β causes an increase and reduction in the bearing capacity for small and large values of ϕ' respectively. To further explore the source of these differences, soil failure mechanisms corresponding to $\beta = 90°$, 75° and 30° are presented in Figure 6.9 for $\phi' = 15°$ and 45°. The mechanisms are interpretted from the mesh refinement in the final UB FELA calculations. For $\phi' = 15°$ a reduction in β causes an increase in the size of the failure mechanism, due to the greater embedded depth of the caisson apex point (see Figures 6.9a, 6.9c and 6.9e). For $\phi' = 45°$, while a reduction in β from 90° to 75° causes an increase in the size of the failure mechanism on the internal side, this is balanced by a reduction in the mechanism on the external side (see Figures 6.9b and 6.9d). A further reduction in β to 30° causes the failure mechanism to move entirely to the internal side (Figure 6.9f).

6.4.2 Influence of external embedment depth

FELA calculations of the influence of the dimensionless external embedment depth, h/B, on the vertical bearing capacity are plotted in Figure 6.10. The raw N' values are presented in

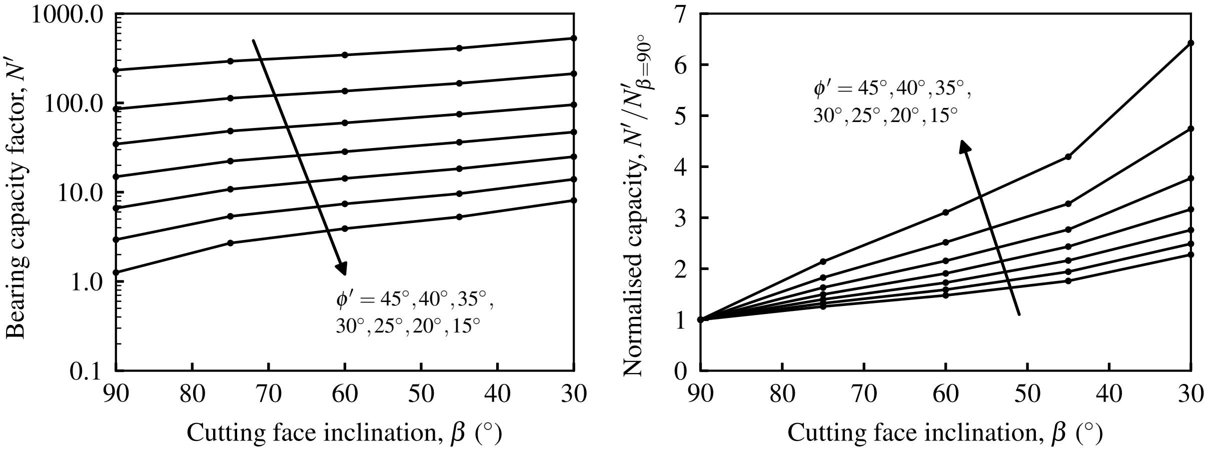

(a) $\alpha_f = 1$ (b) $\alpha_f = 1$

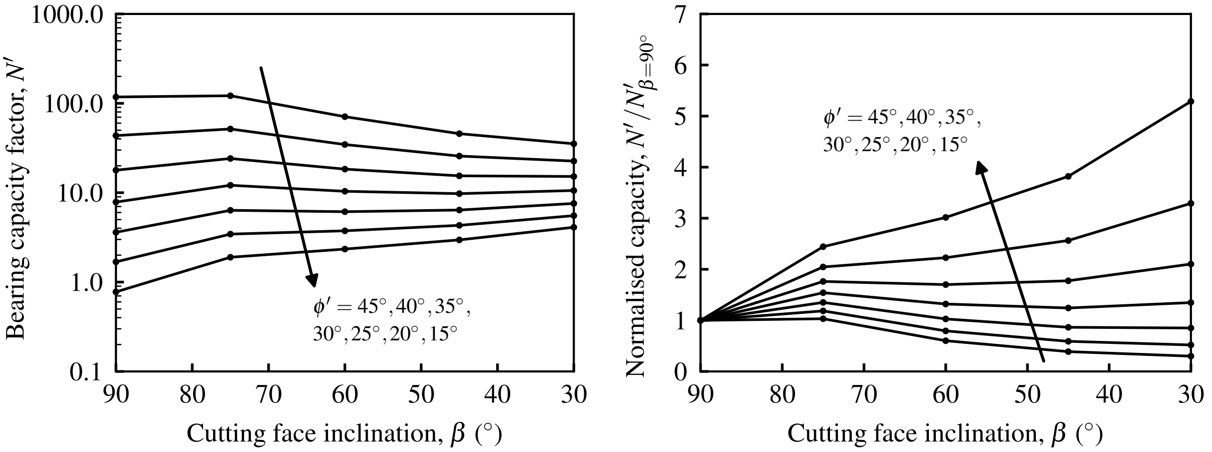

(c) $\alpha_f = 0$ (d) $\alpha_f = 0$

Figure 6.8 FELA-calculated influence of cutting face taper angle, β, on vertical bearing capacity: (a) N' ($\alpha_f = 1$), (b) $N'/N'_{\beta=90°}$ ($\alpha_f = 1$), (c) N' ($\alpha_f = 0$), (d) $N'/N'_{\beta=90°}$ ($\alpha_f = 0$); flat surface ($h/B = 0$), plane strain ($B/R = 0$), $\psi' = \phi'$

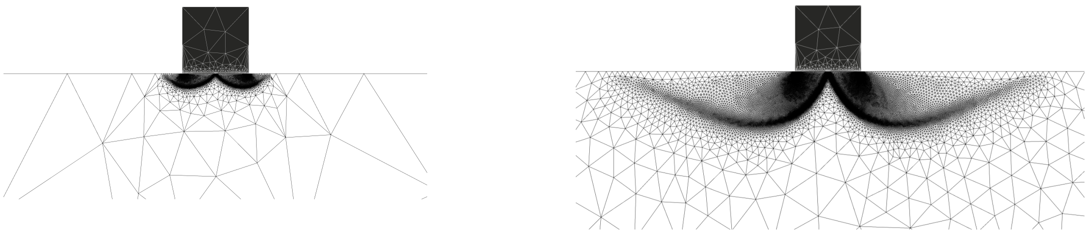

(a) $\beta = 90°$, $\phi' = 15°$ (b) $\beta = 90°$, $\phi' = 45°$

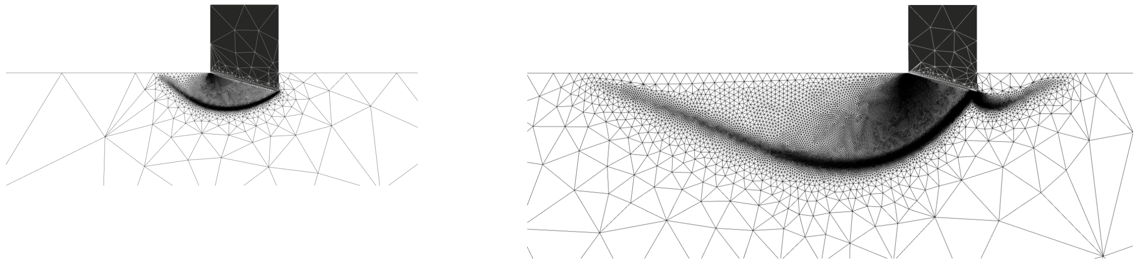

(c) $\beta = 75°$, $\phi' = 15°$ (d) $\beta = 75°$, $\phi' = 45°$

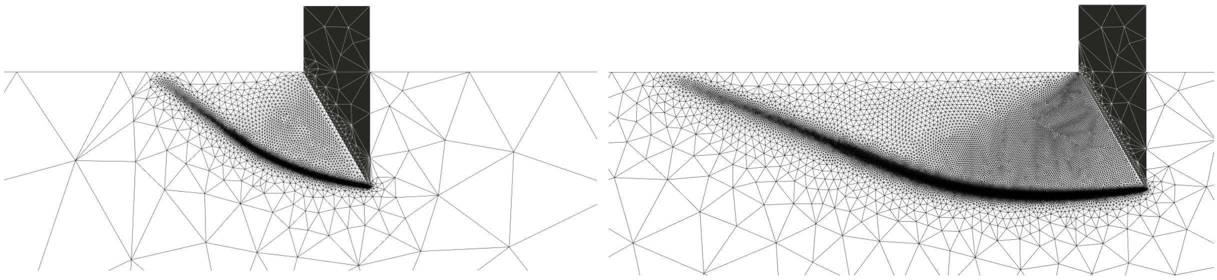

(e) $\beta = 30°$, $\phi' = 15°$ (f) $\beta = 30°$, $\phi' = 45°$

Figure 6.9 FELA-calculated influence of cutting face taper angle, β, on soil failure mechanisms for a smooth face ($\alpha_\mathrm{f} = 0$); flat surface ($h/B = 0$), plane strain ($B/R = 0$), $\psi' = \phi'$

Figures 6.10a and 6.10c for $\alpha_\mathrm{f} = 1$ and 0 respectively; Figures 6.10b and 6.10d present the same results with N' normalised by the corresponding flat surface values, $N'_{h=0}$. For the sake of clarity, only salient values of β and ϕ' are considered in this and subsequent figures. It can be observed that the influence of h/B is highly dependent on the cutting face taper angle and roughness, and the soil friction angle.

For example in the case of $\alpha_\mathrm{f} = 1$, h/B has a negligible influence on N' for $\beta = 30°$ regardless of soil ϕ'. For $\beta = 75°$, an increase in h/B causes a minor increase in N' for $\phi' = 20°$ and a significant increase for $\phi' = 45°$. These results indicate that an increase in h/B has a significant influence on bearing capacity for high-ϕ' soil and flatter taper angles (large β) with a rough cutting face. For the $\beta = 75°$ analyses, there also appears to be a critical embedment depth,

h_{crit}, beyond which further increasing h has a negligible effect on N'. For the case of $\phi' = 45°$ and $\beta = 75°$, an approximate value of $h_{\mathrm{crit}}/B = 10$ is obtained. Moreover, h appears to have a significantly greater influence on bearing capacity for a rough cutting face (Figure 6.10b). Figure 6.10d shows the influence of h to be virtually negligible for a smooth face at all β and ϕ' values considered.

The underpinning cause for the occurrence of h_{crit} is explored via the soil failure mechanisms presented in Figures 6.11a–c, corresponding to points (i) to (iii) marked on Figure 6.10b. Aside from increasing the confining stress acting on the soil shear failure planes, an increase in h/B from 0 to 5 also causes an extension of the soil failure mechanism on the external side of the

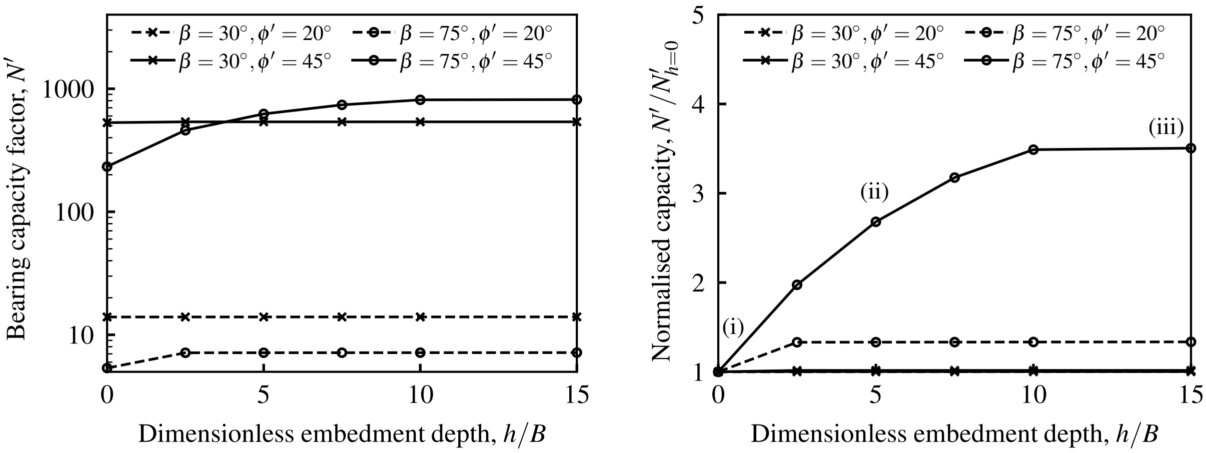

(a) $\alpha_{\mathrm{f}} = 1$ (b) $\alpha_{\mathrm{f}} = 1$

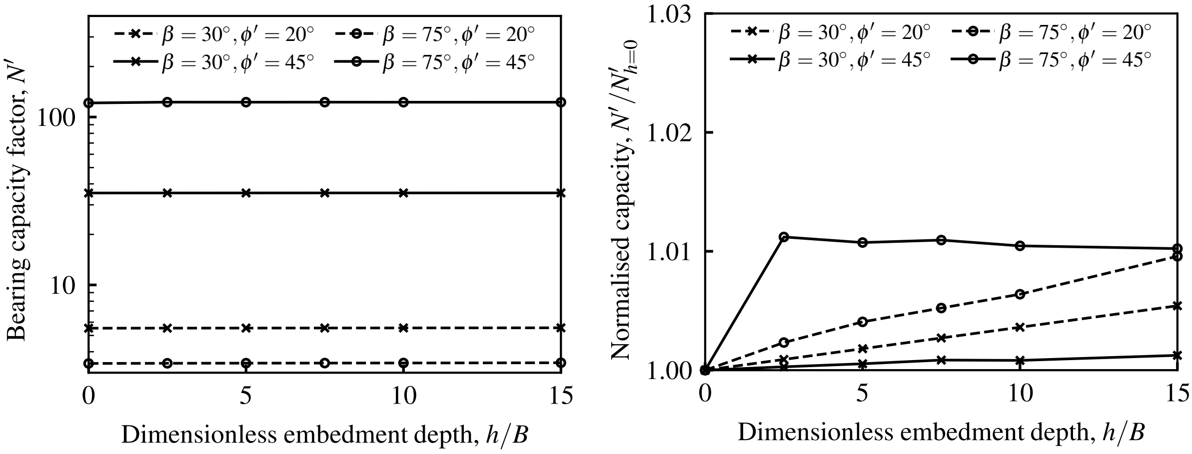

(c) $\alpha_{\mathrm{f}} = 0$ (d) $\alpha_{\mathrm{f}} = 0$

Figure 6.10 FELA-calculated influence of embedment depth, h, on the vertical bearing capacity: (a) N' ($\alpha_{\mathrm{f}} = 1$), (b) $N'/N'_{h=0}$ ($\alpha_{\mathrm{f}} = 1$), (c) N' ($\alpha_{\mathrm{f}} = 0$), (d) $N'/N'_{h=0}$ ($\alpha_{\mathrm{f}} = 0$); plane strain ($B/R = 0$), $\psi' = \phi'$

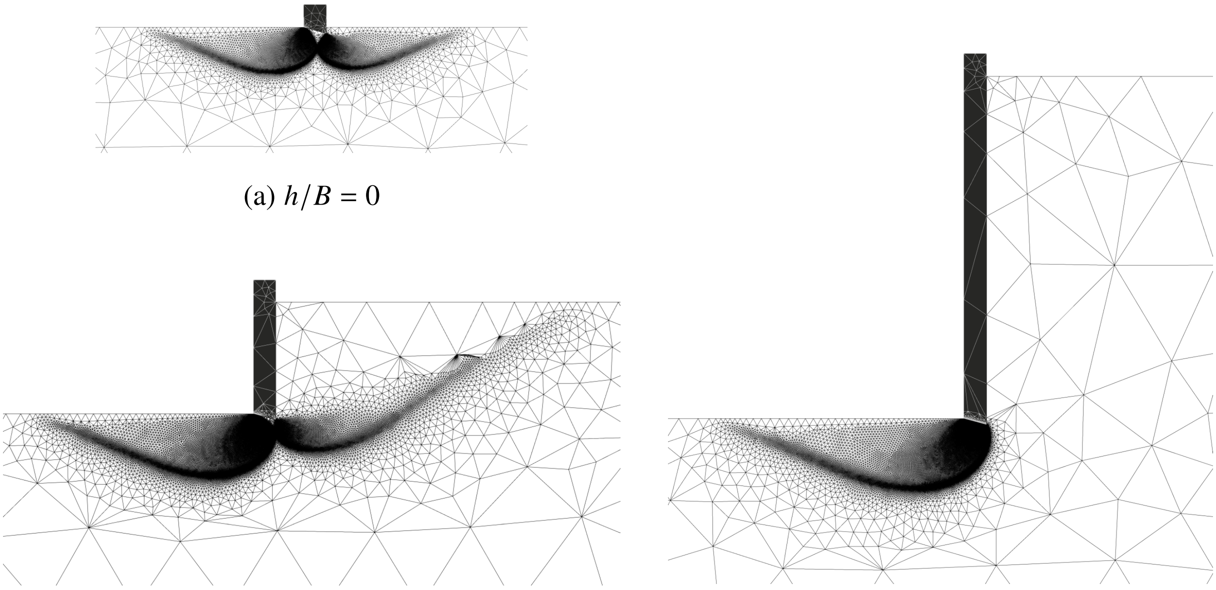

(a) $h/B = 0$

(b) $h/B = 5$

(c) $h/B = 15$

Figure 6.11 FELA-calculated influence of external embedment depth, h, on soil failure mechanisms for a rough cutting face ($\alpha_\mathrm{f} = 1$) with $\beta = 75°$ and $\phi' = 45°$; plane strain ($B/R = 0$), $\psi' = \phi'$

caisson wall (Figure 6.11b). However, it can be seen that an increase in h/B from 5 to 15 causes the soil failure mechanism to become confined to the internal side only (Figure 6.11c). Thus, any further increases in embedment causes a negligible increase in capacity, for the problem considered here. Cases which have an internal soil failure mechanism at $h/B = 0$ (e.g. $\beta = 30°$ at all ϕ' considered) continue to show an internal mechanism only at $h/B > 0$, hence explaining the negligible influence of embedment depth and the non-existence of h_crit in these results.

6.4.3 Influence of caisson radius

Figure 6.12 presents the FELA-calculated influence of caisson radius on the vertical bearing capacity for a typical deep embedment case ($h/B = 15$). The capacity factor N' is normalised by the corresponding plane strain values, $N'_{R=\infty}$, and the results are plotted as a function of the reciprocal of the dimensionless caisson radius, B/R. In general, the development of the logarithm of $N'/N'_{R=\infty}$ appears to be an approximately linear response to an increase in B/R for both $\alpha_\mathrm{f} = 1$ (Figure 6.12a) and $\alpha_\mathrm{f} = 0$ (Figure 6.12b). In all cases, a decrease in caisson radius (increase in B/R) causes an increase in the normalised bearing capacity. This can be attributed to an increase in radial stress caused by a decrease in caisson radius. However, the gradients of the curves presented in Figure 6.12 appear to be dominated by ϕ': high-ϕ' soil causes a significant dependency of N' on B/R, regardless of α_f.

In contrast, the cutting face taper angle has less of an influence on this relationship. For smaller caisson radii an increase in β from 30° to 75° causes a reduction in $N'/N'_{R=\infty}$ for $\alpha_\mathrm{f} = 1$. From the corresponding failure mechanisms presented in Figures 6.13a and 6.13b for $\beta = 30°$ and 75° respectively, it can be observed that both failure mechanisms extend to the external side of the caisson at the smaller caisson radii, compared to only an internal failure mechanism in the plane strain case (Figure 6.11c). The external mechanism corresponding to $\beta = 30°$ extends further downwards into soil with higher confining stresses (and therefore strength), causing a greater contribution to the bearing capacity. Conversely, for $\alpha_\mathrm{f} = 0$ an increase in β from 30° to 75° causes only a marginal increase in $N'/N'_{R=\infty}$. From Figures 6.13c and 6.13d it can be observed that reducing the caisson radius causes the soil failure mechanism to be confined internally regardless of β.

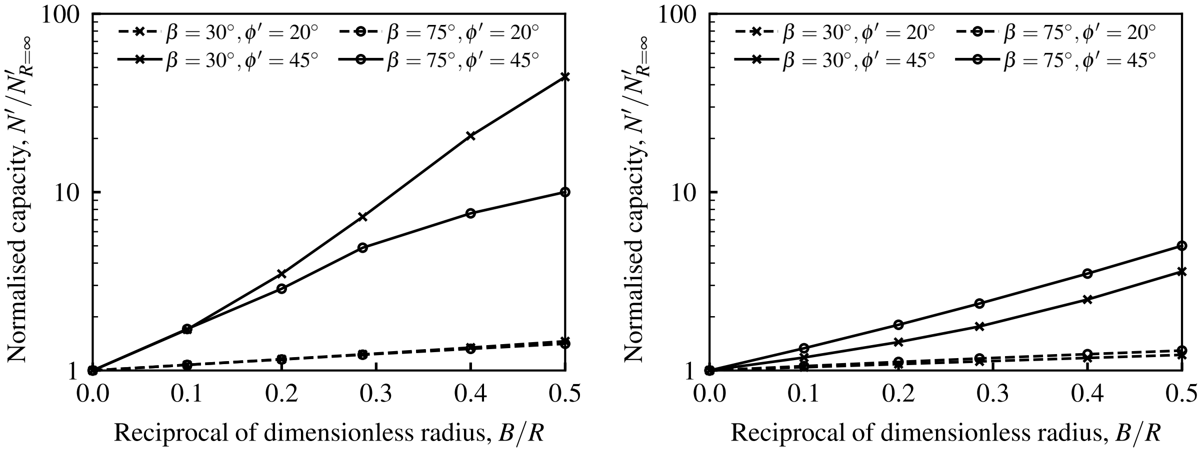

(a) $\alpha_\mathrm{f} = 1$

(b) $\alpha_\mathrm{f} = 0$

Figure 6.12 FELA-calculated influence of the caisson internal radius, R, on the vertical bearing capacity normalised by the corresponding plane strain values, $N'/N'_{R=\infty}$, for a deep embedment of $h/B = 15$; $\psi' = \phi'$

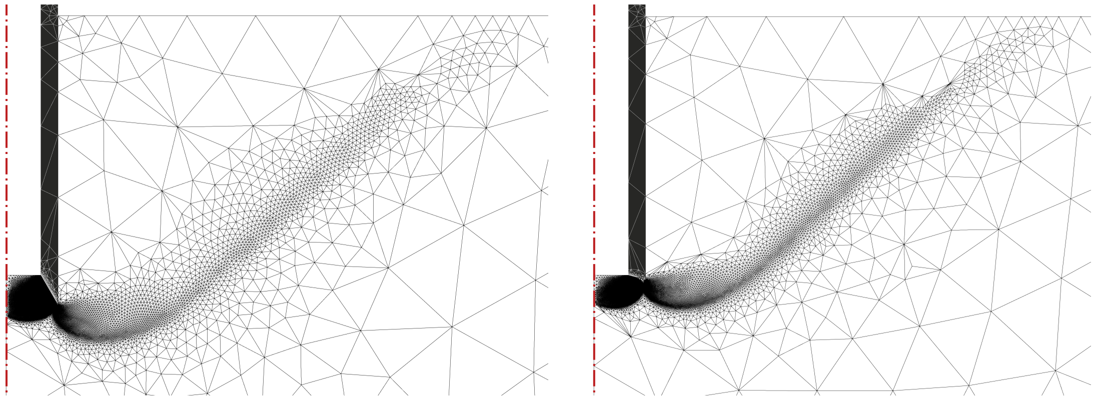

(a) $\beta = 30°$, $\alpha_\mathrm{f} = 1$ (b) $\beta = 75°$, $\alpha_\mathrm{f} = 1$

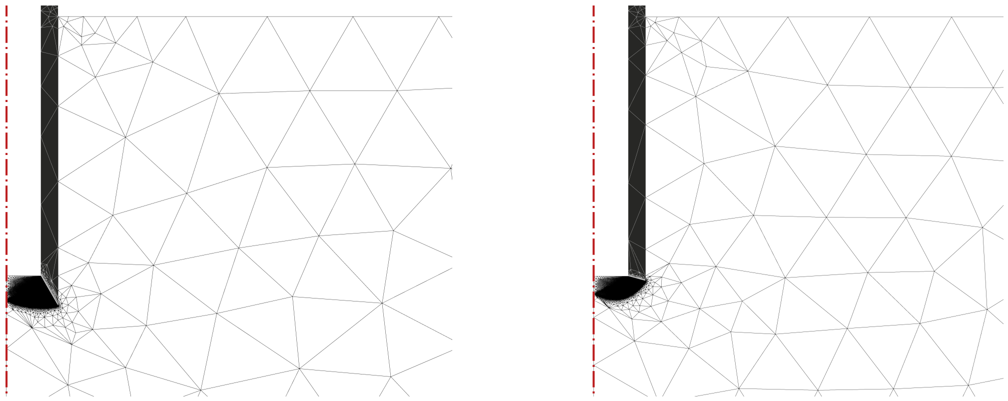

(c) $\beta = 30°$, $\alpha_\mathrm{f} = 0$ (d) $\beta = 75°$, $\alpha_\mathrm{f} = 0$

Figure 6.13 FELA calculations of the soil failure mechanisms for a small diameter caisson ($B/R = 0.5$) at deep embedment $h/B = 15$ with different cutting face taper angles and interface roughness; $\phi' = 45°$, $\psi' = \phi'$

6.4.4 Influence of soil non-associativity

All of the results presented thus far in this chapter have been conducted with FELA and therefore have assumed an associated flow rule for the Mohr-Coulomb material. In Figure 6.14a, the role of soil non-associativity on the vertical bearing capacity for a rough cutting face with $\beta = 45°$ at $h/B = 0$ is investigated using FEA. Also superimposed on this plot are the corresponding FELA results from Figure 6.8a. For the associated flow analyses ($\psi' = \phi'$), there is good agreement between the FELA and FEA calculations, with a maximum 3.5% difference at $\phi' = 40°$. A reduction in ψ' (non-associated flow) leads to a decrease in the vertical bearing resistance in all cases. In Figure 6.14b, the FEA results are normalised by the corresponding FEA associated flow values, $N'_{\psi'=\phi'}$. The reduction in bearing capacity is greater for a larger degree of non-

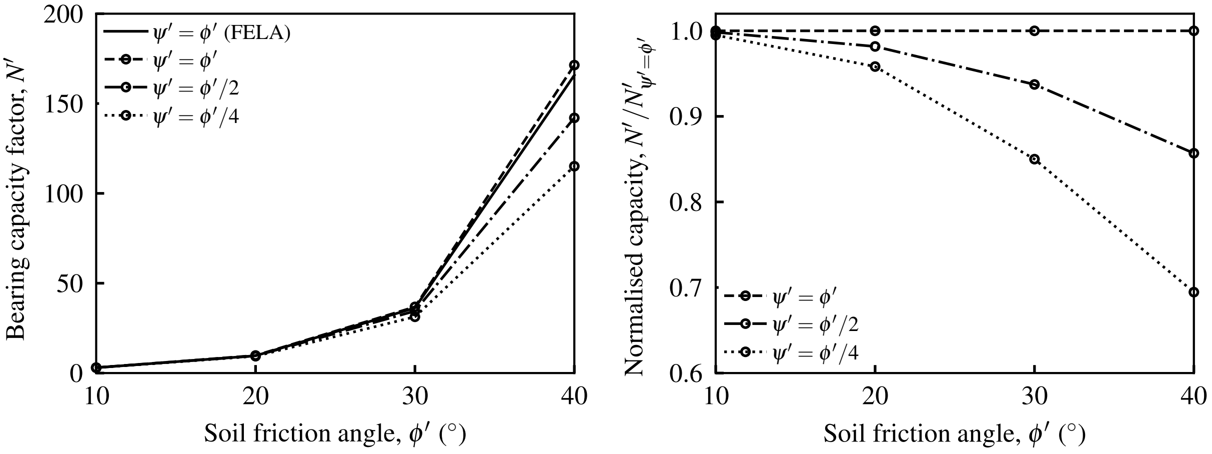

(a) (b)

Figure 6.14 FEA-calculated influence of soil non-associativity on the vertical bearing capacity for a rough $\beta = 45°$ cutting face: (a) N', (b) $N'/N'_{\psi'=\phi'}$; flat surface ($h/B = 0$), plane strain ($B/R = 0$)

associativity, $\phi' - \psi'$. Furthermore, the results show the influence of non-associativity is strongly dependent on ϕ'; at low-ϕ' the influence is negligible, whereas at high-ϕ' there is a significant reduction in N' compared to associated flow. These observations are in agreement with previous FEA studies on strip footings (Frydman and Burd, 1997; Loukidis and Salgado, 2009), and ring footings (Benmebarek *et al.*, 2012).

The FEA-calculated influence of non-associativity on N' for rough cutting face is plotted as a function of β in Figure 6.15. Only a single high value of $\phi' = 40°$ is considered for brevity, influenced by the observations of Figure 6.14. Again it can be seen that there is relatively close

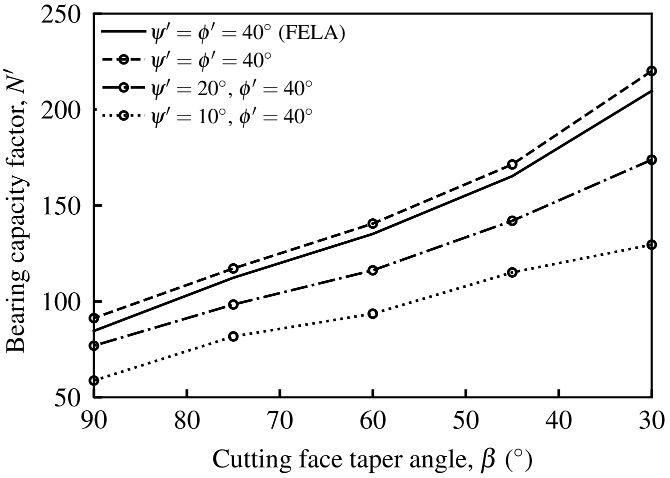

Figure 6.15 FEA-calculated influence of soil non-associativity on the relationship between N' and β for a rough cutting face ($\alpha_f = 1$); flat surface ($h/B = 0$), plane strain ($B/R = 0$)

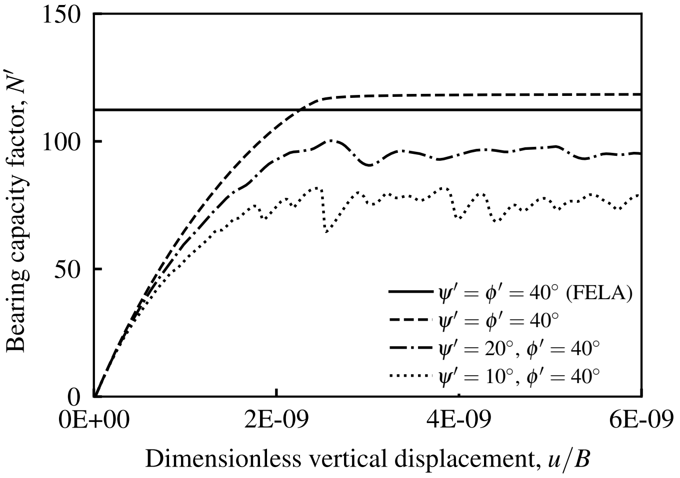

Figure 6.16 Example of the non-dimensionalised load-displacement responses calculated using FEA for a rough cutting face with $\beta = 75°$; flat surface ($h/B = 0$), plane strain ($B/R = 0$)

agreement between the FEA and selected FELA results for the associated flow analyses for all β, and that there is a significant reduction in N' for non-associated flow cases ($\psi' < \phi'$). The effect of non-associativity appears to only have very minor dependence on β.

In Figure 6.16, it can be seen that soil non-associativity causes oscillations to manifest in the non-dimensionalised load-displacement curves when $\psi' < \phi'$. These oscillations are exacerbated with high-ϕ soil and by an increase in $\phi' - \psi'$. In this study, the collapse loads in Figures 6.14 and 6.15 are selected as the maximum observed load, in accordance with the approach taken by Loukidis and Salgado (2009). The failure mechanisms corresponding to the FEA calculations in Figure 6.16 are shown in Figure 6.17. A reduction in ψ' causes a change in the shape of the failure mechanism as well as a reduction in overall size, elucidating the observed reduction in N'. Another important consequence of non-associativity is the presence of thin localised shear bands. These features of non-associated flow behaviour are well-documented and do not undermine the validity of the present FEA results (De Borst and Vermeer, 1984; Drescher and Detournay, 1993; Vermeer, 1990).

6.4.5 Horizontal reaction force

The FEA calculations are also able to provide insights into the development of horizontal force, H, on the caisson cutting face during vertical penetration. The results are presented in terms

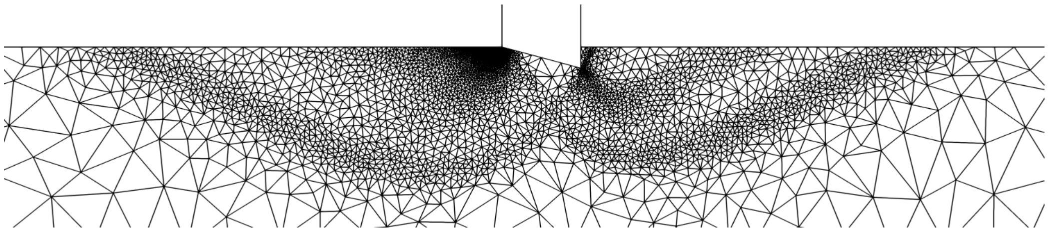

(a) $\psi' = 40°$

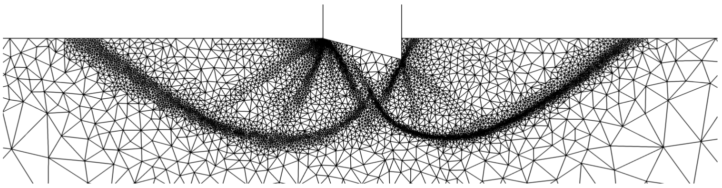

(b) $\psi' = 20°$

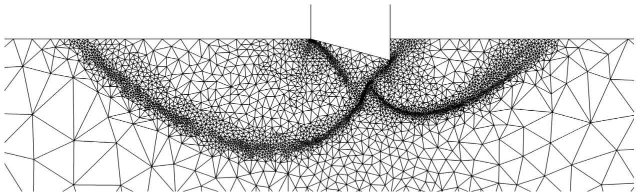

(c) $\psi' = 10°$

Figure 6.17 FEA calculated influence of soil non-associativity on soil failure mechanisms for $\beta = 45°$ footing with a rough cutting face ($\alpha_f = 1$); $\phi' = 40°$, flat surface ($h/B = 0$), plane strain ($B/R = 0$)

of a dimensionless horizontal capacity factor $H' = 2(H/A)/\gamma' B_w$, with parameters as defined for Equation 6.1. Figure 6.18 presents the FEA-calculated influence of β on H' for a shallow plane strain footing. For both rough (Figure 6.18a) and smooth (Figure 6.18c) cutting faces, much greater horizontal forces develop for steeper cutting face inclinations (lower β). This can be attributed to the increased horizontal projected area of the cutting face. As expected, larger horizontal forces are experienced with rough faces compared to smooth, and the horizontal force drops to zero in the all of the flat footing cases ($\beta = 90°$).

Interestingly, although both N' and H' increase dramatically with ϕ', the relative magnitude is different depending on face roughness. Figures 6.18b and 6.18d plot the ratio between the horizontal and vertical capacities, H'/N', for $\alpha_f = 1$ and 0 respectively. For a smooth face, H'/N' increases with ϕ' for all β (Figure 6.18d). The horizontal force can be seen to exceed the vertical capacity in the case of a steep cutting face ($\beta < 45°$) at high friction angles. Conversely

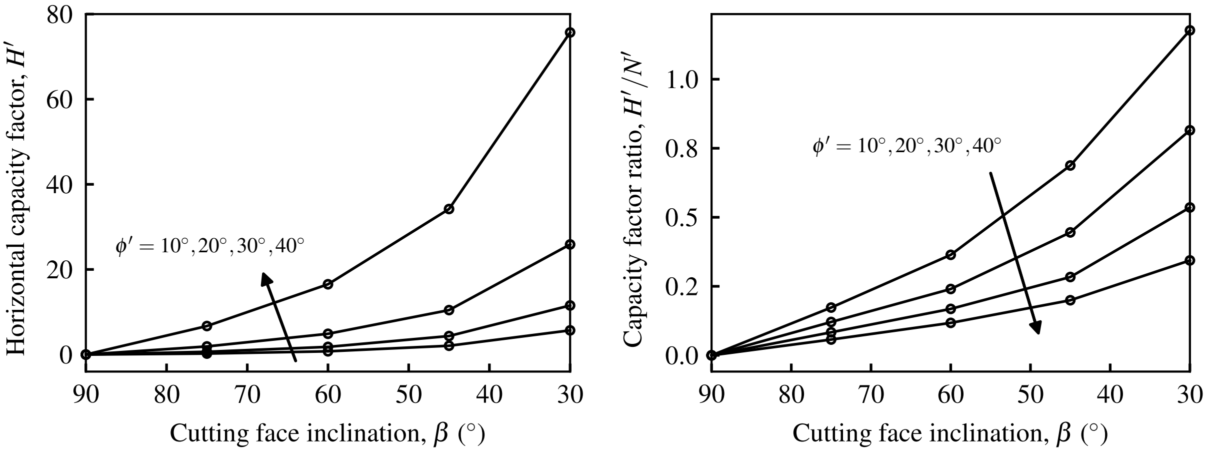

(a) $\alpha_f = 1$

(b) $\alpha_f = 1$

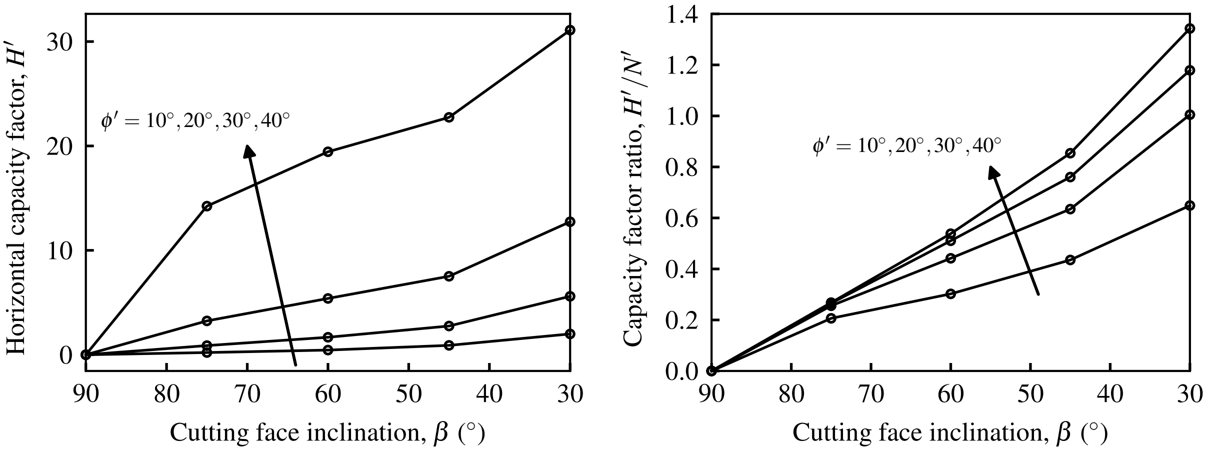

(c) $\alpha_f = 0$

(d) $\alpha_f = 0$

Figure 6.18 FEA-calculated influence of cutting face taper angle β on horizontal capacity: (a) H' ($\alpha_f = 1$), (b) H'/N' ($\alpha_f = 1$), (c) H' ($\alpha_f = 0$), (d) H'/N' ($\alpha_f = 0$); flat surface ($h/B = 0$), plane strain ($B/R = 0$), $\psi' = \phi'$

for a rough face, H'/N' decreases with ϕ' for all β. The horizontal force again exceeds the vertical capacity for a steep cutting face, but only at low friction angles.

Figures 6.19a and 6.19b plot the FEA-calculated influence of α_f on H' and N' respectively for a shallow plane strain footing at $\phi' = 30°$. For all β considered, increasing the cutting face roughness causes an increase in N', which is attributable to an increase in the size of the soil failure mechanisms. However, the influence of α_f on H' is observed to depend highly on β. For $\beta = 30$, 45 and 60°, H' increases to a maximum value at an intermediate α_f, before decreasing as roughness increases further.

The influence of α_f on H' is determined by the soil failure mechanisms. For $\beta = 30$, 45 and

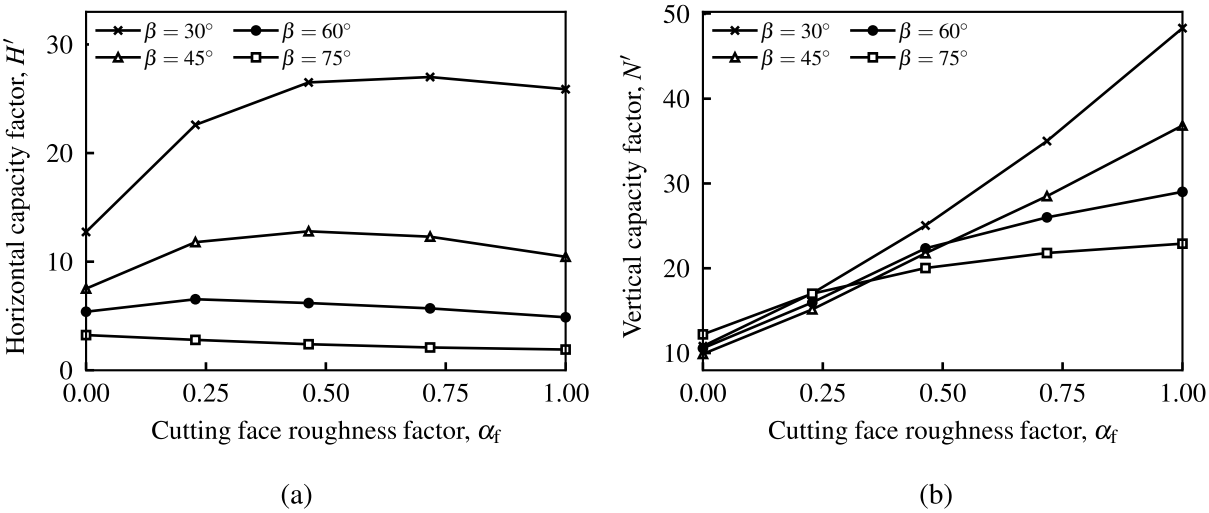

Figure 6.19 FEA-calculated influence of cutting face interface roughness α_f on bearing capacity with $\phi' = 30°$: (a) H', (b) (a) N'; flat surface ($h/B = 0$), plane strain ($B/R = 0$), $\psi' = \phi'$

60° in Figure 6.19a, at low α_f the soil failure mechanism is only present on the internal side of the footing. As α_f increases, the maximum H' occurs when an external mechanism begins to form. The decrease in H' at higher α_f is attributable to a 'balancing' of the horizontal force, as the increased roughness causes a greater increase in size of the external failure mechanism. For $\beta = 75°$ in Figure 6.19a, an external failure mechanism is present for all $0 \leq \alpha_\mathrm{f} \leq 1$. Therefore, the horizontal failure mechanism 'balancing' leads to a monotonic decrease in H' with increasing α_f. For cases when only an internal mechanism is present for all $0 \leq \alpha_\mathrm{f} \leq 1$, increasing α_f causes an increase in both N' and H'. This occurs for steep footings at low ϕ'.

6.5 Consideration of an external cutting shoe

6.5.1 Influence of cutting shoe thickness

The influence of a cutting shoe inclusion with a dimensionless thickness t/B on the vertical bearing capacity is presented in Figures 6.20a and 6.20b for a rough and smooth cutting face respectively. These results are plotted as the calculated N' values normalised by the corresponding capacity with no cutting shoe, $N'_{t=0}$. In these initial analyses the cutting shoe is assumed to have zero length ($l/B = 0$) and to be smooth ($\alpha_\mathrm{s} = 0$).

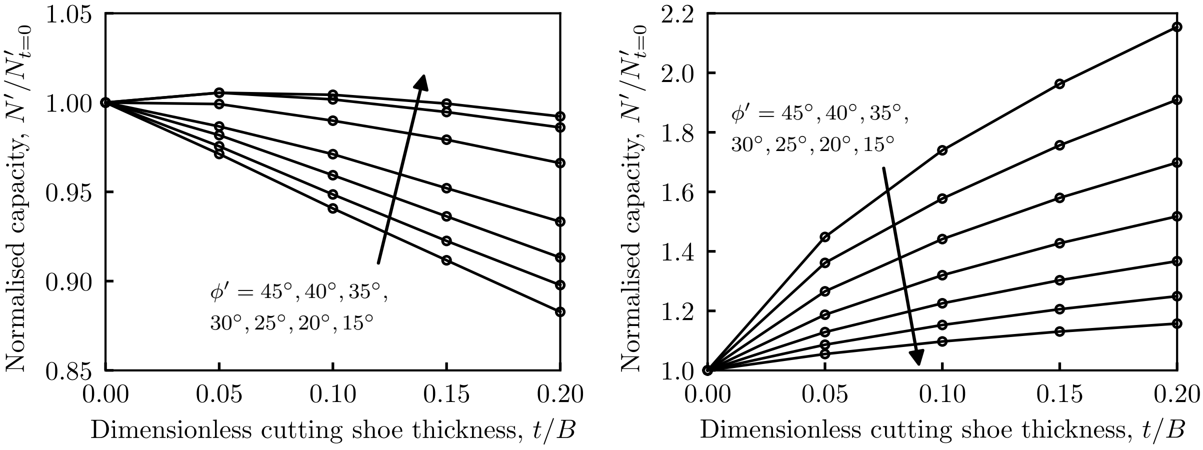

(a) $\alpha_\mathrm{f} = 1$

(b) $\alpha_\mathrm{f} = 0$

Figure 6.20 FELA-calculated influence of dimensionless cutting shoe thickness, t/B, on the vertical bearing capacity of a $\beta = 45°$ footing; flat surface ($h/B = 0$), plane strain ($B/R = 0$), smooth shoe ($\alpha_\mathrm{s} = 0$), no shoe length ($l/B = 0$), $\psi' = \phi'$

Considering first the results for $\alpha_\mathrm{f} = 0$ (Figure 6.20b), an increase in t/B causes a significant increase in capacity relative to the 'no shoe' case. This is particularly the case for high-ϕ' soil due to significant changes in the soil failure mechanism. Figure 6.21 shows the soil failure mechanisms corresponding to $t/B = 0$ and 0.1 for the extremum friction angles ($\phi' = 20°$ and 45°). It can be seen that the failure mechanism is confined entirely to the internal side, for all values of ϕ', when no cutting shoe is used (e.g. Figures 6.21a and 6.21c). For low-ϕ' soil, the cutting shoe causes a larger and deeper mechanism to form but the mechanism remains on the internal side only (see Figure 6.21b). In contrast, for high-ϕ' soil the cutting shoe causes the failure mechanism to develop on both the internal and external sides (Figure 6.21d), hence resulting in a greater increase in $N'/N'_{t=0}$ compared to at low-ϕ'. The details in Figures 6.21b and 6.21d show that the change in failure mechanism is primarily due to the formation of a rigid 'false head' directly beneath the cutting shoe, which increases in size with t/B. This causes both an increase in the confining stress on the failure surfaces and an increase in their length, as the failure mechanism forms from the tip of the false head.

For $\alpha_\mathrm{f} = 1$ (Figure 6.20a), the presence of a cutting shoe causes a decrease in normalised capacity $N'/N'_{t=0}$. A noteworthy point is that although N' decreases, the absolute capacity still increases with $t > 0$; this is caused by the definition of N' containing B_w, which increases with t. For low-ϕ', the soil failure mechanism only forms on the internal side and a small false head

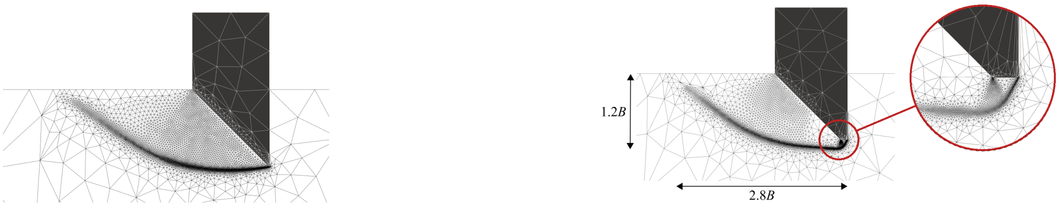

(a) $t/B = 0$, $\phi' = 20°$ (b) $t/B = 0.1$, $\phi' = 20°$

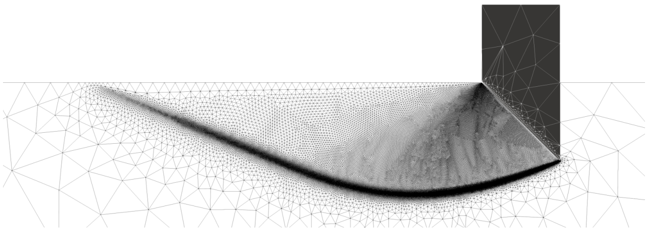

(c) $t/B = 0$, $\phi' = 45°$

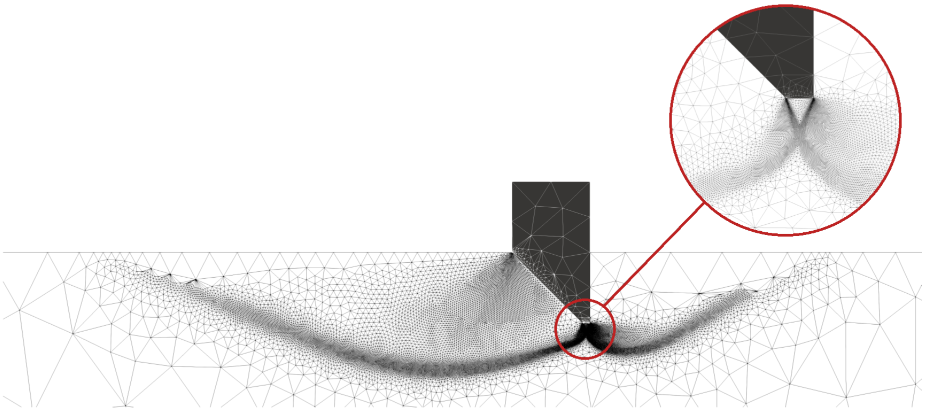

(d) $t/B = 0.1$, $\phi' = 45°$

Figure 6.21 FELA calculations of the soil failure mechanisms for a $\beta = 45°$ footing with a smooth cutting face ($\alpha_\mathrm{f} = 0$); flat surface ($h/B = 0$), plane strain ($B/R = 0$), smooth shoe ($\alpha_\mathrm{s} = 0$), no shoe length ($l/B = 0$), $\psi' = \phi'$

again forms beneath the cutting shoe (see Figures 6.22a and 6.22b). For high-ϕ' soil, the failure mechanism forms a much larger rigid wedge along the cutting face, both with and without a cutting shoe, as shown in Figures 6.22c and 6.22d. This effectively steepens the taper of the cutting face (i.e. the apparent β angle decreases), as the failure mechanism extends from the tip of the wedge. A smaller secondary false head forms beneath the cutting shoe for $t/B > 0$, with an additional shear band in the mechanism on the external side (see Figure 6.22d). This only has a minor influence on the bearing capacity as the majority of the failure mechanism remains unchanged, including the larger wedge of soil trapped at the cutting face.

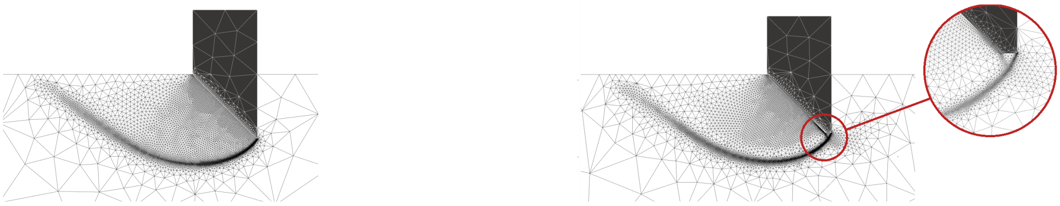

(a) $t/B = 0$, $\phi' = 20°$ (b) $t/B = 0.1$, $\phi' = 20°$

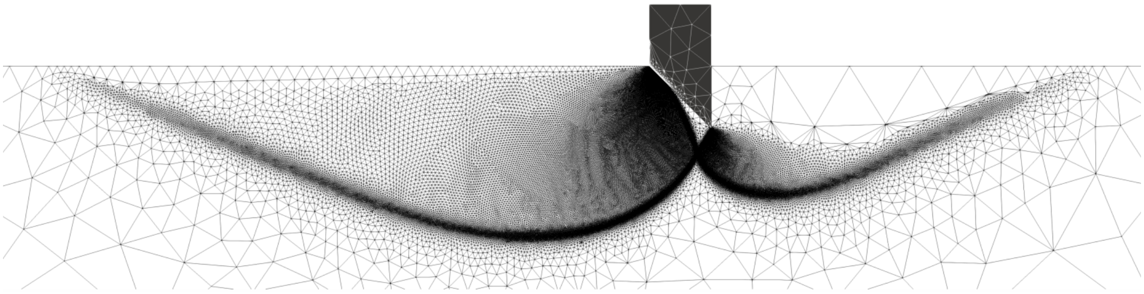

(c) $t/B = 0$, $\phi' = 45°$

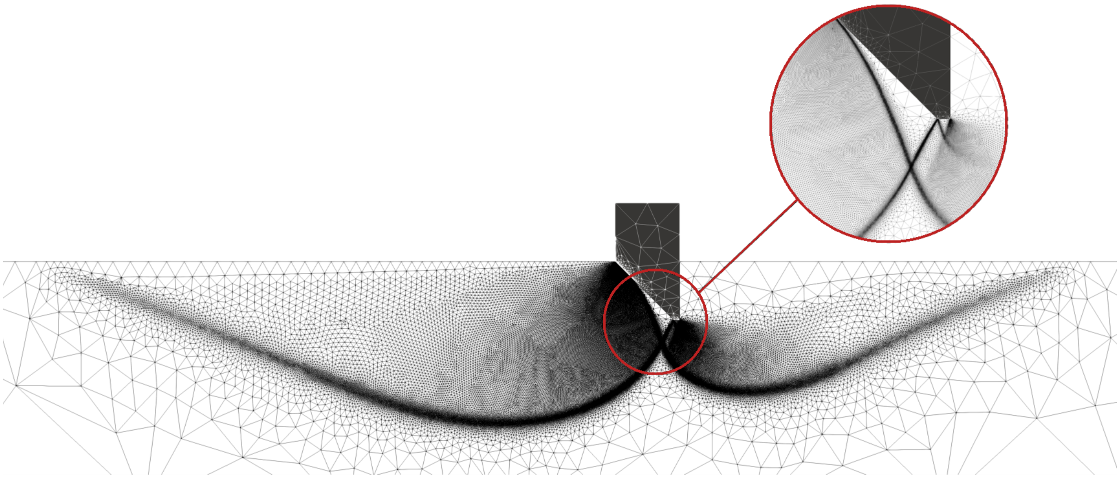

(d) $t/B = 0.1$, $\phi' = 45°$

Figure 6.22 FELA calculations of the soil failure mechanisms for a $\beta = 45°$ footing with a rough cutting face ($\alpha_{\mathrm{f}} = 1$); flat surface ($h/B = 0$), plane strain ($B/R = 0$), smooth shoe ($\alpha_{\mathrm{s}} = 0$), no shoe length ($l/B = 0$), $\psi' = \phi'$

6.5.2 Influence of cutting shoe length

The influence of the dimensionless cutting shoe extension length l/B on the vertical bearing capacity is considered in Figures 6.23 and 6.25 for $\alpha_{\mathrm{f}} = 1$ and $\alpha_{\mathrm{f}} = 0$ respectively. The FELA-calculated capacities are again normalised by the no cutting shoe values, $N'_{t=0}$. In all cases, extending the cutting shoe ahead of the apex of the cutting face increases the normalised bearing resistance. This is to be expected as the cutting shoe extends deeper into the soil with increased

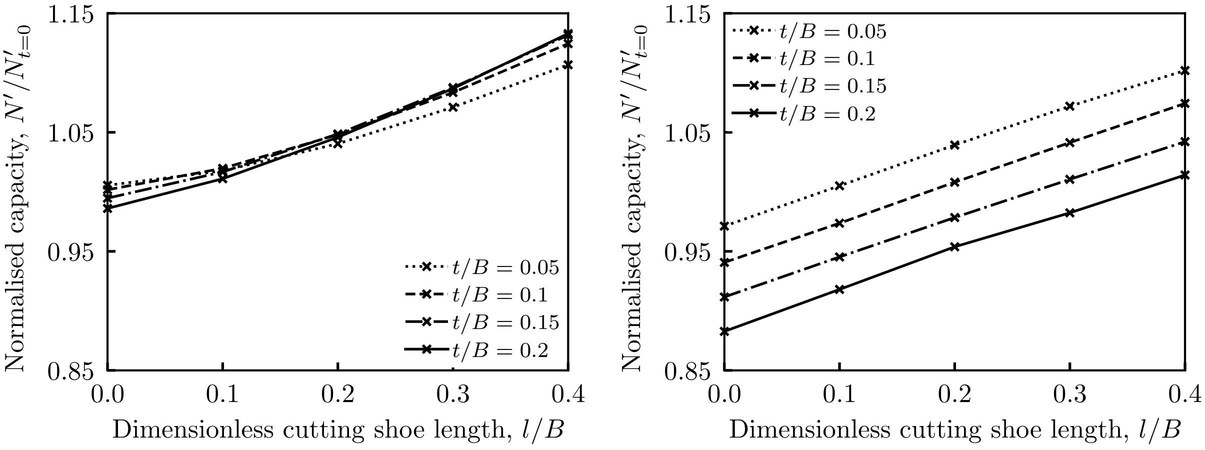

(a) $\phi' = 20°$

(b) $\phi' = 45°$

Figure 6.23 FELA calculations of the influence of cutting shoe dimensionless extension length, l/B, on the vertical bearing capacity of a $\beta = 45°$ footing with a rough cutting face ($\alpha_\text{f} = 1$); flat surface ($h/B = 0$), plane strain ($B/R = 0$), smooth shoe ($\alpha_\text{s} = 0$), $\psi' = \phi'$

l, resulting in increased confining stresses on the soil shear planes and a larger failure mechanism size. Interestingly, normalising the bearing capacity in this way achieves a negligible influence of t/B on the trends in these figures, particularly for soils with low-ϕ'. Similarly, Figures 6.23 and 6.25 do not show a clear trend with respect to ϕ'. This can be attributed to complex changes that occur in the failure mechanisms as the cutting shoe extends ahead of the taper face.

Examples of the failure mechanisms at extremum friction angles are given in Figure 6.24 and 6.26 for $\alpha_\text{f} = 1$ and $\alpha_\text{f} = 0$ respectively, where values of $t/B = 0.1$ and $l/B = 0.4$ are used for illustrative purposes. For $\alpha_\text{f} = 0$ and $\phi' = 20°$, Figure 6.26a shows that an extension of the cutting shoe ahead of the taper face causes the soil failure mechanism to extend to the external side which was not present for the $l/B = 0$ case (see Figure 6.21b). At $\phi' = 45°$, increasing l leads to a deeper 'external mechanism' forming, as shown in Figure 6.26b. In all cases with a smooth cutting face, the internal mechanism forms at the apex of the cutting face and is relatively unaffected by changes to the cutting shoe length.

Conversely for $\alpha_\text{f} = 1$ and $\phi' = 20°$, a wedge of soil becomes 'trapped' behind the cutting shoe (Figure 6.24a) which is not present when $l/B = 0$ (see Figure 6.22b). This again causes an effective steepening of the footing, resulting in no external mechanism developing and an enlarging of the internal mechanism. Figure 6.24b shows that for $\phi' = 45°$ the rigid soil wedge at the cutting face increases in size with increasing l, now forming from the tip of the shoe.

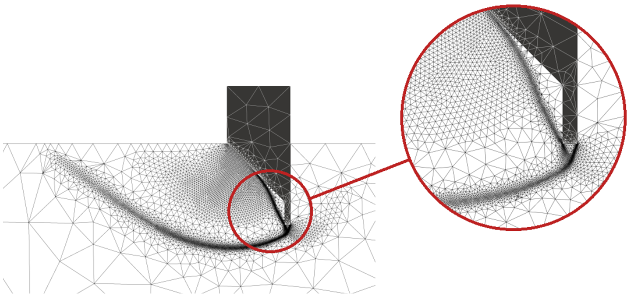

(a) $\phi' = 20°$

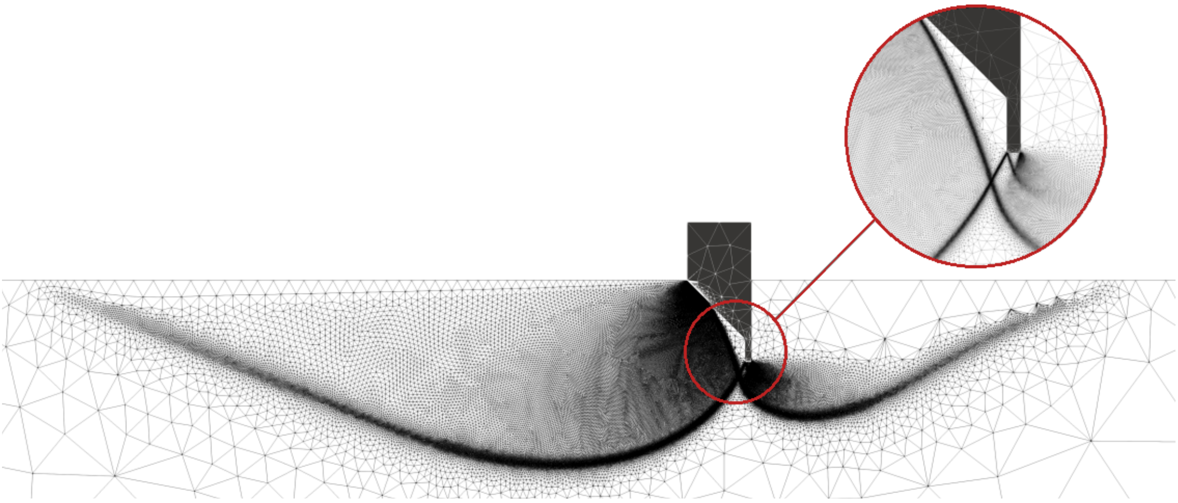

(b) $\phi' = 45°$

Figure 6.24 FELA calculations of the soil failure mechanisms for a $\beta = 45°$ footing with cutting shoe of $t/B = 0.1$ and $l/B = 0.4$ and a rough cutting face ($\alpha_\mathrm{f} = 1$); flat surface ($h/B = 0$), plane strain ($B/R = 0$), smooth shoe ($\alpha_\mathrm{s} = 0$), $\psi' = \phi'$

6.5.3 Influence of embedment depth and cutting shoe roughness

All analyses presented in Sections 6.5.1 and 6.5.2 consider shallow embedments ($h/B = 0$) and a fully smooth cutting shoe ($\alpha_\mathrm{s} = 0$), to isolate friction effects from the bearing resistance contribution. Including the effects of cutting shoe friction would be expected to lead to higher overall bearing resistances. To explore this, additional FELA calculations were performed with a cutting shoe of varying roughness. The effect was considered over a range of embedment depths (h/B) with a typically sized cutting shoe used in practice ($t/B = 0.07$ and $l/B = l_\mathrm{b}/B = 0.25$). The presented results only consider extremum values of ϕ', for clarity.

Figure 6.27 plots the predicted influence of the dimensionless embedment depth, h/B, on the vertical bearing capacity. The results are normalised by the no cutting shoe case values, $N'_{t=0}$, at the corresponding h/B. Similar to the observations in Section 6.4.2, the results reveal

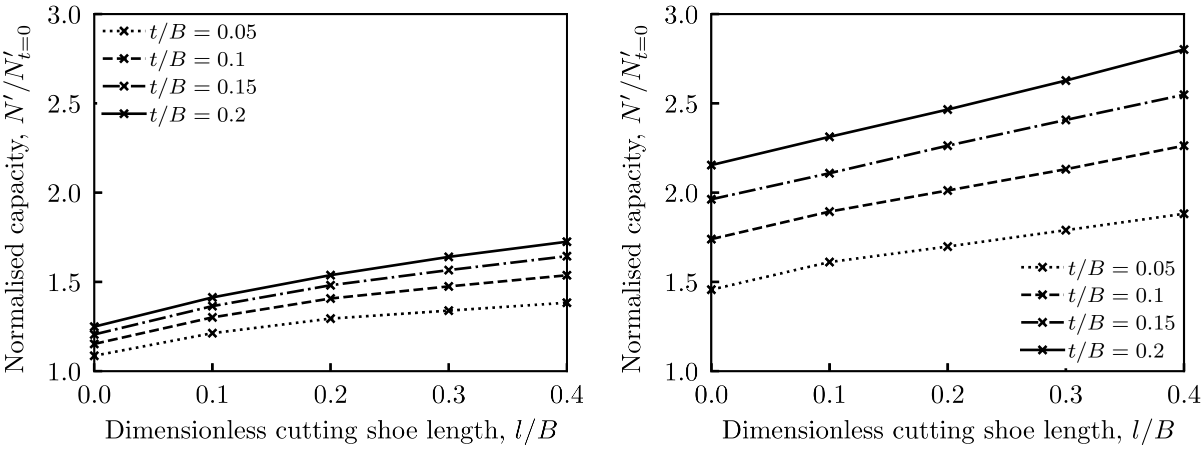

(a) $\phi' = 20°$

(b) $\phi' = 45°$

Figure 6.25 FELA calculations of the influence of cutting shoe dimensionless extension length, l/B, on the vertical bearing capacity of a $\beta = 45°$ footing with a smooth cutting face ($\alpha_\mathrm{f} = 0$); flat surface ($h/B = 0$), plane strain ($B/R = 0$), smooth shoe ($\alpha_\mathrm{s} = 0$), $\psi' = \phi'$

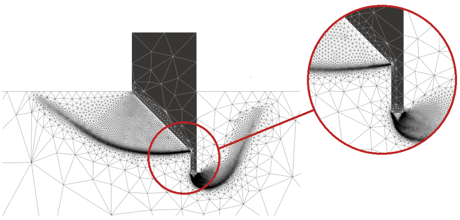

(a) $\phi' = 20°$

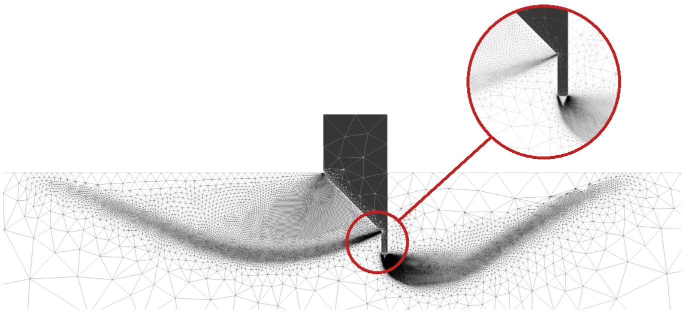

(b) $\phi' = 45°$

Figure 6.26 FELA calculations of the soil failure mechanisms for a $\beta = 45°$ footing with cutting shoe of $t/B = 0.1$ and $l/B = 0.4$ and a smooth cutting face ($\alpha_\mathrm{f} = 0$); flat surface ($h/B = 0$), plane strain ($B/R = 0$), smooth shoe ($\alpha_\mathrm{s} = 0$), $\psi' = \phi'$

the occurrence of a ‘critical embedment depth’ beyond which a further increase in h/B has a negligible effect on N'. This is again attributed to the failure mechanism becoming confined only to the internal side of the caisson for $h > h_{\mathrm{crit}}$, whilst both an external and internal mechanism is present for $h < h_{\mathrm{crit}}$. The addition of a cutting shoe significantly influences the relationship between h/B and N', which also appears highly dependent on the roughness of the cutting shoe.

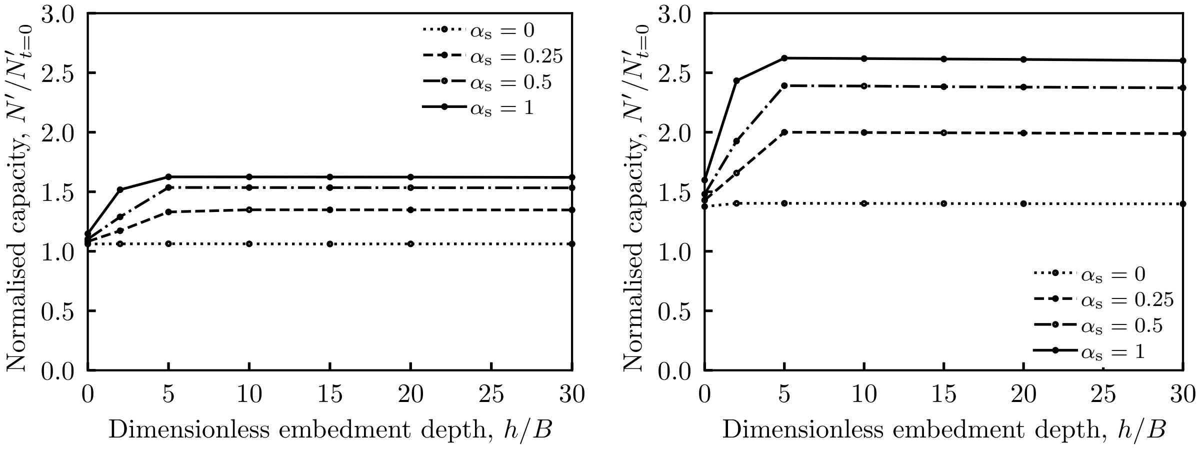

(a) $\alpha_f = 1$, $\phi' = 20°$

(b) $\alpha_f = 0$, $\phi' = 20°$

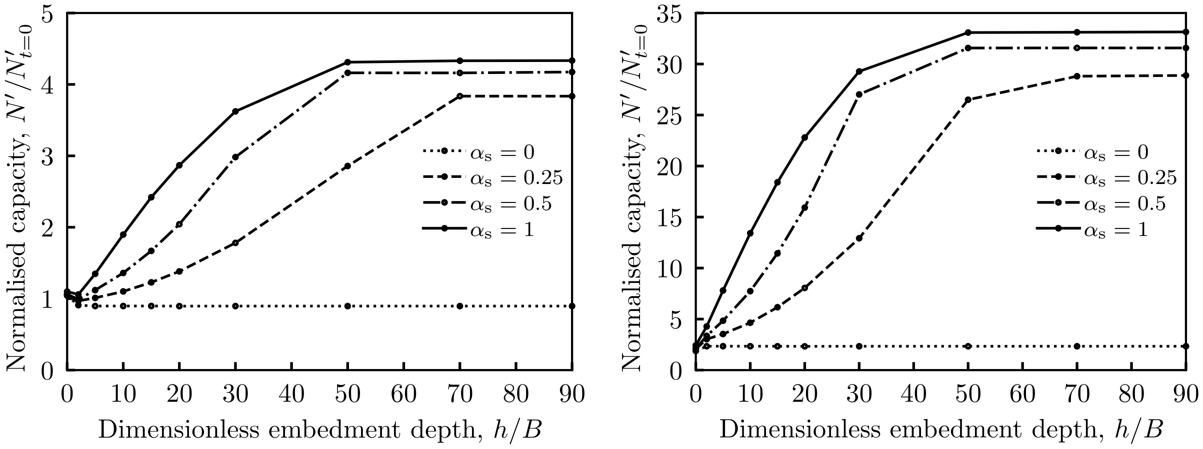

(c) $\alpha_f = 1$, $\phi' = 45°$

(d) $\alpha_f = 0$, $\phi' = 45°$

Figure 6.27 FELA-calculated influence of dimensionless external embedment depth, h/B, on vertical bearing capacity for a $\beta = 45°$ footing with a range of cutting shoe roughness factors α_s. Cutting shoe geometry is $t/B = 0.07$, $l/B = l_b/B = 0.25$; plane strain ($B/R = 0$), $\psi' = \phi'$

In all cases, the inclusion of a smooth cutting shoe ($\alpha_s = 0$) appears to cause a minor increase in bearing capacity and an insignificant alteration to the role of h/B. This is because the failure mechanism remains largely unchanged and is confined to the internal side at a very similar h/B. Interestingly, Figure 6.27c shows that in the case of a rough cutting face ($\alpha_f = 1$) and $\phi' = 45°$, the use of a smooth cutting shoe actually reduces the bearing capacity factor. This is again attributed to the effective steepening of the footing from the cutting shoe (see Section 6.5.2), confining the failure mechanism to the internal side at lower embedment depths compared to when no cutting shoe is used. However, it is worth noting in this specific case the absolute bearing force does actually increase compared to the no cutting shoe case, but due to

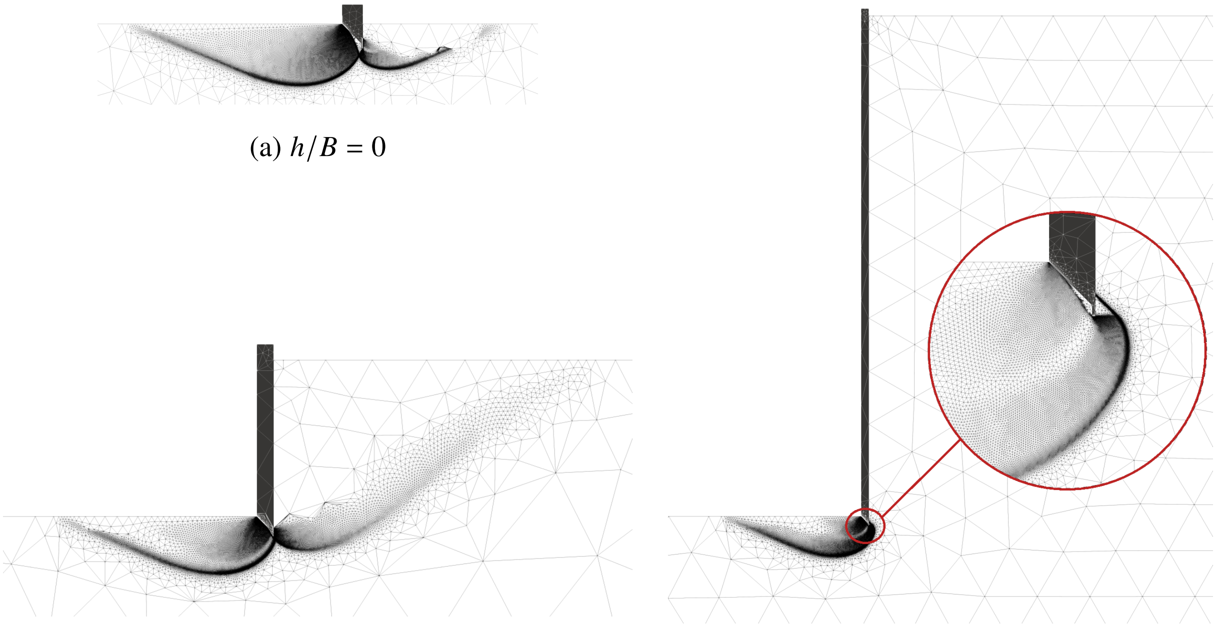

(a) $h/B = 0$

(b) $h/B = 30$

(c) $h/B = 90$

Figure 6.28 FELA calculations of the soil failure mechanisms for a $\beta = 45°$ footing in $\phi' = 45°$ soil. Cutting shoe geometry is $t/B = 0.07$, $l/B = l_b/B = 0.25$; plane strain ($B/R = 0$), rough face ($\alpha_f = 1$), rough shoe ($\alpha_s = 1$), $\psi' = \phi'$. The models are not shown with the same scale, for clarity

the increased embedded width caisson wall, B_w, the value of N' decreases.

Increasing the roughness of the cutting shoe results in significantly larger bearing capacities and greater dependence on embedment depth, particularly for high-ϕ' soils. For example, the inclusion of a fully rough cutting shoe ($\alpha_s = 1$) in $\phi' = 20°$ soil causes an increase in bearing capacity (relative to at $h/B = 0$) by a factor of approximately 1.42 and 1.64 below a critical embedment depth of $h_{crit}/B \approx 5$, for $\alpha_f = 1$ and $\alpha_f = 0$ respectively (Figures 6.27a and 6.27b). In comparison, the corresponding increases with no cutting shoe are negligible. This can be attributed to the failure mechanism being fully internal at all h/B with no cutting shoe, but the rough cutting shoe causes an external mechanism to form to h_{crit}.

In contrast a much deeper critical embedment depth occurs for $\phi' = 45°$, as shown in Figures 6.27c and 6.27d, between $h/B = 50$ and 70 depending on the cutting shoe roughness. Salient failure mechanisms for the $\alpha_f = 1$ and $\alpha_s = 1$ case are shown in Figure 6.28. For a cutting shoe with $\alpha_s > 0$, the external failure mechanism remains for much deeper embedment depths (Figure 6.28a and 6.28b), before transitioning to an internal mechanism (Figure 6.28c).

This transition occurs at a much deeper h_{crit} than observed for the no cutting shoe case and this leads to a significant increase in the bearing capacity, particularly for a rough cutting shoe. In this case, the capacity increases (relative to at $h/B = 0$) by a factor of approximately 5.36 and 13.7 for $\alpha_{\mathrm{f}} = 1$ and $\alpha_{\mathrm{f}} = 0$ respectively (see Figures 6.27c and 6.27d). The detail in Figure 6.28c shows that the rough external cutting shoe surface (of total length $l + l_{\mathrm{b}}$) causes a wedge of soil on the outside of the caisson to be dragged downwards. The external wedge, in turn, causes a larger and deeper failure mechanism that encompasses the full extent of the cutting shoe.

6.5.4 Influence of caisson radius

The results presented in Sections 6.5.1-6.5.3 consider plane strain conditions, which are applicable to large diameter caissons. The influence of caisson radius, R, on the vertical bearing capacity was explored using the same typically sized cutting shoe as in Section 6.5.3 for a deep embedment of $h/B = 30$. Figure 6.29 plots the predicted vertical bearing capacity as a function of the reciprocal of the dimensionless caisson radius, B/R. The results are normalised by the corresponding plane strain value ($N'_{R=\infty}$). As observed in Section 6.4.3, an increase in B/R (i.e. smaller caisson radius) causes an increase in $N'/N'_{R=\infty}$ in all cases, due to an increase in radial stress and therefore confining stress. The results for both $\alpha_{\mathrm{f}} = 1$ (Figure 6.29a) and $\alpha_{\mathrm{f}} = 0$ (Figure 6.29b) show that for high-ϕ' soil there is a significant dependency of the bearing capacity on B/R, regardless of the cutting shoe design. The addition of a smooth cutting shoe causes an increase in the bearing resistance with B/R for all cases considered here. A similar, but greater, increase is also observed for a rough cutting shoe in low-ϕ' soil. In these cases, the failure mechanism is only present on the internal side of the footing. For $\phi' = 45°$, the addition of a rough cutting shoe causes the relationship between B/R and $N'/N'_{R=\infty}$ to become non-linear. This is because of the presence of an external failure mechanism, which is present throughout the range of B/R considered in Figure 6.29.

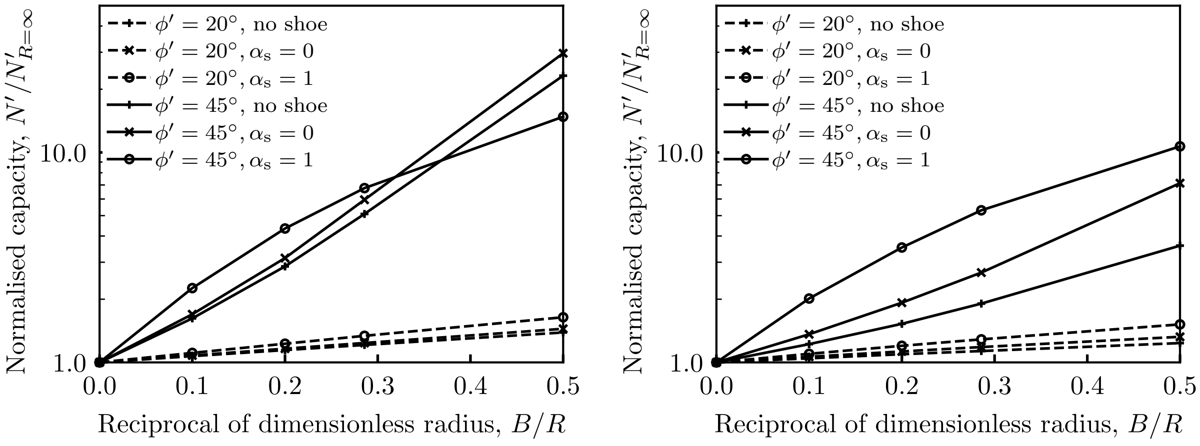

(a) $\alpha_f = 1$

(b) $\alpha_f = 0$

Figure 6.29 FELA-calculations of the influence of the caisson internal radius, R, on the vertical bearing capacity for a $\beta = 45°$ footing with a range of cutting shoe roughness factors α_s. Cutting shoe geometry is $t/B = 0.07$, $l/B = l_b/B = 0.25$; $h/B = 30$, $\psi' = \phi'$

6.6 Limitations of modelling

The analyses presented in this chapter have important limitations which should be carefully considered when taking these results into account for design in practice. Modelling of drained materials is a complex problem and the simple Mohr-Coulomb constitutive model used in this study may not closely represent realistic soil behaviour. The shear resistance, stiffness and dilatancy of sand has strong dependence on its density, confining stress and the shear strain it is subject to. A non-linear failure envelope provides a better prediction of the shear strength of sands, particularly at low confining pressures (Bolton, 1986).

The FEA results show that soil associativity has a significant influence on the bearing capacity for this problem and the use of associated flow is likely to provide an over-estimate of the bearing capacity when applied to practical problems (e.g. Loukidis and Salgado, 2009). An overestimate of caisson bearing resistance may lead to uncontrolled sinking or 'runaway'. These risks can be managed on site by, for example, flooding the caisson to avail of additional buoyant uplift forces or deploying 'brakes' on the top supporting ring beam. However, the primary risk during caisson construction in sands is failure to sink to formation level, arising from underestimation of the soil penetration resistances (to the point where they exceed the self-weight of the structure). The resulting bias of the present calculations are therefore on the safe side for this problem such that these results may be transferred to practice with confidence.

For the calculations with a cutting shoe, a simple rectangular cross-section was adopted for the modelling and more complex realistic geometries (with bevelled edges, for example) are likely to have a non-negligible influence. Furthermore, the influence of soil non-associativity was not considered for the cutting shoe analyses, for the sake of expediency whilst remaining on the safe side for this problem. Similarly, the present treatment of the annulus as a perfectly smooth rigid boundary tacitly assumes that the annulus remains open during sinking. However, failure of the annulus is possible in sands and this may lead to even more complex failure mechanisms. The 'wished-in-place' installation process also neglects the influence of any deformation-induced changes to the soil on the vertical capacity, such as geometry changes (e.g. soil heave) or alteration of the soil material properties. Large displacements may also have considerable impact on the soil-structure interface roughness as the caisson sinks, with changes in the interface friction angle and possible grain crushing occurring.

6.7 Summary

This chapter has described a numerical study of the vertical bearing capacity of a caisson cutting face embedded in cohesionless soil. Finite element limit analyses were used to explore the role of the cutting face taper angle and roughness, caisson external embedment depth and caisson radius on the vertical soil reaction. A limited number of additional calculations were also completed using finite element analysis, to assess the role of soil non-associativity and the development of horizontal reaction.

The parametric study revealed that the influence of the cutting face taper angle on the bearing capacity is highly dependent on both the soil friction angle and the roughness of the cutting face. For a rough cutting face, a steepening of the taper angle was shown to increase the vertical bearing capacity for all values of ϕ'. In contrast, for a smooth interface, a steepening of the cutting face caused an increase in the bearing capacity for low-ϕ' soil and a reduction for high-ϕ' soil. The results also revealed the existence of a critical external embedment depth beyond which any further increases in embedment had a negligible influence on the bearing capacity. Finally, a reduction in the caisson radius was shown to cause a significant increase in the bearing capacity due to an increase in radial stress, and therefore confining stress, in the soil towards the internal side of the caisson wall. The role of the caisson radius on the bearing capacity was largely controlled by the soil friction angle, where high-ϕ' soil exhibited a greater dependency on the caisson radius.

The effect of including an external cutting shoe on the caisson vertical bearing capacity was also considered using additional FELA calculations. It was revealed that the inclusion of a cutting shoe has a significant influence on the vertical soil reaction during sinking and is highly dependent on the roughness of the cutting face, the soil friction angle and the caisson embedment depth. The inclusion of a typical-sized cutting shoe used in industry is observed to cause substantial increases in bearing capacity for deep caisson embedments in high-ϕ' soil. In particular, the influence of cutting shoe roughness was shown to be considerable.

The numerical results suggest interesting soil-structure interaction behaviours at the caisson cutting face. Significant complexities are also demonstrated by the introduction of an external cutting shoe. These results highlight the additional risks associated with the construction of deep open caisson shafts in dense sands. However, the results also indicate dependence of the bearing capacity on specific design and construction features. This highlights significant opportunity to customise or optimise the structure for improved control and risk reduction during construction for a given project.

Chapter 7

Applications and discussion

7.1 Introduction

This chapter presents critical discussion on the application of the results of the caisson experimental testing (Chapter 5) and numerical modelling (Chapter 6). The numerical methodologies in Chapter 6 are compared against laboratory testing results and current design methods. The FELA results are used to inform the development of new simplified closed-form expressions amenable for use in routine design. The implications of the findings on design decisions and the selection of construction features are also explored.

7.2 Validation of numerical modelling

For comparison and validation of the modelling in Chapter 6, the same numerical methods were used to predict the bearing capacity of the experimental tests conducted by Royston (2018). The laboratory-scale tests considered the displacement-controlled vertical penetration of tapered aluminium test pieces into samples of coarse LB sand. This resembles a plane-strain approximation of a caisson cutting face at shallow depths. The vertical and horizontal reaction forces on the test piece are measured using a three DOF 'Cambridge-type' load cell attached between the loading rig and the test piece. Further details of the material properties, test procedures and full results are provided in Royston (2018).

The FELA and FEA methodologies used for these additional analyses are as described in Section 6.3, except for the following changes to reflect the experimental test conditions. The

Table 7.1 Parameters adopted for the FELA and FEA calculations for comparison with caisson bearing experimental testing by Royston (2018)

Parameter	**Value**
Footing width, B	100 mm
Footing out-of-plane thickness	96 mm
Cutting face taper angle, β	75°, 60°, 45°, 30°
Soil friction angle, ϕ'	34.3°
Soil unit weight, γ'	15.0 kN/m^3
Cutting face interface friction angle, δ_f	$0.78\phi'$
Vertical surface interface friction angle, $\delta_\mathrm{v,ext}$	$0.55\phi'$

calculation parameters used are outlined in Table 7.1. To model the shallow depths in the tests, analyses are conducted with an embedded width, B_w, in ten increments over the range $0 - B$, where B is the thickness of the test pieces (100 mm). This gives a 'wished-in-place' approximation of the continuous vertical penetration procedure. Only the low-density tests are considered for these comparisons, as this minimises the influence of dilation. Based on the mean D_R of 0.18 (with a standard deviation of 0.03), a soil unit weight of $\gamma' = 15\,\mathrm{kN/m^3}$ is assumed. A soil friction angle of $\phi' = 34.3°$ is assumed, which is a value widely adopted for experimental testing on the same LB sand in the geotechnical group at the University of Oxford (e.g. LeBlanc *et al.*, 2010; Richards *et al.*, 2020; Schnaid, 1990).

It is unlikely that zero shear stress will develop on the external vertical surface of the test pieces, as assumed in Chapter 6 (Figure 6.1). The cutting face of the experimental test pieces was deliberately roughened, whereas the external vertical surface was machined to give a smooth finish (Royston, 2018). The roughness of the cutting face is assumed to be defined by an interface friction angle, δ_f, of $0.78\phi'$, based the sand-rough steel interface tests described by Potyondy (1961). Similarly, the interface friction angle on the vertical external surface, $\delta_\mathrm{v,ext}$, is assumed to be $0.55\phi'$, based on a sand-smooth steel interface (Potyondy, 1961).

Figure 7.1 plots the measured vertical reaction force, V, against B_w, alongside the FELA-calculated equivalent values, for footings with different taper angles, β. There is relatively good

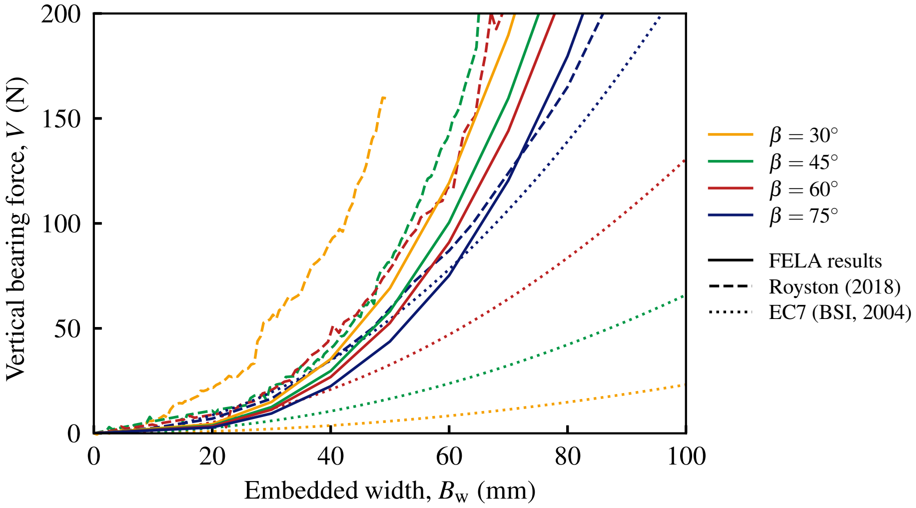

Figure 7.1 Comparison of the vertical bearing force measured in the loose sand tests of Royston (2018) with predictions using FELA (present study) and Equation 2.12 from EC7 (BSI, 2004)

agreement between the measured and FELA-calculated vertical load response, with excellent agreement at β = 75°. The agreement deteriorates at steeper inclination angles, particularly with β = 30°. However, relatively good agreement is still observed at the industry-favoured β = 45° inclination, with FELA under-predicting the experimental predictions by 22.5% at $B_w = B/2 = 50\,\text{mm}$. FELA also captures the rate of increase of V with B_w well across the range of embedments considered. Potential reasons for the under-predictions include dilation of the sand during failure, and heave of the sand observed in the tests, which is not captured by the 'wished-in-place' numerical analyses. The heave increases throughout penetration, hence explaining the decreased agreement at greater B_w values.

Figure 7.1 also plots the bearing capacity predicted by Equation 2.12 from EC7 (BSI, 2004), using the same parameters as in Table 7.1. Although close agreement is again observed at β = 75°, there is significantly greater under-predication of the experimental vertical force at all other inclination angles. There is a 79.7% under-prediction at $B_w = B/2 = 50\,\text{mm}$, which rapidly increases with further embedment. Furthermore, Equation 2.12 shows a much greater dependence of V on β, with a significant reduction in resistance predicted at steeper inclination angles. This was not observed in the experimental results, which show the vertical resistance to increase with smaller β, for a given B_w. The FELA results agree with experimental data,

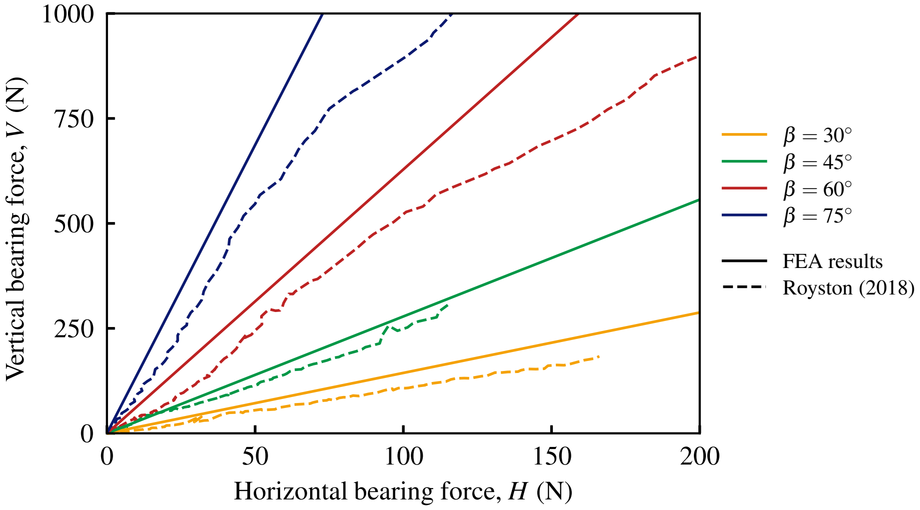

Figure 7.2 Comparison of the vertical and horizontal bearing forces measured in the loose sand tests of Royston (2018) with predictions using FEA (present study)

showing the same influence of β albeit with a slightly reduced dependence.

Figure 7.2 plots V against the horizontal force, H, during vertical penetration. Good agreement is observed between the FEA-calculated values and the experimental results for $V < 750\,\mathrm{N}$ and $H < 120\,\mathrm{N}$. FEA over-predicts the ratio V/H and interestingly agreement is worse for larger values of β. The deviation in the responses at $\beta = 60$ and 75° at higher forces is caused by the footings becoming fully embedded (above the top of the cutting face), which was not considered in the numerical modelling. The relative magnitudes of V and H are strongly dependent on the assumed interface roughness values, which may not exactly match the experimental test pieces.

Figure 7.3 shows the failure mechanisms from the loose sand tests of Royston (2018) with the FELA-predicted failure mechanisms from the present study overlaid in green. Relatively good agreement is observed for β =30° and β =45°. At β =45°, the experimental mechanism extends slightly deeper in the soil but has smaller lateral extent (Figure 7.3b). Much worse agreement is seen for β =60° in Figure 7.3c. FELA predicts a significantly larger internal mechanism and the simultaneous formation of an external mechanism, which is not present in the experimental mechanism. This potentially explains the over-prediction of V/H in Figure 7.2, as the external mechanism in the numerical results 'balances' the horizontal force contribution from the internal mechanism (as seen in Section 6.4.5).

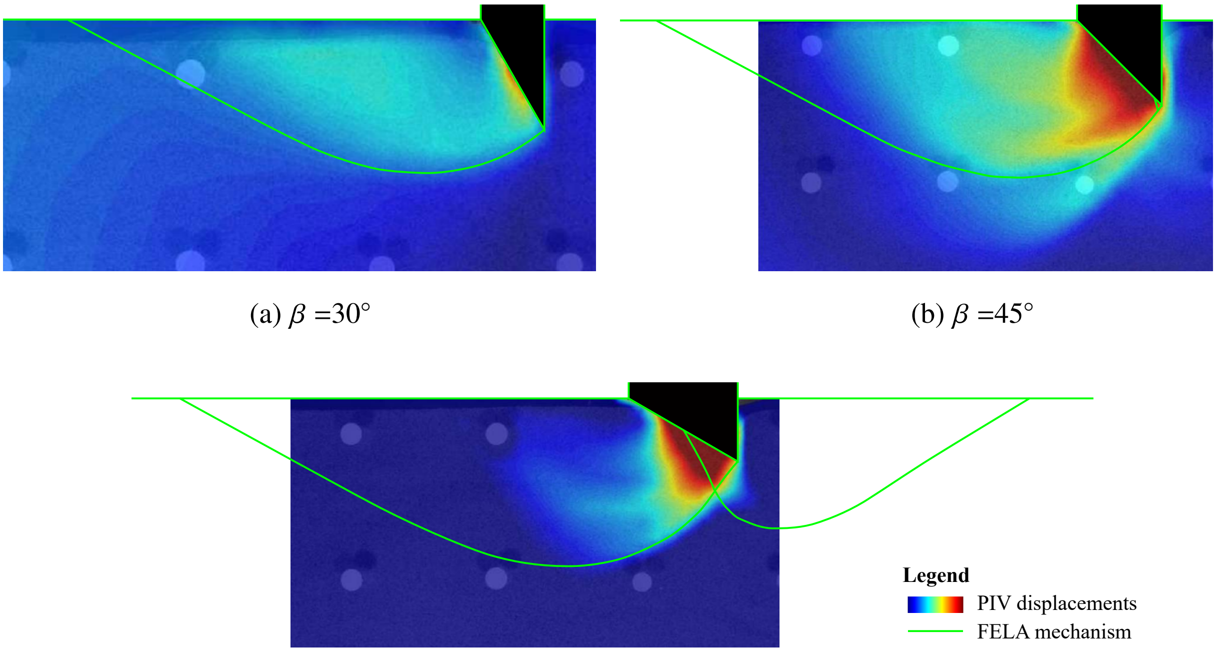

(a) β =30°

(b) β =45°

(c) β =60°

Figure 7.3 PIV-calculated soil failure mechanisms in loose sand tests by Royston (2018), overlaid with corresponding FELA-calculated soil failure mechanisms (green lines): (a) β =30°, (b) β =45°, (c) β =60°

The failure mechanism comparisons highlight inconsistency with the observations in Figure 7.1. Although there appears to be a better match between the experimental measured bearing forces and FELA calculations at larger β, this is contradicted by the greater difference in the deformation fields. The PIV-observed failure mechanisms suggest that soil compressibility has a large effect on the bearing resistance at low relative densities. This is particularly apparent in Figure 7.3c, where large displacements are observed locally beneath the footing and competitively smaller displacements occur further away. The effects of soil compressibility are beyond the scope of the current numerical study and further work is needed to understand its impact.

7.3 Development of design method for caisson bearing in sand

While direct numerical analyses of geotechnical problems are becoming more commonplace, simplified design approaches remain an integral part of preliminary design. This is particularly the case for the design of open caisson shafts, where the selection of the cutting face and shoe geometry are construction details and therefore most commonly rest with the contractor.

The FELA results presented in Section 6.4 were therefore used to inform the development of closed-form analytical equations amenable for use in routine design. Only the deep condition ($h/B = 15$) is considered for this purpose, as it is most representative of geometries likely to be encountered in practice (Royston, 2018; Royston *et al.*, 2022a). It is found empirically that the following expression can be used to capture the bearing capacity factor for a plane-strain cutting face, $N'_{R=\infty}$, which is applicable to large diameter caissons:

$$N'_{R=\infty} = 1366 \tanh \left([94.2x - 768.3y + 674.3] \times 10^{-2} \right) + 2.8 \tag{7.1}$$

$$x = \tanh \left([28.2\alpha_\mathrm{f} - 14.7\beta - 217.9\phi'] \times 10^{-3} + 10.87 \right) \tag{7.2}$$

$$y = \tanh \left([-25.8\alpha_\mathrm{f} - \beta - 14.58\phi'] \times 10^{-2} + 8.62 \right) \tag{7.3}$$

where both β and ϕ' are in degrees and tanh functions are are used to capture the non-linearity in the data. As this method is informed from FELA results only, it is restricted to the assumption of associated flow conditions. Equation 7.1 was then used to re-calculate the bearing capacity of all plane strain analyses at $h/B = 15$ considered in the preceding parametric study; the results are compared to the FELA output in Figure 7.4 where good agreement can be observed.

Recognising that the logarithm of $N'/N'_{R=\infty}$ was shown to vary approximately linearly with B/R (see Figure 6.12), the following expression was used to extend Equation 7.1 to axisymmetric conditions:

$$N' = \exp \left[m \left(\frac{B}{R} \right) \right] N'_{R=\infty} \tag{7.4}$$

where the curve-fitting parameter m represents the gradient of the data in the parameter space shown in Figure 6.12. An expression for m was developed by fitting a linear relationship to these data and further regressing the fitted slope on the parameters α_f, β and ϕ'. This exercise yielded the following expression:

$$m = \exp \left([78.9\phi' + 327\alpha_\mathrm{f} - 2301] \times 10^{-3} \right) \tag{7.5}$$

Figure 7.5 compares calculations determined using Equations 7.1–7.5 to the FELA output for all 708 parameter combinations at $h/B = 15$, including both plane strain and axisymmetric conditions. While there is generally good agreement between both sets of calculations, the present analytical approach provides a slight over-prediction at low bearing capacities compared to the FELA output. While this agreement can be improved further by introducing additional non-linearity in the present analytical equations (particularly Equations 7.4 and 7.5) this leads to a significant increase in model complexity. The proposed model was therefore adopted as a reasonable balance between fidelity and complexity.

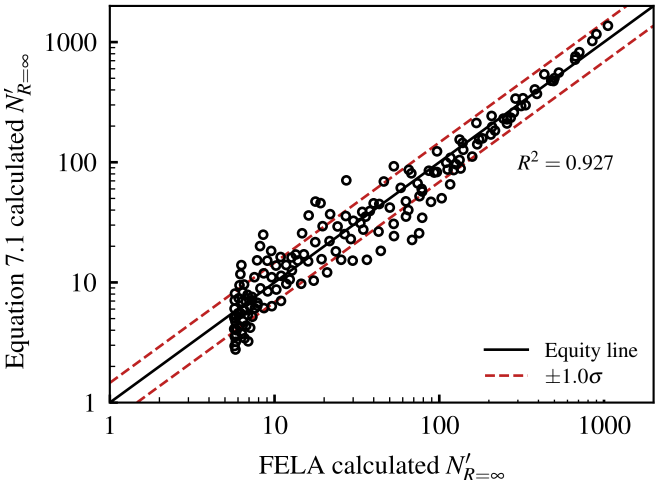

Figure 7.4 Comparison between calculated values of the plane strain bearing capacity factor, $N'_{R=\infty}$, determined using Equation 7.1 and FELA (h/B = 15 only); σ = standard deviation

The methods introduced above only consider a single deep embedment case, influenced by the significant complexity of the overall parameter space considered in Section 6.4. Whilst this is useful for assessing permanent state bearing capacity at formation depth, it is less applicable for calculation of the resistance at different stages of the sinking process, where the bearing is strongly influenced by both the internal and external overburden depths. A design method which can capture this dependence is useful to aid in planning the sequencing of concrete pours and excavation. A similar method was developed for undrained soils by Royston *et al.* (2022b), but a similar method does not yet exist for sands. Given the significantly increased complexity of

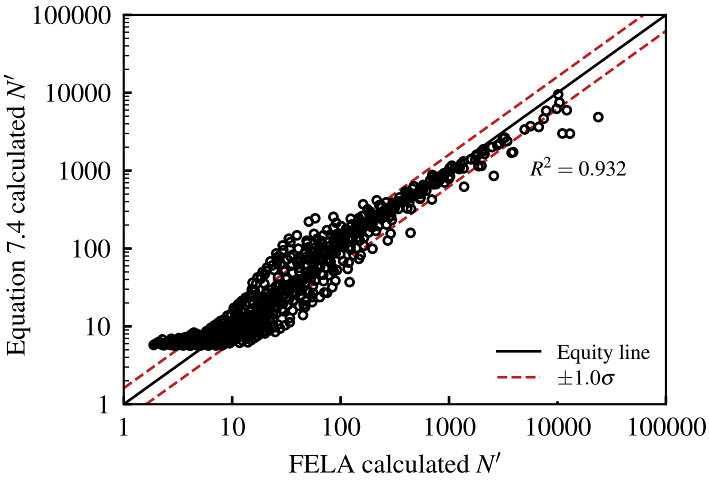

Figure 7.5 Comparison between calculated values of the bearing capacity factor, N', determined using Equation 7.4 and FELA for all analyses with h/B = 15; σ = standard deviation

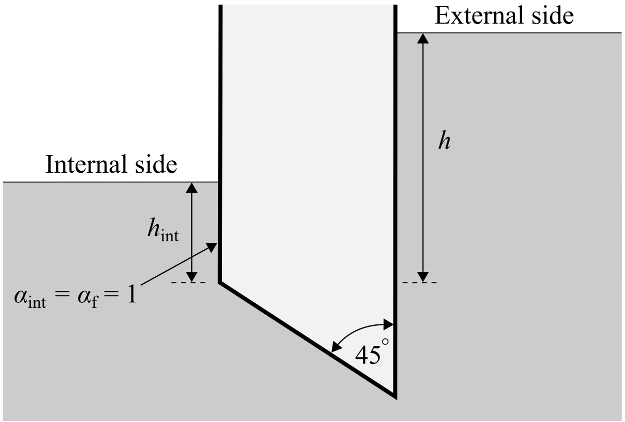

Figure 7.6 Definition of internal and external overburden soil depths for the design method in Equation 7.6

the parameter space in sands, only a fully rough plane strain footing ($\alpha_{\text{f}} = 1$; $B/R = 0$) with β = 45° is considered. This would be appropriate conditions to consider for a large diameter caisson based on typical industry practice.

A series of 196 further FELA calculations were conducted to consider the influence of internal overburden soil depth, h_{int}, defined in Figure 7.6, as all analyses in Chapter 6 were conducted with $h_{\text{int}} = 0$. The analyses considered combinations of h and h_{int} over the increments $h = h_{\text{int}}$ = 0, 0.5, 1, 2.5, 5, 7.5, 10, with $h_{\text{int}} \leq h$ in all cases and ϕ' = 15–45°. Other than the differences specified, the problem definition and FELA methodology is as described in Section 6.3.1. Although deep internal embedment depths are likely to be unrealistic for construction in sands, they are included for completeness.

It is found empirically that the following expression can be used to capture the bearing capacity factor for a plane-strain cutting face, with β = 45° and α_{f} = 1:

$$N'_{R=\infty} = 15508\,(1 + \tanh\left[2.72x - 1.14y - 1.36\right]) \tag{7.6}$$

$$x = \tanh\left(\left[35.0\phi' + 26.4h_{\text{int}} + 7.50h\right] \times 10^{-3} - 2.04\right) \tag{7.7}$$

$$y = \tanh\left(\left[-28.7\phi' - 267h_{\text{int}} + 7.55h\right] \times 10^{-3} + 0.800\right) \tag{7.8}$$

Figure 7.5 compares the outputs determined using Equations 7.6-7.8 and plane strain FELA for all 196 parameter combinations with β = 45° and α_{f} = 1. Excellent agreement is observed between the calculation and FELA outputs in all cases (R^2 = 0.998). The lower complexity

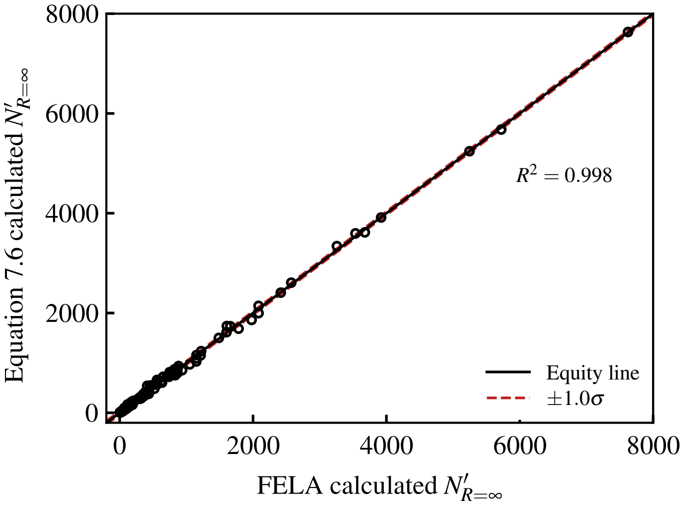

Figure 7.7 Comparison between calculated values of the bearing capacity factor, $N'_{R=\infty}$, determined using Equation 7.6 and FELA for analyses with $\beta = 45°$ and $\alpha_{\mathrm{f}} = 1$

when considering a single β and α_{f} leads to significantly improved agreement compared to Figures 7.4 and 7.5. As Equation 7.6 gives a very high fidelity representation of the numerical data across all embedment depths considered, this gives confidence in applying the method for design purposes.

7.4 Implications for design and construction

7.4.1 Cutting face

From the parametric space considered in Chapter 6, the caisson parameters that can be selected in design, or influenced during construction, are the cutting face geometry and roughness, and the cutting shoe. The caisson radius and depth are typically fixed by the intended purpose of the structure. Whilst the wall thickness, B, must also be selected for a given design, it is typically constrained to provide sufficient weight to overcome friction or to resist uplift from flotation in the permanent case.

The results of Chapter 6 indicate that reducing the interface roughness of the cutting face reduces both the vertical and horizontal forces on the caisson due to bearing. It is therefore desirable for construction practice to ensure α_{f} is minimised. For typical caisson construction, the inclined cutting face is formed using an angled hand-formed bearing pad cast in-situ using

(a) (b)

Figure 7.8 Caisson shaft cutting face formation: a) Breaking out a bearing pad prior to sinking, b) removable pre-cast blocks

low strength concrete (Royston, 2018). The first caisson wall pour is formed on top of this pad, which is then broken out and excavated to begin sinking. An example of this shown in Figure 7.8a, where a relatively rough and uneven cutting face can be observed.

An alternative approach is to form the cutting face using a series of angled precast concrete blocks, as shown in Figure 7.8b. The caisson wall is poured on top of these blocks with a membrane in between. The blocks are then simply removed to initiate sinking. This process produces a smoother and more consistent cutting face surface, which reduces the vertical bearing resistance during construction. Furthermore, the improved uniformity of the cutting face geometry ensures more consistent resistance around the circumference, potentially aiding in maintaining verticality.

Abrasion of the cutting face will occur throughout sinking due to frictional contact with the soil. This can increase the interface roughness during sinking (as experienced in Section 5.2.4.2). This will likely depend strongly on the ground conditions. In difficult ground, the cutting face could be lined with steel, which typically has a reduced interface roughness (e.g. Potyondy, 1961) and has a greater resistance to abrasion compared to concrete. This comes with high associated cost, but could tie into the steel cutting shoe and create a very robust cutting face surface. This would have additional benefits in ground containing boulders, which can result in point loading and damage to the cutting face and shoe. Partial lining of the cutting face with steel in this manner is shown in Nonveiller (1987). Another potential option, where there is risk of high resistance, is to install additional lubricant injection ports at the toe of the cutting face. Lubrication of the cutting face towards the caisson interior could help to reduce the interface friction coefficient and avoid the need for excessive excavation beneath the cutting face.

The optimal selection of cutting face taper angle, β, is complex and will likely be a compromise between several competing factors. The numerical results in Section 6.4.1 and the comparisons in Section 7.2 might suggest that a steeper cutting face (reduced β) is less desirable in sands. For a given B_w at shallow embedment depths, a steeper taper produces a larger failure mechanism and therefore a higher capacity, which is accentuated in high-ϕ' soil. However, the major benefit of reducing β is that it encourages the soil failure mechanism to form only towards the inside of the structure. The external failure mechanism observed at higher β values significantly increases the bearing capacity at deeper embedment depths (Section 6.4.2). Displacement of soil outside of the caisson is also highly undesirable, particularly in close proximity to other structures, and may also adversely impact the stability of the over-cut. This behaviour is also strongly coupled with cutting face roughness, as increased α_f causes external mechanisms to form for lower β. Based on the numerical bearing results, a taper angle of $\beta \leq 45°$ is recommended in sands. One exception to this would be for small radii caissons in high ϕ' soil, due to the increased confinement on the large failure mechanism with low β.

There are several other factors that must be considered with the selection of a low β angle. In difficult conditions, it can be necessary to excavate soil from beneath the cutting face, to reduce B_w and therefore the bearing resistance. Decreasing β can aid in excavating soil adjacent to the cutting face, due to the increased clearance height. This is particularly applicable when excavating with a clamshell bucket from the ground level. However, decreasing β greatly increases the horizontal or radial outward force on the cutting face, particularly with high α_f and ϕ'. This may have implications on the structural design of the RC wall, through increased tensile hoop strain.

Another important consideration with selection of β is the connection between the RC wall and the cutting shoe. The steel cutting shoe is typically tied into wall at the apex of the cutting face using reinforcing steel, as as shown in Figures 1.6 and 7.8b. With low β, the connection to

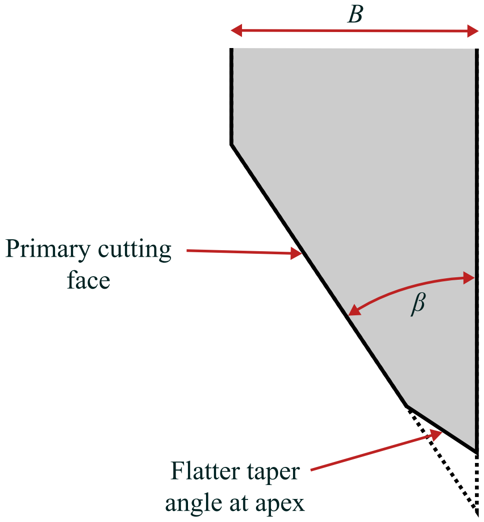

Figure 7.9 Illustration of a biangular cutting face, with a flatter taper angle at the apex

the cutting shoe is of lower stiffness, due to the longer and slimmer concrete section, and less robust, due to less reinforcement in the region. This is a particular concern in ground containing boulders, which result in point loading and potential buckling of the cutting shoe (Tomlinson, 2001). A potential solution to this problem could be to opt for a 'biangular' cutting face, as shown in Figure 7.9. A steep β is used over the majority of the inner edge of the caisson wall, changing to a larger angle towards the apex, similar to a 'secondary bevel' on a chisel. This truncates the thin apex from the cutting face, allowing a higher stiffness connection to the shoe. A similar cutting shoe profile appears to have been applied by Chandler *et al.* (1984).

7.4.2 Cutting shoe

The design of the caisson cutting shoe is another feature that is subject to several constraints. This is largely driven by the different roles that the shoe may perform, which include:

a) Over-cut creation and support fluid delivery (Figure 7.10a). The cutting shoe creates the over-cut required to form the annulus around the exterior surface of the caisson. This facilitates reduction of the frictional resistance, through the use of lubricating slurry.

b) Internal groundwater control (Figure 7.10b). The internal excavation level is often dewatered to enable excavation 'in the dry' by locating excavators at the dig level (as in Figure 7.8a). Extending the cutting shoe length ahead of the apex of the cutting face

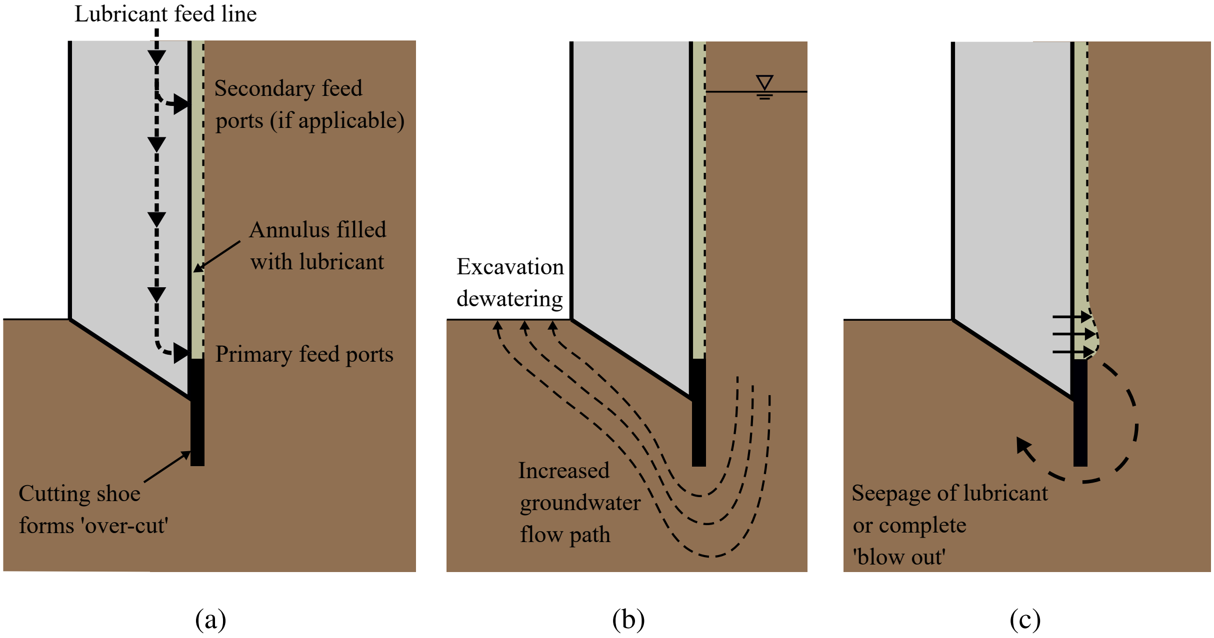

Figure 7.10 Schematic illustration of the main roles of the cutting shoe in open caisson construction: (a) over-cut creation and lubricant delivery; (b) groundwater control; and (c) lubricant seepage/blow-out prevention

increases the groundwater flow path from the exterior soil to the dewatered internal excavation level and potentially 'seals off' permeable sand lenses ahead of the excavation level, thereby relaxing pumping requirements on site.

c) Support fluid seepage/blow-out prevention (Figure 7.10c). By increasing the groundwater flow path, the cutting shoe length also reduces the likelihood of support fluid loss through seepage from the annulus to the internal excavation level. For deep shafts, where the hydraulic pressure of the support fluid at the base of the annulus is high, the cutting shoe also helps to prevent a complete 'blow-out' of the annulus, involving a rotational soil failure mechanism, as shown in Figure 7.10c.

The bearing capacity analyses in Section 6.5 demonstrated that a typical cutting shoe causes notable increases in the bearing resistance, due to the increased embedded footing width and the larger and deeper soil failure mechanisms. Both the cutting shoe size and interface roughness should ideally be minimised to reduce these effects. However, it is clear that the roles outlined above are potentially of greater importance to the sinking process. In particular, the decrease in frictional resistance from a fully supported annulus is likely to greatly exceed the increase in

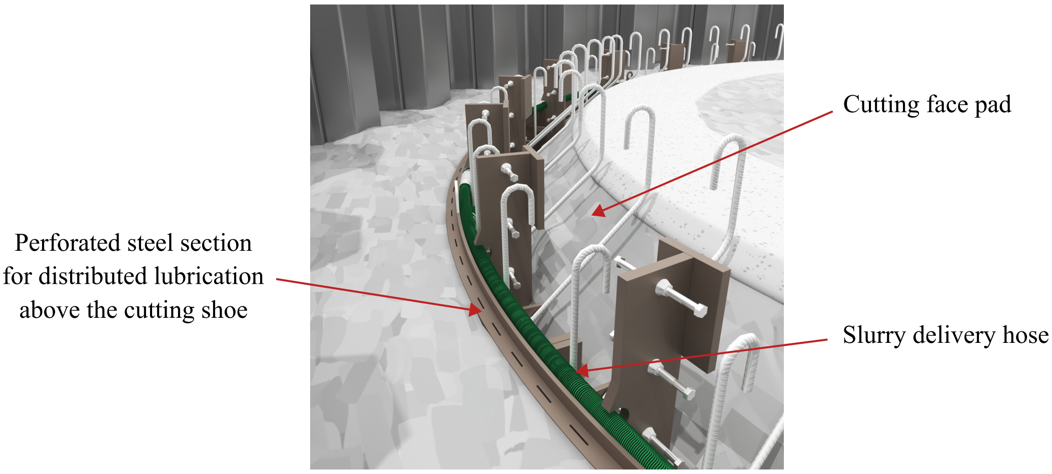

Figure 7.11 System for distributed delivery of lubricant to the annulus above the cutting shoe used by Ward & Burke Construction Ltd

bearing resistance from the cutting shoe, especially for deep caissons. The design of the cutting shoe is therefore highly site-specific and further work is needed to assess the other roles of the shoe, towards seeking greater optimisation.

7.4.3 Friction and lubrication

The experimental test results in Chapter 5 demonstrated the effectiveness of interface lubrication in reducing skin friction in sands. Furthermore, the creation a lubricated over-cut annulus was shown to give a greater reduction in global friction, through more effective distribution of lubricant across the interface surface. In contrast, the use of a non-lubricated over-cut in sands was shown to be counter-productive, resulting in an increase in the normal and frictional stresses.

There is potential for optimisation of the method of lubricant delivery to the over-cut. The use of discrete lubricant injection ports was shown to be ineffective in lubricating a wide area, when the sand was in direct contact with the concrete. There is the risk of sand collapse occurring directly above the cutting shoe (similar to in the dry over-cut test in Section 5.4.2), potentially 'cutting off' the spread of lubricant around the annulus. To maximise the likelihood of full annulus lubrication, a greater density of ports could be used above the shoe. Alternatively, a 'distributed' lubrication delivery system could be used, an example of which is illustrated in Figure 7.11. In this, lubricant flows around a perforated steel channel on top of the cutting shoe. When pressurised, the lubricant is forced out of the holes in the channel, filling the annulus more evenly around the caisson circumference.

7.5 Case study

To illustrate the potential influence of some of the recommendations in Section 7.4, a recent case study is considered involving the construction of a 32 m ID open caisson in dense sand by Ward & Burke Construction Ltd in Blackpool, UK (see Figure 1.4). The bearing capacity of the caisson was considered using the FELA methodology in Section 6.3.1, with different values of β, α_f and cutting shoes. The key caisson and soil parameters documented for this caisson are presented in Table 7.2. For the purposes of this study, the bearing capacity was considered over the embedment range h = 0–12.5 m. Additional details of the project are presented in Royston (2018) and Royston *et al.* (2022a).

Figure 7.12a plots the FELA-calculated influence of β and α_f on the vertical bearing capacity for the Blackpool caisson, with no cutting shoe. At zero embedment, a fully rough footing with $\beta = 30°$ results in an increase in capacity by a factor of 2.0 over $\beta = 60°$. However, for $h/B > 6$ the bearing resistance experienced with $\beta = 60°$ has exceeded that of the steeper cutting faces. This is caused by the formation of an external mechanism at lower embedment depths with the

Table 7.2 Parameters adopted in the FELA analyses of the Blackpool caisson case study

Parameter	**Value**
Internal radius, R	16 m
Wall thickness, B	1.25 m
Cutting face taper angle, β	30, 45, 60°
Soil friction angle, ϕ'	40°
Soil unit weight, γ'	20.0 kN/m^3
Over-cut thickness, t	0, 75 mm
Cutting shoe length, l	0, 250 mm
Cutting shoe back length, l_b	250 mm
Cutting face interface roughness, α_f	0.5,1
Cutting shoe interface roughness, α_s	0,0.5,1

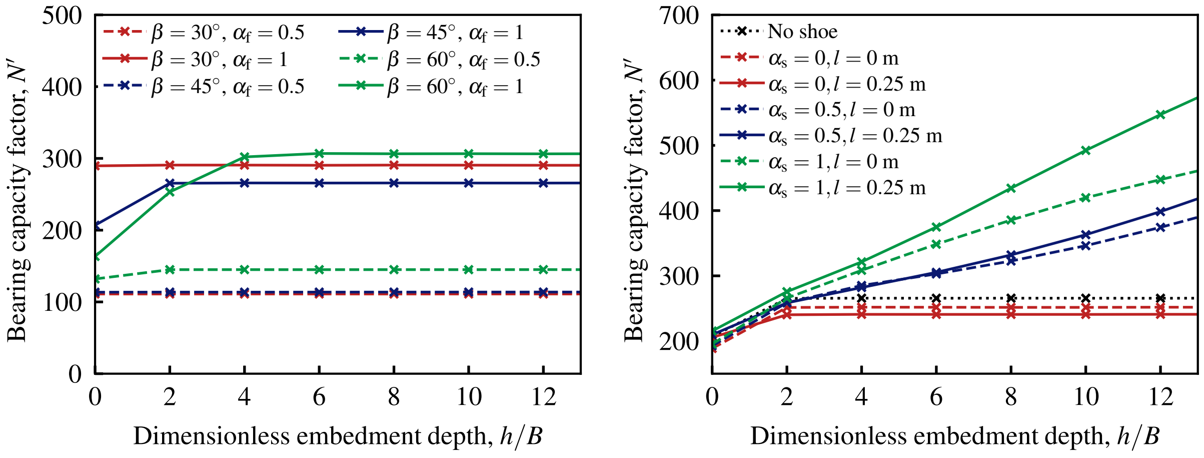

(a) (b)

Figure 7.12 FELA calculations of the vertical bearing capacity for the Blackpool case study: (a) Influence of β and α_f with no shoe, (b) Influence of cutting shoe with $\beta = 45°$ and $\alpha_f = 1$

shallower taper. For all β considered, increasing the cutting face roughness from $\alpha_f = 0.5$ to 1 increases the bearing capacity at deep embedments by a factor of 2.1–2.6. This emphasises the significant reductions in resistance that are possible by controlling the interface roughness.

Figure 7.12b plots the FELA-calculated vertical bearing resistance for the Blackpool caisson using several different cutting shoe designs, with $\beta = 45°$ and $\alpha_f = 1$. At the final embedment depth of $h = 12.5$ m, it can be seen that the choice of the cutting shoe has a remarkable influence on the calculated capacity. For the case of a smooth cutting shoe, there is very little change in the bearing resistance relative to the no cutting shoe case and the critical embedment depth is reached at $h = 2$ m. In contrast, for non-smooth cutting shoes, a significant increase in the bearing capacity with depth is observed and the cutting shoe extension length begins to have an appreciable influence. For $\alpha_s = 0.5$ and 1, the results show that achieving the critical embedment depth is unlikely for this project and therefore deeper embedments are expected to increase the bearing capacity further. The decrease in N' observed with the smooth cutting shoe is an artefact of the increase embedded width in Equation 6.1 with $t > 0$. This highlights the importance of achieving a smooth finish with the fabrication of the cutting shoe, particularly where a long extension is required for groundwater or lubricant control.

7.6 Summary

This chapter has considered applications of the modelling results in this thesis. The numerical modelling methodologies employed in Chapter 6 were demonstrated to compare favourably with the laboratory-scale experimental testing of Royston (2018), showing marked improvement over the current EC7 design calculation. The FELA outputs were used for inform the development of simplified closed-form expressions for calculation of caisson bearing capacity in sand.

Finally, implications of the modelling results on caisson construction were explored, with recommendations made for the selection of specific design features and construction practices. The effects of these recommendations were illustrated using FELA calculations on a case study of a recent caisson construction project.

Chapter 8

Conclusions

8.1 Introduction

This thesis has explored the soil-structure interaction during construction of reinforced concrete open caisson shafts in sand. Numerical modelling was used to systematically investigate the bearing capacity beneath the caisson wall and the influence of salient construction features. Laboratory-scale experimental testing provided insights into the development of skin friction and the use of lubrication at the external caisson-soil interface during sinking. Novel optical force sensor technology was also developed as part of this research. This was applied to create a specialised sensor for the robust measurement of contact stresses in underground construction applications, which subsequently facilitated detailed SSI insights in the caisson friction laboratory testing. This chapter summarises the main contributions of the research and outlines suggestions for future work.

8.2 Key Contributions

8.2.1 Development of novel sensor technology

8.2.1.1 Multi-axis force sensing with FBGs

a) A new framework for the instrumentation of multi-axis force sensors with FBGs was developed in Chapter 3, informed by a state-of-the-art review of force sensing technology summarised in Section 2.4. The sensor structure and instrumentation philosophy are tailored specifically to FBGs, mitigating several of the key issues encountered in previous

FBG-based force sensor attempts.

b) The main novelty is the use of a machine learning model (Section 3.4) coupled with explicit temperature calibration, to automatically determine the sensor input-output mapping and handle temperature compensation. This facilitates a significant reduction in the required number of strain measurements and relaxation of their positioning, when compared with an equivalent design based on conventional arithmetic combinations (Section 3.8).

c) A numerical 'virtual twin' model was shown to be an effective means of simulating the sensor during design. This has been demonstrated using both a bespoke analytical model for a simple sensor structure (Section 3.5.2), and 3D FEA for a more complex designs (Sections 4.3.2–4.3.3). This approach facilitated efficient exploration of different FBG instrumentation strategies (Section 3.6), alongside iterative refinement.

d) A physical prototype of an exemplar six DOF column sensor demonstrated that the framework is implementable with FBGs in practice (Section 3.7). Excellent calibration results were observed, including effective handling of temperature dependence.

e) There are significant commercial opportunities stemming from this research, demonstrated by the filing of two patent applications from the findings of Chapters 3 and 4. The use of a basic prismatic sensor structure, coupled with practical 'snake-like' optical fibre layouts and innovative instrumentation processes (such as used in Section 4.4.2), enables rapid manufacture of the sensors at low cost. The use of optical technology potentially enables multi-axis force sensing in applications where current solutions are not well-suited. The adoption of optical sensing systems is expected to increase in future, given recent innovations in FBG manufacturing techniques and ongoing research into low-cost optical interrogator technologies.

8.2.1.2 SSCS sensor development

a) A new sensor was created for detailed measurement of contact stresses at a soil-structure interface in Chapter 4. The framework described in Chapter 3 was implemented to facilitate the use of optical sensing in the form of FBGs, to overcome the major limitations of electrical sensing highlighted in recent field monitoring (e.g. Phillips *et al.*, 2019; Royston *et al.*, 2022a).

b) The sensor measures the full interface stress state, including total normal stress and bi-directional shear stresses, which very few sensors in the literature are capable of measuring (Section 2.3.2). A means of effective stress measurement was also developed, using deformation of the novel sensor structure under pore pressure loading and an extension to the machine learning framework (Sections 4.2.1–4.2.3). Proof-of-concept of this was demonstrated through numerical simulation (Section 4.3.4) and a physical prototype sensor (Section 4.4.3).

c) Validation testing in Section 4.5 builds confidence that the sensor provides accurate contact stress measurements in typical soil-structure interface scenarios. Furthermore, application of the sensors in the laboratory scale testing in Chapter 5 demonstrated that they are well-suited to the complex frictional interfaces in caisson sinking and pipejacked tunnelling. This highlighted real-world improvements over comparable high-quality electrical sensors.

d) Physical prototyping of the sensor raised the importance of considering FBG birefringence during sensor design. This is likely to be a common issue faced in developing packaged sensors with FBGs, particularly when seeking miniaturisation.

e) Specific design decisions regarding the sensor structure (Section 4.3.4) and overall sensor implementation (Section 4.4.1) were made to limit sensor compliance, maximise sensitivity and faithfully reflect the structural interface surface. Despite this, the sensor technology presented in this thesis represents a compromise between sensing accuracy and the practical benefits of using fibre optics, including robustness and simplified connectivity. For many underground construction applications this is a suitable trade-off, as the reliable detection of the presence of normal and shear contact stresses is of greater value than outright accuracy.

8.2.2 Caisson friction in sand

a) A novel large interface testing apparatus was developed to faithfully simulate the external SLSI during caisson sinking (Section 5.2). Salient features captured by the apparatus include the concrete surface (Section 5.2.4.2), over-cut creation (Section 5.3.5), lubricant delivery (Section 5.2.5) and large shearing displacements. Detailed measurements of the interface stresses were obtained using the new SSCS sensors described in Chapter 4.

b) A suite of experimental tests were presented considering caisson friction in dense sand, focusing on the behaviour at low stress levels. The tests provided insights into different interface conditions, including over-cut formation (Section 5.4.2) and the use of bentonite slurry lubrication (Section 5.4.3).

c) Reduction of the local interface friction via lubrication with bentonite slurry was demonstrated to be highly effective at low stress levels. The formation of an over-cut annulus was shown to achieve greater distribution of the lubricant over the interface compared with direct injection into the sand sample.

d) The use of a non-lubricated over-cut in sand was observed to cause increased lateral stresses and frictional resistance. PIV was used to show sand displacement occurring into the over-cut void, which agrees with caisson field monitoring observations in the literature.

8.2.3 Caisson bearing resistance in sand

a) 2D FELA has been demonstrated to be a useful tool in analysing the bearing resistance at the base of a caisson wall. It facilitates efficient exploration of the wide salient parameter space, whilst providing accurate bearing capacity solutions through adaptive mesh refinement. 2D FEA, with a user-defined material model and custom adaptive mesh refinement, has also been used to consider the caisson bearing capacity problem and overcome some of the limitations associated with FELA. The use of 2D FEA was focused on a more targeted parametric space, to understand the role of soil non-associativity (Section 6.4.4) and the horizontal reaction force (Section 6.4.5), without excessive computational cost.

b) The influence of the cutting face inclination angle on vertical bearing capacity was shown to have strong dependence on both the soil friction angle and cutting face roughness (Section 6.4.1). Similar complex dependencies were also demonstrated for the horizontal resistance (Section 6.4.5). The results revealed the existence of a 'critical' external embedment depth, beyond which the bearing capacity remains constant (Section 6.4.2). The vertical bearing capacity was also shown to strongly increase for smaller caisson radii (Section 6.4.3), particularly with high soil friction angles. The observed dependencies and behaviours were explained using analysis of changes to the soil failure mechanisms in the numerical results.

c) Soil non-associativity was shown to cause a reduction in bearing capacity for high friction angles (Section 6.4.4). A reduction in the size of the soil failure mechanism and the presence of localised shear bands was observed, alongside associated oscillations in the load-displacement response. This is consistent with other numerical research on bearing capacity problems in non-associated flow materials.

d) The parametric study also identified that an external cutting shoe can cause substantial increases in caisson vertical bearing capacity, particularly for deep embedments in high friction angle soils. The influence of cutting shoe geometry (Sections 6.5.1–6.5.2) and interface roughness (Section 6.5.3) were revealed via complex changes induced in the soil failure mechanisms.

e) The 2D FELA results showed good agreement with the experimental test results of Royston (2018), capturing a similar influence of the cutting face inclination angle (Section 7.2). Comparison against the calculations in EC7 (BSI, 2004) highlighted critical limitations of the current methods being used in routine design, including significant under-prediction of the vertical resistance. The 2D FELA outputs were used to inform the development of closed-form design calculations for the vertical penetration resistance of open caisson shafts embedded in cohesionless soils (Section 7.3).

8.3 Recommendations for future work

Application of new sensors

The new sensor technology described in Chapters 3 and 4 can be further developed in several directions. Application of the SSCS sensors in field monitoring on a live underground construction process is necessary to confirm their robustness and build confidence in their outputs. Although the novel effective stress measurement concept was demonstrated in Chapter 4, further work is required to implement the sensor in practice. Refinements of the calibration methods are required, including further exploration of the influence of the load components on the boundary conditions for the sensor thermal response. Future work might also explore optimisation of the design for different applications, including smaller-scale models for laboratory testing and high capacity models for field monitoring.

Advanced modelling of caisson penetration

The numerical study of caisson bearing capacity in Chapter 5 facilitated exploration of a wide parameter space of salient features, but is subject to several simplifications and limitations (as discussed in Section 6.6). A study using more advanced numerical modelling is required to more faithfully capture the full caisson construction process. This could include using a large deformation formulation, such as the coupled Eulerian-Lagrangian method, to simulate the continuous penetration process and soil removal. Furthermore, the application of an advanced constitutive model could provide more realistic sand material behaviour. A model capable of capturing the effects of soil compressibility and the dependence of strength and dilatancy on density, confining stress and shear strain could improve the inconsistencies observed in Section 7.2.

Consideration of the influence of ancillary structures, such as a guide collar and sheet piled cofferdam, would also be a valuable extension to the bearing capacity numerical study herein. This would be complemented by further experimental testing of caisson bearing capacity, particularly at deeper embedment depths and over a range of caisson radii.

Cutting shoe investigations

The influence of an external cutting shoe on caisson vertical bearing capacity in sand was considered in this thesis (Section 6.5). To inform optimisation of cutting shoe design for particular applications, further investigations are required into the other roles of the cutting shoe. This may include exploration of cutting shoe thickness for effective lubricant delivery in different soils and consideration of cutting shoe length, for internal groundwater control and prevention of lubricant blow-out.

Further direct extensions to the numerical bearing study would consider the influence of soil non-associativity, as well as the horizontal force exerted on the shoe and the structural implications for the caisson. A comparable study in cohesive soil would also be of great value, building on the research of Royston *et al.* (2022b).

Caisson friction

Although the laboratory-scale testing in Chapter 5 was able to capture many of the key features of a lubricated caisson-soil interface, the observed behaviours are limited to low stress levels. Extending these tests to higher stresses, by using boundary stress control to model the increased overburden at typical caisson depths, is likely to be an important area of future work. This would build confidence in the applicability of the identified mechanisms at full-scale. Furthermore, caisson friction was considered in Chapter 5 with bentonite slurry lubrication in dense sand samples. Future work could therefore explore the extent to which the identified SLSI mechanics differ across a range of sample densities and different soil types, as well as the use of alternative lubricant fluids, such as polymers.

Caisson uplift resistance

A separate design concern for open caisson shafts in the permanent state is flotation resistance, as their large depth and diameter can result in significant groundwater-induced uplift pressures on the base. Further experiments exploring the frictional capacity of grouting the soil-structure interface after prior lubrication would be of great value, as this is typically neglected in design. Other opportunities include exploring the potential of using underreaming or various forms of anchors to increase uplift resistance (e.g. Sheil *et al.*, 2023).

8.4 Summary

Open caisson shafts are being used worldwide to provide underground solutions to help secure the continued operation of vital infrastructure. The safe and efficient design of these structures is critical, particularly as shafts are constructed of greater size and in more challenging environments, and as conservatism is reduced to decrease material usage and embodied carbon. The research in this thesis aims to enhance understanding of the SSI during the caisson sinking process, which is an area with limited dedicated literature or applicable design methods. The numerical modelling and laboratory-scale experimental testing in this thesis have provided important insight into the bearing and frictional resistances in sand. Furthermore, the advancements in sensing technology presented herein provide the basis for more robust and streamlined measurement solutions for future underground construction monitoring.

This thesis forms part of coordinated programme of research at the University of Oxford, which aims to improve understanding of underground construction processes through developing advanced methods for measuring, monitoring and modelling soil-structure interaction. By working closely with industry partners, this hopes to expedite the application of new technology and methods into practice and maximise the potential contributions in future works.

References

Abbo, A. J., Lyamin, A. V., Sloan, S. W., and Hambleton, J. P. (2011). A C2 continuous approximation to the Mohr–Coulomb yield surface. *International Journal of Solids and Structures*, 48(21), 3001–3010. https://doi.org/10.1016/j.ijsolstr.2011.06.021.

Abbo, A. J. and Sloan, S. W. (1995). A smooth hyperbolic approximation to the Mohr-Coulomb yield criterion. *Computers & Structures*, 54(3), 427–441. https://doi.org/10.1016/0045-7949(94)00339-5.

Abdrabbo, F. and Gaaver, K. (2012). Challenges and Uncertainties Relating to Open Caissons. *DFI Journal - The Journal of the Deep Foundations Institute*, 6(1), 21–32. https://doi.org/10.1179/dfi.2012.002.

Agarwal, S. L. and Venkatesan, S. (1965). An instrument to measure skin friction and normal earth pressure on deep foundations. *ASTM STP392 - Instruments and Apparatus for Soil and Rock Mechanics*. Lafayette, Indiana, USA: ASTM, 152–169. https://doi.org/10.1520/STP41285S.

Allenby, D. and Kilburn, D. (2015). Examples of open caisson sinking in Scotland. *Proceedings of the Institution of Civil Engineers - Geotechnical Engineering*, 168(1), 3–15. https://doi.org/10.1680/geng.13.00117.

Allenby, D., Waley, G., and Kilburn, D. (2009). Examples of open caisson sinking in Scotland. *Proceedings of the Institution of Civil Engineers - Geotechnical Engineering*, 162(1), 59–70. https://doi.org/10.1680/geng.2009.162.1.59.

Anagnostopoulos, C. and Georgiadis, M. (1993). Interaction of Axial and Lateral Pile Responses. *Journal of Geotechnical Engineering*, 119(4), 793–798. https://doi.org/10.1061/(ASCE)0733-9410(1993)119:4(793).

API (2002). *RP 2A-WSD: Recommended Practice for Planning, Designing and Constructing Fixed Offshore Platforms — Working Stress Design*. American Petroleum Institute.

Bayo, E. and Stubbe, J. R. (1989). Six-Axis Force Sensor Evaluation and a New Type of Optimal Frame Truss Design for Robotic Applications. *Journal of Robotic Systems*, 6(2), 191–208. https://doi.org/10.1002/rob.4620060206.

Bekhti, R., Duchaine, V., and Cardou, P. (2014). Miniature capacitive three-axis force sensor. *2014 IEEE/RSJ International Conference on Intelligent Robots and Systems*. Chicago, Illinois, USA: IEEE, 3939–3946. https://doi.org/10.1109/IROS.2014.6943116.

Benmebarek, S., Remadna, M. S., Benmebarek, N., and Belounar, L. (2012). Numerical evaluation of the bearing capacity factor N'_γ of ring footings. *Computers and Geotechnics*, 44, 132–138. https://doi.org/10.1016/j.compgeo.2012.04.004.

Benmebarek, S., Saifi, I., and Benmebarek, N. (2017). Undrained Vertical Bearing Capacity Factors for Ring Shallow Footings. *Geotechnical and Geological Engineering*, 35, 355–364. https://doi.org/10.1007/s10706-016-0110-y.

Berme, N., Lawes, P., Solomonidis, S., and Paul, J. P. (1975). A Shorter Pylon Transducer for Measurement of Prosthetic Forces and Moments during Amputee Gait. *Engineering in Medicine*, 4(4), 6–8. https://doi.org/10.1243/EMED_JOUR_1975_004_032_02.

Bicchi, A. (1992). A criterion for optimal design of multi-axis force sensors. *Robotics and Autonomous Systems*, 10(4), 269–286. https://doi.org/10.1016/0921-8890(92)90005-J.

Bienen, B., Byrne, B. W., Houlsby, G. T., and Cassidy, M. J. (2006). Investigating six-degree-of-freedom loading of shallow foundations on sand. *Géotechnique*, 56(6), 367–379. https://doi.org/10.1680/geot.2006.56.6.367.

Bolton, M. D. (1986). The strength and dilatancy of sands. *Géotechnique*, 36(1), 65–78. https://doi.org/10.1680/geot.1986.36.1.65.

Brachman, R. W. I., Moore, I. D., and Rowe, R. K. (2001). The performance of a laboratory facility for evaluating the structural response of smalldiameter buried pipes. *Canadian Geotechnical Journal*, 38(2), 260–275. https://doi.org/10.1139/t00-102.

Bransby, P. L. (1972). *Cambridge contact stress transducers*. Report No. CUED/C-SOILS/LN2. Department of Engineering, University of Cambridge.

Brinch Hansen, J. (1970). *A revised and extended formula for bearing capacity*. Bulletin No. 28. Copenhagen: The Danish Geotechnical Institute.

BSI (1996). *BS 1377-2: 1990 Soils for civil engineering purposes - Part 2: Classification tests*. London, UK: BSI.

BSI (2002). *BS 1377-4: 1990 Soils for civil engineering purposes - Part 4: Compaction-related tests*. London, UK: BSI.

BSI (2004). *Eurocode 7: Geotechnical design - Part 1: General rules (BS EN 1997-1)*. London: British Standards Institution.

BSI (2007). *Eurocode 7: Geotechnical design - Part 2: Ground investigation and testing (BS EN 1997-2)*. London: British Standards Institution.

BSI (2016). *BS ISO 3310-1:2016 Test sieves - Technical requirements and testing - Part 1: Test sieves of metal wire cloth*. London, UK: BSI.

Byrne, B. W. and Houlsby, G. T. (2005). Investigating 6 degree-of-freedom loading on shallow foundations. *Proceedings of the First International Symposium on Frontiers in Offshore Geotechnics*. Perth, Australia: CRC Press, 477–482. https://doi.org/10.1201/NOE0415390637.

Cassidy, M. J. and Houlsby, G. T. (2002). Vertical bearing capacity factors for conical footings on sand. *Géotechnique*, 52(9), 687–692. https://doi.org/10.1680/geot.2002.52.9.687.

Chandler, J. A., Peraino, J., and Rowe, P. W. (1984). Jamuna River 230 kV Crossing - Bangladesh III. Construction of foundations. *Proceedings of the Institution of Civil Engineers*, 76(4), 965–984. https://doi.org/10.1680/iicep.1984.1172.

Chao, L.-P. and Yin, C.-Y. (1999). The six-component force sensor for measuring the loading of the feet in locomotion. *Materials & Design*, 20(5), 237–244. https://doi.org/10.1016/S0261-3069(99)00009-6.

Chavda, J. T. and Dodagoudar, G. R. (2018). Finite element modelling of extent of failure zone in c-ϕ soil at the cutting edge of open caisson. *Numerical Methods in Geotechnical Engineering IX*. Vol. 2. Porto, Portugal: Taylor & Francis, 999–1007.

Chavda, J. T. and Dodagoudar, G. R. (2022a). Experimental studies on a circular open caisson. *International Journal of Physical Modelling in Geotechnics*, 22(2), 70–87. https://doi.org/10.1680/jphmg.20.00050.

Chavda, J. T. and Dodagoudar, G. R. (2022b). Finite element evaluation of bearing capacity factors for cutting face of open caissons. *International Journal of Geotechnical Engineering*. https://doi.org/10.1080/19386362.2022.2080962.

Chavda, J. T., Mishra, S., and Dodagoudar, G. R. (2020). Experimental evaluation of ultimate bearing capacity of the cutting edge of open caisson. *International Journal of Physical Modelling in Geotechnics*, 20(5), 281–294. https://doi.org/10.1680/jphmg.18.00052.

Chen, W.-F. (1975). *Limit Analysis and Soil Plasticity*. 1st ed. Vol. 7. Developments in Geotechnical Engineering. Elsevier.

Chu, J. and Gan, C. L. (2004). Effect of void ratio on K_0 of loose sand. *Géotechnique*, 54(4), 285–288. https://doi.org/10.1680/geot.2004.54.4.285.

Correia, R., Li, J., Staines, S., Chehura, E., James, S. W., Kutner, J., Dewhurst, P., Ferreira, P., and Tatam, R. P. (2009). Fibre Bragg grating based effective soil pressure sensor for geotechnical applications. *Proceedings of SPIE 7503, 20th International Conference on Optical Fibre Sensors, 75030F*. Edinburgh, Scotland: SPIE, 75030F-1 to 75030F–4. https://doi.org/10.1117/12.835751.

Cunningham, D. M. and Brown, G. W. (1952). Two devices for measuring the forces acting on the human body during walking. *Proceedings of the Society for Experimental Stress Analysis*, 9(2), 75–90.

D'Alessio, P. and Taylor, A. (2016). *Overcoming Inclusions within Diaphragm Walls at Cambridge Heath Shaft Whitechapel*. Technical Paper - Crossrail Learning Legacy. ICE Publishing.

Dao, D. V., Toriyama, T., Wells, J., and Sugiyama, S. (2002). Six-degree of freedom micro force-moment sensor for application in geophysics. *Technical Digest. MEMS 2002 IEEE International Conference. Fifteenth IEEE International Conference on Micro Electro Mechanical Systems (Cat. No.02CH37266)*. Las Vegas, Nevada, USA, 312–315. https://doi.org/10.1109/MEMSYS.2002.984265.

De Borst, R. and Vermeer, P. A. (1984). Possibilites and limitations of finite elements for limit analysis. *Géotechnique*, 34(2), 199–210. https://doi.org/10.1680/geot.1984.34.2.199.

Department for Business, Innovation & Skills (2013). *Construction 2025*. Industrial Strategy. London, UK: HM Government.

Drescher, A. and Detournay, E. (1993). Limit load in translational failure mechanisms for associative and non-associative materials. *Géotechnique*, 43(3), 443–456. https://doi.org/10.1680/geot.1993.43.3.443.

Dwarakanath, T. A., Dasgupta, B., and Mruthyunjaya, T. S. (2001). Design and development of a Stewart platform based force–torque sensor. *Mechatronics*, 11(7), 793–809. https://doi.org/10.1016/S0957-4158(00)00048-9.

Emmons, M. C., Carman, G. P., Mohanchandra, K. P., and Richards, W. L. (2009). Characterization and birefringence effect on embedded optical fiber Bragg gratings. *Proceedings of SPIE 7295, Health Monitoring of Structural and Biological Systems 2009*. Ed. by Tribikram Kundu. Vol. 7295. San Diego, California, USA: SPIE. https://doi.org/10.1117/12.815539.

Faustin, N. E., Elshafie, M. Z. E. B., and Mair, R. J. (2018). Case studies of circular shaft construction in London. *Proceedings of the Institution of Civil Engineers - Geotechnical Engineering*, 171(5), 391–404. https://doi.org/10.1680/jgeen.17.00166.

FBGS (2022). *What is the Minimum Bend Radius of the Fiber?* URL: https://fbgs.com/faq/what-is-the-minimum-bend-radius-of-the-fiber/ (visited on 01/23/2022).

Fernandez Fernandez, A., Berghmans, F., Brichard, B., Mégret, P., Decréton, M., Blondel, M., and Delchambre, A. (2001). Multi-component force sensor based on multiplexed fibre Bragg grating strain sensors. *Measurement Science and Technology*, 12(7), 810–813. https://doi.org/10.1088/0957-0233/12/7/310.

Fischer, G. R., Gerszewski, W. L., Barchok, F. J., and Yavarow, M. K. (2004). Deep Caisson Sinking in Soft Soils, Grand Forks, North Dakota. *Proceedings of the 5th International Conference on Case Histories in Geotechnical Engineering*. New York, NY, USA: University of Missouri-Rolla, MO, USA, Paper 1.67. URL: https://scholarsmine.mst.edu/icchge/5icchge/session01/42.

Fontana, M., Marcheschi, S., Salsedo, F., and Bergamasco, M. (2012). A Three-Axis Force Sensor for Dual Finger Haptic Interfaces. *Sensors*, 12(10), 13598–13616. https://doi.org/10.3390/s121013598.

Frydman, S. and Burd, H. J. (1997). Numerical Studies of Bearing Capacity Factor N_γ. *Journal of Geotechnical and Geoenvironmental Engineering*, 123(1), 20–29. https://doi.org/10.1061/(ASCE)1090-0241(1997)123:1(20).

Gorinevsky, D. M., Formalsky, A. M., and Schneider, A. Y. (1997). *Force Control of Robotic Systems*. 4th ed. Boca Raton: CRC Press.

Griffiths, D. V. (1982). Computation of bearing capacity factors using finite elements. *Géotechnique*, 32(3), 195–202. https://doi.org/10.1680/geot.1982.32.3.195.

Heerema, E. P. (1978). Predicting Pile Driveability: Heather As An Illustration Of The ”Friction Fatigue” Theory. *SPE European Petroleum Conference*. SPE European Petroleum Conference. London, UK: Society of Petroleum Engineers. https://doi.org/10.2118/8084-MS.

Hill, K. O. and Meltz, G. (1997). Fiber Bragg grating technology fundamentals and overview. *Journal of Lightwave Technology*, 15(8), 1263–1276. https://doi.org/10.1049/el:19910971.

Hjiaj, M., Lyamin, A. V., and Sloan, S. W. (2005). Numerical limit analysis solutions for the bearing capacity factor N_γ. *International Journal of Solids and Structures*, 42(5–6), 1681–1704. https://doi.org/10.1016/j.ijsolstr.2004.08.002.

HM Treasury (2020). *National Infrastructure Strategy*. Policy paper.

Hoerl, A. E. and Kennard, R. W. (1970). Ridge regression: Biased estimation for nonorthogonal problems. *Technometrics*, 12(1), 55–67. https://doi.org/10.1080/00401706.1970.10488634.

Houlsby, G. T. and Byrne, B. W. (2005a). Design procedures for installation of suction caissons in clay and other materials. *Proceedings of the Institution of Civil Engineers - Geotechnical Engineering*, 158(2), 75–82. https://doi.org/10.1680/geng.2005.158.2.75.

Houlsby, G. T. and Byrne, B. W. (2005b). Design procedures for installation of suction caissons in sand. *Proceedings of the Institution of Civil Engineers - Geotechnical Engineering*, 158(3), 135–144. https://doi.org/10.1680/geng.2005.158.3.135.

Houlsby, G. T. and Martin, C. M. (2003). Undrained bearing capacity factors for conical footings on clay. *Géotechnique*, 53(5), 513–520. https://doi.org/10.1680/geot.2003.53.5.513.

Huang, J., Wong, C. Y., Pham, D. T., Wang, Y., Ji, C., Su, S., Xu, W., Liu, Q., and Zhou, Z. (2018). Design of a Novel Six-Axis Force/Torque Sensor based on Optical Fibre Sensing for Robotic Applications. *Proceedings of the 15th International Conference on Informatics in Control, Automation and Robotics (ICINCO 2018).* Vol. 1. Porto, Portugal, 517–524. https://doi.org/10.5220/0006911705170524.

Igoe, D. J. P., Gavin, K. G., and O'Kelly, B. C. (2011). Shaft Capacity of Open-Ended Piles in Sand. *Journal of Geotechnical and Geoenvironmental Engineering*, 137(10), 903–913. https://doi.org/10.1061/(ASCE)GT.1943-5606.0000511.

International Tunnelling and Underground Space Association (2019). *Tunnel Market Survey 2019.*

ISI (1982). *IS 9527-1 (1981): Code of practice for design and construction of port and harbour structures, Part 1: Concrete monoliths*. New Delhi, India: ISI.

ISO (2011). *Metallic materials — Calibration of force-proving instruments used for the verification of uniaxial testing machines*. International Organization for Standardization.

Jamiolkowski, M., Ladd, C. C., Germaine, J. T., and Lancelotta, R. (1985). New developments in field and laboratory testing of soils. State-of-the-art report. *Proceedings of the 11th International Conference on Soil Mechanics and Foundation Engineering*. Balkema, 57–153.

Jamiolkowski, M., Lo Presti, D. C. F., and Manassero, M. (2003). Evaluation of relative density and shear strength of sands from CPT and DMT. *Soil behavior and soft ground construction: proceedings of the symposium. Geotechnical Special Publication No. 119*. American Society of Civil Engineers, 201–238. https://doi.org/10.1061/40659(2003)7.

Jefferis, S. A., Troughton, V., and Lam, C. (2011). Polymer systems for fluid supported excavations. *Geotechnical issues in construction: short paper series and 2nd conference* (Nov. 10, 2009). Vol. X513. London, UK: CIRIA, 7–12.

Jennings, J. E. and Burland, J. B. (1960). Rand soil-pressure cell for low pressures, high accuracy and long-term stability. *Journal of Scientific Instruments*, 37(6), 193–195. https://doi.org/10.1088/0950-7671/37/6/304.

Kang, C.-G. (2001). Closed-form force sensing of a 6-axis force transducer based on the Stewart platform. *Sensors and Actuators A: Physical*, 90(1), 31–37. https://doi.org/10.1016/S0924-4247(00)00564-1.

Khasawneh, Y. A., Al-Omari, A. A., and Sharo, A. A. (2017). Distress of a Large Diameter Underground Reinforced Concrete Shaft. *Congress on Technical Advancement 2017.*

Congress on Technical Advancement. Duluth, Minnesota, USA: ASCE, 184–196. https://doi.org/10.1061/9780784481035.017.

Kim, C. and Lee, C.-H. (2016). Development of a 6-DoF FBG force–moment sensor for a haptic interface with minimally invasive robotic surgery. *Journal of Mechanical Science and Technology*, 30(8), 3705–3712. https://doi.org/10.1007/s12206-016-0732-2.

Kim, D., Lee, C. H., Kim, B. C., Lee, D. H., Lee, H. S., Nguyen, C. T., Kim, U. K., Nguyen, T. D., Moon, H., Koo, J. C., Nam, J.-D., and Choi, H. R. (2013). Six-axis capacitive force/torque sensor based on dielectric elastomer. *Proceedings of SPIE 8687, Electroactive Polymer Actuators and Devices (EAPAD) 2013*. Vol. 86872J. San Diego, California, USA: SPIE, 1–9. https://doi.org/10.1117/12.2009970.

Kim, G.-S. (2007). Design of a six-axis wrist force/moment sensor using FEM and its fabrication for an intelligent robot. *Sensors and Actuators A: Physical*, 133(1), 27–34. https://doi.org/10.1016/j.sna.2006.03.038.

Kim, G.-S., Kang, D.-I., and Rhee, S.-H. (1999). Design and fabrication of a six-component force/moment sensor. *Sensors and Actuators A: Physical*, 77(3), 209–220. https://doi.org/10.1016/S0924-4247(99)00208-3.

Krabbenhoft, K., Karim, M. R., Lyamin, A. V., and Sloan, S. W. (2012). Associated computational plasticity schemes for nonassociated frictional materials. *International Journal for Numerical Methods in Engineering*, 90(9), 1089–1117. https://doi.org/10.1002/nme.3358.

Krabbenhoft, K., Lyamin, A. V., Hjiaj, M., and Sloan, S. W. (2005). A new discontinuous upper bound limit analysis formulation. *International Journal for Numerical Methods in Engineering*, 63(7), 1069–1088. https://doi.org/10.1002/nme.1314.

Krabbenhoft, K., Lyamin, A. V., and Krabbenhoft, A. (2016). *OptumG2: Theory*. Optum Computational Engineering.

Kumar, J. and Ghosh, P. (2005). Bearing capacity factor N_γ for ring footings using the method of characteristics. *Canadian Geotechnical Journal*, 42(5), 1474–1484. https://doi.org/10.1139/t05-051.

Lam, C., Jefferis, S. A., and Gifford Goodhue Jr., K. (2010). Observations on Viscosity Reduction of PHPA Polymer Support Fluids. *Proceedings of sessions of GeoShanghai 2010*. GeoShanghai International Conference 2010. Vol. GSP 205. Shanghai, China: ASCE, 184–191. https://doi.org/10.1061/41106(379)23.

LeBlanc, C., Houlsby, G. T., and Byrne, B. W. (2010). Response of stiff piles in sand to long-term cyclic lateral loading. *Géotechnique*, 60(2), 79–90. https://doi.org/10.1680/geot.7.00196.

Lee, J. K., Jeong, S., and Lee, S. (2016). Undrained bearing capacity factors for ring footings in heterogeneous soil. *Computers and Geotechnics*, 75, 103–111. https://doi.org/10.1016/j.compgeo.2016.01.021.

Lehane, B. M., Jardine, R. J., Bond, A. J., and Frank, R. (1993). Mechanisms of Shaft Friction in Sand from Instrumented Pile Tests. *Journal of Geotechnical Engineering*, 119(1), 19–35. https://doi.org/10.1061/(ASCE)0733-9410(1993)119:1(19).

Lindquist, E. S. and Jameson, R. (2011). *Secant Pile Shoring - Developments In Design And Construction*. Deep Foundations Institute.

Liu, S. A. and Tzo, H. L. (2002). A novel six-component force sensor of good measurement isotropy and sensitivities. *Sensors and Actuators A: Physical*, 100(2–3), 223–230. https://doi.org/10.1016/S0924-4247(02)00135-8.

Loukidis, D. and Salgado, R. (2009). Bearing capacity of strip and circular footings in sand using finite elements. *Computers and Geotechnics*, 36(5), 871–879. https://doi.org/10.1016/j.compgeo.2009.01.012.

Lunne, T., Knudsen, S., Blaker, Ø., Vestgården, T., Powell, J. J. M., Wallace, C. F., Krogh, L., Thomsen, N. V., Yetginer, G., and Ghanekar, R. K. (2019). Methods used to determine maximum and minimum dry unit weights of sand: Is there a need for a new standard? *Canadian Geotechnical Journal*, 56(4), 536–553. https://doi.org/10.1139/cgj-2017-0738.

Magne, S., Rougeault, S., Vilela, M., and Ferdinand, P. (1997). State-of-strain evaluation with fiber Bragg grating rosettes: application to discrimination between strain and temperature effects in fiber sensors. *Applied Optics*, 36(36), 9437–9447. https://doi.org/10.1364/AO.36.009437.

Martin, C. M. (1994). Physical and Numerical Modelling of Offshore Foundations Under Combined Loads. DPhil Thesis. Oxford, UK: University of Oxford.

Martin, C. M. (2004). *User Guide for ABC – Analysis of Bearing Capacity*. OUEL Report No. 2261/03. Department of Engineering Science, University of Oxford.

Martin, C. M. (2011). The use of adaptive finite-element limit analysis to reveal slip-line fields. *Géotechnique Letters*, 1(2), 23–29. https://doi.org/10.1680/geolett.11.00018.

Mason, W. P. and Thurston, R. N. (1957). Use of Piezoresistive Materials in the Measurement of Displacement, Force, and Torque. *The Journal of the Acoustical Society of America*, 29(10), 1096–1101. https://doi.org/10.1121/1.1908710.

Mayall, R. (2019). Monopile Response to Scour and Scour Protection. DEng Portfolio. Oxford, UK: University of Oxford.

Milligan, G. (2000). *Lubrication and soil conditioning in tunnelling, pipe jacking and microtunnelling: A state of the art review*. Technical Report. Geotechnical Consulting Group.

Müller, M. S., Hoffmann, L., Buck, T. C., and Koch, A. W. (2009). Fiber Bragg Grating-Based Force-Torque Sensor with Six Degrees of Freedom. *International Journal of Optomechatronics*, 3(3), 201–214. https://doi.org/10.1080/15599610903144146.

National Infrastructure Commision (2017). *Congestion, Capacity, Carbon: Priorities for national infrastructure*.

Nayak, G. C. and Zienkiewicz, O. C. (1972). Convenient Form of Stress Invariants for Plasticity. *Journal of the Structural Division, ASCE*, 98(4), 949–954.

Newman, T. G. and Wong, H.-Y. (2011). Sinking a jacked caisson within the London Basin geological sequence for the Thames Water Ring Main extension. *Quarterly Journal of Engineering Geology and Hydrogeology*, 44, 221–232. https://doi.org/10.1144/1470-9236/09-055.

Nonveiller, E. (1987). Open Caissons for Deep Foundations. *Journal of Geotechnical Engineering*, 113(5), 424–439. https://doi.org/10.1061/(ASCE)0733-9410(1987)113:5(424).

Northcutt, S. and Wijewickreme, D. (2013). Effect of particle fabric on the coefficient of lateral earth pressure observed during one-dimensional compression of sand. *Canadian Geotechnical Journal*, 50(5), 457–466. https://doi.org/10.1139/cgj-2012-0162.

O'Dwyer, K. G., McCabe, B. A., Sheil, B. B., and Hernon, D. P. (2018). Blackpool South Strategy project: analysis of pipe-jacking records. *Proceedings of Civil Engineering Research in Ireland (CERI 2018)*. Dublin, Ireland: CERAI, 265–270.

Othonos, A. (1997). Fiber Bragg gratings. *Review of Scientific Instruments*, 68(12), 4309–4341. https://doi.org/10.1063/1.1148392.

Phillips, B. (2023). Soil-lubricant-structure interface mechanics for microtunnelling. DPhil Thesis. Oxford, UK: University of Oxford.

Phillips, B. M., Royston, R., Sheil, B. B., and Byrne, B. W. (2019). Instrumentation and Monitoring of a Concrete Jacking Pipe. *International Conference on Smart Infrastructure and Construction 2019 (ICSIC)*. Cambridge, UK: ICE Publishing, 457–462. https://doi.org/10.1680/icsic.64669.457.

Phillips, D. T. P. (2002). Field tests on single piles subjected to lateral and combined axial and lateral loads. PhD thesis. Dublin, Ireland: University of Dublin, Trinity College.

Potts, D. M. and Zdravković, L. (2001). *Finite element analysis in geotechnical engineering: Application*. London, UK: Thomas Telford.

Potyondy, J. G. (1961). Skin Friction between Various Soils and Construction Materials. *Géotechnique*, 11(4), 339–353. https://doi.org/10.1680/geot.1961.11.4.339.

Praetorius, S. and Schößer, B. (2017). *Bentonite Handbook - Lubrication for Pipe Jacking*. 1st ed. Berlin, Germany: Ernst & Sohn.

Prandtl, L. (1920). Über die Härte plastischer Körper. *Nachrichten von der Gesellschaft der Wissenschaften zu Göttingen, Mathematisch-Physikalische Klasse*, 74–85.

Puller, M. (1996). *Deep excavations: A practical manual*. 1st ed. Thomas Telford.

Redshaw, S. C. (1954). A sensitive miniature pressure cell. *Journal of Scientific Instruments*, 31(12), 467–469. https://doi.org/10.1088/0950-7671/31/12/313.

Reilly, C. C. and Orr, T. L. L. (2017). Physical modelling of the effect of lubricants in pipe jacking. *Tunnelling and Underground Space Technology*, 63, 44–53. https://doi.org/10.1016/j.tust.2016.11.005.

Reissner, H. (1924). Zum Erddruckproblem. *Proceedings of the 1st International Congress for Applied Mechanics*. 1st International Congress for Applied Mechanics. Delft, Netherlands: Waltman (J Waltman jr.), 295–311.

Richards, I. A. (2019). Monopile foundations under complex cyclic lateral loading. DPhil Thesis. Oxford, UK: University of Oxford.

Richards, I. A., Byrne, B. W., and Houlsby, G. T. (2020). Monopile rotation under complex cyclic lateral loading in sand. *Géotechnique*, 70(10), 916–930. https://doi.org/10.1680/jgeot.18.P.302.

Romiti, A. and Sorli, M. (1992). Force and moment measurement on a robotic assembly hand. *Sensors and Actuators A: Physical*, 32(1–3), 531–538. https://doi.org/10.1016/0924-4247(92)80039-6.

Royston, R. (2018). Investigation of Soil-Structure Interaction for Large Diameter Caissons. DPhil Thesis. Oxford, UK: University of Oxford.

Royston, R., Phillips, B. M., Sheil, B. B., and Byrne, B. W. (2016). Bearing capacity beneath tapered blades of open dug caissons in sand. *Proceedings of Civil Engineering Research in Ireland 2016*. Ed. by J. Goggins. Galway, Ireland: Civil Engineering Research Association of Ireland, 473–478.

Royston, R., Sheil, B. B., and Byrne, B. W. (2022a). Monitoring the construction of a large-diameter caisson in sand. *Proceedings of the Institution of Civil Engineers - Geotechnical Engineering*, 175(3), 323–339. https://doi.org/10.1680/jgeen.19.00266.

Royston, R., Sheil, B. B., and Byrne, B. W. (2022b). Undrained bearing capacity of the cutting face for an open caisson. *Géotechnique*, 72(7), 632–641. https://doi.org/10.1680/jgeot.20.P.210.

Saha, M. C. (1978). Ultimate bearing capacity of ring footings on sand. MEng Thesis. Roorkee, UP, India: University of Roorkee.

Scheinman, V. D. (1969). Design of a computer controlled manipulator. MS Thesis. Stanford, California, USA: Stanford University.

Schmertmann, J. H. (1976). *An Updated Correlation between Relative Density* D_R *and Fugro-Type Electric Cone Bearing,* q_c. Contract Report DACW 39-76 M 6646 WES.

Schnaid, F. (1990). A study of the cone-pressuremeter test in sand. DPhil Thesis. Oxford, UK: University of Oxford.

Schwamb, T. (2014). Performance Monitoring and Numerical Modelling of a Deep Circular Excavation. PhD thesis. Cambridge, UK: University of Cambridge.

Seibold, U., Kubler, B., and Hirzinger, G. (2005). Prototype of Instrument for Minimally Invasive Surgery with 6-Axis Force Sensing Capability. *Proceedings of the 2005 IEEE International Conference on Robotics and Automation*. 2005 IEEE International Conference on Robotics and Automation. Barcelona, Spain: IEEE, 496–501. https://doi.org/10.1109/ROBOT.2005.1570167.

Shahriari, B., Swersky, K., Wang, Z., Adams, R. P., and de Freitas, N. (2016). Taking the Human Out of the Loop: A Review of Bayesian Optimization. *Proceedings of the IEEE*, 104(1), 148–175. https://doi.org/10.1109/JPROC.2015.2494218.

Sheil, B. B. (2021). Hybrid Framework for Forecasting Circular Excavation Collapse: Combining Physics-Based and Data-Driven Modeling. *Journal of Geotechnical and Geoenvironmental Engineering*, 147(12), 04021140. https://doi.org/10.1061/(ASCE)GT.1943-5606.0002683.

Sheil, B. B., Martin, C. M., Byrne, B. W., Plant, M., Williams, K., and Coyne, D. (2018a). Full-scale laboratory testing of a buried pipeline in sand subjected to cyclic axial displacements. *Géotechnique*, 68(8), 684–698. https://doi.org/10.1680/jgeot.16.P.275.

Sheil, B. B., Royston, R., and Byrne, B. W. (2018b). Real-Time Monitoring of Large-Diameter Caissons. *Proceedings of China-Europe Conference on Geotechnical Engineering, SSGG*. Ed. by W. Wu and H.-S. Yu. Vol. 1. Vienna, Austria: Springer, 725–729. https://doi.org/10.1007/978-3-319-97112-4_162.

Sheil, B. B., Templeman, J. O., Orazalin, Z., Phillips, B. M., and Song, G. (2023). Undrained uplift resistance of under-reamed open caisson shafts. *Géotechnique*, Ahead of Print. https://doi.org/10.1680/jgeot.21.00090.

Shewchuk, J. R. (1996). Triangle: Engineering a 2D quality mesh generator and Delaunay triangulator. *Applied Computational Geometry: Towards Geometric Engineering*. Workshop on Applied Computational Geometry. Vol. 1148. Lecture Notes in Computer Science, 203–222. https://doi.org/10.1007/BFb0014497.

Shewchuk, J. R. (2002). Delaunay refinement algorithms for triangular mesh generation. *Computational Geometry*, 22(1–3), 21–74. https://doi.org/10.1016/S0925-7721(01)00047-5.

Simulia (2020). *Abaqus User Documentation 2020*. Dassault Systèmes Simulia Corp., Providence, RI, USA.

Sloan, S. W., Abbo, A. J., and Sheng, D. (2001). Refined explicit integration of elastoplastic models with automatic error control. *Engineering Computations*, 18(1/2), 121–154. https://doi.org/10.1108/02644400110365842.

Staheli, K., Frost, D., and Iscimen, M. (2006). Studies of Interface Friction Between Jacking Pipe Materials and Frictional Soils and the Impact On Jacking Forces. *NASTT No-Dig 2006*. NASTT No-Dig 2006. Nashville, Tennessee, USA: NASTT, D-2-04 - 1–11.

Stanier, S. A., Blaber, J., Take, W. A., and White, D. J. (2016). Improved image-based deformation measurement for geotechnical applications. *Canadian Geotechnical Journal*, 53(5), 727–739. https://doi.org/10.1139/cgj-2015-0253.

Stroud, M. A. (1971). The behaviour of sand at low stress levels in simple shear apparatus. PhD thesis. Cambridge, UK: University of Cambridge.

Talesnick, M. and Ringel, M. (2022). Development of a soil boundary friction meter: application to scale model testing. *International Journal of Physical Modelling in Geotechnics*, 22(1), 26–37. https://doi.org/10.1680/jphmg.20.00019.

Talesnick, M. L., Ringel, M., and Avraham, R. (2014). Measurement of contact soil pressure in physical modelling of soil–structure interaction. *International Journal of Physical Modelling in Geotechnics*, 14(1), 3–12. https://doi.org/10.1680/ijpmg.13.00008.

Tapper, L. (2013). Bearing capacity of perforated offshore foundations under combined loading. DPhil Thesis. Oxford, UK: University of Oxford.

Ter-Galustov, S. A., Ponomarenko, A. I., Opershtein, V. L., and Ivanov, V. D. (1966). Experience in sinking an open caisson in a thixotropic lining. *Soil Mechanics and Foundation Engineering*, 3, 128–131. https://doi.org/10.1007/BF01703486.

Terzaghi, K. (1943). *Theoretical Soil Mechanics*. New York: John Wiley & Sons, Inc. https://doi.org/10.1002/9780470172766.

Thomas, H. S. H. and Ward, W. H. (1969). The Design, Construction and Performance of a Vibrating-Wire Earth Pressure Cell. *Géotechnique*, 19(1), 39–51. https://doi.org/10.1680/geot.1969.19.1.39.

Tibshirani, R. (1996). Regression Shrinkage and Selection via the Lasso. *Journal of the Royal Statistical Society. Series B (Methodological)*, 58(1), 267–288. https://doi.org/10.1111/j.2517-6161.1996.tb02080.x.

Tomlinson, M. J. (2001). *Foundation Design and Construction*. 7th ed. Harlow: Prentice Hall.

Uesugi, M. and Kishida, H. (1986). Frictional Resistance at Yield between Dry Sand and Mild Steel. *Soils and Foundations*, 26(4), 139–149. https://doi.org/10.3208/sandf1972.26.4_139.

Uesugi, M., Kishida, H., and Uchikawa, Y. (1990). Friction between dry sand and concrete under monotonic and repeated loading. *Soils and Foundations*, 30(1), 115–128. https://doi.org/10.3208/sandf1972.30.115.

UK Research and Innovation (2018). *Industrial Strategy Challenge Fund - Transforming construction*. URL: https://www.ukri.org/innovation/industrial-strategy-challenge-fund/transforming-construction/ (visited on 08/26/2019).

United Nations (2018). *World Urbanization Prospects: The 2018 Revision*. ST/ESA/SER.A/420.

Van der Laag, D. A. M. (2016). Design and Calibration of a Multi-Axial Load Cell for Quasi-Static and Dynamic Testing. MSc Thesis. Delft, Netherlands: Delft University of Technology.

Vermeer, P. A. (1990). The orientation of shear bands in biaxial tests. *Géotechnique*, 40(2), 223–236. https://doi.org/10.1680/geot.1990.40.2.223.

Vesić, A. S. (1973). Analysis of Ultimate Loads of Shallow Foundations. *Journal of the Soil Mechanics and Foundations Division*, 99(1), 45–73. https://doi.org/10.1061/JSFEAQ.0001846.

Waterways Experiment Station (1944). *Soil Pressure Cell Investigation (Interim Report)*. Technical Memorandum 210-1.

Weiler Jr., W. A. and Kulhawy, F. H. (1982). Factors Affecting Stress Cell Measurements in Soil. *Journal of the Geotechnical Engineering Division*, 108(12), 1529–1548. https://doi.org/10.1061/AJGEB6.0001393.

White, D. J. and Bolton, M. D. (2002). Observing friction fatigue on a jacked pile. *Constitutive and Centrifuge Modelling: Two Extremes*. Workshop on Constitutive and Centrifuge Modelling. Monte Verità, Switzerland: CRC Press, 347–354.

White, D. J. and Lehane, B. M. (2004). Friction fatigue on displacement piles in sand. *Géotechnique*, 54(10), 645–658. https://doi.org/10.1680/geot.2004.54.10.645.

White, J. R. F. (2020). Laboratory Investigation into the Behaviour of Sand at Low Confining Stresses. DPhil Thesis. Oxford, UK: University of Oxford.

Xiong, L., Jiang, G., Guo, Y., and Liu, H. (2018). A Three-Dimensional Fiber Bragg Grating Force Sensor for Robot. *IEEE Sensors Journal*, 18(9), 3632–3639. https://doi.org/10.1109/JSEN.2018.2812820.

Yao, Q., Yang, X.-G., and Li, H.-T. (2014). Construction Technology of Open Caisson for Oversize Surge Shaft in Drift Gravel Stratum. *Electronic Journal of Geotechnical Engineering*, 19, 5725–5738.

Zhao, L. and Wang, J. H. (2008). Vertical bearing capacity for ring footings. *Computers and Geotechnics*, 35(2), 292–304. https://doi.org/10.1016/j.compgeo.2007.05.005.